



**Materials
Science and
Technology**

**Materiaal-
wetenskap
en -tegnologie**

CSIR

WNNR

**CAVITATION EROSION: THE EFFECT
OF FLUID AND FLOW PARAMETERS**

by

J G Auret

**TRIBOLOGY AND SURFACE ENGINEERING PROGRAMME
JULY 1992**

**CAVITATION EROSION - THE EFFECT OF FLUID
AND FLOW PARAMETERS**

Johannes Gerhardus Auret

**A thesis submitted to the Faculty of Engineering, University of the Witwatersrand,
Johannesburg, in fulfilment of the requirements for the degree of Doctor of Philosophy**

Pretoria, 1992

I declare that this thesis is my own, unaided work. It is being submitted for the degree of Doctor of Philosophy in the University of the Witswatersrand, Johannesburg. It has not been submitted before for any degree or examination in any other University.

J. by Dinet

15th day of July 1992

ABSTRACT

This thesis describes an investigation into the effect of fluid and flow parameters on cavitation dynamics and cavitation erosion. A rotating disc test apparatus was developed for flow-type cavitation studies. A vibratory test device was also developed to study the role of cathodic and anodic potentials applied to cavitating bodies. Some major results are given below.

Erosion peaks at about 50 °C in water, but under certain conditions material degradation caused by increased corrosion rate cancels out thermodynamic effects at higher temperatures. An erosion peak is also observed as a function of static pressure. Damage increases with velocity until cavitation is fully developed, at which stage the influence of velocity becomes negligible. The changes in erosion zone geometry and mass loss caused by temperature, velocity and pressure variations may be correlated with the effect these parameters have on the cavitation pressure profile. Efforts are described to develop a system for measuring this profile in the rotating disc device.

Water quality including dissolved ions, as well as solid and gas impurities, influences both cavitation inception and the amount of cavitation damage caused. The synergism between cavitation erosion and corrosion causes high damage rates in corrosive, cavitating liquids. Solid impurities at medium concentrations may enhance or retard cavitation damage substantially, depending on the physical properties of the solid. Below the saturation level, increasing concentration of dissolved air in water results in a slight decrease in damage, but damage can be almost completely eliminated by the release of air bubbles into the cavitation region.

Another important result is that the gas developed by the application of external potentials to a cavitating body provides protection against cavitation erosion through a gas cushioning mechanism. Cathodic protection of cavitating bodies will thus serve to decrease damage rates even in the case of corrosion-resistant materials like stainless

steels. When anodic potentials are applied, the net effect on damage depends on the balance between accelerated corrosion and thus material dissolution rates, the resulting surface geometry and its effect on the mechanical attack, as well as the gas cushioning effect.

Aan Irma, vir jou vriendskap

Aan my familie, vir jul ondersteuning

Asook aan ons Hemelse Vader wat alles moontlik maak

ACKNOWLEDGEMENTS

1. Professor F.P.A. Robinson, my supervisor at the University of the Witwatersrand, for his inspiring guidance.
2. Mr. G.J. Wright, my Programme Manager at the CSIR, for supporting me during these studies and for supplying substantial financial assistance.
3. All my colleagues who supplied technical advice and assistance, particularly Mr. J. Mokonyane.
4. The Research Organisation of the Chamber of Mines (COMRO), for sponsoring a large part of the research and permitting results to be used in this thesis.

CONTENTS

	Page
DECLARATION	ii
ABSTRACT	iii
ACKNOWLEDGEMENTS	vi
CONTENTS	vii
LIST OF FIGURES	xi
LIST OF TABLES	xviii
LIST OF SYMBOLS AND ABBREVIATIONS	xx
1. INTRODUCTION	1
2. LITERATURE REVIEW	2
2.1 Introduction	2
2.2 Cavitation fluid dynamics	3
2.2.1 Bubble growth	3
2.2.2 Bubble collapse and associated damage models	6
2.2.3 Flow versus vibratory cavitation	10
2.3 Factors influencing erosion damage and damage rates	11
2.3.1 Introduction	11
2.3.2 Dynamic similarity in flows and scale effects	11
2.3.3 Important aspects of cavitation and erosion resistance measurement	14
2.3.4 Pressure and velocity	18
2.3.5 Temperature	20
2.3.6 Size	24
2.3.7 Gas content	24
2.3.8 Corrosion	28

	2.3.9 Solid impurities	30
	2.3.10 Material properties and microstructure	31
2.4	Prediction and testing of erosion	34
	2.4.1 Introduction	34
	2.4.2 Measurement of degree of cavitation development	34
	2.4.3 Erosion testing	36
	2.4.4 Mathematical modelling	39
References		44
3.	TEST RIG DESIGN, EVALUATION AND CALIBRATION	61
	3.1 Selection of concept	61
	3.2 Specifications and design	61
	3.3 Cavitation dynamics and disc design	71
	3.4 Calibration of erosion performance	75
	3.4.1 Introduction	75
	3.4.2 Test procedure	80
	3.4.3 Erosion data and damage characteristics	80
	3.5 Summary	84
References		92
4.	INFLUENCE OF WATER TEMPERATURE AND CORROSION PROCESSES	93
	4.1 Introduction	93
	4.2 Procedure for erosion testing	94
	4.3 Results and discussion	96
	4.3.1 Cavitation dynamics	96
	4.3.2 Erosion data	100
	4.4 Temperature-related material effects on aluminium	110
	4.4.1 Corrosion	110
	4.4.2 Mechanical degradation	115
	4.4.3 Discussion	121

4.5	Summary	124
References		125
5.	INFLUENCE OF STATIC PRESSURE AND VELOCITY	126
5.1	Introduction	126
5.2	Procedure for erosion testing	127
5.3	Results and discussion	127
	5.3.1 Cavitation dynamics	127
	5.3.2 Erosion data	131
5.4	Summary	137
References		138
6.	PRESSURE DIFFERENTIAL	139
6.1	Introduction	139
6.2	Measurement of differential	141
	6.2.1 System using individual miniature pressure sensors	141
	6.2.2 System using strain gauges	145
6.3	Summary	145
References		149
7.	INFLUENCE OF SOLID IMPURITIES	150
7.1	Introduction	150
7.2	Test procedure	153
7.3	Erosion data	153
	7.3.1 40 °C tests	153
	7.3.2 50 °C tests	158
7.4	Discussion	158
7.5	Summary	162
References		163

8.	INFLUENCE OF WATER CHEMISTRY	164
	8.1 Introduction	164
	8.2 Procedure for erosion testing	164
	8.3 Results and discussion	166
	8.4 Summary	169
	References	173
9.	INFLUENCE OF EXTERNALLY APPLIED POTENTIALS	174
	9.1 Introduction	174
	9.2 Vibratory-type test rig	175
	9.3 Preliminary testing	177
	9.4 Test procedure	178
	9.5 Results and discussion	178
	9.6 Summary	196
	References	197
10.	INFLUENCE OF THE AIR CONTENT OF THE WATER	199
	10.1 Introduction	199
	10.2 Erosion test procedure	200
	10.3 Results and discussion	202
	10.4 Summary	202
	References	207
11.	CONCLUSIONS	208
	11.1 General	208
	11.2 Hydropower mining systems	210
	APPENDIX Design drawings for rotating disc test apparatus	213

LIST OF FIGURES

Figure	Page
2.1: Critical size of cavitation nuclei at 26 °C. The bubbles must grow up to the boundary curve before vaporization commences	5
2.2: Raleigh theory of bubble collapse. Collapsing wall velocity, radius, fluid pressure and density are designated by v_w , R , P_0 and ρ , respectively	7
2.3: Jet-collapse models	9
2.4: Typical cavitation or liquid impact "S-shaped" erosion curve	15
2.5: Various forms of the erosion rate versus time curve obtained by different investigators	16
2.6: Cavitation erosion rate versus suppression pressure (or NPSH)	21
2.7: Maximum MDPR versus temperature and vapour pressure for bearing brass (SAE 660)	22
2.8: The influence of temperature on the vapour pressure, viscosity, surface tension and specific gravity of water, gasoline and Na-K eutectic mixture	23
2.9: MDPR versus temperature for SS-316, Al-2024, CS-1018. Vibratory cavitation erosion test in tap water at amplitude 35,1 microns and 2 bar pressure	25
2.10: Inception sigma versus relative air content (hypothetical example)	27
2.11: Erosion rate versus relative air content (hypothetical example)	29
2.12: Cumulative weight loss versus test time for (a) CS-1018 and (b) Al-1100. Vibratory cavitation erosion test in tap water at 18 °C, with 4,52 microns double amplitude and 1 bar pressure	32
2.13: Hypothesized bubble energy spectra for various cavitation conditions at a constant velocity, for a given material in the U-M venturi	35
2.14: Cavitating venturi test section, U-M venturi	37
2.15: Cavitation-damage test section at the Holtwood laboratory, USA	37

2.16:	Shal'nev-type venturi, cavitation behind a circular profile: 1. Walls of the experimental chamber; 2. Model; 3. Test piece; 4. Test piece holding device	38
2.17:	Rasmussen-type rotating disc for cavitation damage with holes for air supply	40
2.18:	Water rotating disc cavitation test device at Pratt and Whitney Aircraft, USA; (a) Cross-section of the PWA rotating disc device, and (b) disc installed in housing (schematic)	41
2.19:	Vibratory cavitation-damage facility at the University of Michigan (U-M)	42
3.1:	Cavitation test rig in its completed form	63
3.2:	Disc design with 12 inducer holes	64
3.3:	Disc and stator configuration inside test chamber	66
3.4:	Mechanical seal (diagramatic)	67
3.5:	Screw-type pump	68
3.6:	Test chamber with stainless steel cooling coil around the inside perimeter	69
3.7:	Shell-and-tube heat exchanger	69
3.8:	Pressure transducer (2 MPa) and chromel-alumel thermocouple installed in the test chamber lid	70
3.9:	Dissolved oxygen probe and copper-constantan thermocouple installed in the flow loop between the reservoir and pump	70
3.10:	Typical flow system used for erosion tests	72
3.11:	(a) Cavitation field formed by middle inducer hole and (b) damage caused by middle inducer and outer inducer holes after 0,5 hours testing	73
3.12:	The influence of various disc design factors on disc power consumption. All other variables were kept constant, although they were not similar for the various graphs	74
3.13:	Disc and sample design for erosion tests: (a) and (b) disc, (c) disc-shaped samples and (d) rectangular samples	76
3.14:	Flow system for cavitation erosion testing of standard materials	81
3.15:	Cavitation field formed behind inducer hole on sample disc	82

3.16:	Cumulative volume loss as a function of test time for (a) the aluminium standard and (b) the two nickel standards	83
3.17:	Relative cavitation erosion resistance of aluminium, nickel and stainless steel standards tested for respectively 12,5; 22,5 and 22,5 hours	86
3.18:	Damage on aluminium sample after (a) 0,5; (b) 1; (c) 3,5 and (d) 4,5 hours of testing	87
3.19:	Undercutting of and material removal from aluminium standard surface due to radial forces exerted by the water	88
3.20:	Undulated surfaces and evidence of material removal on (a) aluminium and (b) stainless steel standards	89
3.21:	Fracture surfaces as a result of material removal from (a) aluminium and (b) nickel standards	90
3.22:	(a) Large hole on aluminium standard where a chunk of material has been removed and (b) striations at the bottom of the hole at higher magnification, indicating failure by a fatigue mechanism	91
4.1:	2S Al alloy samples eroded for 1 hour at 44,8; 49,8; 65,5 and 78,8 °C from top to bottom	97
4.2:	The distance between the downstream edge of the inducer hole and the centre of the main erosion hole, plotted as a function of temperature for the 1 hour tests	98
4.3:	(a) Hypothetical presentation of flow cavitation and (b) the effect of temperature on bubble dynamics. Nuclei extend their travelling distance in the pressure interval below P_v from x_1x_2 at temperature T_1 to x_3x_4 at T_2 .	99
4.4:	Typical temperature and dissolved oxygen variation as a function of test time for the 4 hour tests	101
4.5:	Samples eroded at (a) 49,8 and (b) 78,8 °C. Note the difference in erosion geometry between the A- and B-samples corresponding respectively to the front and back of the disc.	103
4.6:	Large chunk of material which are due to be removed from the edge of the erosion zone on an aluminium sample (magnification x27)	104

4.7:	Effect of temperature for 4 hour and 1 hour erosion tests	106
4.8:	SEM micrographs of samples surfaces corroded at 80 °C, taken (a) within and (b) outside the erosion zone	107
4.9:	SEM micrograph of samples surface eroded at 50 °C, outside erosion zone	108
4.10:	Energy dispersive X-ray spectrum of particles on surfaces eroded at 80 °C	108
4.11:	Typical temperature and dissolved oxygen variation as a function of test time for the 1 hour tests	109
4.12:	Disc design for electric measurements.	112
4.13:	Corrosion cell consisting of 2S Al alloy working electrode (disc), stainless steel auxiliary electrode (inner ring) and stainless steel reference electrode (outer ring)	114
4.14:	Measuring system to investigate the corrosion behaviour of 2S Al alloy in the rotating disc rig	116
4.15:	Bar chart showing the influence of cavitation and temperature on 2S Al alloy corrosion rate	119
4.16:	Rear side of temperature measuring cell showing the two chromel-alumel thermocouples	120
4.17:	Temperature profiles for the WTC and RTC against water temperature at (a) 0,15, (b) 0,18 and (c) 0,20 MPa	123
5.1:	(a) In situ observation of the cavitation cloud and (b) erosion zone on samples A1 to A3. Velocity is 51 m/s and pressure 0,15 MPa	129
5.2:	Cavitation cloud and associated erosion zone for the following sample velocities (m/s) and static pressures (MPa): (a) 48 and 0,10; (b) 48 and 0,12; (c) 48 and 0,135; (d) 51 and 0,12; (e) 51 and 0,135; (f) 51 and 0,15; (g) 51 and 0,25	130
5.3:	The distance between the downstream edge of the inducer hole and the centre of the primary erosion zone, plotted as a function of velocity and pressure	132

5.4:	The distance between the downstream end of the fixed cavity and the centre of the primary hole, plotted as a function of velocity and pressure	133
5.5:	Hypothetical curves of influence of (a) pressure and (b) velocity on cavitation pressure differential	134
5.6:	Curves for volume loss as a function of pressure at 48 and 51 m/s sample velocity	136
6.1:	Normalised pressure as a function of axial position, measured at cavitation inception in a venturi (Re_1 is the Reynolds number at the venturi throat.)	140
6.2:	Sensor holder for miniature pressure sensors	142
6.3:	Holder for miniature pressure sensors mounted in aluminium disc. The sensor is second from the bottom, while the other recesses are filled by aluminium plugs	143
6.4:	Calibration curves for (a) 2 MPa pressure transducer and (b) miniature pressure sensor	144
6.5:	Pressure profile downstream of inducer hole	147
6.6:	New pressure sensor design using strain gauges	148
7.1:	Relative abrasivity of quartzite found in South African mines	151
7.2:	SEM micrographs of (a), (b) PVC and (c), (d) silica powder	154
7.3:	Volume loss as a function of real solids concentration for the 40 °C solids erosion tests	157
7.4:	Volume loss as a function of real solids concentration for the 50 °C solids erosion tests	160
7.5:	SEM micrographs of typical areas outside the erosion zone on samples tested (a) in distilled water and (b) in distilled water mixed with 500 ppm silica	161
8.1:	Volume loss as a function of test time for chemistry erosion tests with (a) 2S Al alloy and (b) low carbon steel BS 1449 samples	168
8.2:	SEM micrographs of 2S Al alloy samples eroded in the artificial mine water showing (a) fine pitting and (b) macropits	170

8.3:	(a) Test surface and (b) rear and sides of low carbon steel BS 1449 samples tested in the artificial mine water showing corrosion pattern	171
8.4:	Optical micrograph of staining (orange colour) as well as fine and large-scale pitting on low carbon steel BS 1449 sample tested in the artificial mine water	172
9.1:	(a) The vibratory-type cavitation test rig after completion, and (b) schematic layout of rig	176
9.2:	The effect of cavitation on a cathodic current applied to a B51S Al alloy sample	179
9.3:	B51S Al alloy sample design	181
9.4:	Volume loss versus test period curves for B51S Al alloy with the following applied currents: (a) 0, (b) cathodic 100 mA, (c) cathodic 50 mA, (d) cathodic 21 mA, (e) anodic 200 mA, (f) anodic 100 mA, (g) anodic 50 mA, (h) anodic 42 mA	184
9.5:	The effect of anodic and cathodic currents on the cavitation erosion of B51S Al alloy	186
9.6:	Relation between anodic current and corrosion rate for a B51S Al alloy sample	187
9.7:	Samples eroded with no external current (left top and bottom), a 100 mA cathodic current (right top), and a 50 mA anodic current (right bottom) applied	187
9.8:	Type 304 stainless steel sample design	190
9.9:	Relation between anodic current and corrosion rate for a type 304 stainless steel sample	191
9.10:	Volume loss versus test period curves for type 304 stainless steel with the following applied currents: (a) 0, (b) cathodic 100 mA, (c) cathodic 75 mA, (d) cathodic 50 mA, (e) anodic 200 mA, (f) anodic 150 mA, (g) anodic 100 mA	193
9.11:	The effect of anodic and cathodic currents on the cavitation erosion of type 304 stainless steel	195
10.1:	Dissolved oxygen (DO) levels for the undersaturated air content tests	203

10.2: 1 hour cumulative volume loss as a function of dissolved air content for the tests under non-saturated conditions	205
10.3: 1 hour cumulative volume loss as a function of air flow rate for the supersaturated air content tests	206

LIST OF TABLES

Table	Page
2.1: Imposed strain rates associated with various mechanical tests	7
2.2: Comparative damage intensities for different types of test facilities	42
3.1: Specified parameter ranges for rotating disc test rig	62
3.2: Test conditions for standard materials	82
4.1: International codes and equivalents for 2S Al alloy	95
4.2: Composition and typical mechanical properties of 2S Al alloy	95
4.3: Fluid and w parameter values for temperature tests lasting 4 hours	101
4.4: Erosion data for the 4 hour temperature tests	102
4.5: Reproducibility of temperature erosion results	104
4.6: Test parameters for 1 hour temperature tests	109
4.7: Erosion data for the 1 hour temperature tests	111
4.8: Test parameters for corrosion rate measurements	117
4.9: Influence of cavitation and temperature on 2S Al alloy corrosion rate	118
4.10: Test parameters for temperature measurements	122
5.1: Test parameters for the pressure and velocity tests	128
5.2: Volume loss as a function of pressure and velocity	135
6.1: Pressure and velocity parameters for the individual sensor-measuring system	142
6.2: Performance and failure history of miniature pressure sensors	146
7.1: Mine water composition (after COMRO, 1983)	152
7.2: Test parameter values for solids erosion tests at 40 °C	155
7.3: Test parameter values for solids erosion tests at 50 °C	155
7.4: Volume loss data for solids erosion test at 40 °C	156
7.5: Volume loss data for solids erosion tests at 50 °C	159
8.1: Composition and mechanical properties of low carbon steel BS 1449 KHR1	165

8.2:	Test parameter values for chemistry erosion tests	167
9.1:	Material data for B51S Al alloy	180
9.2:	Cavitation erosion data for B51S Al alloy with external currents applied	183
9.3:	Material data for AISI type 304 stainless steel	189
9.4:	Cavitation erosion data for type 304 stainless steel with external currents applied	192
10.1:	Test parameter values for air content erosion tests	201
10.2:	Stable dissolved oxygen (DO) values and volume losses for tests with various air content conditions	204

LIST OF SYMBOLS AND ABBREVIATIONS

A_e	=	effective surface area
ASTM	=	American Society for Testing and Materials
α	=	actual gas content of a liquid
α_s	=	saturated gas content of a liquid
C_p	=	pressure coefficient, relating the pressure differential between the surface of a moving submerged object and the bulk of the liquid, with the relative velocity between the object and the liquid
D	=	characteristic dimension (e.g. diameter) of machinery subject to cavitation
DO	=	dissolved oxygen
E	=	elastic modulus
E_T	=	bubble energy flux
ϵ	=	energy required for the removal of a unit volume of material from an eroding surface
$\dot{\epsilon}$	=	strain rate
η	=	liquid viscosity
MDPR	=	mean depth of penetration rate = volume loss rate divided by surface area exposed to cavitation
μ	=	surface tension
NPSH	=	net positive suction head = total absolute head less vapour pressure head (in pumps and turbines)
P_0	=	pressure of undisturbed liquid
P_b	=	bubble pressure
P_i	=	liquid pressure at cavitation inception
P_v	=	vapour pressure
P_s	=	pressure on the surface of an object submerged in a liquid
PVC	=	polyvinyl chloride
R	=	bubble radius

Re_t	=	Reynolds number at a venturi throat
ρ	=	fluid density
SD	=	standard deviation
σ	=	cavitation number
σ_i	=	cavitation number where inception occurs
τ	=	efficiency of bubble energy transfer to the eroding surface
v_0	=	relative velocity between a body submerged in a liquid and the undisturbed bulk of the liquid
v_w	=	bubble wall velocity
ΔV	=	rate of volume loss (VLR)

CHAPTER 1

1. INTRODUCTION

The use of water power or hydropower in South African gold mines offers several advantages, including compatibility with existing infrastructure and economy. A performance-limiting factor in the development of high pressure, high frequency oscillating hydropowered devices, like water hammers and rock drills, was severe damage experienced on critical components. Cavitation erosion was identified as one of the main wear processes. The Chamber of Mines Research Organisation (COMRO) subsequently contracted the CSIR to conduct a fundamental study on the effects of fluid and flow variables on cavitation dynamics and damage, with the aim to develop techniques to control cavitation damage.

This thesis details the investigation done on cavitation erosion and results obtained with the cavitation test rigs developed for the study. A literature review was initially carried out to establish the level of existing knowledge and evaluate existing test rig concepts (Chapter 2). Based on the review and the requirement for compatibility with hydropower conditions, a rotating disc-type rig for the generation of so-called flow-type cavitation was designed, constructed and tested (Chapter 3). It was subsequently used for in situ observation of cavitation dynamics including the effect of fluid and flow parameters, and investigating the effect of these parameters on damage geometry and intensity. Fluid parameters included water temperature (Chapter 4), as well as solid (Chapter 7), chemical (Chapter 8) and air (Chapter 10) impurities in the water. The flow parameters studied were water velocity and pressure (Chapters 5 and 6). As the rotating disc rig was not suitable for studies involving the application of external potentials, a second test rig based on an ultrasonic vibratory probe was also developed for these studies (Chapter 9). In Chapter 11, the results obtained during the investigation are discussed and general conclusions drawn, as well as conclusions pertaining to the minimization of cavitation damage in hydropower equipment.

CHAPTER 2

2. LITERATURE REVIEW

2.1 Introduction

Cavitation means the formation of voids or bubbles within a moving liquid or around a body which is in relative motion with respect to the liquid. The bubbles form due to a local drop in pressure and accompanying rapid vaporization of the liquid. As the bubbles move into areas of higher pressure, they collapse rapidly, producing shock pressures. These pressures are responsible for damage to material in close proximity to the collapsing bubbles - this is cavitation erosion.

In contrast with the formation of bubbles under static conditions in a liquid as in the case of boiling or aeration, cavitation is caused by dynamic pressure reduction. It occurs generally in fluid-handling structures like marine propellers, hydrofoils, dam spillways, gates, and in all forms of pumps and hydraulic turbines. Restricted fluid passage such as valves, venturis, orifices, seals and bearings, give rise to cavitation. It is also sometimes induced by vibration effects under nominally zero flow conditions, as in diesel engine liners and ultrasonic transducers. All of these devices may suffer from cavitation damage to a lesser or greater extent depending on hydrodynamic conditions.

Cavitation and cavitation erosion are mostly associated with negative effects, like loss of material and ultimately destruction of the component, noise and vibration generation and loss of efficiency. A positive application is for cleaning as in ultrasonic baths.

As a wear process, cavitation erosion is a systems problem and is dependent on material, fluid and flow properties. Although almost any material can be damaged by cavitation erosion, the lifetimes of components subject to it can be considerably extended by choosing the most resistant materials which are economically viable. The optimum solution is to select the design and operating conditions of hydraulic machines and

devices such that cavitation will be minimized or displaced to areas where damage is less critical. All of these methods require a basic knowledge of cavitation and the factors influencing it.

Cavitation has thus been intensively studied since about 1900 with the construction of the first steam turbine-driven ships [1], with more than 10 000 papers having been published by 1969 [2]. However, no adequate theory exists to describe the relation between damage and operating conditions. The problem has two aspects: In the first place the relation between damage and liquid properties, flow conditions and material properties for a specific device is still not properly understood. This was confirmed by inconclusive round-robin test results obtained by various laboratories a few years ago [3]. Secondly, no prediction of absolute erosion rates in field machines based on experimental tests or theoretical studies is possible. The term "scale effects" was created to describe all flow phenomena which cause deviations from expected erosion rates.

The present study focused on an improved understanding of the relation between liquid and flow properties versus the amount of cavitation damage caused, in order to facilitate minimizing of cavitation damage, particularly in hydraulic mining equipment. Available information on important aspects of cavitation, and which relate to the work described in the experimental study, is discussed below.

2.2 Cavitation fluid dynamics

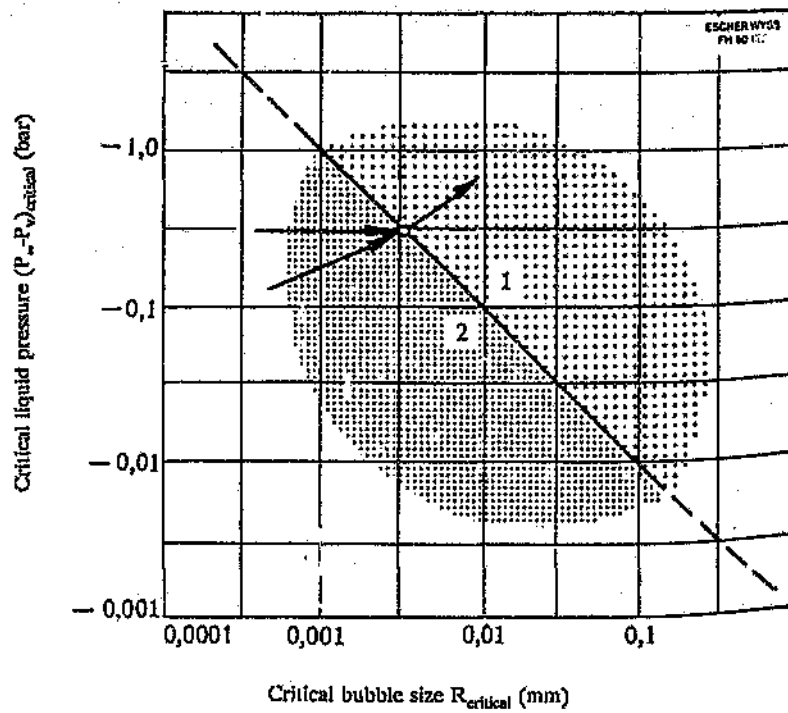
2.2.1 Bubble growth

In practice cavitation occurs at dynamic pressures much higher than the tensile strength of the cavitating fluid. In fact, most fluids cavitate when pressures slightly below their vapour pressure are reached. This phenomenon of seemingly zero tensile strength in liquids is known as the "microbubble paradox". As the terms infers, it refers to the existence of so-called gas or vapour nuclei in a fluid. Theoretically these nuclei or microbubbles cannot exist, since surface tension requires the internal bubble pressure to be larger than the external pressure for a stable condition:

$$P_b - P_0 = \frac{2\mu}{R} \quad (2.1)$$

where P_b and P_0 are respectively bubble and liquid pressure, while μ is surface tension and R bubble radius. This implies that a pure vapour or gas bubble will immediately condense or dissolve, respectively. However, by postulating the presence of micro-impurities in fluids, Harvey [4-7] proved that gas or vapour pockets could be stabilized in unwetted crevices on such impurities. The same principle can of course be applied to boundary walls. Another prominent model for nuclei stabilization is the Fox and Herzfeld organic skin model [8] which assumes a bubble skin containing impurities, and thus capable of withstanding compressive forces. It is also possible that continuous regeneration of nuclei may occur, for example, by cosmic and nuclear radiation [9,10] and free surface gas entrainment.

Equation (2.1) indicates that the underpressure below vapour pressure required for cavitation is dependent on nucleus size as shown in Figure 2.1 by Daily and Johnson [11], so that the larger nuclei will cavitate first. Clearly the size spectrum of the nuclei will have a large influence on the ensuing cavitation and thus damage. Various mechanisms do exist whereby nuclei can grow in their stable range i.e. before the onset of cavitation. Gaseous diffusion may play an important role in the growth of vaporous or gaseous nuclei. Whereas sufficient time may not be allowed for significant diffusion in the case of entrained nuclei, i.e. those travelling with the main flow, stationary nuclei harboured in wall crevices do not suffer from this limitation. A particularly important form of diffusion especially for cases of ultrasonic cavitation is referred to as rectified diffusion. This is the process whereby a net inward flow of gas into the nuclei takes place in an oscillating pressure field due to the increased surface area during the low-pressure part of the cycle [12]. Its effect may be enhanced by pressure variations due to turbulence, pressure pulsations due to a pumping action, etc. Once the nuclei reach their critical size, they become unstable with respect to bubble growth and evolve by rapid vaporization into full-blown cavitation bubbles. Since the bubble has a permanent gas content, this type of cavitation is known as gaseous cavitation as opposed to purely vaporous cavitation.



- 1 Onset of cavitation ($T = 20^{\circ}\text{C}$)
- 2 Stable range: constant gas mass inside bubble

Figure 2.1: Critical size of cavitation nuclei at 20°C . The bubbles must grow up to the boundary curve before vaporization commences

2.2.2 Bubble collapse and associated damage models

Cavitation bubbles invariably collapse due to the increase of the surrounding liquid pressure back to its nominal value. This may happen when the bubbles move further downstream in a flow situation or when the high pressure cycle is applied in the case of vibratory-type cavitation. The collapse is again extremely rapid, and shock-like pressures (see Table 2.1) will be produced which may damage neighbouring solid surfaces. Most investigators agree that cavitation damage is primarily due to mechanical attack with additional effects due to the synergistic interaction between mechanical and corrosive attack. For example, slip lines and surface work-hardening have been observed in metals [13,14]. The single craters formed during the initial stage of damage are roughly symmetrical, usually with a raised rim, as if formed by single impact [15,16] rather than corrosion. In fact, cavitation damage closely resembles liquid impact damage, although it exhibits a much finer scale of pitting.

The exact mechanism of bubble collapse and energy transfer to the eroding surface is still under debate. Several theories have been offered based on both experimental and theoretical results. These are the generation of shock waves due to symmetric single bubble collapses, the impingement of liquid jets generated during asymmetric collapse of single bubbles, the simultaneous effect of both shock waves and jets, and the concerted collapse of bubble clusters [17,18].

Symmetric single bubble collapses

Raleigh [19] was the first to theoretically prove the potential for cavitation damage using a spherical collapse model. His theory is based on the assumption that a cavity with vacuum inside collapses symmetrically in an infinite fluid because of a pressure increase in the fluid. As the cavity size approaches zero, infinite velocity and pressure should be developed in the surrounding fluid (Figure 2.2). Raleigh recognized that the actual pressure at collapse would depend on the amount of non-condensable gas in the bubble, as well as the compressibility of the fluid.

Table 2.1: Imposed strain rates associated with various mechanical tests

Mechanical test	Strain rate $\dot{\epsilon}$, s^{-1}
Creep	10^{-8} – 10^{-3}
Fatigue	10^{-3} – 10
Tensile	10^{-3} – 10^3
High rates of strain and dynamic rupture	10^3 – 10^5
Cavitation erosion	10^4 – 10^6
Shock loading*	10^5 – 10^{10}

*Examples: explosive metal working and welding, projectile impact, dynamic compaction of powders, pulsed radiation, cavitation erosion.

$$v_w = \left(\frac{2 P_0}{3 \rho} \left[\left(\frac{R_0}{R} \right)^3 - 1 \right] \right)^{\frac{1}{2}}$$

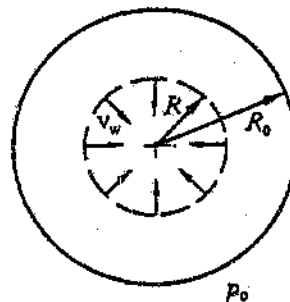


Figure 2.2: Raleigh theory of bubble collapse. Collapsing wall velocity, radius, fluid pressure and density are designated by v_w , R , P_0 and ρ , respectively

Cook [20] expanded the model by including the liquid compressibility. Hickling and Plesset [21] took the effects of both gas content and liquid compressibility into account, showing the incidence of bubble rebound and shock wave generation. However, calculated collapse pressures did not appear sufficient to cause the observed damage on strong materials. The next improvement of the model came from Hammitt et al. [22,23], Lauterborn [24] and Bahl and Ray [25]. By including also liquid viscosity and surface tension, these studies produced damaging pressures and identified the potential importance of surface fatigue.

Asymmetric single bubble collapses

An alternative mechanism is the formation of microjets that suggested by Kornfeld and Suvarov [26]. Eisenberg [27] also argued that damaging jets could form during the asymmetric collapse of cavitation bubbles. Naude and Ellis [28] confirmed asymmetric collapse and jet impingement on a solid neighbouring surface by high-speed photography. Jet velocities were high enough to damage even the most resistant materials.

A whole plethora of workers e.g. [29-36] did similar photographic studies. Figure 2.3 shows three different conceptions derived from these of the way in which the bubbles collapse under different starting conditions. As in the case of spherical bubble collapse, a prerequisite for damage is that the bubble must be close to the surface. The jet must impinge perpendicularly onto the surface for highest efficiency.

Concerted collapse of bubble clusters

Single bubble collapse ignore the mutual influence of bubbles collapsing in close proximity [37]. However, this effect will become significant in cavitating fluids where a high density of bubbles collapse simultaneously, the prime example being ultrasonic transducers in zero flow surroundings. Vyas and Preece [13,38] using a vibratory test rig identified the formation of small individual pits on fcc metals as well as undulation of the surfaces. The undulations developed into craters from which material loss occurred, whereas the pits did not have a significant effect. The formation of the craters as well

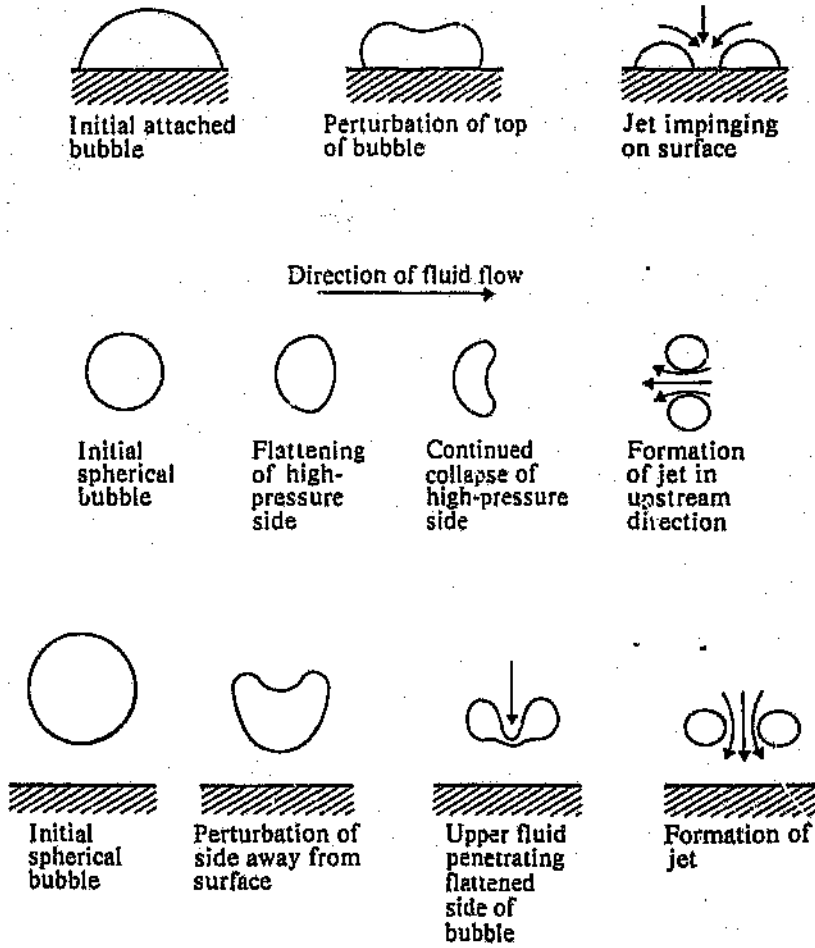


Figure 2.3: Jet-collapse models

an extensive plastic deformation could not be the result of single bubble collapses and was ascribed to the shock wave caused by the concerted collapse of many bubbles.

Hansson et al. [39,40] also using a vibratory test rig, ascribed erosion to the concerted collapse of numerous bubbles, but in a slightly different fashion. Collapse proceeded from the bubble cloud boundary inwards, so that the inner cavities experienced an ever increasing superimposed pressure field which reached a maximum at the cloud centre. Erosion was caused by jet impact (bubbles close to the surface) and shock waves from single cavity collapses (bubbles further away) and was strongest at the centre.

Indications are therefore that cavitation damage in a flowing system is caused mainly by asymmetric bubble collapse due to the pressure and velocity gradients and jet impingement. On the other hand, the high concentration of bubbles and symmetric pressure field may enhance concerted bubble collapse in vibratory cavitation. These differences shed light on the question why vibratory and flow-type test rigs yield different results under nominally similar test conditions.

2.2.3 Flow versus vibratory cavitation

From the preceding discussion, it would appear that several differences in bubble dynamics exist between flow and vibratory cavitation, including the role of rectified diffusion (Section 2.2.1), bubble collapse geometry (Section 2.2.2), and degasification of fluids experiencing vibratory cavitation [41]. As a result, investigators have found that flow and vibratory cavitation have incompatible damage mechanisms [17,42] and a lack of agreement between erosion results [17,43].

This fact highlights the importance of the present study, as the majority of literature results on fluid and flow parameter effects on cavitation erosion have been obtained using vibratory test rigs (as described in the remainder of this chapter).

2.3 Factors influencing erosion damage and damage rates

2.3.1 Introduction

So far it has become clear that cavitation involves an entire sequence of events including bubble nucleation, growth and collapse. The factors controlling cavitation also control the extent of cavitation damage. These factors include fluid properties like compressibility, surface tension, density and vapour pressure; fluid conditions like solids content, gas/vapour content and temperature; and flow parameters like pressure and velocity. The additional category is materials' properties including mechanical and chemical properties. The role of these properties in the erosion process will be discussed.

The comparison of cavitation erosion between various devices and under different hydrodynamic conditions requires an understanding of the concept of dynamic similarity between flows, as well as the various ways of expressing damage.

2.3.2 Dynamic similarity in flows and scale effects

It is highly desirable to have a single parameter defining dynamically similar cavitation, and thus also erosion conditions. Such a parameter should also describe for which flow conditions cavitation will be absent, incipient or developing through various stages.

Preferably a single parameter should serve these purposes. However, since cavitation is influenced by a host of variables this is not possible. Instead, it has become general practice [41] to use a basic parameter based on elementary similarity conditions, and indicate the effect of other variables as deviations from the predictions of the basic parameter. This basic parameter is called the cavitation number (σ) and involves the flow variables of absolute pressure and velocity.

Consider a simple liquid with constant properties and containing an submerged object. Relative motion between the object and the surrounding liquid results in a variation in pressure along the surface of the object. The difference between the pressure at a point

on the object and the pressure in the undisturbed bulk of the liquid is proportional to the square of the relative velocity. This relation can be expressed as the negative of the usual pressure coefficient C_p :

$$-C_p = \frac{(P_0 - P_s)_d}{\rho v_0^2 / 2} \quad (2.2)$$

where ρ = liquid density
 v_0 = velocity of the undisturbed liquid relative to the body
 P_0 = pressure of the undisturbed liquid
 P_s = pressure at a point on the surface of the object
 $(P_0 - P_s)_d$ = pressure differential due to dynamic effects of the fluid motion (For convenience, the subscript d will be omitted after this point.)

At some point on the object, P_s will be a minimum, P_{\min} , so that:

$$(-C_p)_{\min} = \frac{P_0 - P_{\min}}{\rho v_0^2 / 2} \quad (2.3)$$

In the absence of cavitation, this pressure value will depend only on the geometry of the object for a certain set of relative velocity and pressure values. Cavitation can be induced by changing the geometry or by changing the relative velocity and pressure values. In the latter case, this can be done by either increasing v_0 at fixed P_0 or lowering P_0 at fixed v_0 . Either way the local pressure at any point on the object will be reduced and so will P_{\min} . If surface tension of the liquid is ignored, the pressure P_{\min} will be the pressure inside the cavity. Cavitation will occur at a point where the normal stresses in the liquid drop to zero, that is where the pressure P_{\min} equals the vapour pressure P_v of the liquid. By replacing P_{\min} with P_v in Equation (2.3), we can define a cavitation

parameter

$$\sigma = \frac{P_0 - P_v}{\rho v_0^2 / 2} \quad (2.4)$$

The value of σ at which cavitation inception occurs is designated as σ_i . At this value, tiny cavities appear at or near the place on the object where the minimum pressure exists. As σ decreases further by continual increase in v_0 or decrease in P_0 , the zone of cavitation will grow. Thus the cavitation parameter assumes a definite value at each stage of cavitation development of a particular body: For inception, $\sigma = \sigma_i$; for advanced stages of cavitation, $\sigma < \sigma_i$. Values of σ at inception and subsequent stages of cavitation depend primarily on the geometry of the immersed object.

The parameter σ can thus be used to relate the conditions of flow, i.e. v_0 and P_0 to the possibility of cavitation occurring, as well as the degree of cavitation to be expected between different flow systems. In principle, a full-scale device may be designed to restrict the degree of cavitation based on the results obtained from a test rig under similar σ conditions. However, since other parameters than liquid pressure and relative velocity influence cavitation in a relatively unpredictable way, this application of σ is severely limited. The name "scale effects" has been given to the influence of these parameters on cavitation, and thus cavitation erosion in similar σ systems.

Evidently, a basic understanding of scale effects is essential to the optimum design and operation of hydraulic machinery. The situation is summarized in Hammitt's most recent book on cavitation [43]: "Cavitation scale effects apply to all important aspects of cavitation, i.e. inception and damage, as well as performance. Inception and damage affects are probably in general of greater, but not exclusive, importance.. Damage scale affects are here taken to include all these phenomena which result in a change in cavitation-damage rates in a given flow regime occurring as a result of changes in operating conditions such a velocity, pressure, machine size, fluid and fluid conditions (e.g. temperature), all at constant sigma, with geometric and nominal similarity

maintained. In most cases the operative mechanisms, and the fact that such changes in damage rates exist at constant sigma, are fairly clear. However, it is generally not possible in the present state of the art to estimate the changes to be expected other than empirically. In most cases, reliable empirical information is also not available, although in many cases it is at least possible to know the direction of the trends to be expected. Hopefully, within the next decade or two, these matters will be substantially clarified as a result of continuing research." The present study has dealt elaboratively with various important scale effects, with emphasis on their role in the mining industry.

2.3.3 Important aspects of cavitation and erosion resistance measurement

The "amount" of cavitation and erosion under a specific set of hydrodynamic conditions can be quantified in a number of ways. Some of these will be discussed in more detail in Section 2.4. The most popular and most widely used method is undoubtedly the measurement of the erosion resistance of a material, since the influence of fluid, flow and material properties is included. Numerous studies have been made (e.g. [41]) under widely different conditions. Sensible interpretation of these require an understanding of some important aspects of erosion measurement as discussed below.

The basic results of cavitation erosion testing are usually expressed as mass or volume loss (the latter of course if the sample density is available) as a function of testing time. A common practice is to compare the degree of erosion after the same period of testing. However, it has been found [43] that the gradient of such an erosion curve, i.e. the erosion rate changes with time, producing a typical S-shaped erosion-time curve (see Figure 2.4). Several forms of the erosion rate versus time curves have been reported, and some of these are illustrated schematically in Figure 2.5. All the investigations reported here employed a vibratory horn technique with samples attached to the horn tip.

Figure 2.5(a) is due to Thiruvengadam and Preiser [45] and Eisenberg et al. [46] who defined four zones, i.e. the incubation zone in which the erosion rate increased to a maximum, the attenuation zone in which the erosion rate decreased, and the final steady

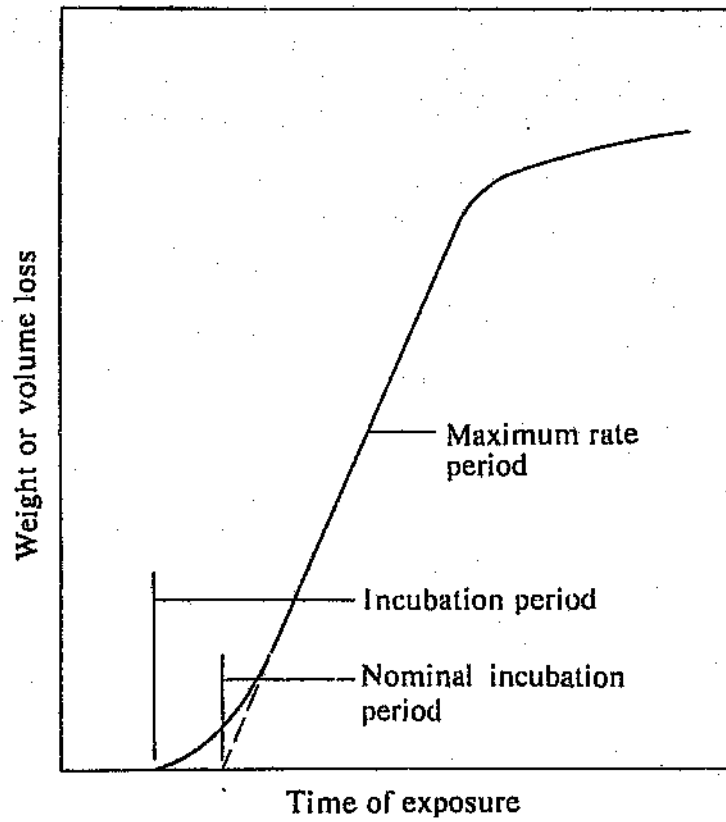


Figure 2.4: Typical cavitation or liquid impact "S-shaped" erosion curve

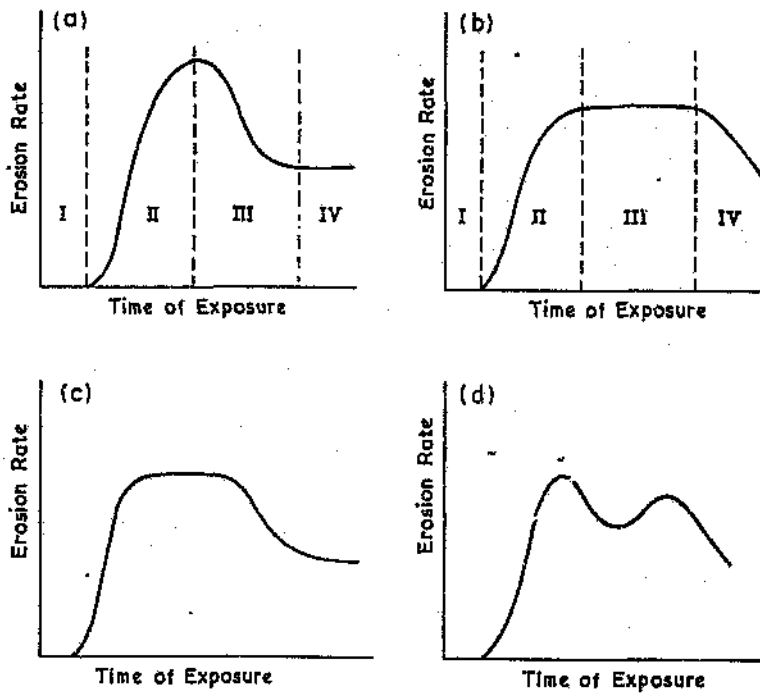


Figure 2.5: Various forms of the erosion rate versus time curve obtained by different investigators

state zone (zones I to IV, respectively). They ascribed the first three zones to the condition of the specimen surface, while the steady state zone was considered representative of the erosion characteristics of the specimen material and thus to be used for comparison with other materials.

Hobbs [47] and Plesset and Devine [48] disputed both the form of the erosion rate-time relationship and the significance of zone IV. They also divided the erosion rate curve into four zones (Figure 2.5(b)) namely incubation period, transition period during which the damage begins locally and spreads over the whole test area accompanied by an erosion rate increase, maximum constant rate and finally decreasing rate period. The reason for the latter was enlargement of the pits formed during the maximum rate period to such an extent that cavitation collapse was attenuated by trapped air or water. They identified therefore the maximum rate period as suitable for material correlation.

Tichler et al. [50] also found a steady state period but identified a second such period (Figure 2.5(c)). During the first, the erosion rate was high and the surface rather uniformly attacked. The second corresponded with the surface being saturated with deep, isolated craters and a relatively low erosion rate. Matsumara et al. [51] found a similar relation to Figure 2.5(a) for some metals, while for others two peaks (Figure 2.5(d)) were observed.

Heymann [52] offered an alternative explanation for the various erosion rate curves in Figure 2.5. The erosion-time curve (Figure 2.4) has to be differentiated to yield erosion rate, and this procedure will magnify the uncertainty and error included in the data. The exact shape of the resulting curve is then very much dependent on personal interpretation. Assuming a fatigue erosion mechanism, Heymann developed a statistical model which could yield any of the observed curves in Figure 2.5. He concluded that the shape of the curve depended on the bubble dynamics characteristic of the specific test. While the erosion rate would, in the absence of other influences, tend towards a steady state value as proposed in [45], this would only happen at a stage when the sample surface has roughened sufficiently to cause the hydrodynamic changes mentioned in [48].

The incubation period is another zone on the erosion curve utilized as an indication of erosion resistance. Studies using this approach were summarized by Rao et al [49] who reviewed the relation between material properties and the incubation period.

The above discussion emphasizes the importance of normalizing data to be compared and which was acquired using different test rigs or dissimilar test conditions. One approach is to use a standard material throughout and determine erosion rates relative to that of the standard material [53,54]. Another is to determine a relative rate of erosion (the ratio between the rate of erosion and the peak rate) and the relative exposure time (the ratio between the exposure time and that corresponding to the peak erosion rate) [55,56]. A prerequisite for such normalization procedures is that the whole erosion curve as a function of time is known, and not only a single point as for earlier tests [57]. Thus many workers publish the whole curve of erosion (mass loss) or erosion rate against test time. A popular way to express erosion rate in the case of relatively uniform attack (as for the vibratory-type test rig) is to divide erosion volume or erosion rate by the eroded area, the resulting data being called respectively mean depth of penetration (MDP) or mean depth of penetration rate (MDPR). The situation is much simpler if only relative results are required, as typified by studies to determine the trends associated with certain hydrodynamic or fluid variables. Cumulative mass or volume loss after a specified period of testing, peak erosion rate or incubation period are measured as indications of erosion resistance. A widely used measure of the development of cavitation is inception sigma σ_1 (e.g. [43]).

2.3.4 Pressure and velocity

Variations in pressure and velocity are responsible for the best known cavitation erosion scale effects. However, both parameters should be varied to keep the cavitation parameter (Equation (2.4)) constant as required for true scale effects. Most previous investigations did not meet this requirement, and Hammitt [43] called the observed results "pseudo" scale effects.

Knapp [41,58] carried out water-tunnel tests in which the effect of velocity at constant

sigma was established by counting the number and size of cavitation pits formed on aluminium per unit area and unit time. Although the effect on pit size was significant, the number of pits was found to increase exponentially with velocity:

$$\text{pitting rate} = (v_2 - v_1)^n \quad (2.5)$$

where $v_2 > v_1$ and $n \sim 6$ for these tests. Since $P_0 \propto v^2$ for constant sigma (Equation (2.4)), this increase could mainly be ascribed to increased collapse violence of the bubbles, and thus a larger number of damaging collapses. Another reason is the higher rate at which bubbles are fed into the cavitation region.

Venturi tests in which the geometry of the cavitation region was kept constant while sigma varied slightly, were reported by Hammitt and Robinson [59,60]. The erosion rate increased exponentially similar to Equation (2.5), but the exponent was between 1,7 and 4,9 in water, while even lower values were obtained in mercury. In the latter case, a negative exponent was observed at high velocities. A similar result came from venturi tests by Rao and Chandrasekhara [61]: Increased velocity initially gave rise to an increase in the erosion rate exponent from 6 to 17, but at higher velocities the exponent became negative. Various workers [62-64] found exponents between 5 and 10 using rotating disc-type test apparatus.

The decrease in erosion rates at high velocities reported from venturi tests may be explained in hydrodynamic terms. As velocity is increased, the number of cavitating bubbles and the extent of the cavitation region also increases. For cavitation near initiation this will result in increased erosion rates. In the case of well-developed cavitation, however, the pressure becomes essentially vapour pressure in the cavitation region, so that a further velocity increase does not enhance damage any further. In general, the relation between velocity and erosion rate will thus depend on the effect of velocity on the dynamic pressure reduction.

When the liquid pressure (P_0 in Equation (2.4)) is increased consistently, the erosion rate

goes through a maximum as shown in Figure 2.6. This behaviour was reported both for vibratory [65-69] and venturi-type [60, 61, 70-73] test devices. Its existence is ascribed to the fact that at low pressures the pressure differential for collapse and thus resulting damage is low. At increased pressures the collapse energy increases, but at the same time the number of cavitating bubbles diminishes. As a result of these opposing mechanisms, maximum damage occurs at an intermediate pressure value.

2.3.5 Temperature

The influence of liquid temperature variation on cavitation erosion arises from several factors, including: (a) changes in liquid properties like viscosity, vapour pressure, surface tension and density, and the effect of these changes have on bubble dynamics, (b) changes in dissolved gas content of the fluid and (c) material property changes [18]. Several studies have been carried out to investigate temperature effects, mainly using the vibratory test rig [65-69, 74-76] although some older work was done in flowing devices of the venturi type [73, 77]. The latter results were however incomplete and did not allow for final conclusions. Results from the vibratory-type rig with temperatures ranging between the melting and boiling points of several liquids, indicated that erosion rate increased slightly with temperature up to a maximum and then decreased dramatically (Figure 2.7). The peak generally occurred about midway between the freezing and the boiling points. Although controversy exists about the exact cause for the low temperature decrease, Leith [78] argued that the high viscosity and surface tension of the fluid (Figure 2.8) were responsible for reduction in bubble collapse energy. Other hypotheses were increased gas solubility and bubble collapse cushioning [79,80], inhibition of corrosion [80] and the combined effect of these changes [81].

The damage reduction at elevated temperature was generally associated with the so-called thermodynamic effect. When the local liquid pressure drops sufficiently for cavitation to take place, a cavitating bubble grows by vaporization. In this process latent heat is extracted from the surrounding liquid layer, i.e. the vapour pressure inside the bubble drops thus retarding bubble growth. Since vapour pressure changes exponentially with temperature (Figure 2.8), the effect is more pronounced at elevated temperature.

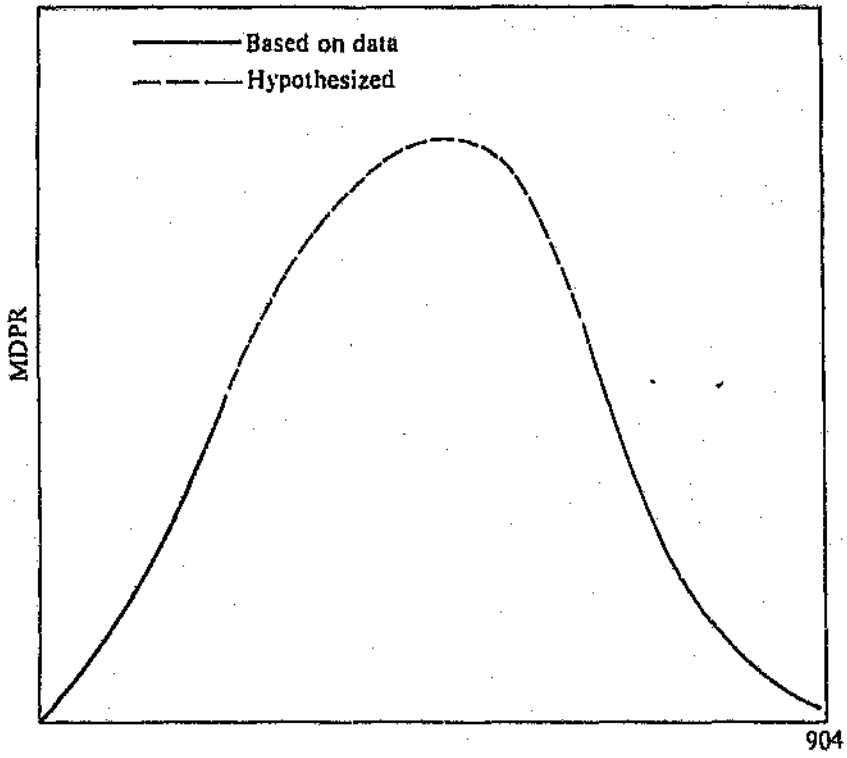


Figure 2.6: Cavitation erosion rate versus suppression pressure (or NPSH)

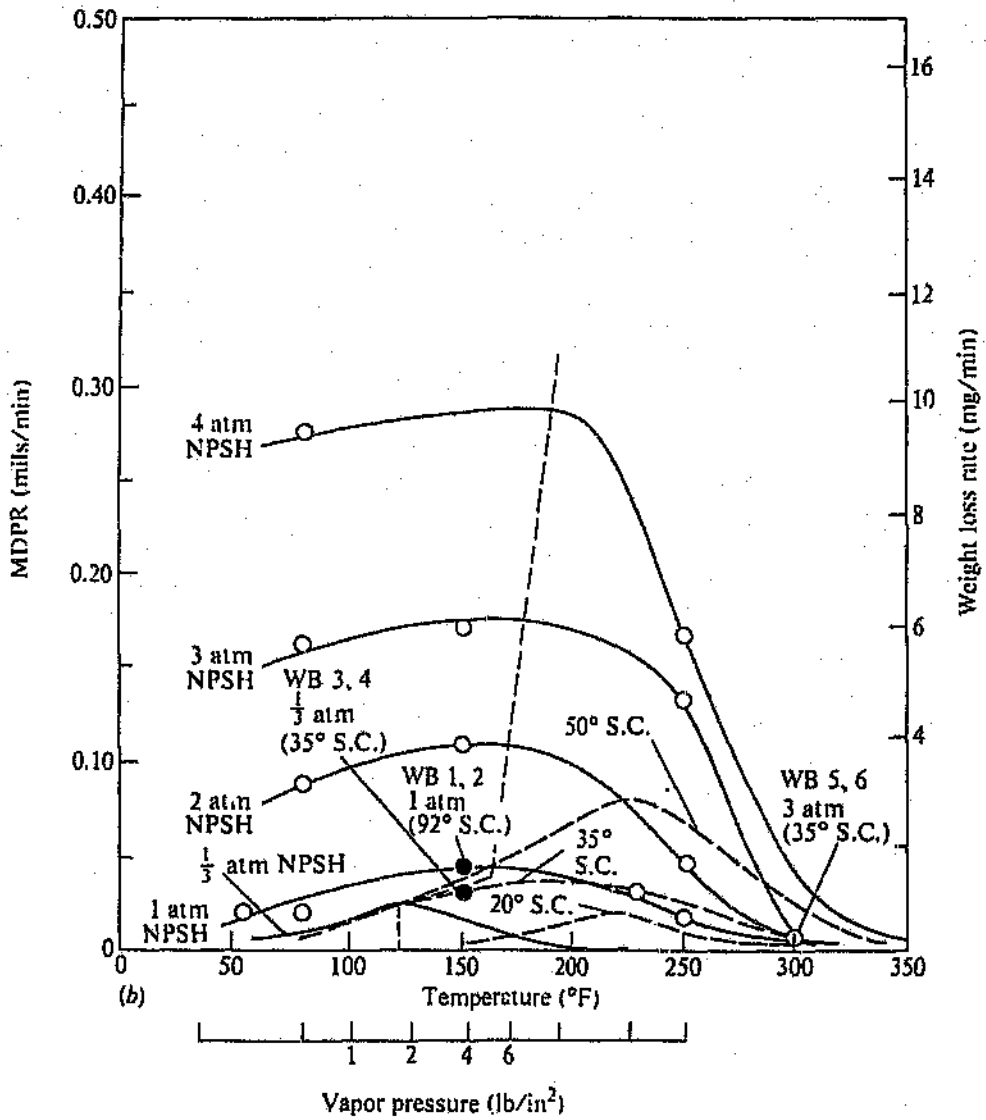


Figure 2.7: Maximum MDPR versus temperature and vapour pressure for bearing brass (SAE 660)

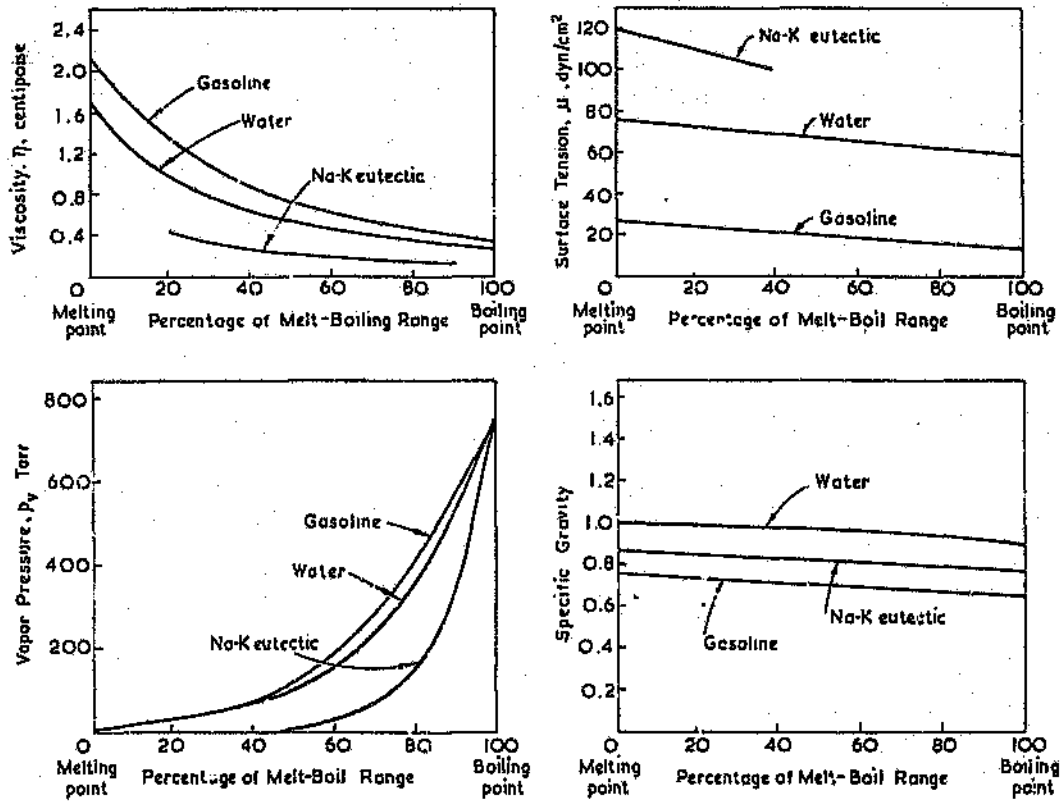


Figure 2.8: The influence of temperature on the vapour pressure, viscosity, surface tension and specific gravity of water, gasoline and Na-K eutectic mixture

An opposing mechanism at elevated temperature namely material weakening and increased corrosion rate as a result of increased temperature will become more noticeable in the case of low melting point materials. An example was reported for an aluminium alloy in [82], where a second rise in erosion rate occurred (Figure 2.9).

2.3.6 Size

The problem of size scale effects between machines of various sizes (typically model and prototype) is a highly complex one. One reason is that constant sigma does not imply a constant cavitation regime [43]. Ignoring this problem, it is generally assumed that the area of erosion varies as the square of any characteristic dimension [43]:

$$\text{area of erosion} \propto D^n \quad (2.6)$$

where $n = 2$. Assuming similarity in hydrodynamic conditions the erosion rate should be proportional to the damaged area and thus to the square of D .

However, theoretical [83] and experimental studies in venturi devices [84-88], pumps and turbines [43,87,89,90] and a rotating disc apparatus [91] indicated an erosion rate exponent of between 2 and about 5. Rao and Buckley [92,93] found that the exponent in Equation (2.6) varied between 1,6 and 3,4 for tests at constant sigma in venturi and rotating disc devices. Furthermore they indicated that bubble collapse energy would be a play-off between increased bubble size as a result of longer exposure to underpressure, and a decrease in the number of bubbles in the cavitation region. They ascribed the observed range of erosion rate exponents to the combined contribution of the area effect and the hydrodynamic effect.

2.3.7 Gas content

The existence of cavitation at positive liquid pressures depends on the presence of small gas pockets or nuclei [7]. Thus gas (or air) content is an extremely important factor in

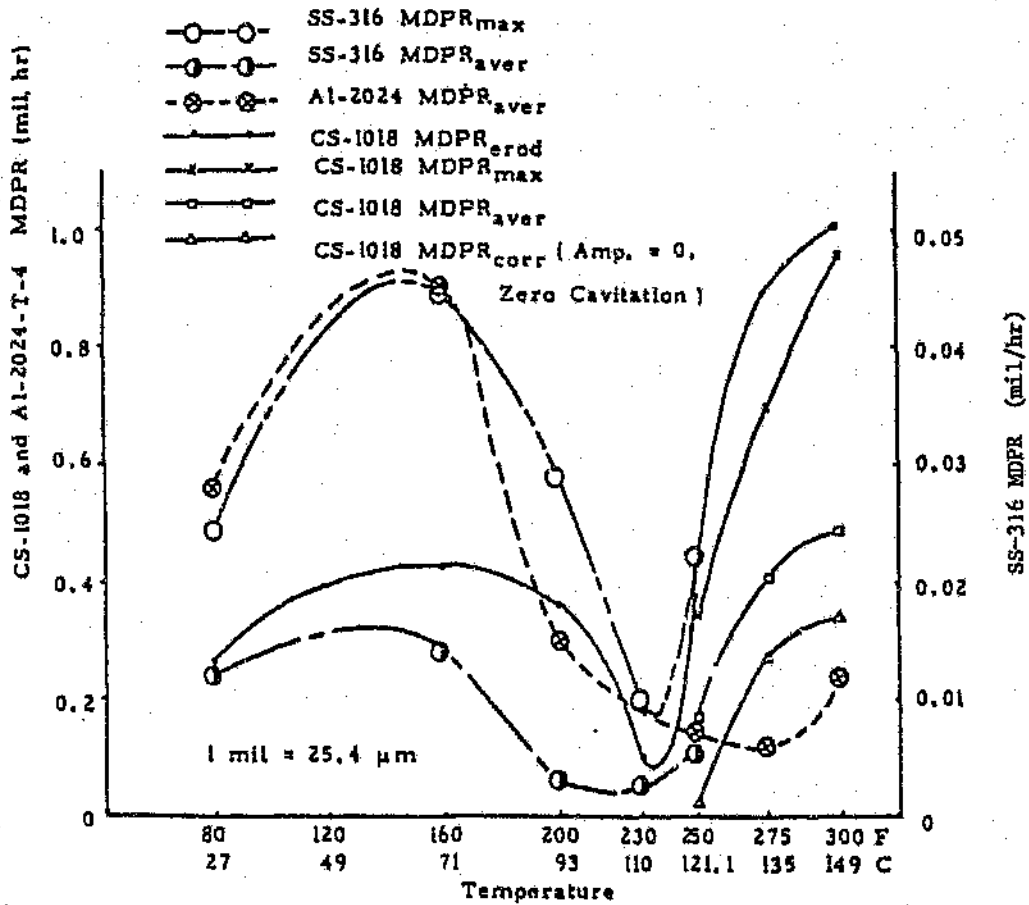


Figure 2.9: MDPR versus temperature for SS-316, Al-2024, CS-1018. Vibratory cavitation erosion test in tap water at amplitude 35.1 microns and 2 bar pressure

various aspects of cavitation, including nucleation and cavitation inception, bubble dynamics, collapse damage and chemical reactivity of the eroded surface.

The nucleation threshold of a liquid depends very strongly on the number and size distribution of the nuclei in the liquid [11]. These microbubbles probably cover the (diameter range of 10^{-6} to 10^{-4} mm [43]. Volume-wise the portion of so-called entrained gas is extremely small ($\sim 10^{-6}$ of total gas content). The remaining dissolved gas constitutes the largest portion of the total gas content and may play an important role in bubble growth, especially in situations where prolonged diffusion or rectified diffusion (see Section 2.2.1) takes place. Thus bubble collapse will be retarded due to the presence of a finite volume of gas in the bubble and damage will decrease.

Chemically active gases like oxygen will influence corrosion reaction rates on the eroding surface. In the case of less noble materials, the rate of corrosion will increase. The influence of gases on more noble materials or those protected by the formation of surface layers, is determined by the balance between the rates of corrosion and layer formations [94]. This last aspect will be covered in more detail in Section 2.3.8.

Numerous studies regarding the influence of air or gas content on cavitation inception sigma (Section 2.3.2) have been reported (see [43] for a summary). The largest percentage of these were in flow cavitation systems, although some work was done in vibratory test rigs as well. In general, inception sigma was found to increase with increasing gas content, as illustrated in Figure 2.10. However, the dynamic processes are not yet fully understood, mainly for two reasons. Firstly it is extremely difficult to measure the nuclei population and size distribution, although the existence of a number of promising laboratory-scale measuring systems have been reported. These include optical and acoustic techniques and the measurement of electrical conductivity in the fluid [43]. Secondly, it is not possible to describe in sufficient detail the actual flow patterns and thus to derive the pressure and velocity history of a given nucleus.

Studies of the effects of gas content on cavitation damage are far more limited. Reported results include theoretical modelling [21,95] and experimental studies in venturi

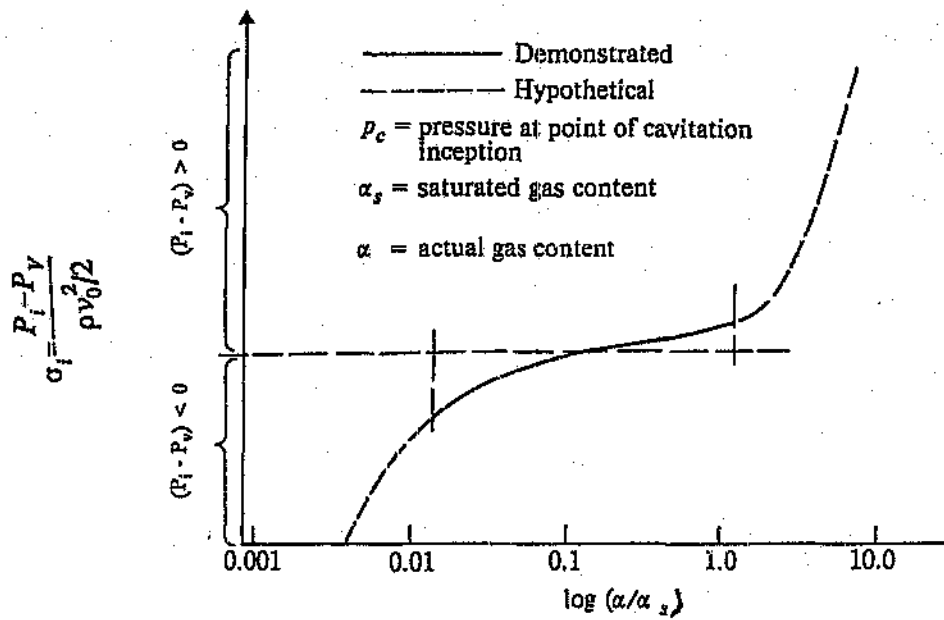


Figure 2.10: Inception sigma versus relative air content (hypothetical example)

[72,96,97], rotating disc [96,97] and vibratory [65,98,99] test rigs. The presence of gas in a liquid stimulates nucleation and may thus at high sigma determine the existence or not of cavitation. Once cavitation has been established, further increase in gas content will for the same reason enlarge the number of cavitation bubbles, the collapse of which may contribute to cavitation damage. However, large quantities of entrained or dissolved air has been found to reduce damage [41]. This may be related to increased gas content in collapsing bubbles and thus cushioning of collapse, or to more rapid attenuation of shock waves in the surrounding liquid [43]. These opposing mechanisms result in the occurrence of a peak in the hypothetical erosion rate curve (Fig 2.11).

In summary, accurate prediction of either cavitation inception or damage rate for a certain set of hydrodynamic conditions is impossible due to experimental and theoretical limitations. However, fairly firm qualitative trends have been established (Figures 2.10 and 2.11).

2.3.8 Corrosion

Numerous studies (e.g. [100-105,46]) have shown that the combined damage due to simultaneously acting cavitation and corrosion effects can be much larger than when the two effects act separately. Industrial examples include marine propellers, hydraulic turbines (sometimes even in fresh water), and diesel engine piston liners. This synergism between the mechanical and chemical attack may be ascribed to the following interactive mechanisms:

1. In addition to its inherently detrimental effect, corrosive attack roughens the damaging surface and thus enhances cavitation erosion. A contradicting view [104] was that mechanically stressed layers is removed by corrosion, leaving an unstressed surfaces less prone to cavitation attack.
2. Cavitation erosion impact on the surface removes any protective layer which may normally inhibit rapid corrosion with most materials, thus exposing fresh, chemically active surface. The presence of corrosive gases like oxygen at elevated temperatures in collapsing bubbles [107,43] may also contribute to corrosion.

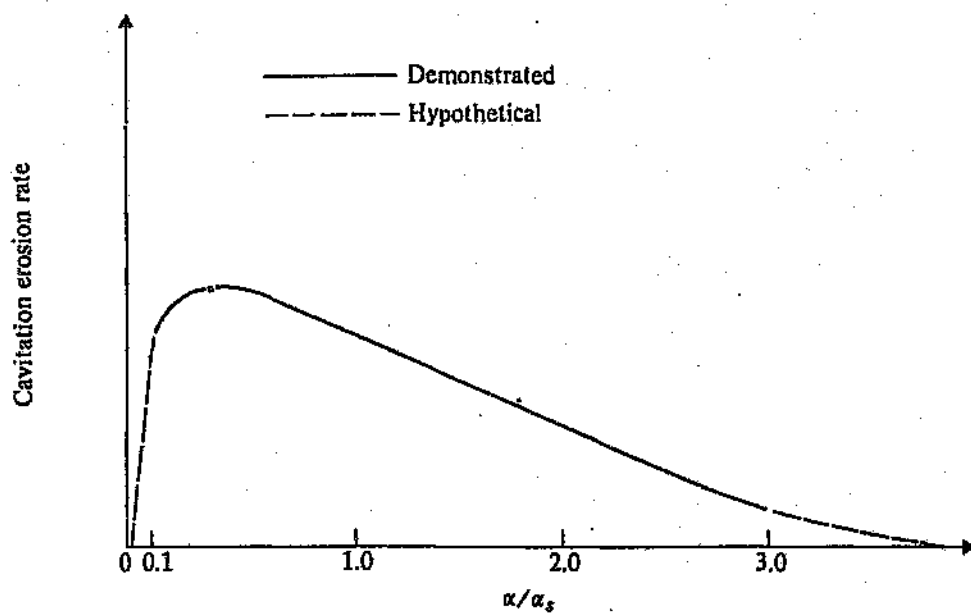


Figure 2.11: Erosion rate versus relative air content (hypothetical example)

The rate of corrosive attack on metallic materials is controlled by the inherent resistance of the material against corrosion, as well as external factors like the chemistry and temperature of the liquid and the application of cathodic and anodic potentials or currents.

It was reported in the past [100,101] that the application of a cathodic potential protects the eroding surface. Agreement was not reached on the exact nature of the protective action which could be due to diminishing of corrosion rates [100] or cushioning of bubble collapse by the development of electrolytic gas at the eroded surface [101] or perhaps both of these. Results from studies [46,100,106,108,109] where both cathodic and anodic potentials were applied to cavitating metallic specimens, were contradictory. In some cases, damage increased continuously as the voltage was changed from strongly negative, through zero, to positive, the highest damage rates occurring in the latter regime. In other cases, damage was reduced for both anodic and cathodic potentials. All these experiments were carried out in test facilities of the vibratory type, and more work is required to clarify the issue.

2.3.9 Solid impurities

It is obvious that cavitating slurries, i.e. liquids containing a high percentage of solids, will cause high erosion rates due to the combined onslaught of cavitation erosion and solid particle impingement [43]. However even relatively low concentrations of solids may influence cavitation. In fact, the presence of partially unwetted microscopic solid impurities in nominally pure fluid facilitates nucleation by stabilization of microbubbles [4-7,110] or decreasing the tensile strength of the fluid [10]. This will cause increase of inception sigma and the number of cavitating bubbles. However the presence of dissolved macromolecules in fluids was found to suppress cavitation as described below.

Recently, a number of workers [112-117] reported the results of investigations in vibratory and flow-type test rigs to evaluate the effect of small quantities of soluble low-friction polymers in water and other cavitating liquids. A decrease in inception sigma was generally found, i.e. cavitation inception was inhibited. This was ascribed to

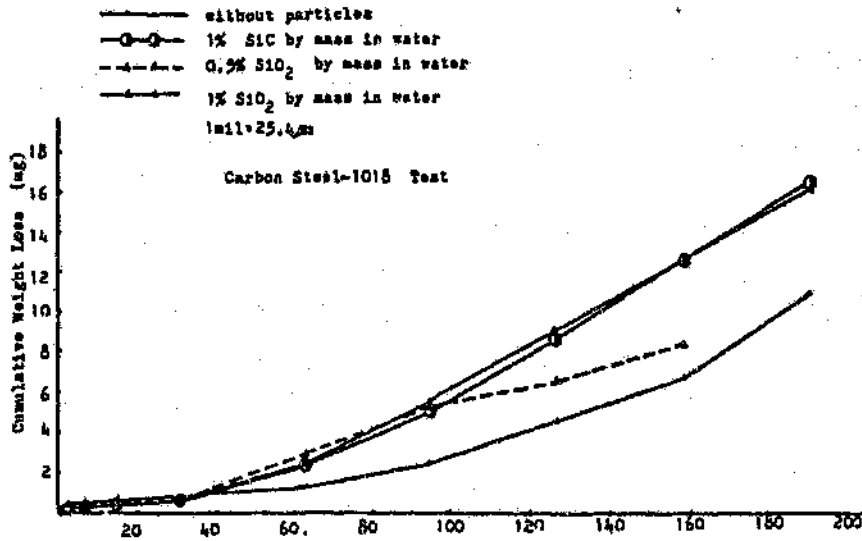
either hydrodynamic changes by the reduction of turbulence, or the consumption of tensile energy from the fluid to stretch the visco-elastic molecules. Reduction of cavitation damage was reported by Sun [112] and Kimoto [113].

The effect of microscopic solid particles on cavitation erosion under fully developed cavitation conditions has been investigated by Wang and Hammitt [118] in a vibratory facility. Aluminium and carbon steel samples were eroded in water containing SiC and SiO₂ particles. In the later stages of testing, substantially increased damage rates were observed (Figure 2.12). The enhanced erosion damage was associated with the inclusion of the hard, abrasive particles in microjets impinging on the eroding surface, causing an abrasion-erosion effect. Enhanced nucleation should have played a minor role in these and similar tests since the cavitation conditions were already optimized.

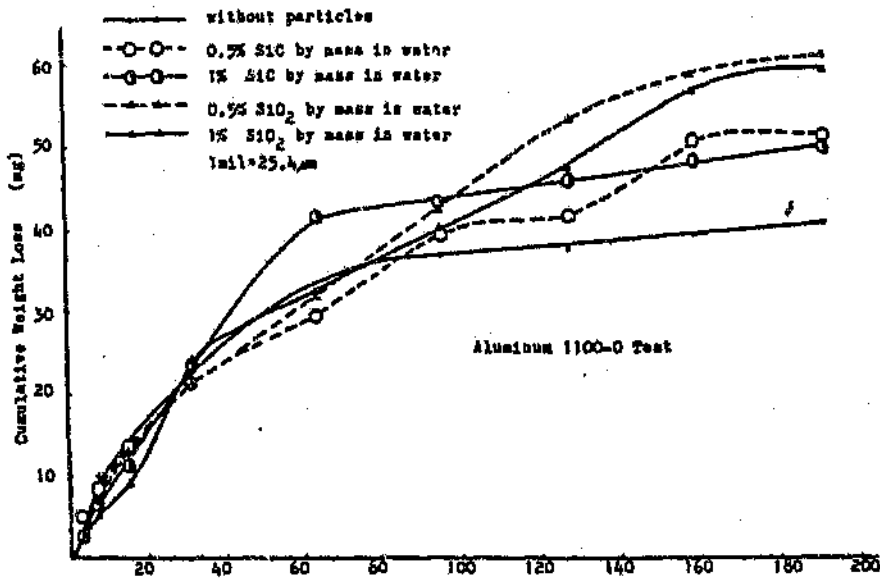
2.3.10 Material properties and microstructure

In general it has not been possible to provide accurate correlations between measurable bulk material properties and measured erosion rates. Part of the problem is the employment of unsatisfactory experimental procedures [119]. Firstly, many results are based on qualitative data and comparative tests. Secondly, data was mainly obtained with vibratory test rigs which do not produce realistic cavitation erosion in terms of practical applications. Thirdly, a lack of information on the shape of the erosion-time curve has made comparison of many results infeasible. Different features of the curve have been considered typical of cavitation erosion, including incubation period [49], peak erosion rate [47, 48] and steady state [45,46].

Various investigators have reported correlations between different material parameters and cavitation damage, but only for limited ranges of materials [18]. Hardness has traditionally been considered a good index to erosion resistance [64,74,120,121], and the same or similar materials usually show a fairly consistent increase in resistance with a power of hardness. However, curves for different materials or alloy types do not coincide [54].



(a)



(b)

Figure 2.12: Cumulative weight loss versus test time for (a) CS-1018 and (b) Al-1100. Vibratory cavitation erosion test in tap water at 18 °C, 4,52 microns double amplitude and 1 bar

In the case of very ductile materials, the strain energy to fracture as defined by the area under a tensile stress-strain curve was found to correlate well with erosion resistance [46, 122], since this reflects the ability of a material to absorb impact energy. On the other hand, very poor correlation was found in other cases [47,53,54], and another parameter, i.e. ultimate resilience defined as $F^2/2E$ was proposed, where F is the fracture strength and E the elastic modulus. Ultimate resilience represents the failure energy if rupture is in the brittle mode, and seems to be more suitable for tough materials, including stainless steels and cobalt alloys.

Since fatigue may be important in cavitation erosion [39,123], some workers investigated the existence of a threshold value below which no erosion occurred. Thomas and Brunton [124] found a fairly good relationship between the strain energy required for fatigue fracture and erosion rate in the case of ductile materials such as copper, brass, mild steel and 18Cr-8Ni stainless steel. Similar relations have been reported by Okada et al. [125] for cast iron and carbon steels.

The main reason [18] for the lack of agreement between the physical parameters determined by tensile and hardness tests and erosion resistance is that these tests are carried out under quasi-static loading conditions, while cavitation impact is in the form of dynamic, high-stress, short-term impulses (Table 2.1). These shock-loading conditions enhance the strain-rate sensitivity of material deformation and fracture which is dependent on microstructure. Thus recently a number of investigators have described the influence between microstructural aspects and cavitation erosion, as summarized in [18] and [19].

It was found that materials possessing a mechanism for the absorption of cavitation energy, such as work hardenability, have high resistance to erosion. Examples are brasses and bronzes, Stellites and austenitic stainless steels, which work harden respectively through planar slip, twinning and the transformation to martensite. On the other hand, in multiphase alloys (e.g. copper alloys and Stellites), the strength of the matrix and its ability to retain second phase particles determine the resistance of the material. In general, a smaller grain size enhances erosion performance. The high erosion resistance

of Co is due to fine-scale twinning which effectively reduces the average grain size.

2.4 Prediction and testing of erosion

2.4.1 Introduction

Despite the problems associated with prediction of cavitation erosion, a number of useful methods have been developed to establish at least qualitatively the degree of erosion to be expected due certain hydrodynamic and material properties. These include measuring the "amount" of cavitation, erosion testing in laboratory test rigs or in field devices, and modelling of expected erosion resistance.

2.4.2 Measurement of degree of cavitation development

The basic assumption in using this approach is that the amount of damage increases as the bubble cloud develops. Initially, cavitation noise (caused by bubble collapse) was used as an indication of erosion power [126-128]. This method is limited by the fact that a given noise level can be produced by either a large number of low-energy non-damaging bubble collapses, or a few high-energy collapses causing damage. Thus an improved method was to measure the number and strength of impacts delivered to the cavitating surface [59, 129-136]. In this way, a bubble energy spectrum can be derived as illustrated in Figure 2.13, the area under each curve giving an indication of total energy delivered to the surface. This gives a relation of the form

$$MDPR = c(\text{spectrum area})^{\frac{1}{n}} \quad (2.7)$$

with erosion damage, where the constant c is empirically calculated and n was found to vary from 1 to 5.

Noise emitted by a cavitating sample is an order of magnitude smaller than cavitation

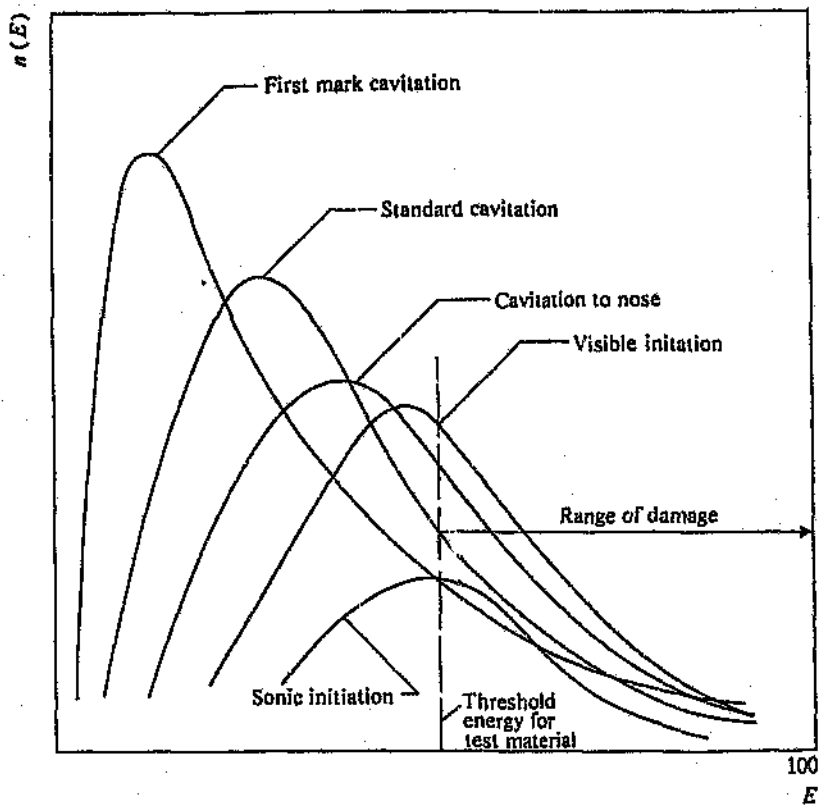


Figure 2.13: Hypothesized bubble energy spectra for various cavitation conditions at a constant velocity, for a given material in the U-M venturi

noise and does not seem to offer scope for erosion prediction at this stage.

2.4.3 Erosion testing

In spite of its limitations, measuring the cavitation erosion resistance of a material in a test rig is the most economic and informative and sometimes the only way to study the influence of fluid, flow and material properties. A number of test configurations have been established for various reasons as discussed below. They can be broadly divided into flow and non-flow devices.

Venturi devices

A venturi device employs a flow restriction to convert pressure into kinetic energy so that the static pressure falls to vapour pressure and cavitation develops. Relatively standard venturis, like the ones from the University of Michigan (U-M) in the USA shown schematically in Figure 2.14 have been used [59,137-139]. Special designs which increase damage rates but do not imitate real cavitation conditions as closely have also been made. One of the earliest is that of Boetcher [140,141] depicted in Figure 2.15, where the cavitating jet impinges upon the test specimen. Another design which has been used in various countries is the one by Shal'nev [84,127,142] shown in Figure 2.16. Flow takes place through a constant area throat across which a cavitation inducer in the form of a pin has been positioned. Cavitation occurs in the wake of the pin, and the test specimens are located flush with the wall in the cavitation region. The complex vortex-type flow geometry produced by the pin prevents generalization of results.

Rotating disc devices

The device consists of a flat disc which is rotated at high frequency in the test fluid. The fluid is kept relatively stationary by radial baffles both sides of the casing which contains the fluid. The disc contains various pins or through-holes which induce cavitation regions when the disc rotates at high enough frequencies. Test specimens are fitted flush with the disc surface in these regions. Rasmussen [62] developed the first rotating disc device

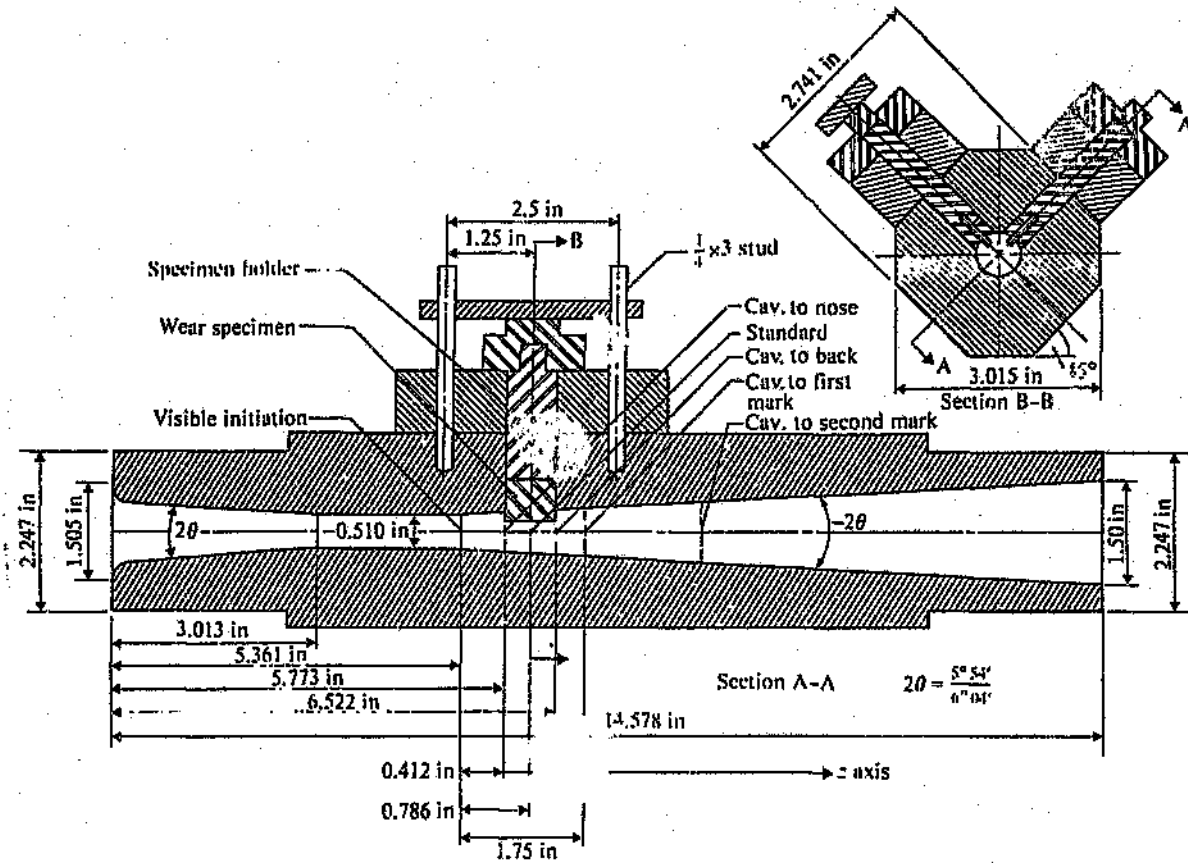


Figure 2.14: Cavitating venturi test section, U-M venturi

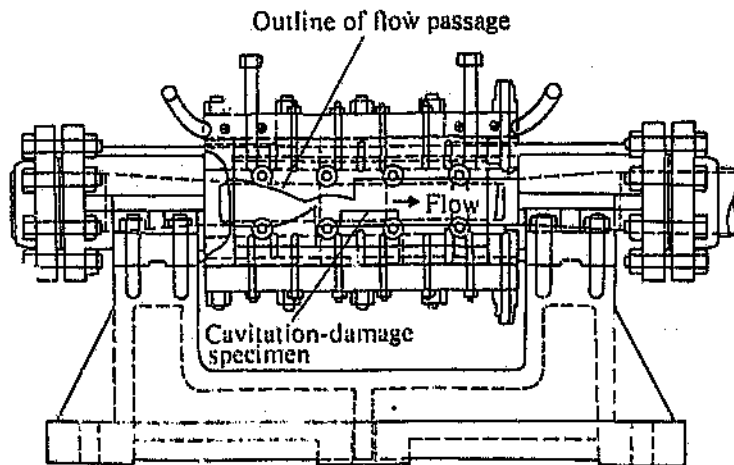


Figure 2.15: Cavitation-damage test section at the Holtwood laboratory, USA

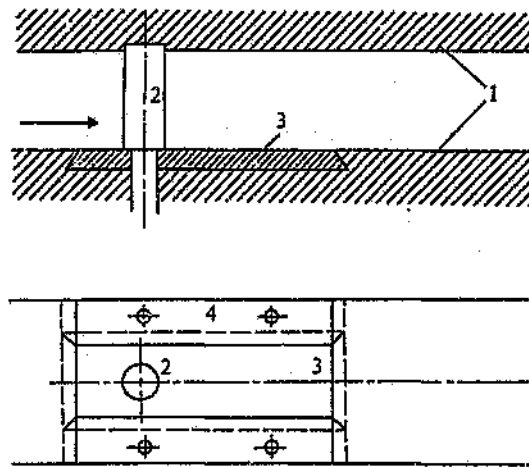


Figure 2.16: Sha'nev-type venturi, cavitation behind a circular profile: 1. Walls of the experimental chamber; 2. Model; 3. Test piece; 4. Test piece holding device

in 1955 (Figure 2.17). Similar rigs were used at Electricité de France in France [83], the US Naval Applied Science Laboratory [143] and in Poland [144]. At Pratt and Whitney Aircraft in the USA a rotating disc device (Figure 2.18) has been built for cavitation tests in water and molten lithium upon refractory metals [63]. In all these case, cavitation damage rates are higher than for the Boetcher- and Shal'nev-type venturis (Table 2.2). However, flow geometries are complicated and do not allow for simple descriptions.

Vibratory cavitation devices

This type of device is the simplest, cheapest and most common of all presently known cavitation devices. In addition, it provides erosion rates of the same order of magnitude as the fastest flowing devices. It is also the only cavitation test device for which an ASTM Standard Method exists [145]. On the negative side, it does not model the very important flow parameter of velocity, so that at present it is not possible to predict damage in a flowing device from vibratory test results. This type of device is most useful for the comparison of material resistances and the evaluation of effects of different fluids, temperatures and pressures. Figure 2.19 shows the U-M vibratory erosion test facility. Usually, the test specimen is attached to the vibrating horn. This introduces stresses in the specimen which may cause damage to weak materials. For this reason, a different specimen geometry has been introduced in which the specimen is held stationary at a relative short distance from the face of the horn [53,146-149].

2.4.4 Mathematical modelling

One of the major objectives of past and present erosion research must be to establish a mathematical model with fluid, flow and material parameters as input data, which would allow the prediction of erosion rates for as yet untested materials. The best hope of achieving a general enough relationship to allow applicability over a broad range of materials is to develop a relation which is directly related to a physical model of the erosion process, is dimensionally consistent, and is as simple as possible. Following this line of reasoning, the basic energy flux model suggested by Hoff et al. [149] is possibly the most promising model to date. The model assumes that the product of the rate of

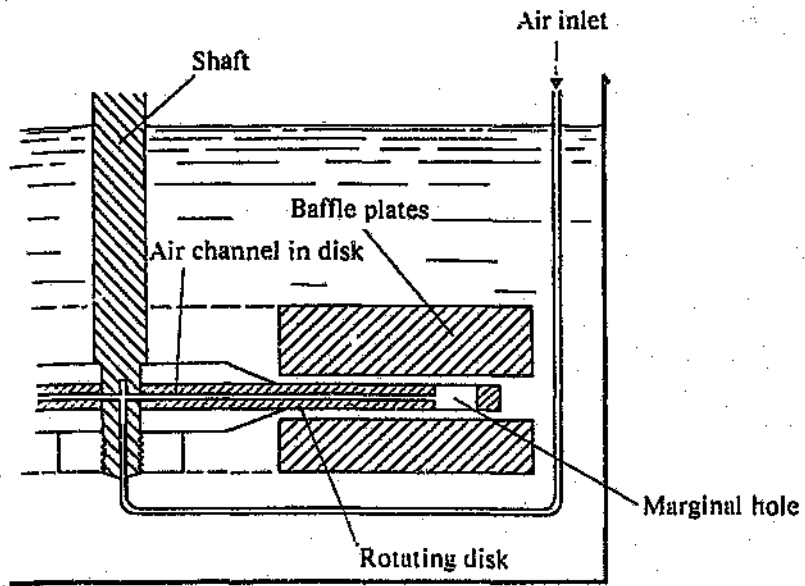


Figure 2.17: Rasmussen-type rotating disc for cavitation damage with holes for air supply

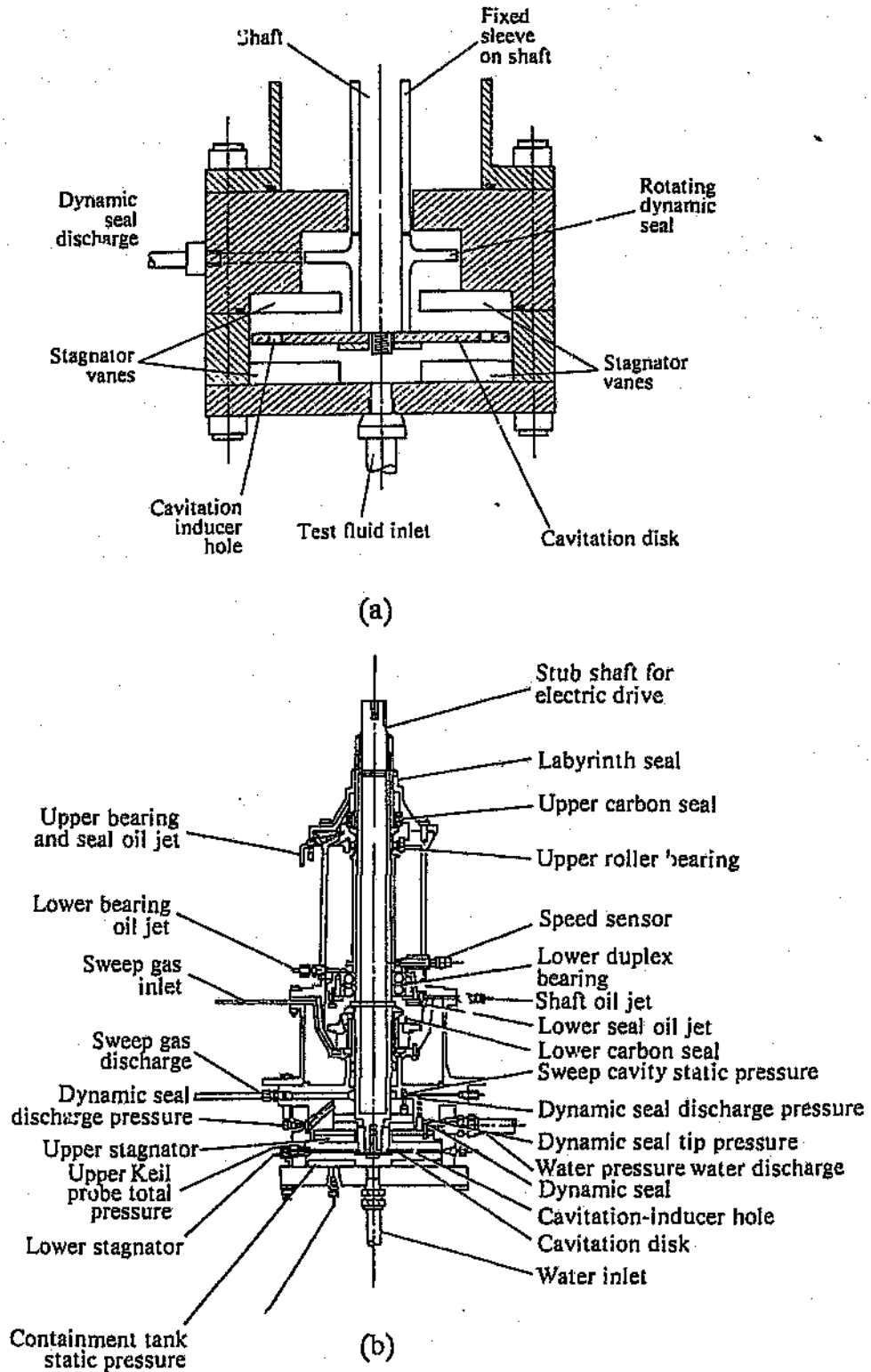


Figure 2.18: Water rotating disc cavitation test device at Pratt and Whitney Aircraft, USA; (a) Cross-section of the PWA rotating disc device, and (b) disc installed in housing (schematic)

Table 2.2: Comparative damage intensities for different types of test facilities

Type of facilities	Intensity, $W/cm^2 \times 10^7$
<i>Magnetostriction†</i>	
Devices 1-7	0.004-2.5
<i>Venturis</i>	
8-9 Boetcher type	$0.1-0.1 \times 10^{-2}$
10 Shal'nev type	0.1
11 Shal'nev type	0.03
12 Shal'nev type	0.1
13 U-M	0.3×10^{-4} [11, 101]
<i>Rotating disk</i>	
14	4
15	0.34
16	1.0

† Vibratory, ultrasonic, or piezoelectric devices are included.

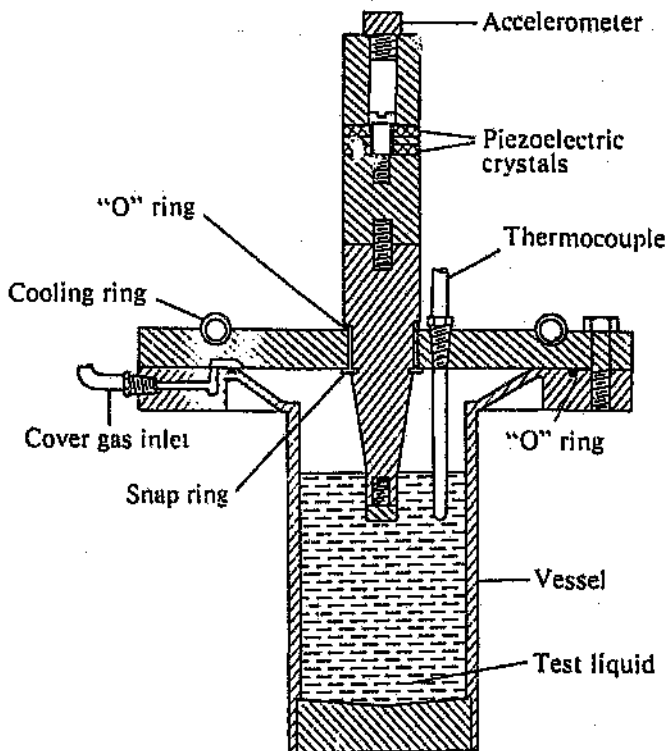


Figure 2.19: Vibratory cavitation-damage facility at the University of Michigan (U-M)

volume loss from the eroded surface, ΔV , and the energy needed to remove unit volume of the material, ϵ , equals the product of the total potentially damaging bubble energy flux, E_T , and the efficiency of the energy transfer to the surface, τ :

$$\Delta V \times \epsilon = E_T \times \tau \quad (2.8)$$

Since

$$\Delta V = MDPR \times A_e \quad (2.9)$$

where A_e is the effective surface area being impinged, Equation (2.8) can be rewritten in the form

$$MDPR = \frac{\tau}{\epsilon} \times \frac{E_T}{A_e} \quad (2.10)$$

Various expressions have been given for E_T [150,151], τ [53,136,152] and ϵ [43] although further development is required.

References

- 1) S.P. Hutton: The Saga of the Singing Kettle, Inaugural Lecture, Southampton University, Mar. 1972.
- 2) M. Robertson: Cavitation Today - An Introduction, in Cavitation State of Knowledge, ASME, pp. 1-9, 1969.
- 3) F.G. Hammitt, C. Chao, C.L. Kling and D.O. Rogers: ASTM Round-Robin Test with Vibratory Cavitation and Liquid Impact Facilities of 6061-T-6511 Aluminum Alloy, 316 Stainless Steel, Commercially Pure Nickel, ASTM Materials Research and Standards, MTRSA, Vol. 10, No. 10, pp. 16-36, Oct.1970.
- 4) E.N. Harvey, D.K. Barnes, W.D. McElroy, A.H. Whiteley, D.C. Pease and K.W. Cooper: Bubble Formation in Animals - I. Physical Factors, J. Cellular and Comp. Physiol., Vol. 24, No. 1, pp. 1-22, Aug. 1944.
- 5) E.N. Harvey, A.H. Whiteley, W.D. McElroy, D.C. Pease and D.K. Barnes: Bubble Formation in Animals - II. Gas Nuclei and their Distribution in Blood and Tissues, J. Cellular and Comp. Physiol., Vol. 24, No. 1, pp. 23-24, Aug. 1944.
- 6) E.N. Harvey, D.K. Barnes, W.D. McElroy, A.H. Whiteley and D.C. Pease: Removal of Gas Nuclei From Liquids and Surfaces, J. Amer. Chem. Soc., Vol. 67, p. 156, 1945.
- 7) E.N. Harvey, W.D. McElroy and A.H. Whiteley: On Cavity Formation in Water, J. Appl. Phys., Vol. 18, No. 2, pp. 162-172, 1947.
- 8) F.E. Fox and K.F. Herzfeld: Gas Bubbles with Organic Skin as Cavitation Nuclei, J. Acoustical Soc. Amer., Vol 26, pp. 984-989, 1954.

- 9) D. Sette and F. Wanderlingh: Nucleation by Cosmic Rays in Ultrasonic Cavitation, *Physical Review*, Vol. 125, pp. 409-417, 1962.
- 10) R.P. Coacci, P. Marietti, D. Sette and F. Wanderlingh: On the Acoustic Study of Nucleation by Energetic Particles in Fluids, *J. Acoustical Soc. Amer.*, Vol. 49, No. 1, pp. 246-252, 1971.
- 11) J.W. Daily and V.E. Johnson: Turbulence and Boundary Layer Effects on Cavitation Inception from Gas Nuclei, *Trans. ASME*, Nov. 1956.
- 12) M.S. Plesset and D.Y. Hsieh: Theory of Gas Bubble Dynamics in Oscillating Pressure Fields, *Physics of Fluids*, Vol. 3, pp. 882-892, 1960.
- 13) B. Vyas and C.M. Preece: Cavitation-induced Deformation of Aluminium, Erosion, Wear, and Interfaces with Corrosion, *ASTM STP 567*, pp. 77-105, 1974.
- 14) C.M. Preece, S. Dakshinamoorthy, S. Prasad and B. Vyas: The Influence of Microstructure on the Cavitation Erosion Resistance of fcc Metals and Alloys, *Proc. 4th Int. Conf. Strength Met. Alloys*, Nancy, France, pp. 1397-1403, 1976.
- 15) F.G. Hammitt: *Cavitation and Multiphase Flow - Theory and Practice*, McGraw-Hill, New York, 1979.
- 16) F.G. Hammitt: Cavitation and Liquid Impact Erosion, Chap. 11, *Wear Control Handbook*, edited by M.B. Peterson, ASME, 1980.
- 17) A. Karimi and J.L. Martin: Cavitation Erosion of Materials, *Int. Met. Rev.*, Vol. 31, No. 1, pp. 1-26, 1986.
- 18) C.M. Preece: Cavitation Erosion, *Treatise on Matls. Sci. Tech.*, Vol. 16, pp. 249-308, 1979.

- 19) Lord Raleigh: On the Pressure Developed in a Liquid During the Collapse of a Spherical Cavity, *Phil. Mag.*, Vol. 34, pp. 94-98, Aug. 1917.
- 20) C.A. Pearsons and S.S. Cook: Investigations into the Causes of Corrosion or Erosion of Propellers, *Trans. Royal Inst. Naval Architects*, Vol. 61, 1919.
- 21) R. Hickling and M.S. Plesset: Collapse and Rebound of a Spherical Bubble in Water, *The Physics of Fluids*, Vol. 7, No. 1, pp. 7-14, Jan. 1964; *AMR* Vol. 17 (1964), Rev. 5963.
- 22) R.D. Ivany and F.G. Hammitt: Cavitation Bubble Collapse in Viscous, Compressible Liquids - Numerical Analysis, *Trans. ASME, J. Basic Engr.*, Vol. 87, Ser. D, No. 4, pp. 997-985, Dec. 1965; *AMR* Vol. 19 (1966), Rev. 3685.
- 23) T. Mitchell and F.G. Hammitt: On the Effects of Heat Transfer upon Collapsing Bubbles, *Nuclear Science and Engineering*, Vol. 53, pp. 263-276, 1974.
- 24) W. Lauterborn: Numerical Investigation of Nonlinear Oscillations of Gas Bubbles in a Liquid, *J. Acoust. Soc. Am.*, Vol. 59, No. 2, pp. 283-293, 1976.
- 25) S.K. Bahl and J. Ray: Collapse and Expansion of a Gas Bubble in a Liquid Subject to Surface Tension, *Sov. Phys. Acoustics*, Vol. 18, pp. 391-393, 1972.
- 26) M. Kornfeld and L. Suvarov: On the Destructive Action of Cavitation, David Taylor Model Basin Report 712, Washington D.C., 1950.
- 27) P. Eisenberg: On the Mechanism and Prevention of Cavitation, David Taylor Model Basin Report 712, Washington D.C., 1950.
- 28) C.F. Naudè and A.T. Ellis: On the Mechanisms of Cavitation Damage by Non-Hemispherical Cavities Collapsing in Contact with a Solid Boundary, *Trans. ASME, J. Basic Engr.*, Vol. 83, Ser. D, No. 4, pp. 648-656, 1961; *AMR* Vol. 15

(1962), Rev. 2727.

- 29) N.D. Shutler and R.B. Mesler: A Photographic Study of the Dynamics and Damage Capabilities of Bubble Collapsing Near Solid Boundaries, Trans. ASME, Vol. 87, Ser. D, J. Basic Engr., pp. 511-517, 1965; AMR Vol. 18 (1965), Rev. 6295.
- 30) T.B. Benjamin and A.T. Ellis: The Collapse of Cavitation Bubbles and the Pressures Thereby Produced Against Solid Boundaries, Phil. Trans. Royal Soc. (London), Ser. A, Vol. 260, No. 1110, pp. 221-240, 1966.
- 31) A.G. Fabula: Some Experiments in Cavitation Bubble Dynamics, M.S. Thesis, Aeronautical Engineering, California Institute of Technology, 1958.
- 32) M. Harrison: An Experimental Study of Single Bubble Cavitation Noise, J. Acoust. Soc. Am., Vol. 24, pp. 776-782, 1952.
- 33) A.T. Ellis: On Jets and Shockwaves from Cavitation. Proc. 6th Symp. on Naval Hydrodyn., Washington D.C., Paper 6, 1966.
- 34) R.D. Ivany, F.G. Hammitt and T.M. Mitchell: Cavitation Bubble Collapse Observations in a Venturi, Trans. ASME, Vol. 88, Ser. D, No. 3, J. Basic Engr., pp. 649-657, 1966; AMR Vol. 20 (1967), Rev. 8667.
- 35) C.L. Kling: A High Speed Photographic Study of Cavitation Bubble Collapse, Ph.D. thesis, University of Michigan, Nuclear Engineering Department, Mar. 1970; also available as Univ. of Mich. ORA Report UMICH 03371-2-T, Mar., 1970.
- 36) C.L. Kling, F.G. Hammitt, T.M. Mitchell and E.E. Timm: Bubble Collapse Near a Wall in Flowing Systems, ASME Cavitation Forum, 1970.
- 37) G.L. Chahine and C.R. Simon: Collapse of a Simulated Multibubble System, Cavitation and Multiphase Flow Forum, ASME, pp. 78-81, 1985.

- 38) B. Vyas and C.M. Preece: Cavitation Erosion of Face Centered Cubic Metals, Metall. Trans. A, ASM and Met. Soc. AIME, Vol. 8A, pp. 915-923, 1977.
- 39) I. Hansson, K.A. Morch and C.M. Preece: A Comparison of Ultrasonically Generated Cavitation Erosion and Natural Flow Cavitation Erosion, Ultrasonics International, IPC Science and Technology Press Ltd., Guildford, UK 77, pp. 267-272, 1978.
- 40) I. Hansson and K.A. Morch: Comparison of the Initial Stage of Vibratory and Flow Cavitation Erosion, Proc. 5th Int. Conf. on Erosion by Solid and Liquid Impact, Royal Aircraft Establishment, Farnborough, UK, pp. 60-1 to 60-9, 1979.
- 41) R.T. Knapp, J.W. Daily and F.G. Hammit: Cavitation, McGraw-Hill, New York, 1970.
- 42) C.M. Preece and J.H. Brunton: A Comparison of Liquid Impact Erosion and Cavitation Erosion, Wear, Vol. 60, pp. 269-284, 1980.
- 43) F.G. Hammit: Cavitation and Multiphase Flow Phenomena, McGraw-Hill, New York, 1980.
- 44) A. Thiruvengadam: A Unified Theory of Cavitation Damage, Trans. ASME, J. Basic Engr., Vol. 85, Ser. D, No. 3, pp. 365-376, 1963.
- 45) A. Thiruvengadam and H.S. Preiser: On Testing Materials for Cavitation Damage Resistance, J. Ship Research, Vol. 8, pp. 39-56, 1964.
- 46) P. Eisenberg, H.S. Preiser and A. Thiruvengadam: On the Mechanisms of Cavitation Damage and Methods of Protection, Trans. Soc. Naval Archit. Mar. Eng, Vol. 73, p. 241, 1965.

- 47) J.M. Hobbs: Experience with a 20 kc Cavitation Erosion Test, Erosion by Cavitation or Impingement, ASTM STP 408, pp. 159-185, 1967.
- 48) M.S. Plesset and R.E. Devine: Effect of Exposure Time on Cavitation Damage, J. Basic Engr., Trans. ASME, Ser.D, Vol. 88, pp. 691-705, 1966.
- 49) P.V. Rao, C.S. Martin, B.C.S. Rao and N.S.L. Rao: Estimation of Cavitation Erosion with Incubation Periods and Material Properties, J. Test. Eval., ASTM, Vol. 9, No. 3, pp. 189-197, May 1981.
- 50) J.W. Tichler, J.S. van den Elsen, and A.W.J. de Gee: Resistance against Cavitation Erosion of 14 Chromium Steels, J. Lubr. Tech., Trans. ASME, Ser. F, Vol. 92, pp. 220-227, 1970.
- 51) M. Matsumura, Y. Suezawa and K. Tsuda: Polyphase Flow Forum, ASME, pp. 16-17, 1972.
- 52) F.J. Heymann: On the Time Dependence of the Rate of Erosion Due to Impingement or Cavitation, Erosion by Cavitation or Impingement, ASTM STP 408, p. 70-, 1967.
- 53) F.G. Hammitt et al: A Statistically Verified Model for Correlating Volume Loss Due to Cavitation or Liquid Impingement, ASTM STP 474, pp. 288-311, 1970.
- 54) F.J. Heymann: Towards Quantitative Prediction of Liquid Impact Erosion, ASTM STP 474, pp. 212-248, 1970.
- 55) A. Thiruvengadam: Scaling Laws for Cavitation Erosion, Tech. Rep. No. 233-15, Hydronautics Inc., Laurel, Maryland, 1971.
- 56) P.V. Rao and D.H. Buckley: Predictive Capability of Long-term Cavitation and Liquid Impingement Erosion Models, Wear, Vol. 94, pp. 259-274, 1984.

- 57) G. Tatnall, K. Foulke and G. Schmitt: Joint Air Force - Navy Supersonic Rain Erosion Evaluation of Dielectric and Other Materials, Rept. NADC-AE-6708, 1967.
- 58) R.T. Knapp: Recent Investigations of Cavitation and Cavitation Damage, Trans. ASME, Vol. 77, pp. 1045-1054, 1955.
- 59) M.J. Robinson and F.G. Hammitt: Detailed Damage Characteristics in a Cavitating Venturi, Trans. ASME, J. Basic Engr., Vol. 89, Ser. D, pp. 161-173, 1967.
- 60) M.J. Robinson: On the Detailed Flow Structure and the Corresponding Damage to Test Specimens in a Cavitating Venturi, Ph.D Thesis, Nuclear Engr. Dept., University of Michigan, 1965.
- 61) B.C.S. Rao and D.V. Chandrasekhara: Internal Report, Size and Velocity Scale Effects on Damage in a Venturi, Civil Engr. Dept., Bangalore Institute of Technology, 1973.
- 62) R.E.H. Rasmussen: Some Experiments on Cavitation Erosion in Water Mixed with Air, in Cavitation in Hydraudynamics, Vol. 20, pp. 1-25, Nat'l Phys. Lab., Teddington, England, Oct. 1955.
- 63) G.M. Wood, L.K. Knudson and F.G. Hammitt: Cavitation Studies with Rotating Disc, Trans. ASME, J. Basic Engr., Vol. 89, Ser. D, pp. 93-110, 1967.
- 64) J.Z. Lichtman and E.R. Weingram: The Use of a Rotating Disc Apparatus in Determining Cavitation Erosion Resistance in Materials, ASME Symp. on Cavitation Research Facilities and Techniques, pp. 185-196, 1964.
- 65) J.M. Hobbs and A. Laird: Pressure, Temperature and Gas Content Effects in the Vibratory test, NEL Report 438, Oct. 1969.

- 66) S.G. Young and J.R. Johnston: Effect of Cover Gas Pressures on Accelerated Damage in Sodium, NASA TN D-4235, Nov. 1967.
- 67) S.G. Young and J.R. Johnston: Accelerated Cavitation Damage of Steels and Syneralloys in Liquid Metals, NASA TN D-3226, May 1966.
- 68) F.G. Hammitt and D.O. Rogers: Effect of Pressure and Temperature Variation in Vibratory Cavitation Damage Test, J. Mech. Engr. Sci., Vol. 12, No. 6, pp. 432-439, 1970.
- 69) F.G. Hammitt and N.R. Bhatt: Cavitation Damage at Elevated Temperature and Pressure, ASME Cavitation and Polyphase Flow Forum, pp. 11-13, 1972.
- 70) F.G. Hammitt: Observations on Cavitation Damage in a Flowing System, Trans. ASME, J. Basic Engr., Vol. 85, Ser. D., pp. 347-359, 1963.
- 71) F.G. Hammitt et al: Initial Phases of Damage to Test Specimens in a Cavitating Venturi, Trans. ASME, J. Basic Engr., Vol. 87, Ser. D, pp. 435-464, 1965.
- 72) P. Tullis and R. Govindarajan: Cavitation and Size Scale Effects for Orifices, Proc. Paper 9605, J. Hydr. Div., ASCE, Vol. 99, No. HY3, pp. 417-430, March 1973.
- 73) J.M. Mousson: Pitting Resistance of Metals under Cavitating Conditions, Trans. ASME. Vol. 59, pp. 399-408, 1937.
- 74) R. Garcia and F.G. Hammitt: Cavitation Damage and Correlation with Material and Fluid Properties, Trans. ASME, J. Basic Engr., Vol. 89, Ser. D, No. 4, pp. 753-763, 1967.
- 75) R.E. Devine and M.S. Plesset: Temperature Effects in Cavitation Damage, CIT Rept. 85-27, Pasadena, Calif., April 1964.

- 76) F.G. Hammitt and N.R. Bhatt: Temperature and Pressure Effects in Vibratory Cavitation Damage Tests in Various Liquids, including Molten Sodium, Proc. 5th Conf. on Fluid Machinery, pp. 393-402, Akademia Kiado, Budapest, Hungary, 1975.
- 77) K.K. Shalnev, J.J. Varga and G. Sebestyen: Scale-effect Investigation of Cavitation Erosion using the Energy Parameter, in Erosion by Cavitation or Impingement, ASTM STP 408, p. 220, 1967.
- 78) W.C. Leith: Prediction of Cavitation Damage in the Alkali Liquid Metals, Proc. Am. Soc. Test. Mater., Vol. 65, pp. 789-800, 1965.
- 79) P. Eisenberg: On the Mechanisms and Prevention of Cavitation, David Taylor Model Basin Rept. No. 712, Washington, 1950.
- 80) M.S. Plesset: Temperature Effects in Cavitation Damage, J. Basic Engr., Trans. ASME, Ser. D, Vol. 94, pp. 559-566, 1972.
- 81) C.J. Heathcock: Cavitation Erosion of Materials, Ph.D thesis, Materials Engineering Dept., University of Cape Town, 1980.
- 82) X. Wang, Y. Zhou and F. G. Hammitt: Vibratory Cavitation Erosion tests at 120-150 °C and 2 bar Suppression Pressure, Cavitation and Multiphase Flow Forum, ASME, pp. 18-21, 1984.
- 83) R. Canavelis: Contribution a l'Etude de l'Erosion de Cavitation dans les Turbomachines Hydrauliques, Ph.D thesis, Faculty of Science, University of Paris, 1966.
- 84) K.K. Shal'nev, J.J. Varga and G. Sebestyen: Investigations of the Scale Effects of Cavitation Erosion, Philos. Trans. R. Soc. London, Ser. A, Vol. 260, No. 110, pp. 256-266, 1966.

- 85) K.K. Shal'nev, J.J. Varga and G. Sebestyen: Scale-effect Investigation of Cavitation Erosion using the Energy Parameter, Erosion by Cavitation or Impingement, ASTM STP 408, pp. 220-238, 1967.
- 86) K.K. Shal'nev, J.J. Varga and G. Sebestyen: Accurate Determination of Scale Effect Formula for Cavitation Erosion, Acta Tech. Acad. Sci. Hung., Vol. 66, pp. 347-367, 1969.
- 87) V. Malyshev and N. Pylaev: Influence of Hydroturbine Size on Cavitation Pitting Intensity, Proc. Conf. on Cavitation, IME, London, pp. 309-312, 1974.
- 88) S.P. Hutton and J.L. Guerrero: The Damage Capacity of some Cavitating Flows, Proc. 5th Conf. on Fluid Machinery, edited by L. Kisbocskoi and A. Szabo, Akademiai Kiado, Budapest, pp. 427-438, 1975.
- 89) W. Meier and H. Grein: Cavitation in Models and Prototypes of Storage Pumps and Pump Turbines, Proc. IAHR Symp., Stockholm, Paper H3, 1970.
- 90) O. Schiele and G. Mollenkopf: Some Views on Different Cavitation Criteria of a Pump, Proc. Conf. on Cavitation, IME, London, pp. 177-185, 1974.
- 91) A.S. Ramamurthy and P. Bhaskaran: Source Size and Velocity Effects on Cavitation Damage, J. Fluids Eng., Vol. 97, No. 3, pp. 384-386, 1975.
- 92) P.V. Rao and D.H. Buckley: Cavitation Erosion Size Scale Effects, Wear, Vol. 96, pp. 239-253, 1984.
- 93) P.V. Rao, B.C.S. Rao and D.H. Buckley: Size Scale Effect in Cavitation Erosion, Cavitation and Multiphase Flow Forum, ASME, pp. 42-45, 1984.
- 94) B. Vyas: Erosion-corrosion, p. 357 in Erosion, Treatise on Materials Science and Technology, Vol. 16, edited by C.M. Preece, Academic Press, 1979.

- 95) R.D. Ivany and F.G. Hammitt: Cavitation Bubble Collapse in Viscous, Compressible Liquids - Numerical Analysis, Trans. ASME, J. Basic Engr., Vol. 87, Ser. D, pp. 977-985, 1965.
- 96) I. Viskovic: Recherches Concernantes l'Influence de la Teneur en Air sur la Cavitation et la Corrosion, Bull. Escher-Wyss, Vol. 19, pp. 83-90, 1940.
- 97) R.E.H. Rasmussen: Experiments on Flow with Cavitation in Water Mixed with Air, Paper 20, Proc. 1955 NPL Symp. on Cavitation in Hydrodynamics, HMSO, London, 1956.
- 98) J.M. Hobbs, A. Laird and W.C. Brunton: Laboratory Evaluation of the Vibratory Cavitation Erosion Test, NEL Rept. 271, East Killbride, Scotland, 1967.
- 99) M.G. Sirotyuk: The Influence of Gas Content and Temperature in Liquids on the Cavitation Process, Acoustics Journal USSR, Vol. 12, No. 1, pp. 87-92, 1966.
- 100) G. Petracchi: Investigation of Cavitation Corrosion (in Italian), Metallurgia Italiana, Vol. 41, pp. 1-6, 1944; English summary in Engr's Digest, Vol. 10, pp. 314-316, 1949.
- 101) M.S. Plesset: Cathodic Protection in Cavitation Damage, Trans. ASME, J. Basic Engr., Vol. 82, Ser. D, pp. 808-820, 1960.
- 102) W.C. Leith and A.L. Thompson: Some Corrosion Effects in Accelerated Cavitation Damage, Trans. ASME, J. Basic Engr., Vol. 82, Ser. D, pp. 795-807, 1960.
- 103) C.M. Preece: Erosion of Metals and Alloys, in Surface Effects in Crystal Plasticity, edited by R.M. Latanision and J.T. Fourie, Noordhoff, Leyden, 1977.

- 104) U.R. Evans: *The Corrosion and Oxidation of Metals*, Edward Arnold, London, 1960.
- 105) T.P. Hoar and J.C. Scully: *Mechanochemical Anodic Dissolution of Austenitic Stainless Steel in Hot Chloride Solution at Controlled Electrode Potential*, *J. Electrochem. Soc.*, Vol. 111, pp. 348-352, 1964.
- 106) A.F. Derendovski, M.K. Bologa and K.K. Shalnev (in Russian): *Dokl. Akad. Nauk. USSR*, Vol. 183, pp. 1292-1294, 1968.
- 107) R. Hickling: *Effects of Thermal Conduction in Sonoluminescence*, *J. Acoust. Soc. Amer.*, Vol. 35, pp. 967-974, 1963.
- 108) R. Simoneau, J.L. Filhey and R. Roberge: in *Cavitation Erosion in Fluid Systems*, edited by W.L. Swift and R.E.A. Arndt, McGraw-Hill, New York, pp. 71-82, 1981.
- 109) F.C. von Altob, H. Buhl and H. Voight: *Werkst. Korros.*, Vol. 24, No. 1020, pp. 606-673, 1973.
- 110) A. Keller, F.G. Hammitt and E. Yilmaz: *Comparative Measurements by Scattered Light and Coulter Counter Method for Cavitation Nuclei Spectra*, *Cavitation and Polyphase Flow Forum*, ASME, pp. 16-18, 1974.
- 111) K.A. Morch: *Cavitation Inception by Solid Particles in Liquid Flows*, *Cavitation and Multiphase Flow Forum*, ASME, pp. 16-18, 1986.
- 112) B. Sun: *Long Chain Polymer Additives Effects on Cavitation Erosion*, *Cavitation and Multiphase Flow Forum*, ASME, pp. 84-86, 1985.
- 113) H. Kimoto: *Cavitation in Purified Water*, *Cavitation and Polyphase Flow Forum*, ASME, pp. 1-2, 1977.

- 114) J.W. Hoyt: Cavitation in Polymer Solutions and Fiber Suspensions, Cavitation and Polyphase Flow Forum, ASME, pp. 9-10, 1977.
- 115) G.L. Chahine and A.K. Morine: The Influence of Polymer Additives on the Collapse of a Bubble between Two Solid Walls, Cavitation and Polyphase Flow Forum, ASME, pp. 7-8, 1980.
- 116) R.E.A. Arndt: Influence of Polymer Additives on Cavitation in Jets, Cavitation and Polyphase Flow Forum, ASME, pp. 9-10, 1980.
- 117) D.H. Fruman: Tip Vortex Cavitation Inhibition by Polymer Additives, Cavitation and Multiphase Flow Forum, ASME, pp. 73-76, 1984.
- 118) X. Wang and F.G. Hammitt: Effects of Solid Particles in Water on Vibratory Cavitation Erosion, Cavitation and Multiphase Flow Forum, ASME, 1984.
- 119) A. Karimi and J.L. Martin: Cavitation Erosion of Materials, Int. Met. Rev., Vol. 31, No. 1, pp. 1-26, 1986.
- 120) A. Laird and J.M. Hobbs: Comparative Erosion Tests on Non-Ferrous Materials, NEL Rept. No. 496, East Killbride, UK, 1971.
- 121) G.C. Gould: in Characterization and Determination of Erosion Resistance, ASTM STP 474, pp. 182-211, 1970.
- 122) A. Thiruvengadam: The Concept of Erosion Strength, in Erosion by Cavitation or Impingement, ASTM STP 408, pp. 22-41, 1967.
- 123) K.S. Zhou and H. Herman: Cavitation Erosion of Titanium and Ti-6Al-4V: Effects of Nitriding, Wear, Vol. 80, pp. 101-113, 1982.

- 124) G.P. Thomas and J.H. Brunton: Drop Impingement Erosion of Metals, Proc. R. Soc. London, Vol. A314, pp. 549-565, 1970.
- 125) T. Okada, Y. Iwai and A. Yamamoto: A Study of Cavitation Erosion of Cast Iron, Wear, Vol. 84, pp. 297-312, 1983.
- 126) I.S. Pearshall and P.J. McNulty: Comparisons of Cavitation Noise with Erosion, ASME Cavitation Forum, pp. 6-7, 1968.
- 127) J.J. Varga and G. Sebestyen: Determination of Hydrodynamic Cavitation Intensity by Noise Measurements, Proc. 2nd Int'l JSME Symp. on Fluid Machinery and Fluidics, pp. 285-292, Sept. 1972; see also J.J. Varga, G. Sebestyen and A. Fay: Detection of Cavitation by Acoustic and Vibration-Measurement Methods, La Houille Blanche, No. 2, pp. 137-149, 1969.
- 128) P.A. Lush and S.P. Hutton: The Relation Between Cavitation Intensity and Noise in a Venturi-Type Section, Proc. Int'l Conf. on Pumps and Turbines, pp. 1-3, NEL, Glasgow, Sept. 1976.
- 129) H. Nowotny: Destruction of Materials by Cavitation (in German), VDI Verlag, Berlin, 1942.
- 130) F. Numachi: An Experimental Study of Accelerated Cavitation Induced by Ultrasonics, Trans. ASME, J. Basic Engr., Vol. 87, pp. 967-976, 1965.
- 131) F. Numachi and M. Hongo: Ultrasonic Shock Waves Emitted by Cavitation at Perforation on Plate/Rept. 1, Rept. Inst. High Speed Mech., Vol. 30, p. 277, 1974.
- 132) V.K. Makarov, A.A. Kortnev, S.G. Suprun and G.I. Okolelov: Cavitation Erosion Spectra Analysis of Pulse-Heights Produced by Cavitation Bubbles, Proc. 6th Non-Linear Acoustics Conf., Odessa Poly. Inst., Moscow, Jul. 1975.

- 133) F. Numachi: Transitional Phenomena in Ultrasonic Shock Waves Emitted by Cavitation on Hydrofoils, *Trans. ASME, J. Basic Engr.*, Vol. 81, p. 153, Jun. 1959.
- 134) F.G. Hammitt, J.B. Hwang, M.K. De et al: Final Report for Argonne National Laboratory Project, University of Michigan ORA Rept. UMICH 013503-2-F, Jun. 1976.
- 135) F.G. Hammitt and J.B. Hwang: Ultrasonic Cavitation Regime Pulse-Count Spectra as Related to Cavitation Erosion, *Proc., 7th Int'l Non-Linear Acoustics Conf.*, Blacksburg, Va, Aug. 1976.
- 136) F.G. Hammitt, S.A. Barber, M.K. De, and A.N. el Hasrouni: Cavitation Damage Prediction from Bubble Collapse Pulse Count Spectra, *Cavitation and Polyphase Flow Forum, ASME*, pp. 25-28, 1977.
- 137) F.G. Hammitt and M.K. De: Cavitation Erosion of Aluminum Considering Bubble Collapse Pulse Height Spectra and Cavitation Erosion Efficiency, *Proc. 1979 Int'l. Wear Conf.*, ASME, Dearborn, Apr. 1979; Rept. No. DRDA UMICH 014456-33-I, Univ. Mich., Ann Arbor, Mich., Aug. 1978.
- 138) F.G. Hammitt, M.K. De, J. Elenz and E. Hunt: Venturi Cavitation Bubble Collapse Pulse Spectra and Observed Pits in Soft Aluminum, *Cavitation and Multiphase Flow Forum, ASME*, pp. 31-33, Jun. 1978.
- 139) F.G. Hammitt, T.D. Helmholdt and M.K. De: Erosion of Soft Aluminum in Cavitating Venturi, *Cavitation and Multiphase Flow Forum, ASME*, Jun. 1979.
- 140) H.N. Boetcher: Failure of Metals due to Cavitation under Experimental Conditions, *Trans. ASME*, Vol. 58, pp. 335-360, 1936.

- 141) A. Lichtarowicz: Cavitation Jet Apparatus for Cavitation Erosion Testing, in *Erosion: Prevention and Useful Applications*, edited by W.F. Adler, ASTM STP 664, Feb. 1979.
- 142) K.K. Shal'nev, R.D. Stepanov and S.P. Kozyrev: Effect of Stressed State of Metals on its Resistance to Cavitation, *Soviet Physics-Doklady*, Vol. 11, No. 9, pp. 822-824, March 1967.
- 143) J.Z. Lichtman, D.H. Kallas, C.K. Chatten and E.P. Cochran (Jr.): Cavitation Erosion of Structural Materials and Coatings, *Corrosion*, pp. 497t-505t, Oct. 1961.
- 144) K. Steller: Personal communications with F.G. Hammitt, Inst. Fluid Flow Mach., Polish Academy Science, Gdansk, Poland, 1976.
- 145) Anonymous: Standard Method of Vibratory Cavitation Erosion Test, ASTM, G 32-72, 1972, and G 32-76, 1976.
- 146) D.J. Kemppainen and F.G. Hammitt: Effects of External Stress on Cavitation Damage, Proc. 13th Congr. IAHR, Kyoto, Japan, Aug. 1969.
- 147) P.R. Scott: Cavitation Resistance of Rock, Ph.D thesis, Dept. Mining Engr., University of Missouri-Rolla, 1979.
- 148) K. Endo, T. Okada and M. Nakashima: A study of Erosion Between Two Parallel Surfaces Oscillating at Close Proximity in Liquids, *J. of Lubr. Tech.*, pp. 229-236, Jul. 1967.
- 149) K. Endo, T. Okada and Y. Baba: Fundamental Studies on Cavitation Erosion, *Bull. of JSME*, Vol. 12, No. 52, pp. 729-737, 1969.
- 150) G. Hoff, G. Langbein and H. Rieger: Material Destruction due to Liquid Impact, ASTM STP 408, pp. 42-69, 1966.

- 151) S.M.A. Selim: Cavitation Erosion in Fluid Flow, Ph.D. thesis, Department of Mechanical Engineering, University of Southampton, 1981.

- 152) F.G. Hammitt, S.A. Barber, M.K. De al. J A.N. el Hasrouni: Predictive Capability for Cavitation Damage from Bubble Collapse Pulse Count Spectra, Proc. Conf. Scaling for Performance Prediction in Rotodynamic Machines, Inst. Mech. Engrs., University of Stirling, Scotland, 6-8 Sept. 1977.

CHAPTER 3

3. TEST RIG DESIGN, EVALUATION AND CALIBRATION

3.1 Selection of Concept

Due to the differences in bubble dynamics and damage characteristics observed between flow and vibratory cavitation erosion (Section 2.2.3), it was decided to develop a flow-type test apparatus which would most accurately simulate the cavitation and damage characteristics observed in water-powered stoping equipment like rockdrills.

A comparison of flow-type test devices (Table 2.2) showed that venturi systems are bulky, expensive and have low damage rates. On the other hand, a rotating disc apparatus allows more than one sample to be tested simultaneously, and damage is produced much more rapidly. However, the cavitation flow dynamics is more complex and has a vortex nature. The latter concept was chosen for the development of a cavitation test facility.

3.2 Specifications and design

The test rig had to facilitate the investigation of cavitation dynamics as well as erosion resistance. Important fluid and flow parameters like velocity, pressure, temperature, test fluid quality and gas content had to be variable over a range compatible to spool valve operating conditions. The selected parameter ranges are shown in Table 3.1.

The detailed design drawings are shown in the Appendix, while the completed rig is shown in Figure 3.1. At this stage, the final disc geometry for sample testing had still to be determined, and for this purpose a test disc made of B51S Al alloy was designed (Figure 3.2).

The disc was situated in a cylindrical pressure chamber and bordered on either side by a stator containing radial vanes to prevent excessive water rotation. The positions of the

Table 3.1: Specified parameter ranges for rotating disc test rig

Parameter	Range	Measurable	Controllable	Comment
Static water pressure	0,1 - 2 MPa	yes	yes	
Water temperature	ambient to 100 °C	yes	yes	
Sample velocity	not specified	yes	yes	determined from disc velocity i.e. assuming test fluid to be stationary
Air content of water	deaerated to supersaturated	yes	yes	measured as dissolved oxygen content
Water flow rate	0 - 30 l/min	yes	yes	
Water quality	neutral to corrosive and containing abrasive solids	yes	yes	to simulate typical mine waters



Figure 3.1: Cavitation test rig in its completed form

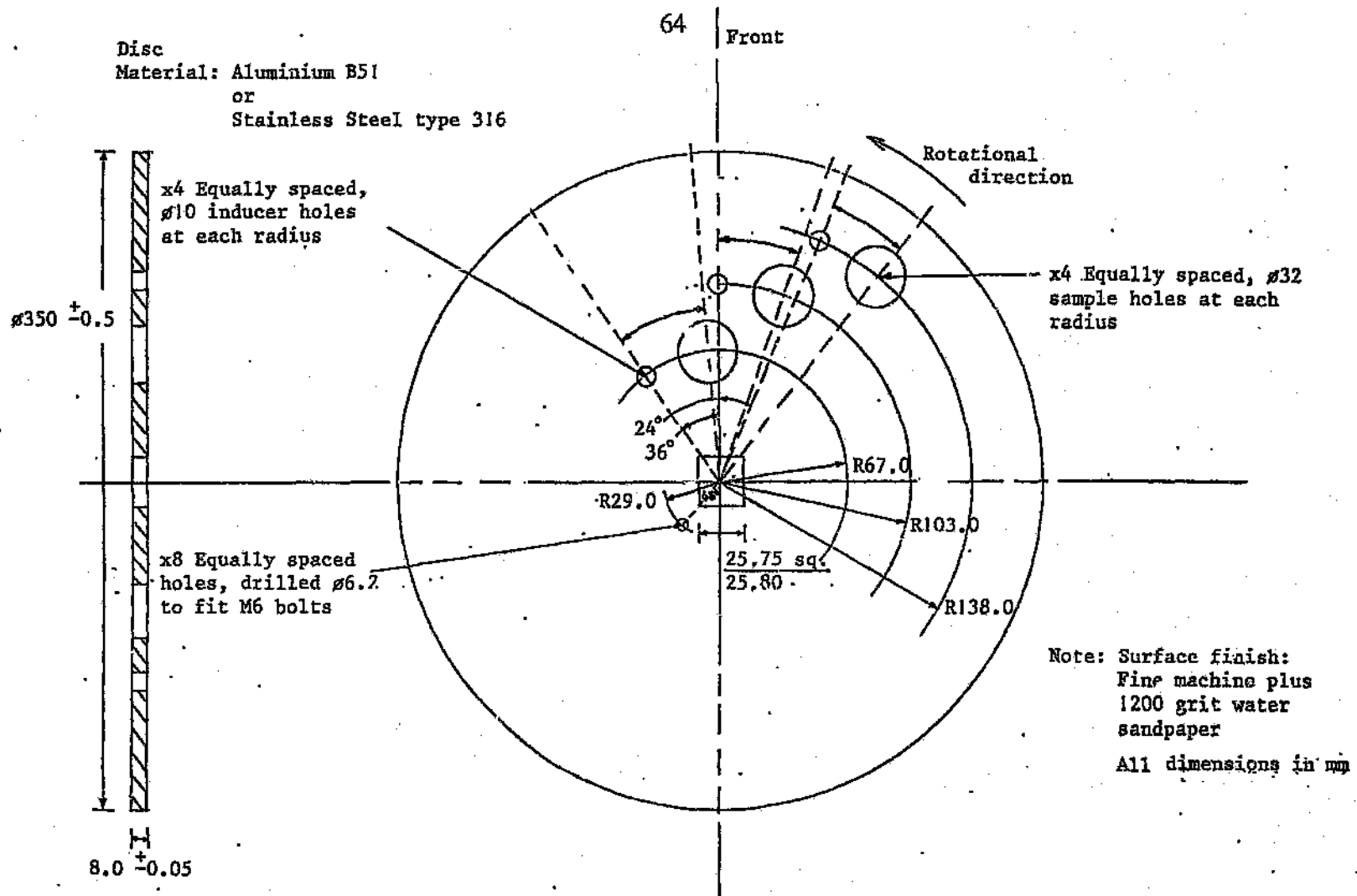


Figure 3.2: Disc design with 12 inducer holes

stators were adjustable to allow for the proper disc-stator distance to be maintained. A schematic presentation of the disc and stator setup is given in Figure 3.3. A transparent window was situated in the lid of the pressure chamber, in such a position that the cavitating regions on the disc could be viewed with the aid of a stroboscope.

The disc drive shaft was made hollow to facilitate electrical connections and sealed with a mechanical seal (Figure 3.4) containing SiC versus WC sealing faces. A 30 kW, 2 pole electric motor (natural frequency 2910 rpm) rotated the disc via a belt and pulley system. The disc speed could be varied by using different pulley size ratios. Water was pumped through the test chamber by means of a 2 MPa, 30 l/min screw-type pump (Figure 3.5). Pressure and flow rate was controlled by three butterfly valves. Water could be recirculated through the test chamber - for this purpose the flow system included a 100 l reservoir - or passed through only once. In order to cater for chemically aggressive waters, the test chamber, stators, drive shaft, valves, reservoir and all connections were made of stainless steel, while pump components were nickel plated. The flow system was completed by reinforced high pressure rubber hose.

Heating of the water was required to reach the test temperature which was mostly above ambient; this was facilitated by a 3 kW heating element in the reservoir. To prevent temperature rises during disc operation, cooling was also necessary. This was supplied by two facilities: a 6 m stainless steel cooling coil running around the inside perimeter of the test chamber (Figure 3.6), and a shell-and-tube heat exchanger (2,43 m² surface area) situated in the flow loop (Figure 3.7).

Instrumentation included:

- a dial-type, 2 MPa pressure gauge downstream of the test chamber
- a 2 MPa strain gauge-based pressure transducer with digital readout, positioned in the test chamber wall (Figure 3.8)
- a chromel-alumel thermocouple with digital readout, positioned in the test chamber wall (Figure 3.8)
- a copper-constantan thermocouple with digital readout, upstream of the pump (Figure 3.9)

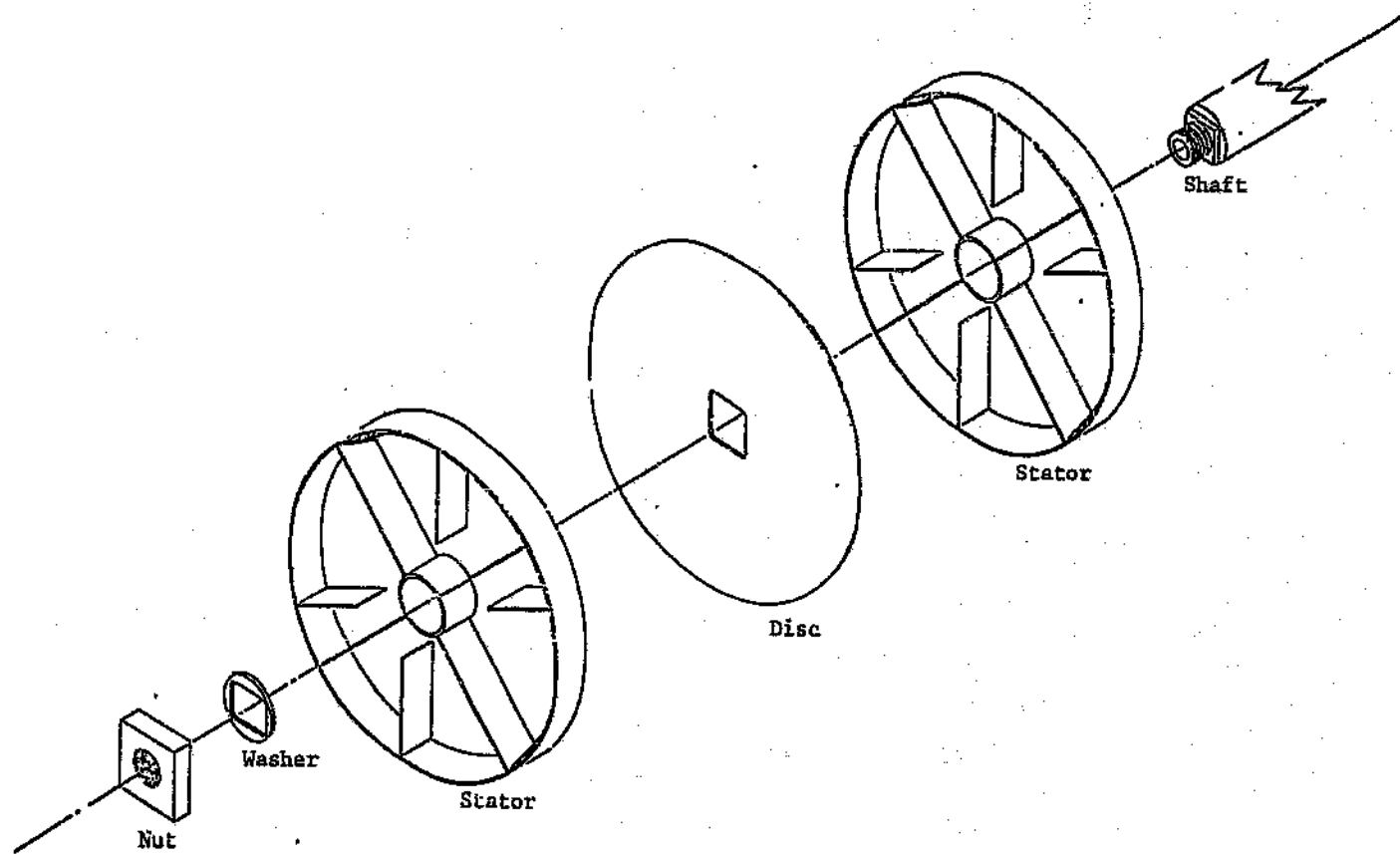


Figure 3.3: Disc and stator configuration inside test chamber

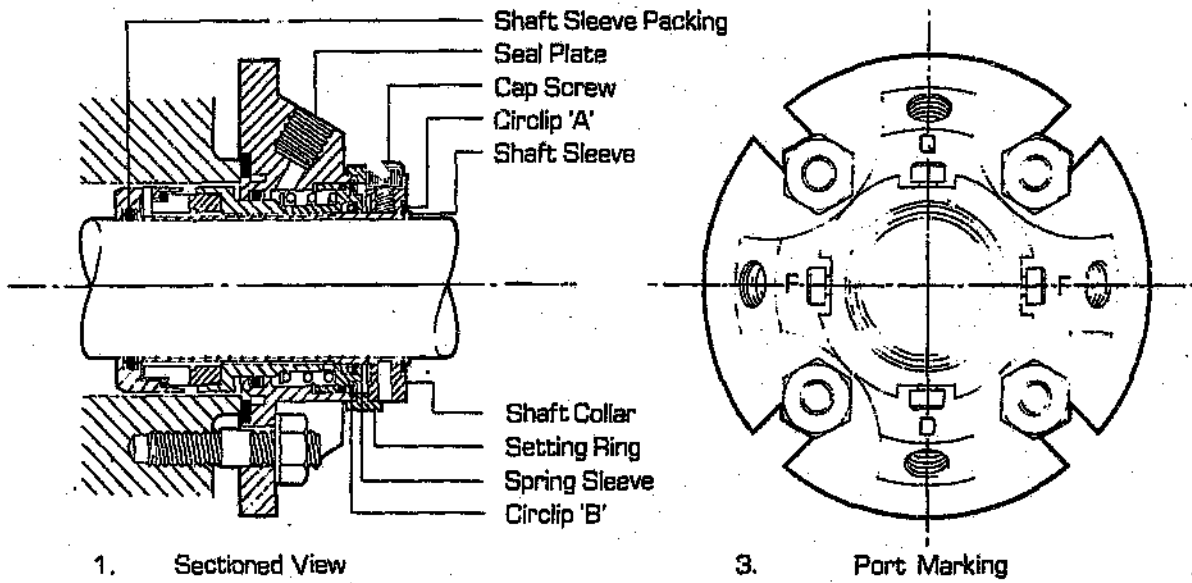


Figure 3.4: Mechanical seal (diagrammatic)

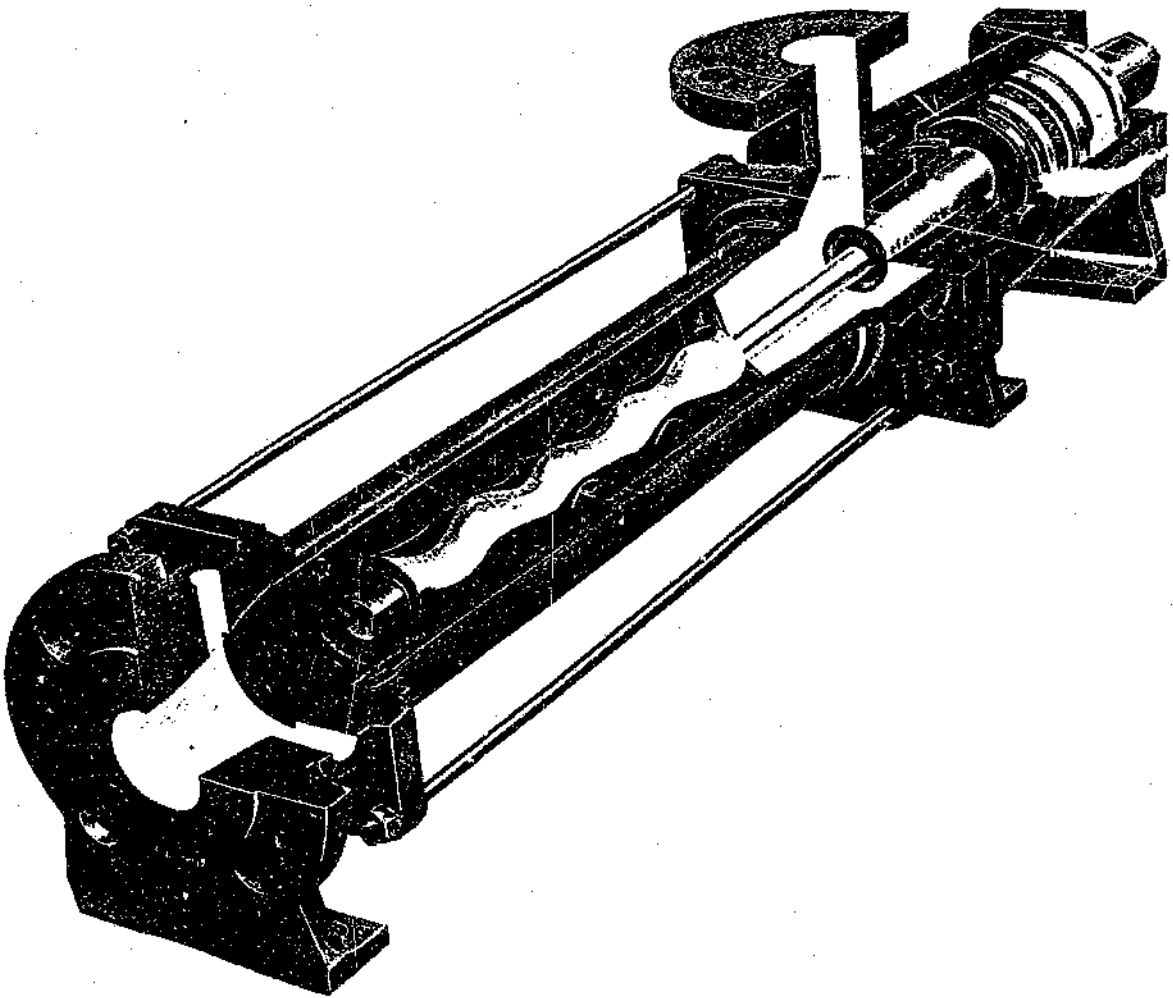


Figure 3.5: Screw-type pump

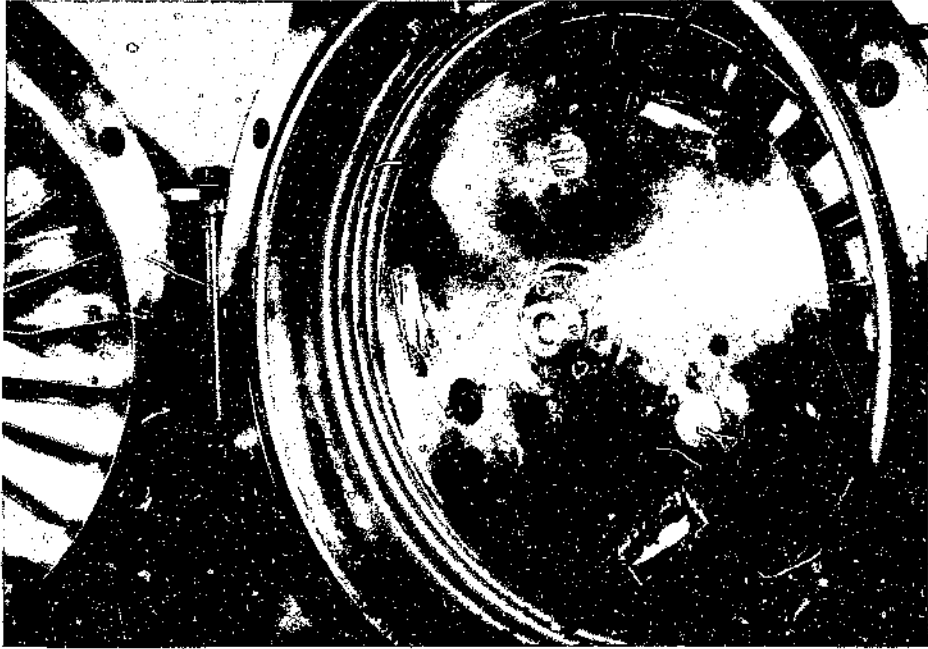


Figure 3.6: Test chamber with stainless steel cooling coil around the inside perimeter

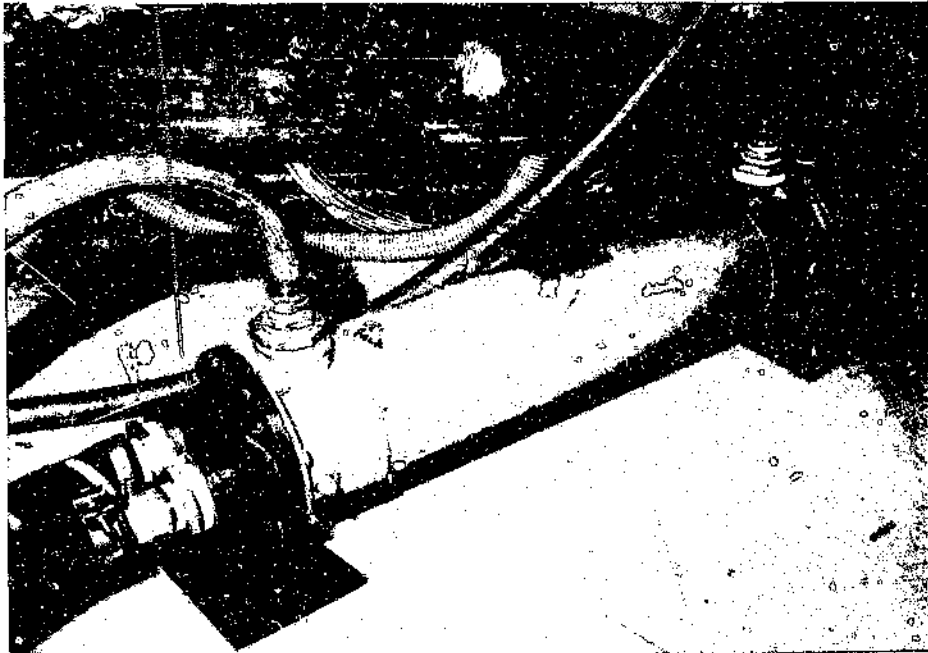


Figure 3.7: Shell-and-tube heat exchanger



Figure 3.8: Pressure transducer (2 MPa) and chromel-alumel thermocouple installed in the test chamber lid

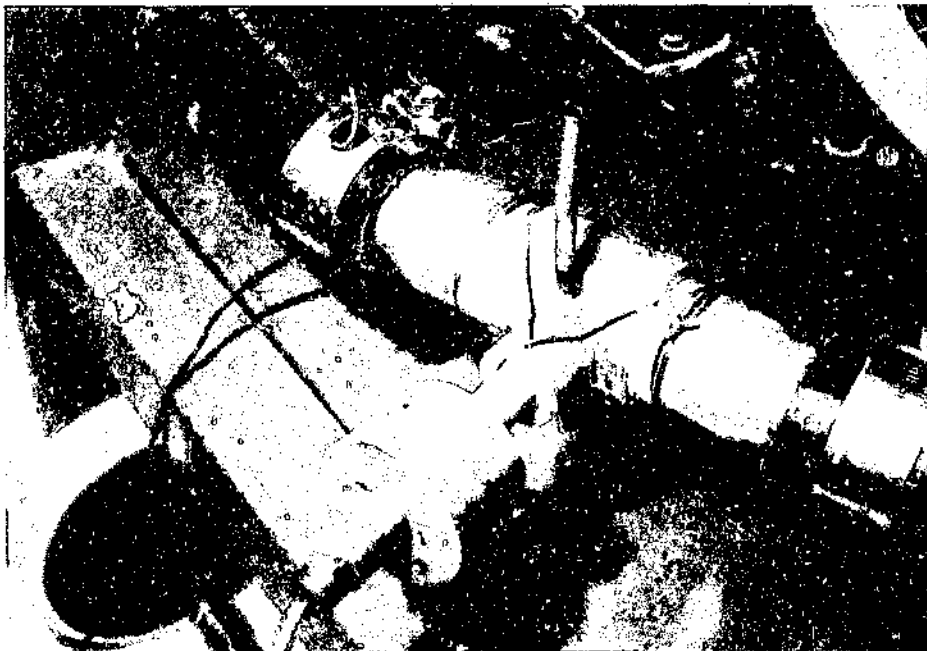


Figure 3.9: Dissolved oxygen probe and copper-constantan thermocouple installed in the flow loop between the reservoir and pump

- at the same location, a dissolved oxygen (DO) probe (max. capacity 30 mg/l), see Figure 3.9
- a glass rotameter for measuring flow rate (max. capacity 40 l/min) on the downstream side of the test chamber
- a hand-held stroboscope for "freezing" the rotating disc and measuring its rotational frequency

A typical flow loop, including instrumentation, is pictured in Figure 3.10.

3.3 Cavitation dynamics and disc design

Previous work with rotating disc-type apparatus [2,3] had shown the importance of factors such as disc flatness and surface finish and the number, size and geometry of cavitation inducer holes. Disc design together with fluid and flow parameters was optimized using the aluminium test disc shown in Figure 3.2.

Figure 3.11 shows the cavitation clouds and associated damage patterns formed on the test disc under a certain set of hydrodynamic conditions. Cavitation was of the vortex type [1,4]. Because of the circular motion of the inducer hole, the cloud was curved towards the centre of the disc. From the hole extended a so-called "fixed" cavity [1] which oscillated in length between a maximum and minimum position. Upon reaching its maximum length, it shed smaller, "travelling" cavities thus shrinking back to the minimum length. Comparison of the cavitation cloud with the erosion zone showed that damage was formed around the maximum position of the fixed cavity, with the centre of the erosion hole normally somewhat downstream of the maximum position. (More detail is given in Chapter 5.) It would thus appear that damage was mainly attributable to the collapse of travelling cavities.

It was found that the cavitation cloud geometry, and with that the erosion zone, changed with velocity, pressure and temperature. (More detailed studies are reported in Chapters 4 and 5.) This demanded careful selection of sample configuration, since for comparison of erosion results damage had to be confined to the sample area. The influence of some disc design factors on disc power consumption is expressed in Figure 3.12.

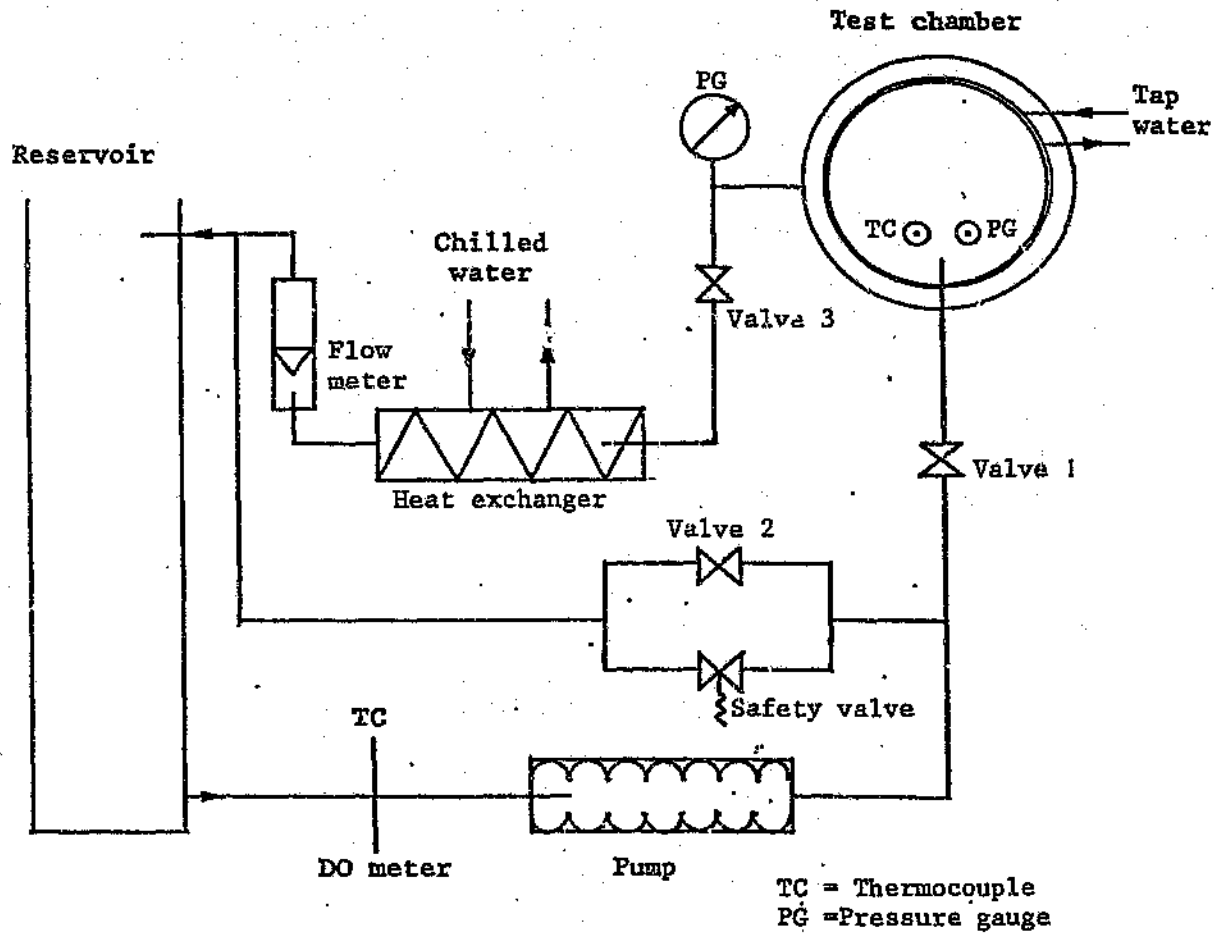
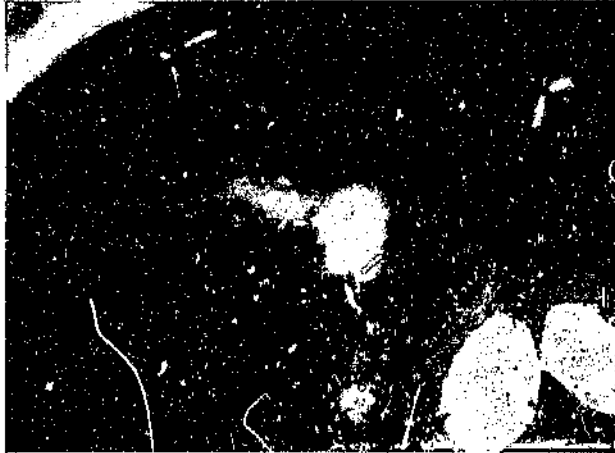
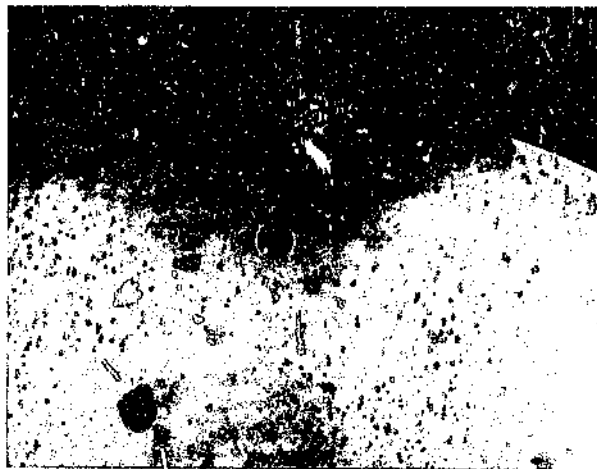


Figure 3.10: Typical flow system used for erosion tests



(a)



(b)

Figure 3.11: (a) Cavitation field formed by middle inducer hole and (b) damage caused by middle inducer and outer inducer holes after 0,5 hours testing

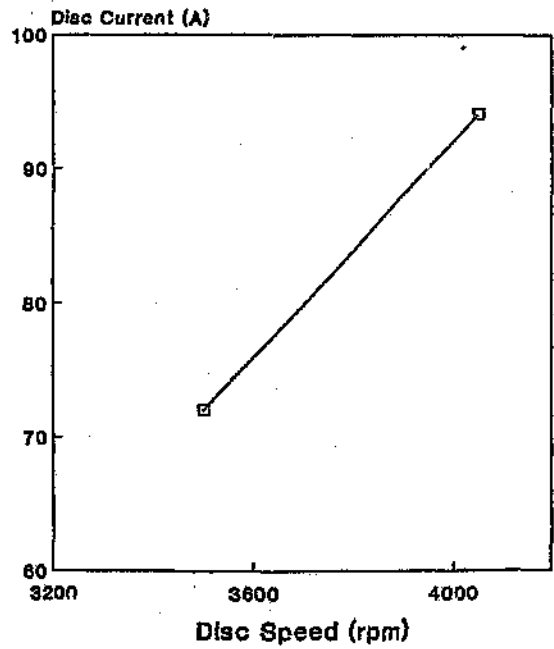
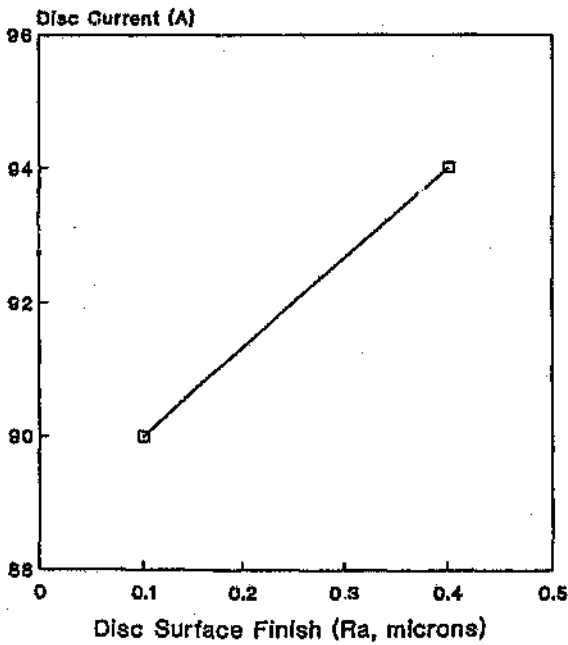
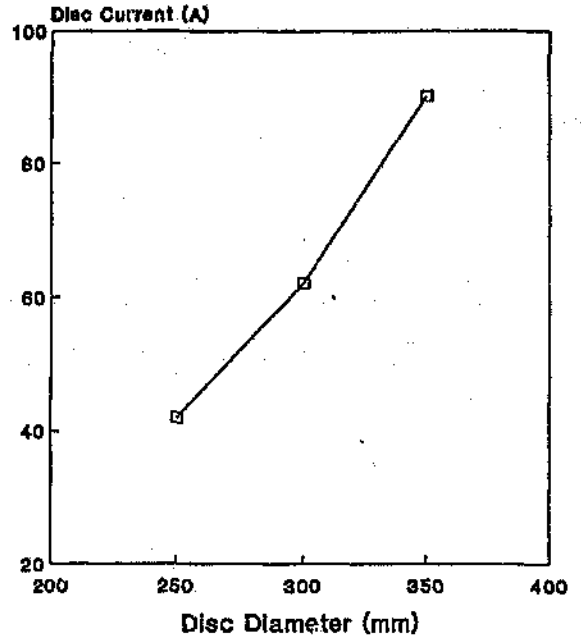
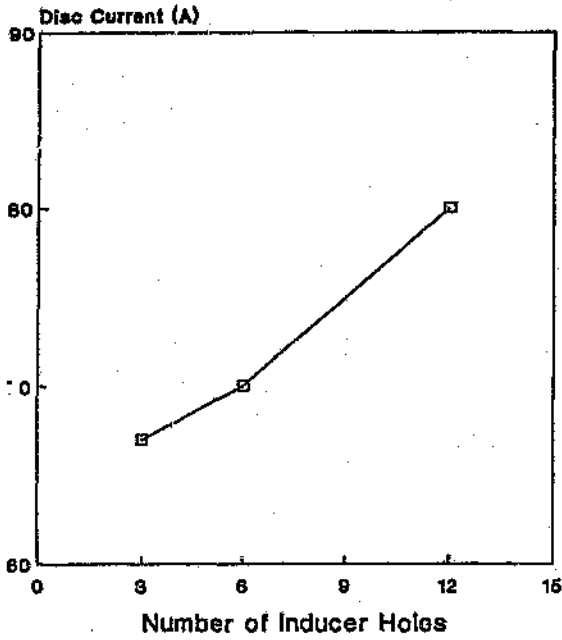


Figure 3.12: The influence of various disc design factors on disc power consumption. All other variables were kept constant, although they were not similar for the various graphs

The final disc design for erosion testing is shown in Figure 3.13. The type 316 stainless steel disc had thickness 8 mm and diameter 350 mm. Disc inducer holes were arranged in two sets of three holes at different disc radii. The smaller radius holes (i.e. lower sample velocity) made provision for round samples and were used to erode the standard materials (next section). Larger, rectangular samples were associated with the larger radius holes. All other erosion testing was done using this geometry for a number of reasons: increased velocity (at constant disc frequency) and thus cavitation intensity, better resolution of changes in the erosion zone, and the elongated sample profile allowed for a wide range on each variable. At each radius (velocity), a maximum of six samples could be tested, arranged in couples, back-to-back at each inducer hole. Whenever less than six samples were tested, the unused sample slots were filled with dummy samples made of type 316 stainless steel. The same held for the sample slots for the configuration not utilized; the associated inducer holes were filled with a polymer. The sample positions on the front (lid side) of the disc were called A1 to A3, while the corresponding positions on the rear side were B1 to B3.

3.4 Calibration of erosion performance

3.4.1 Introduction

Although numerous materials have been tested on the various available cavitation test rigs [1], important information concerning sample manufacture and test conditions is often not available. For this reason, the ASTM arranged a round-robin test programme on three well-characterized materials under carefully controlled test conditions, using vibratory test rigs [5]. This programme confirmed that quantitative agreement between different rigs is poor. However, all the labs ranked the materials (6061-T6511 aluminium alloy, type 316 stainless steel and commercially pure nickel) in the same order of cavitation erosion resistance, i.e. stainless steel being the most resistant, then nickel, then aluminium. In order to evaluate its erosion performance, these "standard" materials were eroded in the rotating disc-type apparatus.

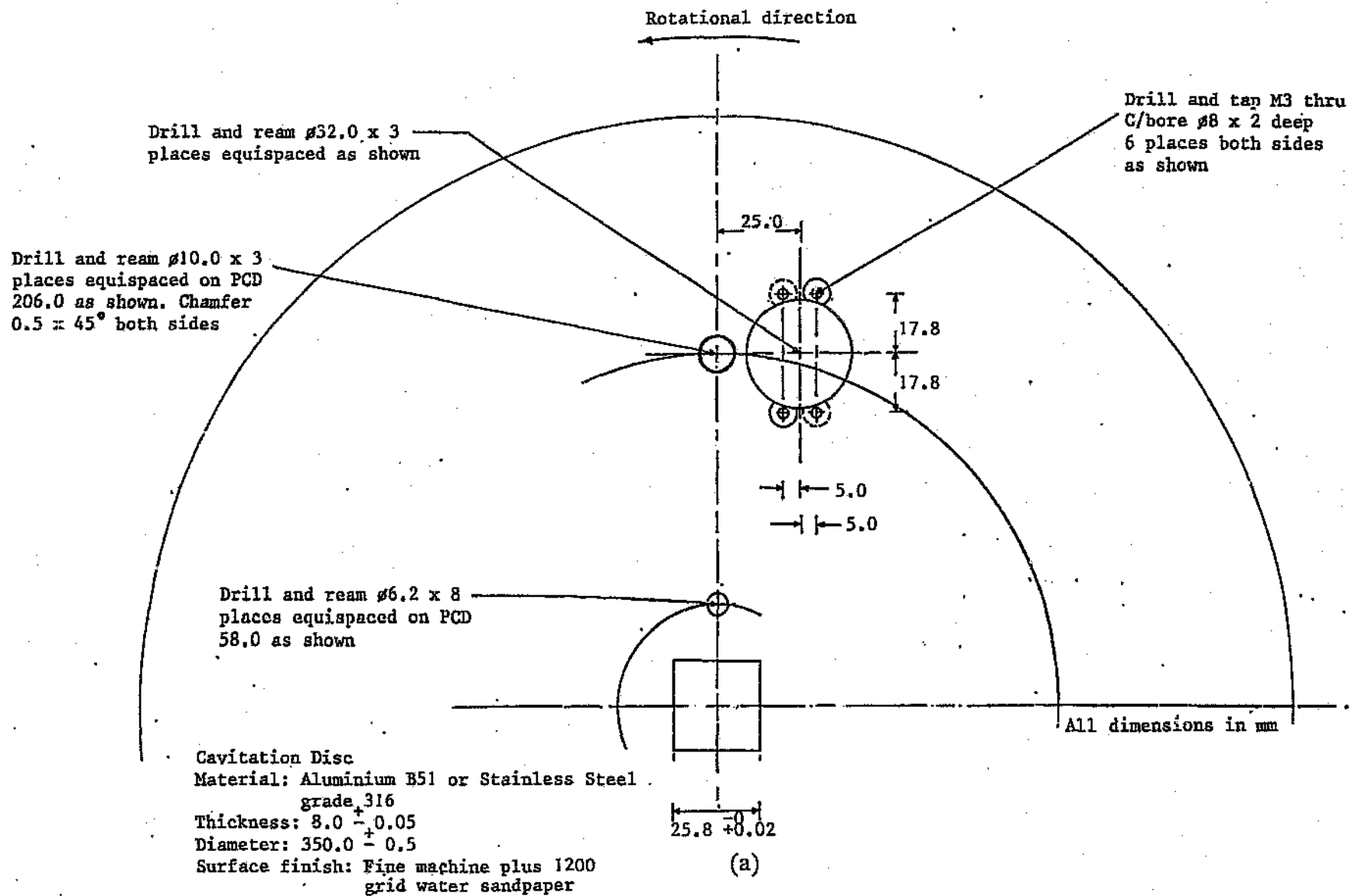


Figure 3.13: Disc and sample design for erosion tests: (a) and (b) disc, (c) disc-shaped samples and (d) rectangular samples

Cavitation disc
 Material: Stainless Steel
 grade 316
 Thickness: 8.0 ± 0.05
 Diameter: 350.0 ± 0.5
 Surface finish: Fine machine
 plus 1200 grit
 water sandpaper

Rotational
 direction

Drill and ream $\phi 10.0 \times 3$
 places equispaced on PCD
 276.0 as shown. Chamfer
 $0.5 \times 45^\circ$ both sides

Drill and tap M3 thru
 C/bore $\phi 8 \times 2.1$ deep
 9 Places both sides as
 shown

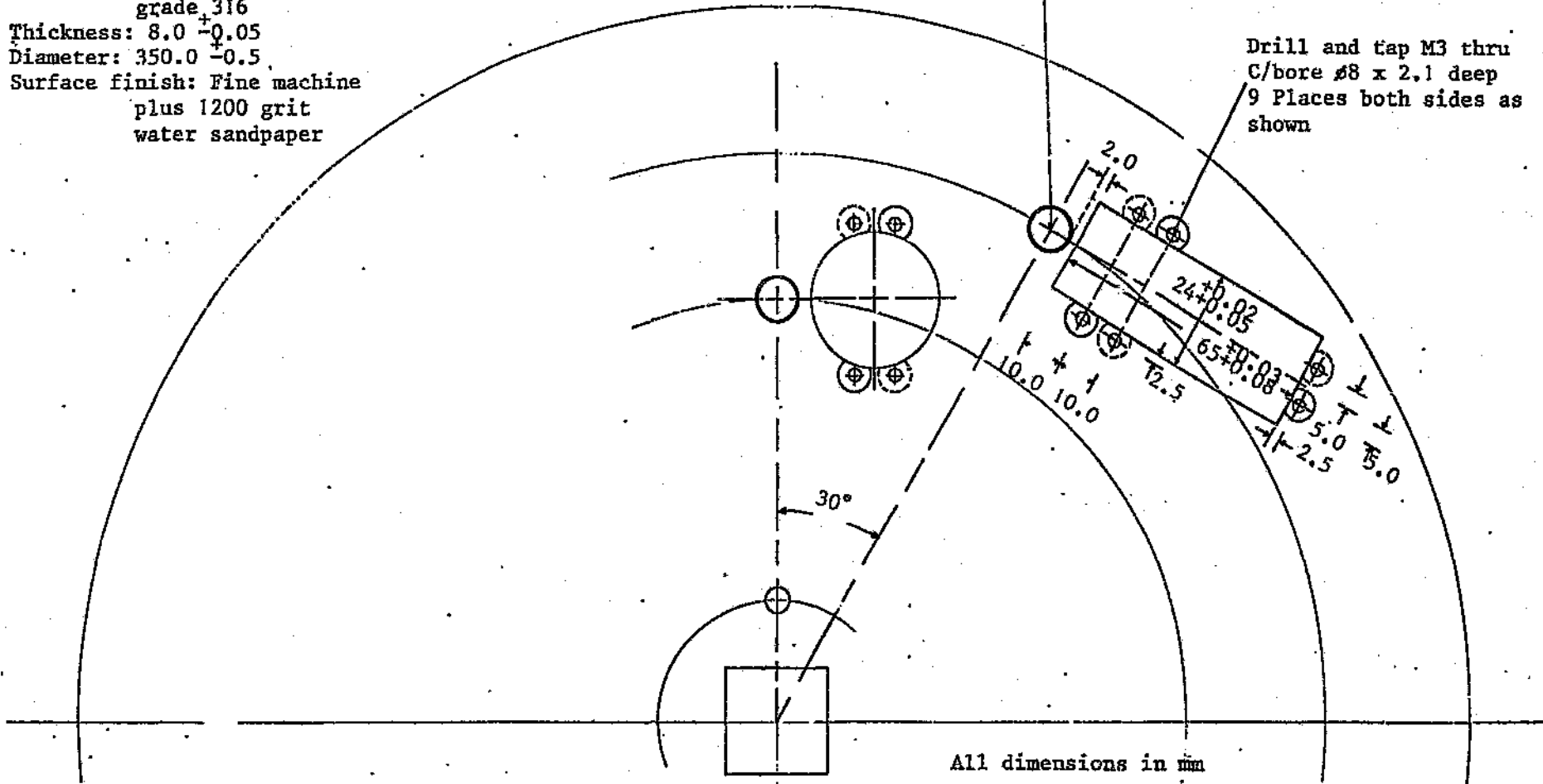
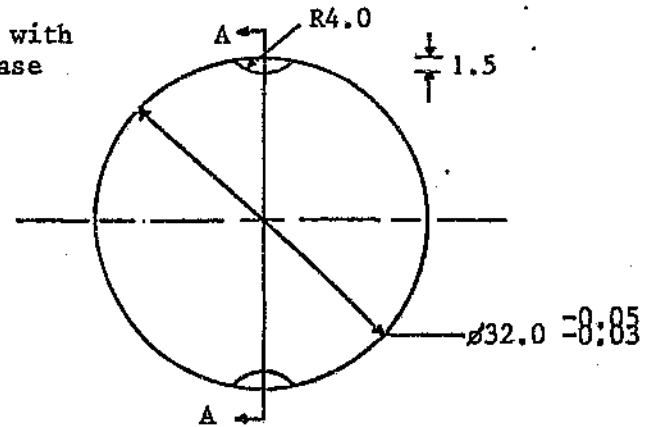


Figure 3.13 (cont):

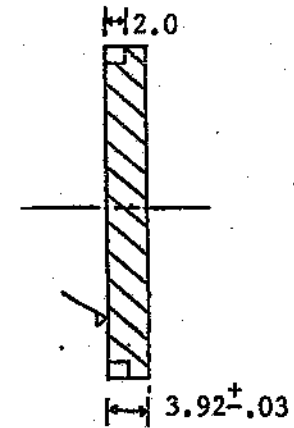
(b)

Sample

Note: Drill clamping holes with
7mm diamond coredrill in case
of ceramic samples



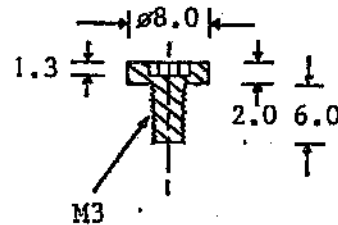
Section AA



All dimensions in mm

✓ = Polish with 1200 grit
water sandpaper

Scale: 2:1
Clamping Bolt
(Made from a Stainless
Steel M5 Allen cap screw)

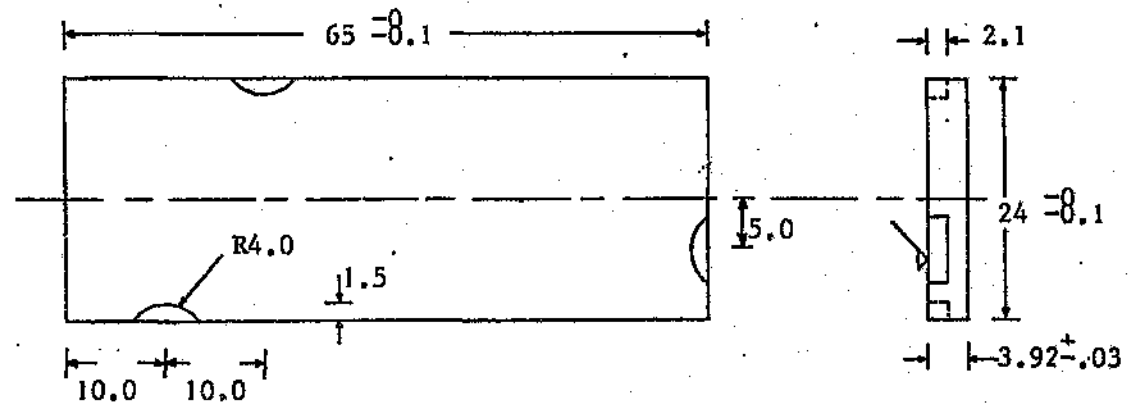


(c)

Figure 3.13 (cont):

Sample

Material: Aluminium 2S or Stainless Steel grade 316



All dimensions in mm

✓ Polish with 1200
grit sandpaper

(d)

Figure 3.13 (cont):

3.4.2 Test procedure

The materials were purchased in rod form and machined into disc-shaped samples as per Figure 3.13. The test fluid was tap water which flowed once through the flow system (Figure 3.14) in order to reduce the temperature in the test chamber. (At this preliminary stage the heat exchanger was not yet available.) The test conditions are shown in Table 3.2.

Two samples of each material were clamped back-to-back behind every inducer pole. Initially water was circulated through the test chamber until all excess air had been removed. The disc drive motor was then switched on and timing started. Flow and fluid variables were monitored in situ at regular time intervals to verify stability. The disc was also regularly inspected by means of the stroboscope to determine whether a proper cavitation field existed (Figure 3.15). Every 30 minutes the motor was stopped for inspection of the erosion zones on the samples. Mass measurements or photographic records could then be taken as required.

For mass measurements, the samples were removed from the disc and cleaned in ethanol with a nailbrush. They were then dried with paper tissue and put in a desiccator under vacuum for 30 minutes. Weighing was to 0,1 milligram on an electronic balance. The samples were then replaced in exactly the same location and orientation for further testing. A total or cumulative test time of 25,5 hours was completed.

3.4.3 Erosion data and damage characteristics

The aluminium sample mounted on the back of the sample disc (with respect to the optical window) underwent relatively minor damage due to a slightly raised leading edge. (This observation confirmed the importance of a flat disc/sample surface.) The other aluminium sample mounted on the front of the disc was tested for 12,5 hours. At this stage it had reached the peak erosion rate. Figure 3.16 shows the volume loss profile for this sample.

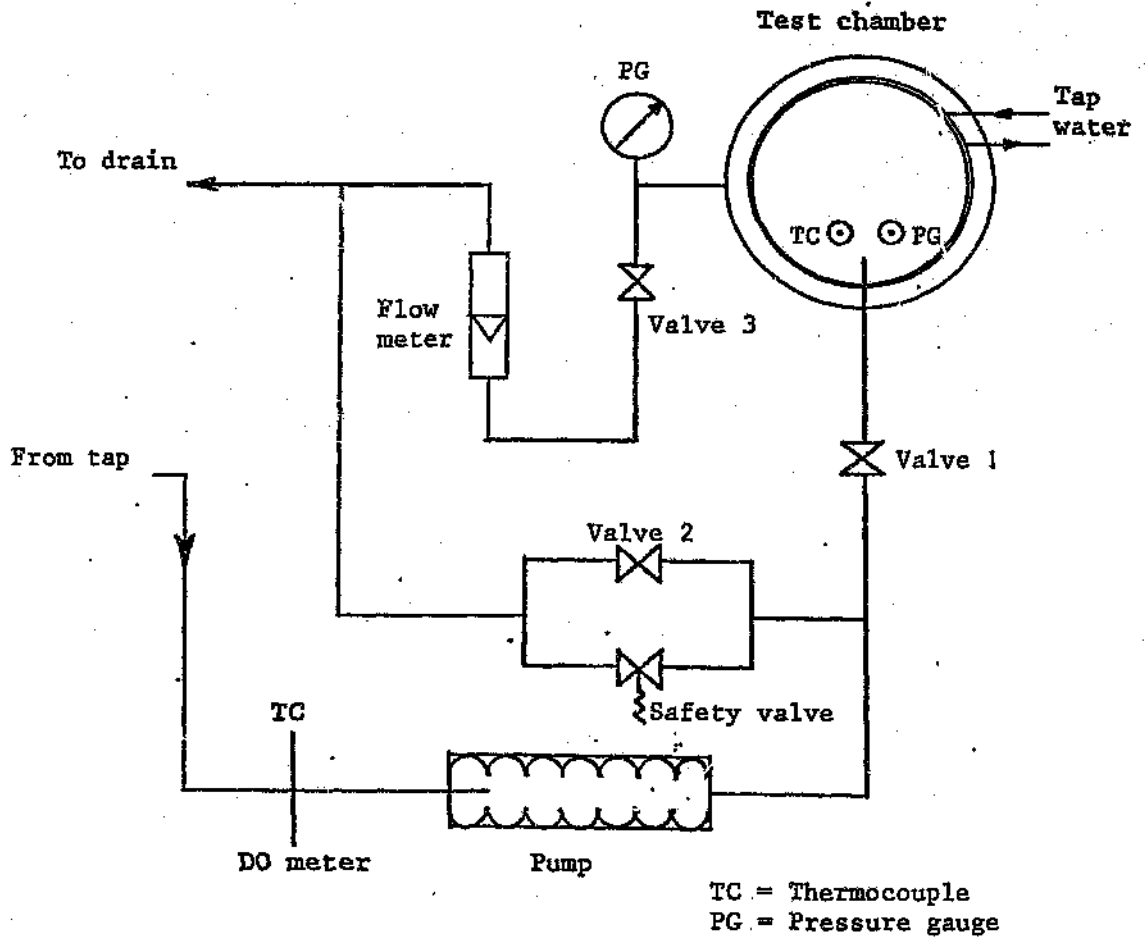


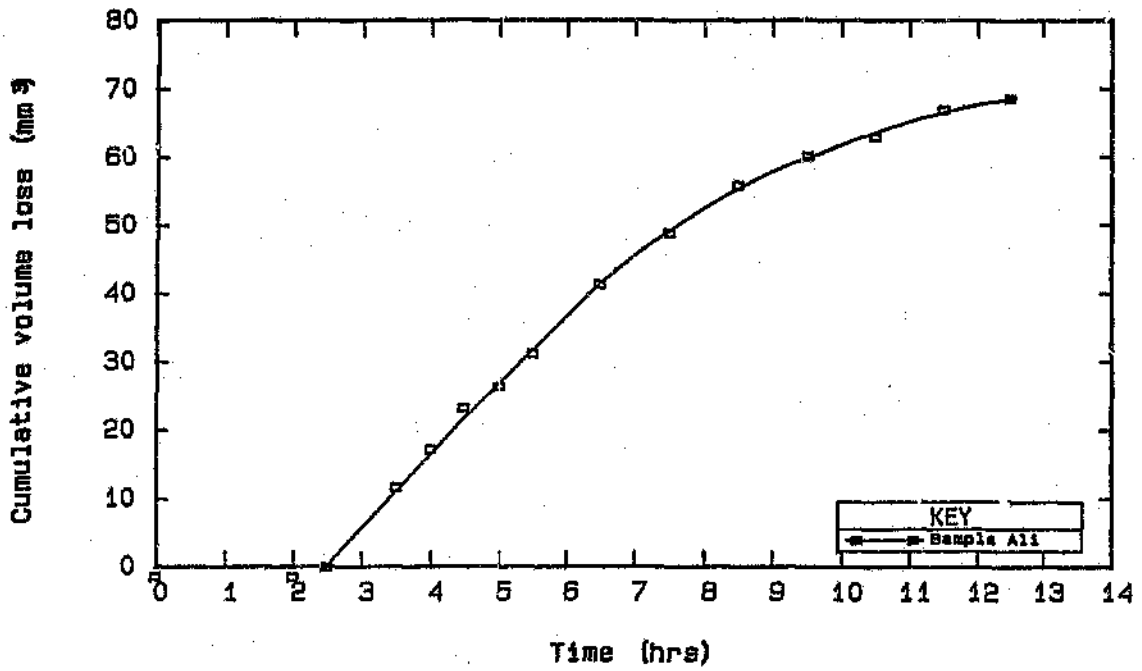
Figure 3.14: Flow system for cavitation erosion testing of standard materials

Table 3.2: Test conditions for standard materials

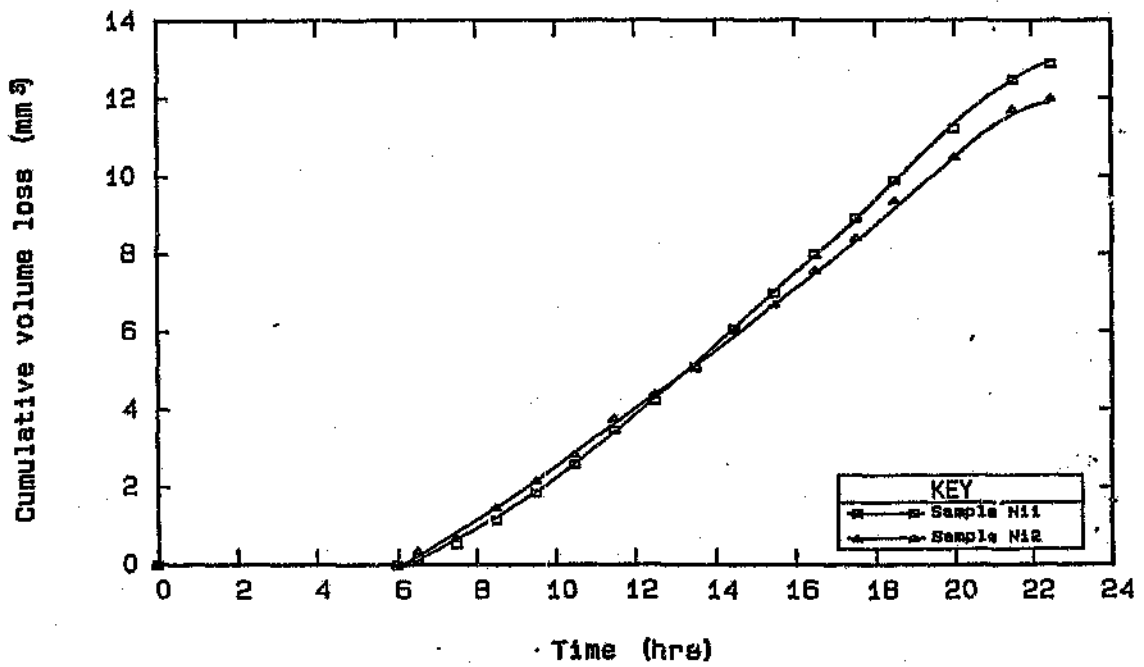
Variable	Value	Comment
Flow rate	60 l/min	Measured volumetrically
Oxygen content	6 mg/l	Measured with DO meter in reservoir
Temperature	33 °C	Measured with thermometer in reservoir
Pressure	Ambient	
Disc speed	3500 rpm	Corresponding to an average sample speed of 38 m/s



Figure 3.15: Cavitation field formed behind inducer hole on sample disc



(a)



(b)

Figure 3.16: Cumulative volume loss as a function of test time for (a) the aluminium standard and (b) the two nickel standards

The two nickel samples were tested for 22,5 hours until they exceeded their peak erosion rate. They exhibited similar volume loss rates (Figure 3.16).

After 22,5 hours, the stainless steel samples had not experienced any measurable volume loss although cavitation damage was visible. This is not surprising since stainless steel is highly resistant to cavitation (compared to aluminium and nickel). Testing was abolished at this stage since the goal of the test programme had been achieved.

The erosion curves displayed in Figure 3.16 were typical S-shaped curves (Figure 2.4) involving an incubation period, a maximum erosion rate period and a period where the erosion rate decreased. Furthermore, the expected ranking of the standards i.e. the stainless steel, nickel and the aluminium alloy in terms of decreasing erosion resistance was achieved (see Figure 3.17).

Eroding surfaces were monitored to follow the progress of damage. Figure 3.18 shows development of the erosion zone on the aluminium alloy. Damage was asymmetric and involved removal of material by undercutting on the inward side of samples (Figure 3.19). On a microscale, damage developed by the deformation of the surface in the form of undulations, eventually leading to material failure and removal (Figure 3.20). This is a typical damage mechanism caused by the shock-loading associated with cavitation [6,7]. Material failure was by ductile shearing (Figure 3.21) as discussed in [6], although an example of fatigue-like failure [8] was found on the aluminium alloy in an area where cavitation intensity was relatively low (Figure 3.22).

Based on these results, it was concluded that the rotating disc test rig operated satisfactorily and generated "typical" cavitation erosion.

3.5 Summary

A flow-type cavitation test facility employing a rotating disc was developed and tested. The main aims of the test rig, i.e. to study cavitation dynamics and erosion, were satisfactorily achieved. The rig was found to generate typical cavitation damage on

materials which erosion characteristics are well known.

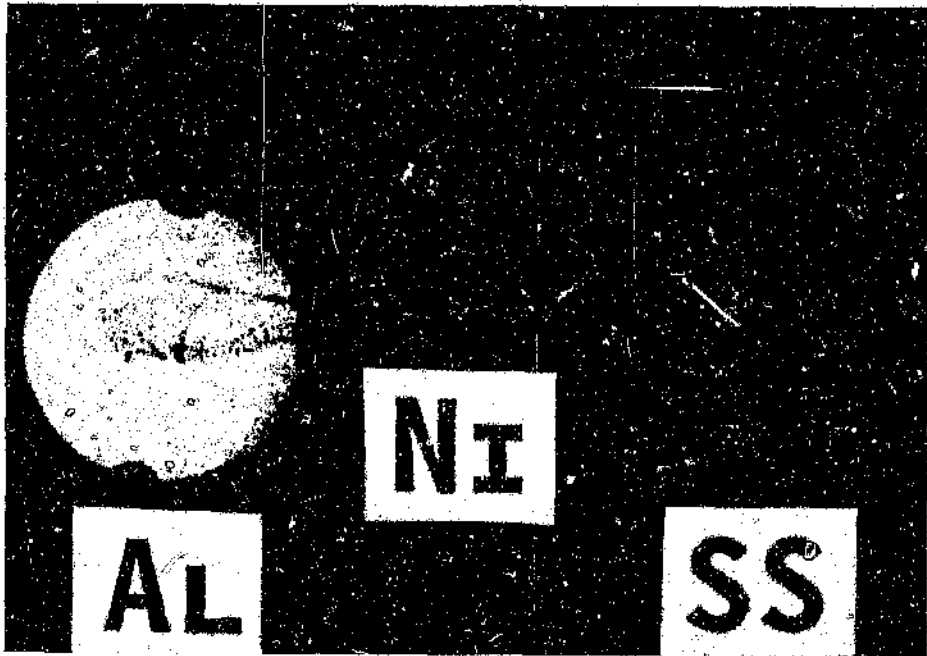
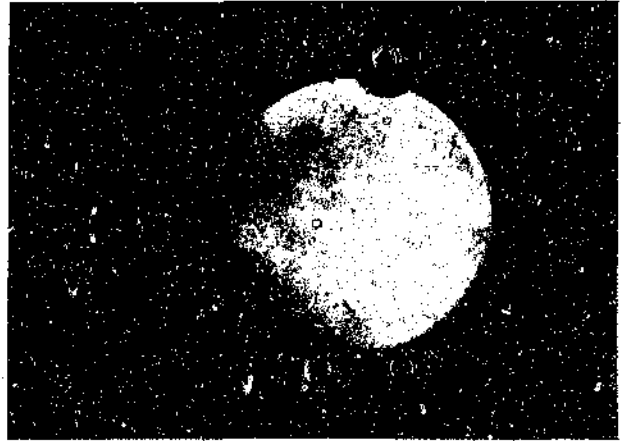


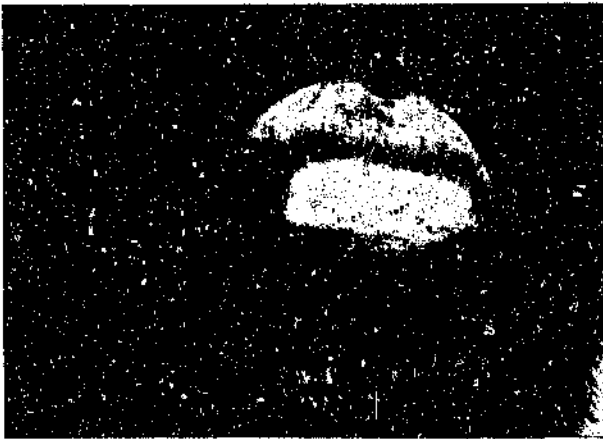
Figure 3.17: Relative cavitation erosion resistance of aluminium, nickel and stainless steel standards tested for respectively 12,5; 22,5 and 22,5 hours



(a)



(b)



(c)



(d)

Figure 3.18: Damage on aluminium sample after (a) 0,5; (b) 1; (c) 3,5 and (d) 4,5 hours of testing

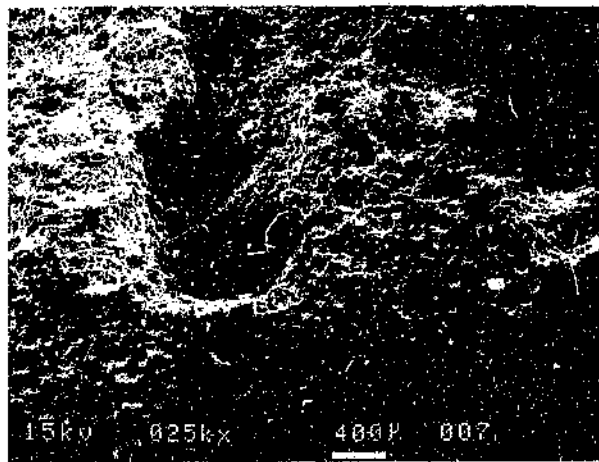
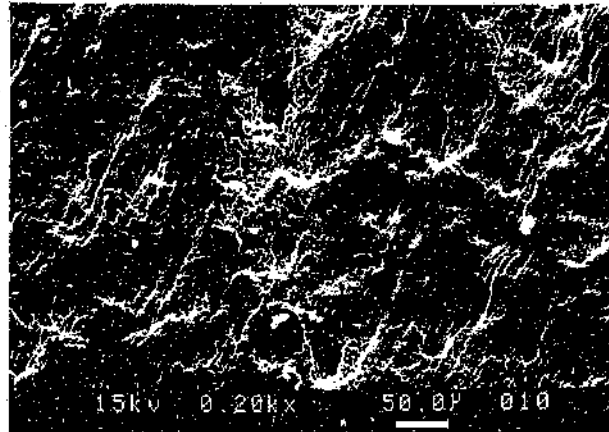
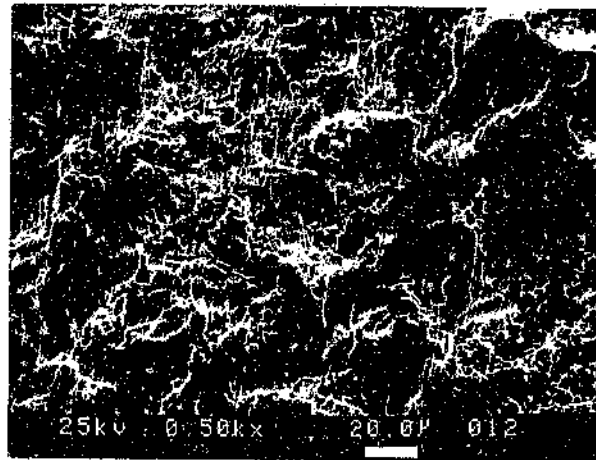


Figure 3.19: Undercutting of and material removal from aluminium standard surface due to radial forces exerted by the water

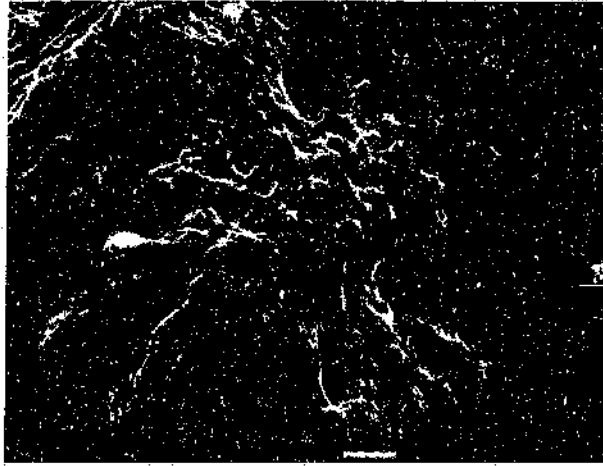


(a)

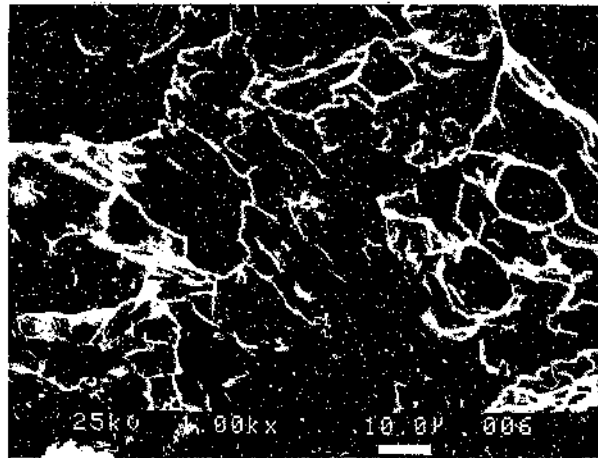


(b)

Figure 3.20: Undulated surfaces and evidence of material removal on (a) aluminium and (b) stainless steel standards

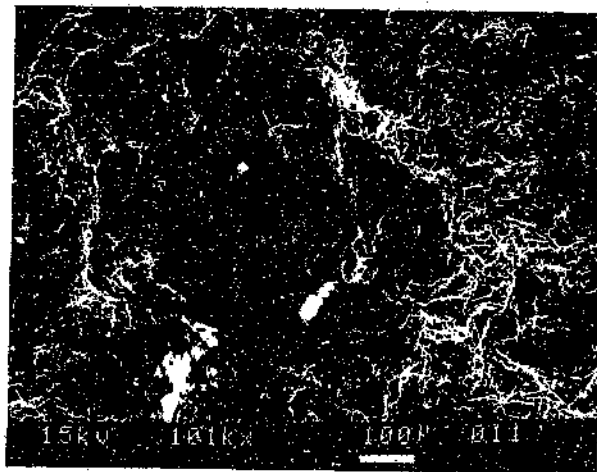


(a)

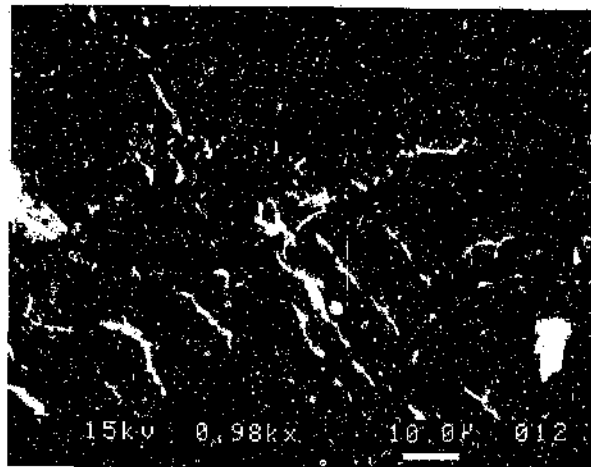


(b)

Figure 3.21: Fracture surfaces as a result of material removal from (a) aluminium and (b) nickel standards



(a)



(b)

Figure 3.22: (a) Large hole on aluminium standard where a chunk of material has been removed and (b) striations at the bottom of the hole at higher magnification, indicating failure by a fatigue mechanism

References

- 1) R.T. Knapp, J.W. Daily and F.G. Hammitt: *Cavitation*, McGraw-Hill, 1970.
- 2) J.Z. Lichtman, D.H. Kallas, C.K. Chatten and E.P. Cochran (Jr.): Study of Corrosion and Cavitation-Erosion Damage, *Trans. ASME*, Vol. 80, No. 1, 1985.
- 3) G.M. Wood: Cavitation Testing Techniques for High-Temperature Liquid Metal Systems, *Symp. Cav. Res. Facil. Tech.*, ASME, 1964.
- 4) F.G. Hammitt: *Cavitation and Multiphase Flow Phenomena*, McGraw-Hill, 1980.
- 5) F.G. Hammitt et al: ASTM Round-Robin Test with Vibratory Cavitation and Liquid Impact Facilities of 6061-T6511 Aluminium Alloy, 316 Stainless Steel, and Commercially Pure Nickel, *Materials Research and Standards*, ASTM, Vol. 10, No. 10, pp. 16-36, Oct. 1970.
- 6) B. Vyas and C.M. Preece: Cavitation-Induced Deformation of Aluminium, Erosion, Wear and Interfaces with Corrosion, *ASTM STP 567*, pp. 77-105, 1974.
- 7) C.M. Preece, S. Dakshinamoorthy, S. Prasad and B. Vyas: *Proc. 4th Int. Conf. Strength Met. Alloys*, Nancy, France, pp. 1397-1403, 1976.
- 8) K.S. Zhou and H. Herman: Cavitation Erosion of Titanium and Ti-6Al-4V: Effects of Nitriding, *Wear*, Vol. 80, pp. 101-113, 1982.

CHAPTER 4

4. INFLUENCE OF WATER TEMPERATURE AND CORROSION PROCESSES

4.1 Introduction

In cases where vibratory cavitation exists, it has been found that a peak erosion rate occurs about halfway between the freezing and boiling points of the cavitating fluid. The dropoff in damage on the low temperature side is ascribed to a combination of factors of which increased viscosity and surface tension may be dominant. At high temperatures approaching the boiling point of the test liquid, damage reduces due to the influence of thermodynamic effects. These issues are described in detail in Section 2.3.5.

Results on the effect of temperature on flow cavitation are scarce and less definite. Although no reason exists as to why the same phenomena should not govern the relation between temperature and erosion, it may be expected that their relative importance may vary due to the inherently different nature of vibratory and flow cavitation. An example is rectified diffusion of heat and gas [1] into developing nuclei leading to collapse cushioning of the resulting bubbles. Thus thermodynamic effects may be more effective in decreasing damage at elevated temperature under vibratory cavitation conditions.

Not much attention has been given to the role of increased corrosion rate and material degradation at increased temperature. These processes will lead to increased erosion rate and will thus oppose the thermodynamic effects. Hammitt et al [2] reported a second rise in erosion rate for a number of alloys tested in a vibratory rig.

In order to shed light on some of the issues described, the erosion resistance behaviour as a function of temperature was studied for aluminium and copper. The unusual behaviour of aluminium was further investigated.

4.2 Procedure for erosion testing

Erosion testing in this study was done in as many instances as possible on a single commercially available material with well-defined properties. The chosen material was 2S Al alloy, an essentially pure aluminium alloy. The American Association (AA) code is Al 1200 H4 as shown in Tables 4.1 and 4.2. The composition and physical properties of the material are given in Table 4.2. Aluminium is cheap, erodes easily [3], is easy to machine and has well-known microstructural behaviour under cavitation attack [4]. Upon observation of apparent anomalies in the erosion performance of 2S Al alloy at high temperatures, a second material had to be tested which would have most of the desirable properties of aluminium, but which would not suffer seriously from increased corrosion rate or mechanical weakening. Commercially pure Cu was chosen for its high melting point and relative chemical inertness.

Rectangular samples were machined according to Figure 3.13(c). The surfaces exposed to cavitation were ground and polished to $R_a \sim 0,1$ microns. The samples were stored in a dry desiccator at all times when not being tested. Before and after each test, they were cleaned in ethanol, dried and weighed to 0,1 of a milligram. The mass loss from each sample was converted to volume loss.

The test fluid, i.e. tap water, was circulated through the flow system shown in Figure 3.10. Water temperature was controlled by the feed rate of chilled water (18°C) and tap water ($\sim 21^\circ\text{C}$) through respectively the heat exchanger and cooling coil, the worst-case standard deviation (SD) being $\pm 1,9^\circ\text{C}$ (once stable conditions had been reached).

Two test series were carried out, one involving a 4 hour test period starting from ambient temperature, the test period for the other being 1 hour after the water had been preheated to the test temperature. This was achieved with the heating element in the reservoir. The results for these series will be described separately.

Table 4.1: International codes and equivalents for 2S Al alloy

American Association (A.A.)	Obsolete Systems	British Standard	Germany	France	Italy
1200	2S	1C	Al99,0	A4	P-APD UNI 3507

Table 4.2: Composition and typical mechanical properties of 2S Al alloy

A.A. ALLOY DESIGNATION	CHEMICAL COMPOSITION									TEMPER*	MECHANICAL PROPERTIES		
	Al min	Cu	Mg	Si	Fe	Mn	Zn	Ti	Cr		0,2% P.S. (MPa)	T.S. (MPa)	% EL in 50 mm
1200	99,0	0,05	-	Fe + Si 1,0	0,05	0,1	0,05	-	-	M (F)	50	90	-
										O (O)	35	85	33
										H4 (H14)	105	125	8

Melting Range	640-660°C
Density (at 20°C) kg/m ³	2710
Linear temperature coefficient of expansion (20-200°C) per °C	25 x 10 ⁻⁶
Thermal conductivity (at 100°C) W/mK	2,18 x 10 ⁻² - 2,22 x 10 ⁻²
Electrical resistivity (microhm cm)	2,9 - 3,0
Modulus of elasticity MPa	70 000
Torsion modulus MPa	26 500
Poisson's ratio	0,33

CONDITION*	DESCRIPTION
M (F)	As manufactured. Material which acquires some temper from shaping processes in which there is no special control over thermal treatment or amount of work/strain hardening.
O	Annealed, soft. Material which is fully annealed to obtain the lowest-strength condition and highest ductility condition.
H2 (H12) H4 (H14) H6 (H16) H8 (H18)	Strain hardened. Material subjected to the application of cold work after annealing (or hot forming), or to a combination of cold work and partial annealing/stabilizing in order to secure the specified mechanical properties. Designations are in ascending order of tensile strength. Note: Alloy 5251 is only available in H3, H6 and H8 tempers.

4.3 Results and discussion

4.3.1 Cavitation dynamics

Investigation of the cavitation cloud (by means of the stroboscope) and the damaged zone on the samples revealed that temperature affected the cavitation geometry. Figure 4.1 shows the damaged zones on the aluminium samples from the front of the disc for various temperatures. The centre of the erosion zone moved further downstream (i.e. away from the inducer hole) and became longer as temperature increased. In order to quantify this effect, Figure 4.2 shows the separation distance between the inducer hole and erosion plotted as a function of temperature. The shape of the erosion zone was fairly constant except for the growth of the small secondary cavitation zone (caused by the main erosion hole) with increasing temperature.

No previous reference has found on the effect of temperature on cavitation geometry, although it may give important clues as to the changes in bubble dynamics. The schematic presentation of flow cavitation in Figure 4.3(a) shows the approximate shape of the pressure gradient which controls cavitation. It has been shown in Figure 2.1 that a unique relation exists between nucleus size and vaporization pressure. Consider for the moment the nuclei which vaporize (cavitate) at exactly vapour pressure P_v . Since P_v increases with temperature (Figure 2.8), these nuclei will start vaporizing earlier, i.e. a shorter distance downstream of the inducer hole as shown in Figure 4.3(b). For the same reason, condensation will occur further downstream than at lower temperature. Thus the cavitation cloud will grow in the downstream direction with increasing temperature. (The upstream end already extends up to the inducer hole in our particular case.) As a result, the erosion zone which coincides approximately with the downstream end of the fixed cavity (Section 3.3, see also [3]) will also move downstream.



Figure 4.1: 2S Al alloy samples eroded for 1 hour at 44,8; 49,8; 65,5 and 78,8 °C from top to bottom

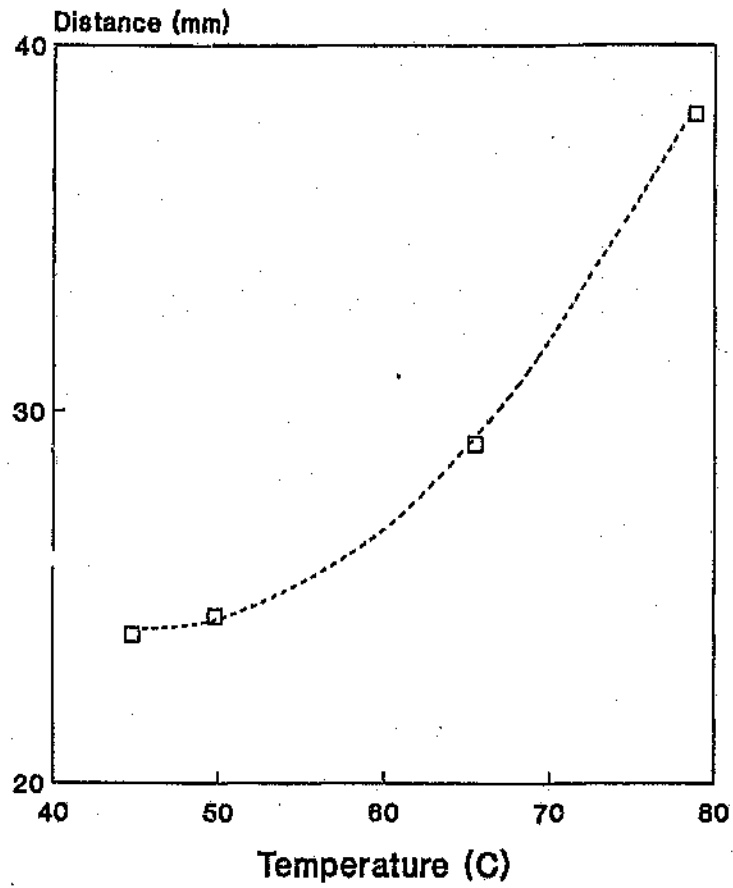
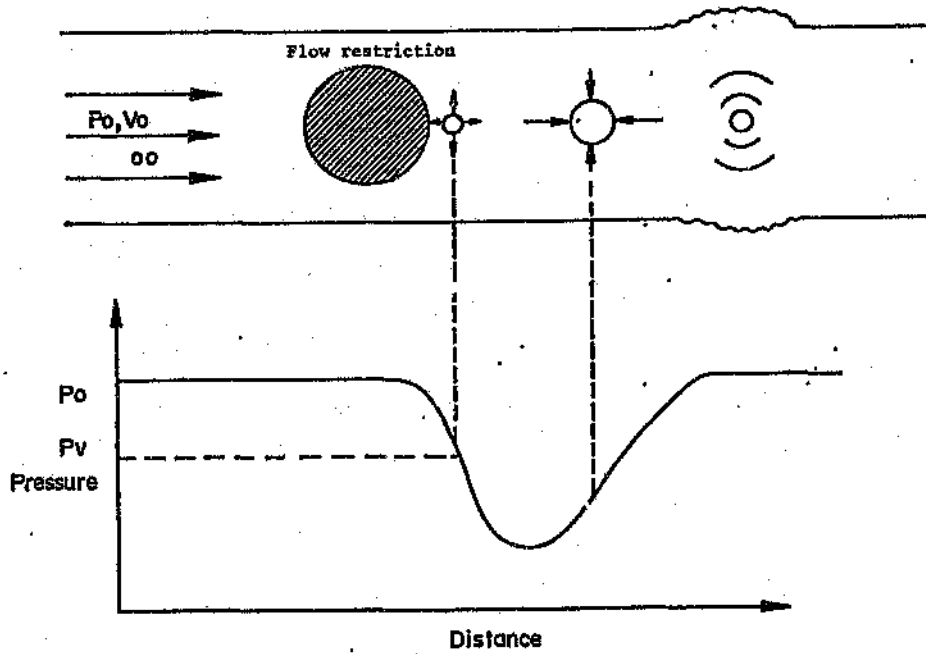
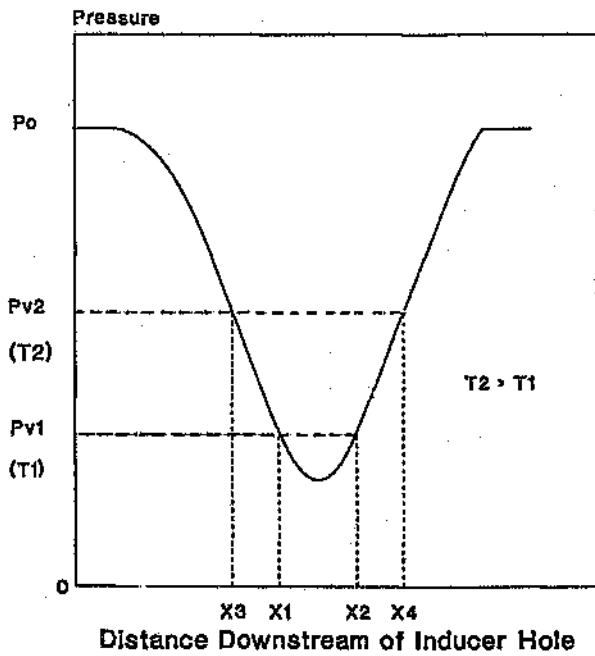


Figure 4.2: The distance between the downstream edge of the inducer hole and the centre of the main erosion hole, plotted as a function of temperature for the 1 hour tests



(a)



(b)

Figure 4.3: (a) Hypothetical presentation of flow cavitation and (b) the effect of temperature on bubble dynamics. Nuclei extend their travelling distance in the pressure interval below P_v from x_1x_2 at temperature T_1 to x_3x_4 at T_2 .

4.3.2 Erosion data

4 hour tests

For these tests, the test parameter values listed in Table 4.3 were used (based on the optimization procedure described in Section 3.3). The water temperature was allowed to rise by the release of cavitation energy up to the test temperature level, from whence it was controlled as discussed before. Thus the DO content which is determined mainly by water temperature, also fluctuated slightly until the stable temperature was achieved. Figure 4.4 shows an example of this behaviour.

Erosion data for the temperature tests is tabulated in Table 4.4. The stabilizing period indicates the time required for the water to reach the required temperature level, while the given temperature range was measured after this period. Analysis of the erosion data showed the following:

- (a) Compared to samples from the front side of the disc (A1 to A3), the samples on the back side (B1 to B3) showed relatively poor reproducibility of volume loss when tested under the same conditions. This was mainly ascribed to cavitation cloud changes induced by the sample clamping bolts on the back side (Figure 4.5). (This problem was subsequently rectified with an improved bolt design.) Thus erosion data for samples A1 to A3 was used to determine temperature effects.
- (b) The average (mean) volume losses were plotted on the erosion curves because the reproducibility of these was better than the reproducibility of individual samples (Table 4.5). This makes physical sense in terms of the fact that any disc-stator misalignment associated with disc removal and replacement will tend to cancel out over the disc surface as a whole. Another factor is that at least part of the volume loss was due to the removal of macroscopic chunks of material (Figure 4.6). Thus averaging over three samples resulted in smoothing of the data.

Table 4.3: Fluid and flow parameter values for temperature tests lasting 4 hours

Parameter	Mean Value	SD	Comment
Pressure (MPa)	0,14	0,002	No direct control. Max. operating temperature 60 °C, so no measurements could be taken for tests above this temperature
Dissolved oxygen (DO) content (mg/l)	7,50	0,71	
Disc velocity (rpm)	3521	24	
Flow rate (l/min)	~30		

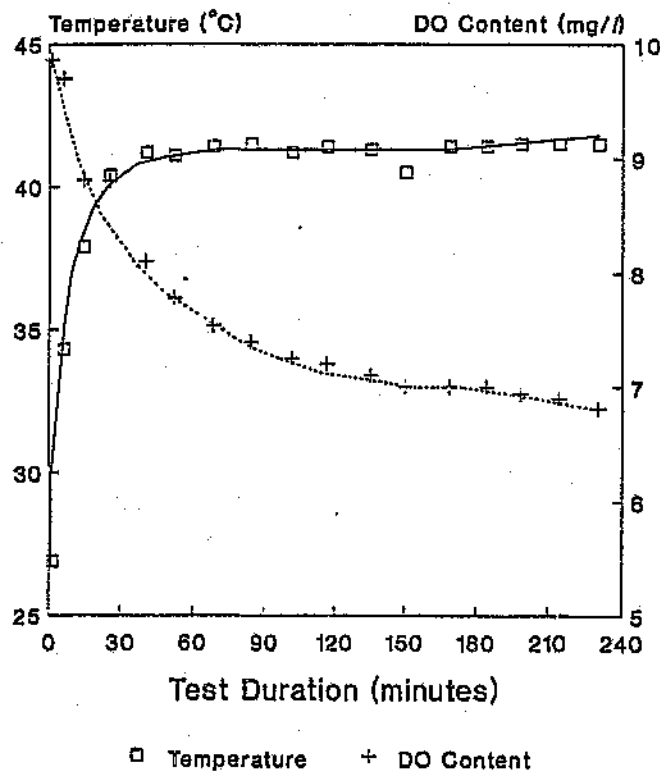
**Figure 4.4:** Typical temperature and dissolved oxygen variation as a function of test time for the 4 hour tests

Table 4.4: Erosion data for the 4 hour temperature tests

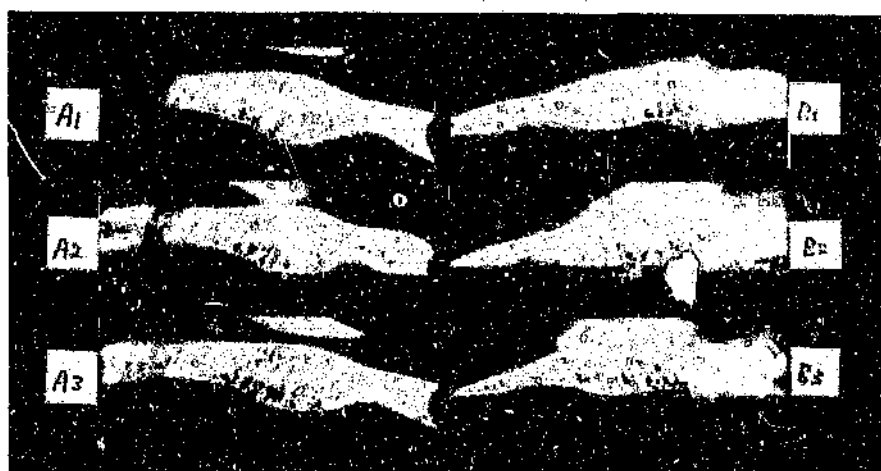
Test	Stabilizing period (min)	Temperature (°C)			4 h cum. volume loss (mm ³)						Average 4 h cum. vol. loss (mm ³)	
		Nom. value	Mean Value	SD	Sample position						Al	Cu
					A1	A2	A3	B1	B2	B3		
10*	16	26,5	26,5	0,4	155,0	28,6 ⁺	149,3	112,6	21,1 ⁺	126,6	152,2	24,9
9	30	41,0	41,2	0,4	174,0	-	144,1	74,7	-	59,4	159,1	-
2	8	49,8	49,8	0,2	165,7	137,3	162,7	137,1	135,8	80,9	155,2	-
3	26	49,8	49,9	0,2	172,2	161,9	173,5	118,1	140,2	95,4	169,2	-
6	20	49,8	51,1	0,6	161,7	25,5 ⁺	146,0	138,3	24,6 ⁺	109,0	153,9	25,1
4	56	78,8	78,5	1,0	246,7	237,0	244,8	200,7	182,5	157,4	242,8	-
7	34	78,8	78,8	0,8	238,2	9,0 ⁺	203,2	200,6	8,9 ⁺	183,4	220,7	9,0

* Flow system was once-through as per Figure 3.14. The cooling water for the heat exchanger was circulated through an ice bath

+ Copper sample



(a)

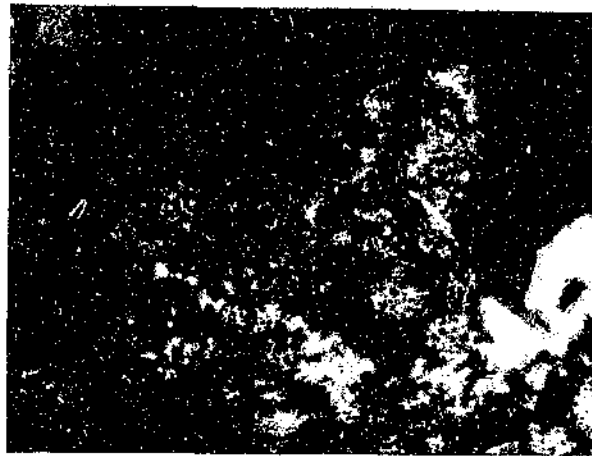


(b)

Figure 4.5: Samples eroded at (a) 49,8 and (b) 78,8 °C. Note the difference in erosion geometry between the A- and B-samples corresponding respectively to the front and back of the disc.

Table 4.5: Reproducibility of temperature erosion results

Nominal Temp (°C)	No. of tests	SD for individual samples			SD for average volume loss
		A1	A2	A3	
49,8	3	5,3	17,4	13,8	8,5
78,8	2	6,0	-	29,4	15,6

**Figure 4.6:** Large chunk of material which are due to be removed from the edge of the erosion zone on an aluminium sample (magnification x27)

Plotting volume loss against temperature for aluminium showed a continuous increase of volume loss with temperature (Figure 4.7). This result was not in line with the usual trend and indicated that the role of material weakening and increased corrosion rate [2] needed further elucidation. Visual examination of samples revealed that those tested at 80 °C had a shiny appearance. A scanning electron microscope (SEM) examination of sample surfaces showed increased corrosion activity both in (Figure 4.8(a)) and outside (Figure 4.8(b)) the erosion zone of samples tested at 80 °C, as opposed to 50 °C (Figure 4.9). It appeared that material was corroded away around second-phase particles containing mainly Al and Fe (Figure 4.10). These are typically Al_6Fe or Al_3Fe [5] and are cathodic to the aluminium solid solution matrix [6]. As a result, corrosion will progress more rapidly in the solid solution immediately surrounding the particles.

To verify that the aluminium result was material-specific, copper was included in the test programme. As illustrated in Figure 4.7, the volume loss for copper decreased drastically above 50 °C. This is in agreement with the "normal" trend.

1 hour tests

These were carried out mainly to confirm the 4 hour test results on aluminium. Improved accuracy of data was achieved by introducing the following changes:

- The test time was decreased to 1 hour, thus preventing the development of secondary cavitation which had at elevated temperature extended to the downstream edge of the sample (Figure 4.5).
- Temperature control (and thus air content stability) was improved by preheating the water before the start of each test (see Figure 4.11).
- Erosion data was obtained for the three samples on the front side of the disc in all cases.

The test parameters are listed in Table 4.6.

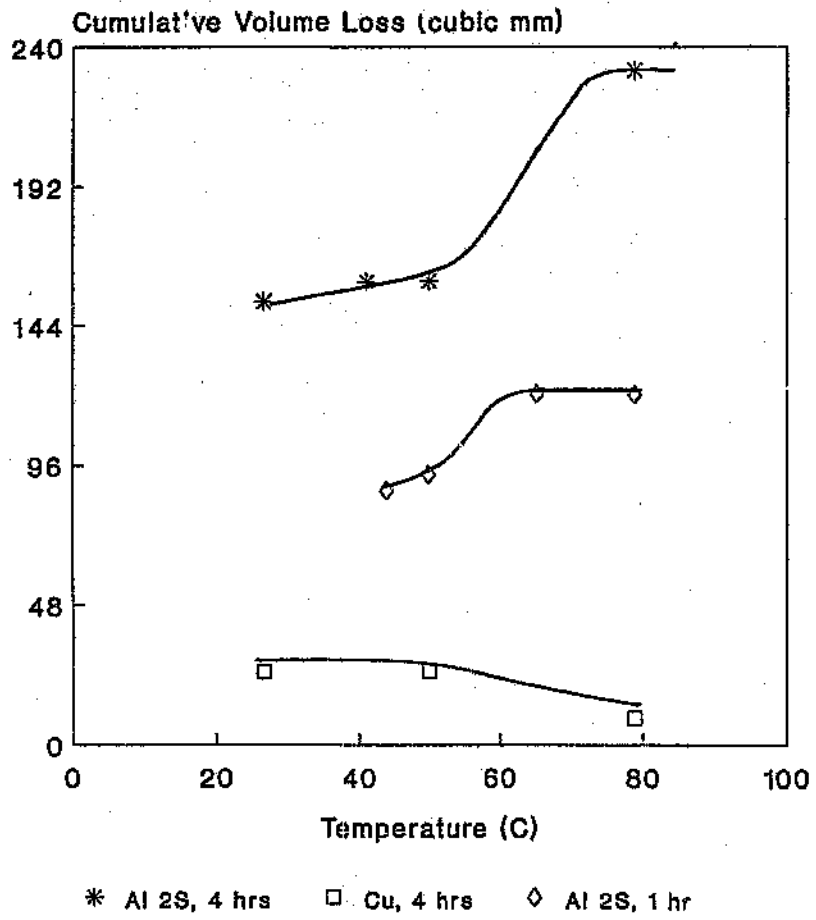
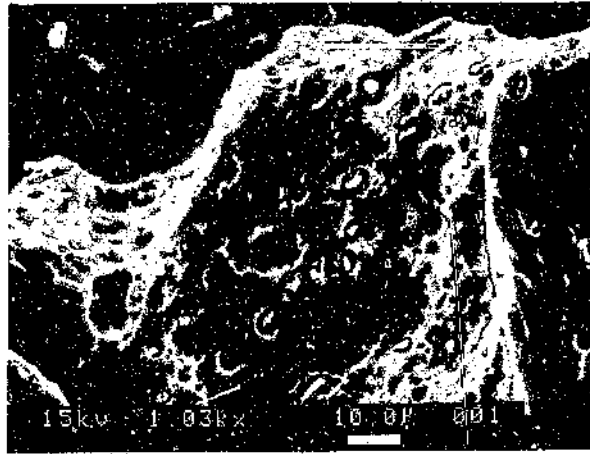
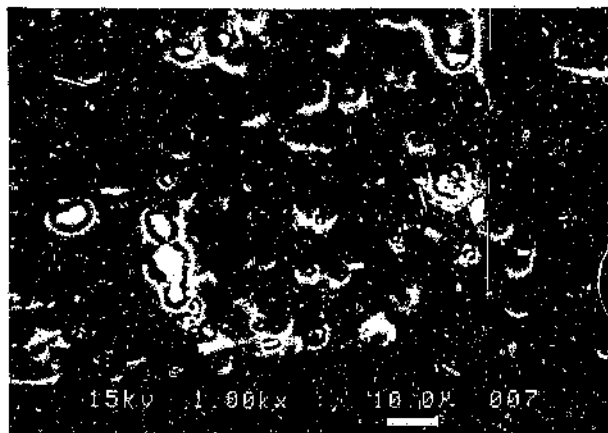


Figure 4.7: Effect of temperature for 4 hours and 1 hour erosion tests



(a)



(b)

Figure 4.8: SEM micrographs of samples surfaces corroded at 80 °C, taken (a) within and (b) outside the erosion zone

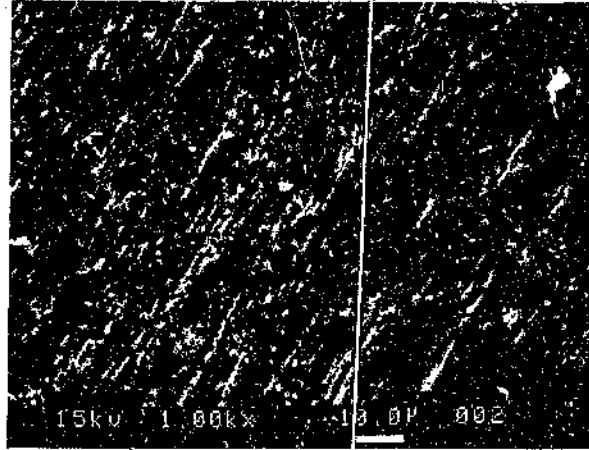


Figure 4.9: SEM micrograph of samples surface eroded at 50 °C, outside erosion zone

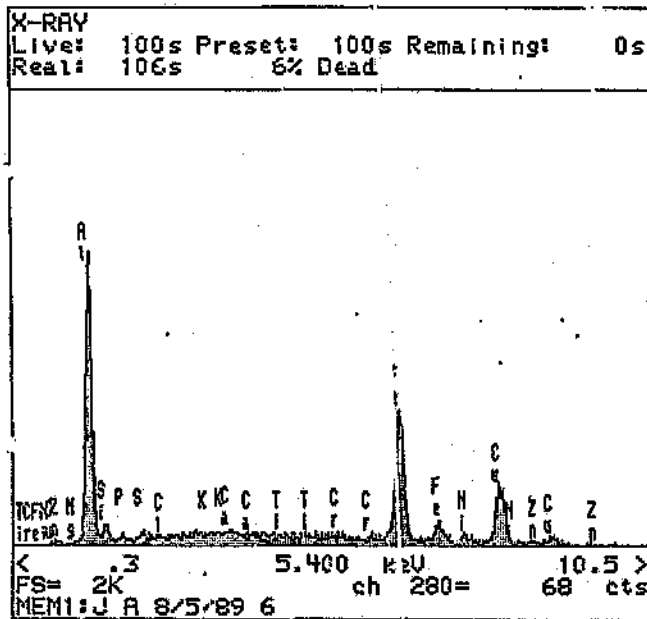


Figure 4.10: Energy dispersive X-ray spectrum of particles on surfaces eroded at 80 °C

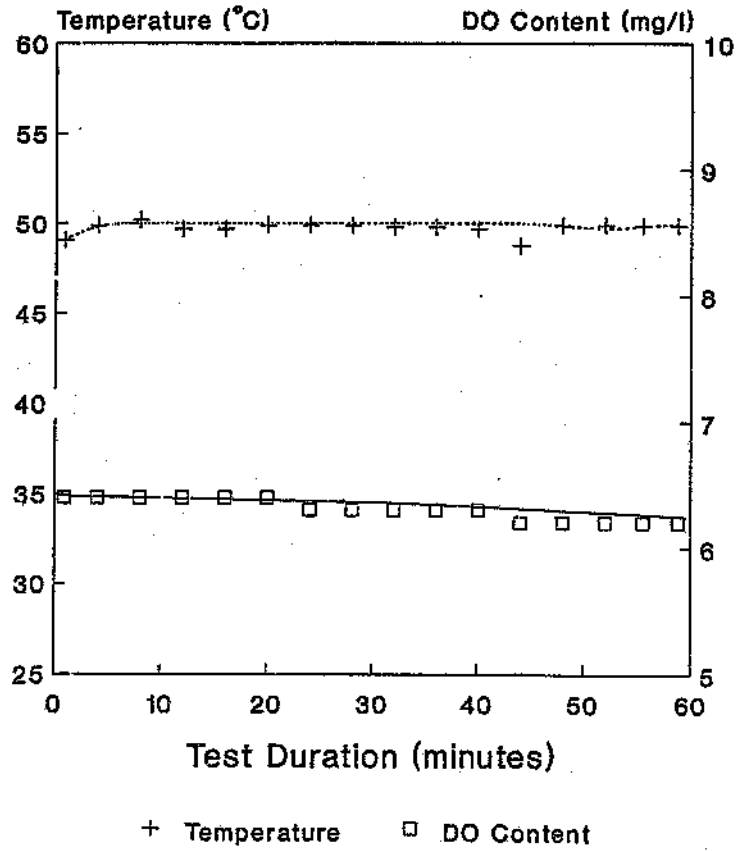


Figure 4.11: Typical temperature and dissolved oxygen variation as a function of test time for the 1 hour tests

Table 4.6: Test parameters for 1 hour temperature tests

Parameter	Mean Value	SD	Comment
Pressure (MPa)	0,15	0,02	No direct control. Max. temperature is 60 °C
Dissolved oxygen (DO) content (mg/l)	6,69	0,45	
Disc velocity (rpm)	3629	14	
Flow rate (l/min)	~30		

Erosion data for the 1 hour tests on aluminium is tabulated in Table 4.7 and plotted in Figure 4.7. The erosion curve indicates that the peak volume loss for aluminium occurred already at approximately 65 °C, but that no significant decrease followed at higher temperatures; in fact, the curve flattened out. This confirms the result from the 4 hour tests on aluminium.

It would thus appear that the erosion behaviour of copper as a function of temperature is governed by the same phenomena (thermodynamic effects, viscosity and surface tension variations etc.) identified previously for vibratory tests. However, in the case of aluminium, inverse material effects seem to override these phenomena under certain conditions. To clarify this issue, the influence of increased temperatures on the corrosion resistance and mechanical strength of aluminium has been investigated, as described below.

4.4 Temperature-related material effects on aluminium

4.4.1 Corrosion

It is well known that cavitation and corrosion, when acting simultaneously, will produce more damage than just the sum of the two separate effects. By implication a relatively small increase in corrosion rate of a sample may thus have a substantial effect on volume loss.

In order to measure the influence of corrosion at elevated temperature on the erosion rate of 2S Al alloy, a special disc-and-sample arrangement, geometrically similar to that of the sample disc in Figure 3.13, was tested in the rotating disc-test rig. It comprized an aluminium disc designed to contain electric wires leading from a sample recess to the hollow drive shaft (Figure 4.12). The corrosion cell shown in Figure 4.13 was constructed to fit into the sample recess. It consisted of a 6 mm diameter sample electrode made from 2S Al alloy, a stainless steel auxiliary electrode and a stainless steel reference electrode which were respectively the inner disc, middle ring and outer ring in Figure 4.13. These were cast in an epoxy into the stainless steel frame shown in the

Table 4.7: Erosion data for the 1 hour temperature tests

Test No.	Temperature (°C)			4 h cum. volume loss (mm ³)			Average 4 h cum. vol. loss (mm ³)
	Nom. value	Mean Value	SD	Sample position			
				A1	A2	A3	
14	35,0	34,9	1,9	92,0	81,7	88,0	87,2
13	49,8	49,8	0,3	96,5	93,8	88,1	92,8
11	65,0	65,2	0,3	126,6	117,1	117,9	120,5
12	78,8	78,7	0,3	114,4	120,5	125,5	120,1

Material: Aluminium B51
 Thickness: 6.0 ± 0.05
 Diameter: 35.0 ± 0.05
 Surface finish: Fine machine plus
 1200 grit water sandpaper
 All dimensions in mm.

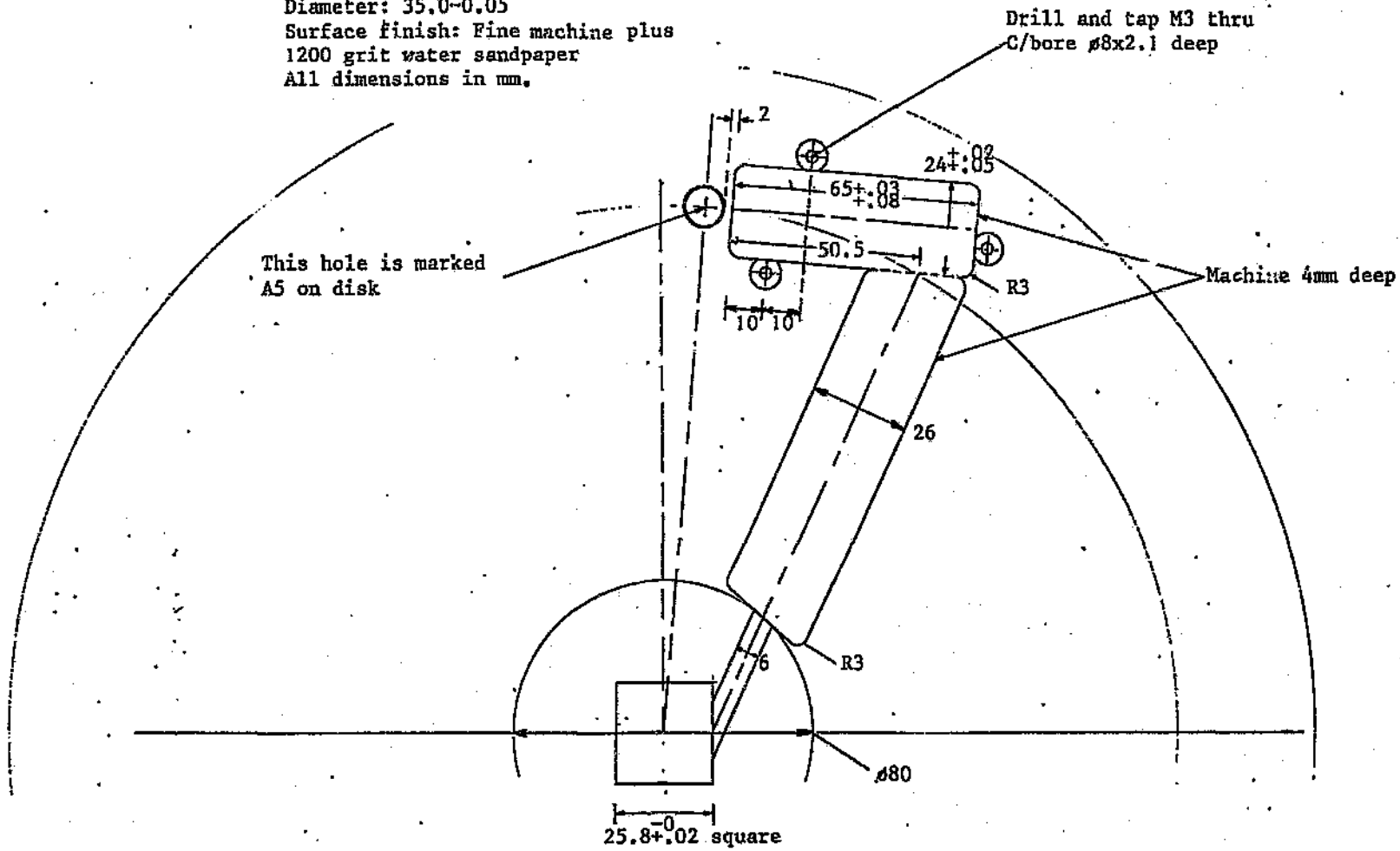
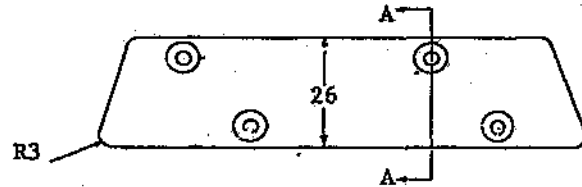
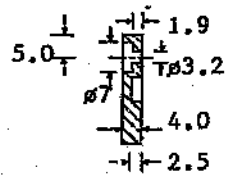


Figure 4.12: Disc design for electric measurements.

Material: Aluminium B51
 All dimensions in mm.



Note: Clamping bolts for cover
 are made from M3 stainless
 steel Allen cap bolts by
 machining 1.5mm off the
 top and 0.5 off the head



Section AA

Figure 4.12 (cont.)

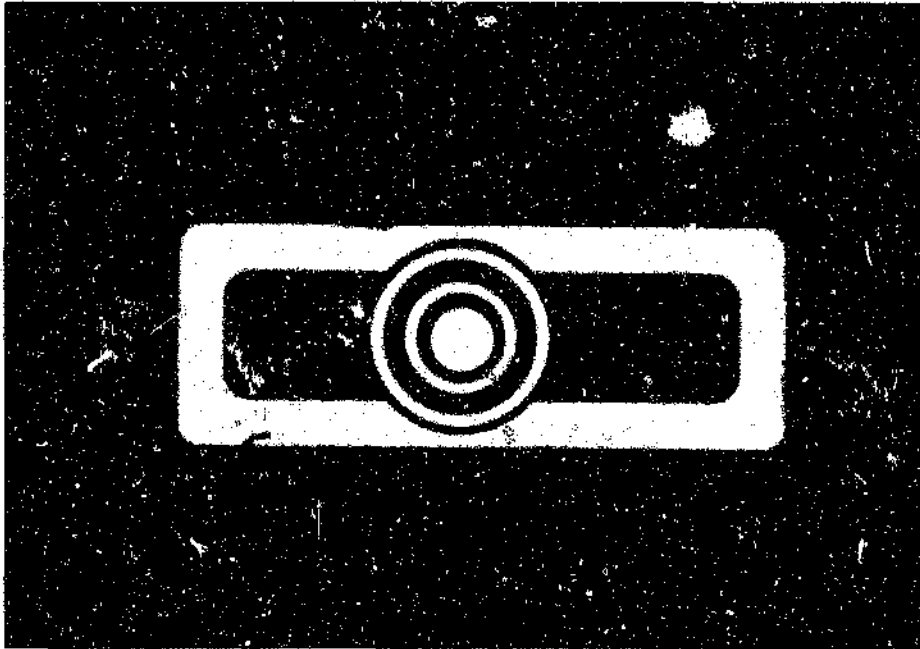


Figure 4.13: Corrosion cell consisting of 2S Al alloy working electrode (disc), stainless steel auxiliary electrode (inner ring) and stainless steel reference electrode (outer ring)

figure. After setting, the exposed cell face was ground and polished flat and the cell was fitted into the disc. The electrode wires were passed along the radial slot in the disc and through the hollow centre of the drive shaft, which was subsequently sealed with epoxy. The wires were connected via a slipping assembly to a potentiostat as illustrated in Figure 4.14.

The test parameters are listed in Table 4.8. Corrosion rates were measured at 50, 60 and 80 °C under three conditions: disc stationary; disc rotating with no cavitation (achieved by filling up the inducer holes); and disc rotating with normal cavitation.

Results are shown in Table 4.9 and Figure 4.15. Important observations are:

- At any particular temperature, the corrosion rate is higher for cavitating as opposed to stationary or rotating only conditions. This demonstrates clearly the synergism between cavitation erosion and corrosion.
- With increasing temperature, the corrosion rate under cavitating conditions becomes higher, i.e. corrosion damage will increase with temperature.

4.4.2 Mechanical Degradation

At approximately 100 °C, significant weakening of aluminium with respect to its ambient properties may have occurred [7]. This will accommodate enhanced plastic deformation and eventually material removal. The work described in this section was carried out to measure the temperature of an eroding 2S Al alloy surface, thereby determining whether local heating due to the intense mechanical working occurred which could result in material weakening.

The same disc and measuring system as in Section 4.4.1 was used. A temperature measuring cell to fit the sample recess was devised as shown in Figure 4.16. It consisted of a 2S Al alloy body which contained a chromel-alumel thermocouple just below the exposed surface in the erosion zone, and another outside the erosion zone. The thermocouples were called respectively the working thermocouple (WTC) and reference

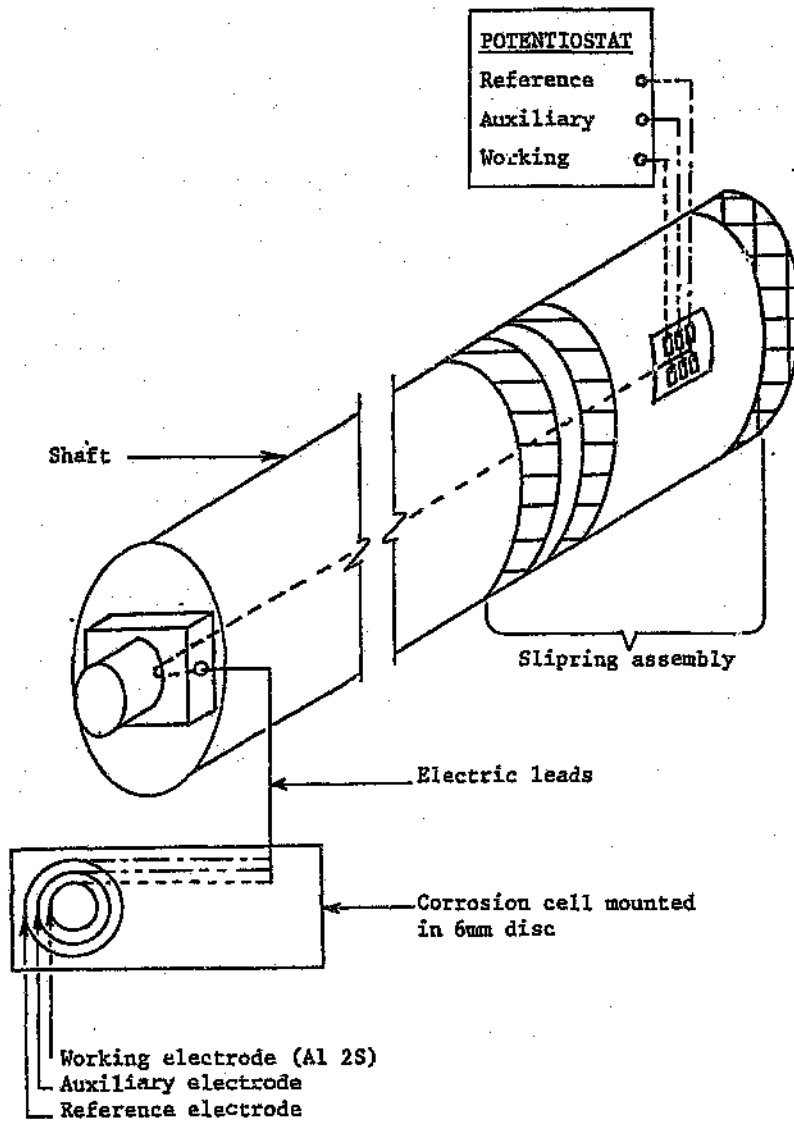


Figure 4.14: Measuring system to investigate the corrosion behaviour of 2S Al alloy in the rotating disc rig

Table 4.8: Test parameters for corrosion rate measurements

Test fluid	Tap water
Temperature (°C): i. mean ii. range	50; 60; 80 1
Static pressure (MPa): i. mean ii. range	0,15 0,01
Flow rate (l/min)	~30
Disc velocity (rpm)	~3600

Table 4.9: Influence of cavitation and temperature on 2S Al alloy corrosion rate

Test parameters		Corrosion rate	Average corrosion rate
Temp (°C)	Disc condition	($\mu\text{m/y}$)	($\mu\text{m/y}$)
50	Stationary	7,9	7,8
		7,6	
	Rotating	348 329	338
50	Cavitating	868	859
		655	
		1272	
		792	
		791	
808			
60	Cavitating	1270	1270
80	Stationary	2174	2085
		1692	
		2388	
80	Rotating	1370	1260
		1287	
		1122	
80	Cavitating	3303	3375
		3236	
		3587	

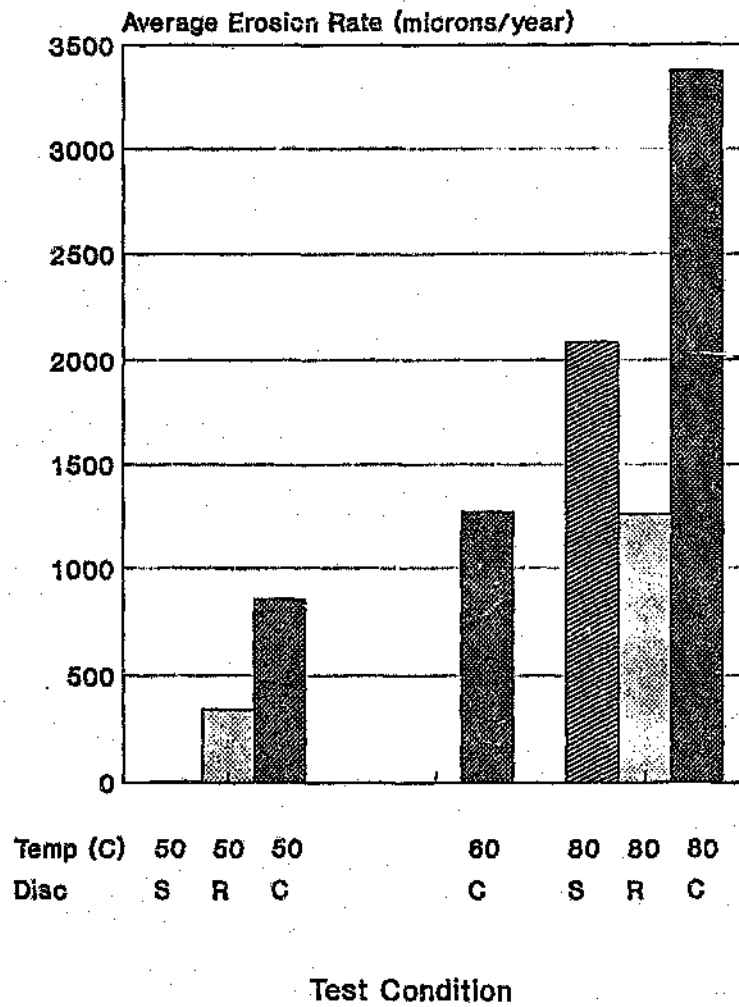


Figure 4.15: Bar chart showing the influence of cavitation and temperature on Al alloy corrosion rate

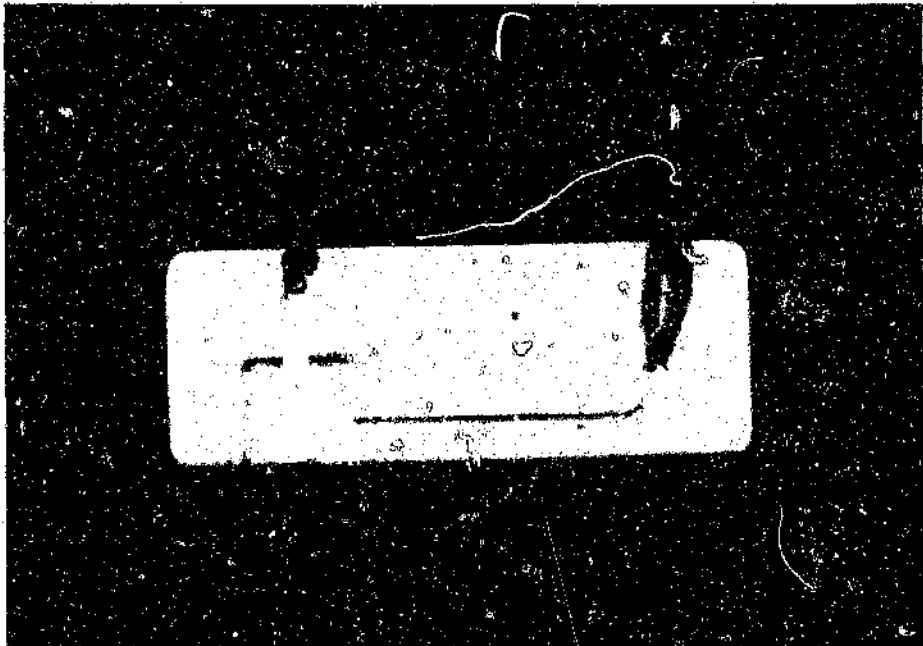


Figure 4.16: Rear side of temperature measuring cell showing the two chromel-alumel thermocouples

thermocouple (RTC). A thermally conductive adhesive was used to hold the thermocouple beads in position. The wires were clad in shrink tubing and cast into a polymer to isolate them from each other and the test water. After installation of the cell into the test chamber, it was heated in water to allow calibration of the thermocouples against a mercury thermometer.

Test parameters for the temperature measurements in the rotating disc test rig are given in Table 4.10. The temperatures of the two thermocouples were measured under these conditions as a function of water temperature and test time. The static pressure was varied to ensure that the WTC would be directly in contact with the surface area experiencing most intense erosion. Measurements were abolished when the depth of the erosion hole became compatible to that of the thermocouples.

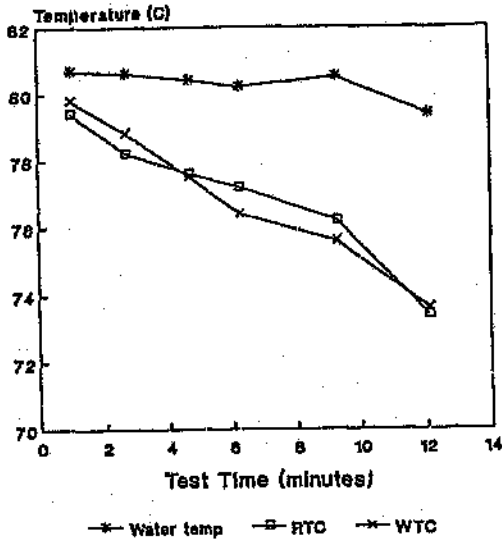
Figure 4.17 shows the measured temperature profiles. There was no significant difference between the readings from WTC and RTC, and the trend was for a slight temperature decrease with time. The temperature level was marginally below that of the test water. Thus indications were that no temperature rise resulted due to the erosion attack, possibly due to the large metallic body of the cell acting as a heat sink. This is in agreement with the results obtained by Singer and Harvey [8].

4.4.3 Discussion

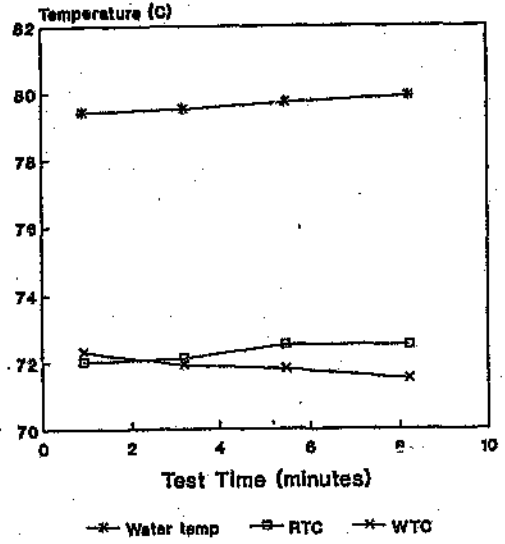
There is no substantial drop in the volume loss of 2S Al alloy at elevated temperatures. As inferred in the literature and confirmed with erosion tests on copper, thermodynamic effects lead to a decrease in cavitation erosion damage at temperatures approaching the boiling point of the cavitating liquid. The high damage rate on aluminium may thus be ascribed to material-related factors, such as increased corrosion rate and mechanical weakening, which oppose the thermodynamic effects. Analysis of these factors showed that the major contribution to the erosion behaviour of 2S Al alloy came from an increase in the corrosion rate.

Table 4.10: Test parameters for temperature measurements

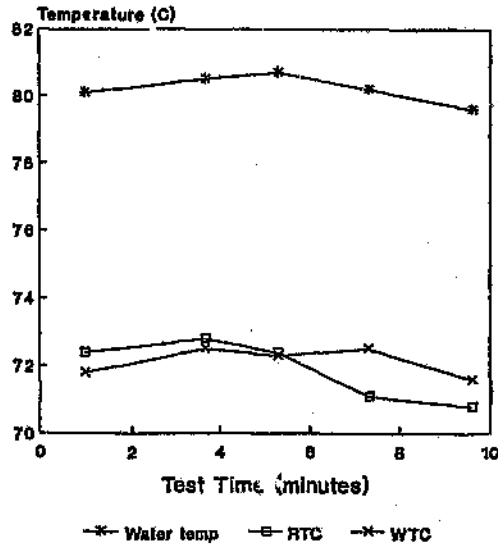
Test fluid	Tap water
Temperature (°C):	
i. mean	80
ii. range	1,3
Static pressure (MPa):	
i. mean	0,15; 0,18; 0,20
ii. range	0,01
Flow rate (ℓ/min)	~30
Disc velocity (rpm)	~3600



(a)



(b)



(c)

Figure 4.17: Temperature profiles for the WTC and RTC against water temperature at (a) 0,15, (b) 0,18 and (c) 0,20 MPa

4.5 Summary

Using aluminium and copper samples in the rotating disc cavitation test apparatus, the effect of water temperature on cavitation dynamics and erosion was studied.

A shift in the position of the erosion zone with changing temperature was observed. This was explained in terms of the effect of temperature on the pressure gradient giving rise to cavitation.

As had been found for vibratory cavitation, the erosion rate in this case (flow cavitation) also increased with increasing water temperature and reached a maximum at ~ 50 °C. However, in contrast with copper which exhibited the usual behaviour, the erosion rate of aluminium did not decrease with further temperature increase.

This apparent anomaly was investigated by employing specially-developed cells for corrosion rate and temperature measurements on a cavitating aluminium sample. It was found that an increase in corrosion rate was responsible for the high cavitation erosion rate at temperatures above 50 °C.

References

- 1) F.G. Hammit: *Cavitation and Multiphase Flow Phenomena*, McGraw-Hill, 1980.
- 2) X. Wang, Y. Zhou and F.G. Hammit: *Vibratory Cavitation Erosion Tests at 120-150 C and 2 bar Suppression Pressure*, *Cavitation and Multiphase Flow Forum*, ASME, 1984.
- 3) R.T. Knapp, J.W. Daily and F.G. Hammit: *Cavitation*, McGraw-Hill, 1970.
- 4) B. Vyas and C.M. Preece: *Cavitation-induced Deformation of Aluminium*, *ASTM STP 567*, pp. 77-105, 1974.
- 5) J.E. Hatch (editor): *Aluminium: Properties and Physical Metallurgy*, ASM, p. 60, 1984.
- 6) R.B. Mears and R.H. Brown: *Causes of Corrosion Currents*, *Ind. Eng. Chem.*, Vol. 33, p. 1007, 1941.
- 7) *Properties and Selection: Nonferrous Alloys and Pure Metals*, *Metals Handbook*, 9th Edition, Vol. 2, ASM, 1979.
- 8) B.G. Singer and S.J. Harvey: *Gas Content and Temperature Effects in Vibratory Cavitation Tests*, *Wear*, Vol. 52, pp. 147-160, 1979.

CHAPTER 5

5. INFLUENCE OF STATIC PRESSURE AND VELOCITY

5.1 Introduction

It was mentioned in Section 2.3.4 that pressure and velocity in a flow cavitation system influence each other. Hydrodynamic similarity in a cavitating system demands a constant cavitation parameter σ (Equation (2.4)). Thus if velocity changes for example, static pressure must change accordingly. Changes in damage characteristics at constant σ are known as scale effects. According to this definition, the changes caused by most of the variables investigated in this study may be termed as scale effects. However, the influence of static pressure or velocity was investigated while keeping the other parameter constant, i.e. σ varied.

Most reported studies were carried out under varying σ conditions. The influence of pressure was investigated in venturi-type and vibratory test rigs. Erosion rate as a function of pressure showed a maximum. The drop-off at the low pressure side was due to a decrease in bubble collapse violence as a result of the smaller pressure differential. At high pressures, the minimum pressure rises and therefore less bubbles can nucleate.

Water tunnels, venturi- and rotating disc-type test devices were used to evaluate the effect of velocity. Damage usually increased with a power of the velocity ranging between 5 and 10, although negative powers had been observed under well-developed cavitation conditions where the pressure became insensitive to velocity changes.

Although numerous investigators studied the nature of the cavitation field by in situ observation [1,2] and the damage mechanisms operating on eroding surfaces [3,4], little information has been published on the relation between cavitation and erosion geometries, and especially the influence of fluid and flow parameters on these. The relation between velocity and pressure, and cavitation and damage characteristics has

thus been investigated in the course of the present study.

5.2 Procedure for erosion testing

The test samples were made of 2S Al alloy. Sample treatment and test procedure were the same as for the temperature tests involving a 1 hour test period (Section 4.2). The three sample positions on the front of the test disc was used because satisfactory results were achieved in this way as described in Section 4.3.2. Samples were eroded for 1 hour in tap water at sample velocities of 48 and 51 m/s and static water pressures of 0,10; 0,12; 0,135; 0,15 and 0,25 MPa. (Not all combinations were tested.) The other test parameters are listed in Table 5.1.

5.3 Results and discussion

5.3.1 Cavitation dynamics

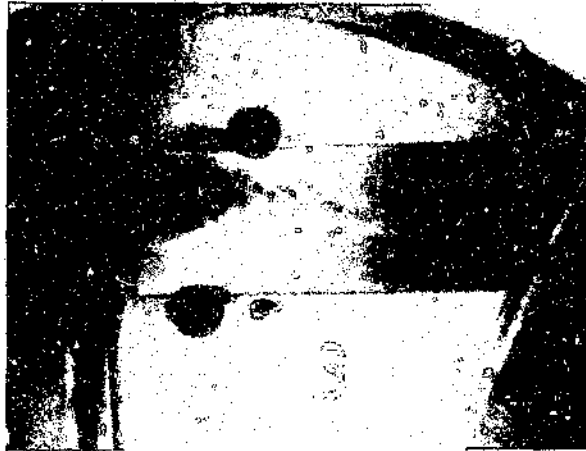
The cavitation cloud was studied in situ under the various velocity and pressure conditions and compared with the erosion zone formed on 2S Al alloy (Figure 5.1). Since damage developed somewhat too quickly on the aluminium samples causing changes in the cloud geometry, stainless steel samples which suffered no visible damage during the test period were used to investigate cloud characteristics.

An interesting phenomenon was "stator cavitation", i.e. cavitation created as a result of the shearing action between the stators and the water. Since inception sigma had to remain constant (Section 2.3.2), this cavitation appeared at higher pressure if the velocity was increased. As a result, the inducer hole cavitation was obscured at $P_0 = 0,10$ MPa and $v_0 = 51$ m/s.

The cavitation clouds and associated erosion zones are sketched in Figure 5.2. Each cloud consisted of a fixed cavity (solid line) and travelling cavities (dashed line) as discussed in Section 3.3. Note the secondary erosion which started forming as a result of the primary erosion hole. Analysis of Figure 5.2 shows that the clouds and zones

Table 5.1: Test parameters for the pressure and velocity tests

Parameter	Mean Value	SD	Comment
Temperature (°C)	52,8	2,6	Water is preheated to nominal value
Dissolved oxygen content (mg/l)	6,7	0,5	
Flow rate (l/min)	~30		



(a)



(b)

Figure 5.1: (a) In situ observation of the cavitation cloud and (b) erosion zone on samples A1 to A3. Velocity is 51 m/s and pressure 0,15 MPa

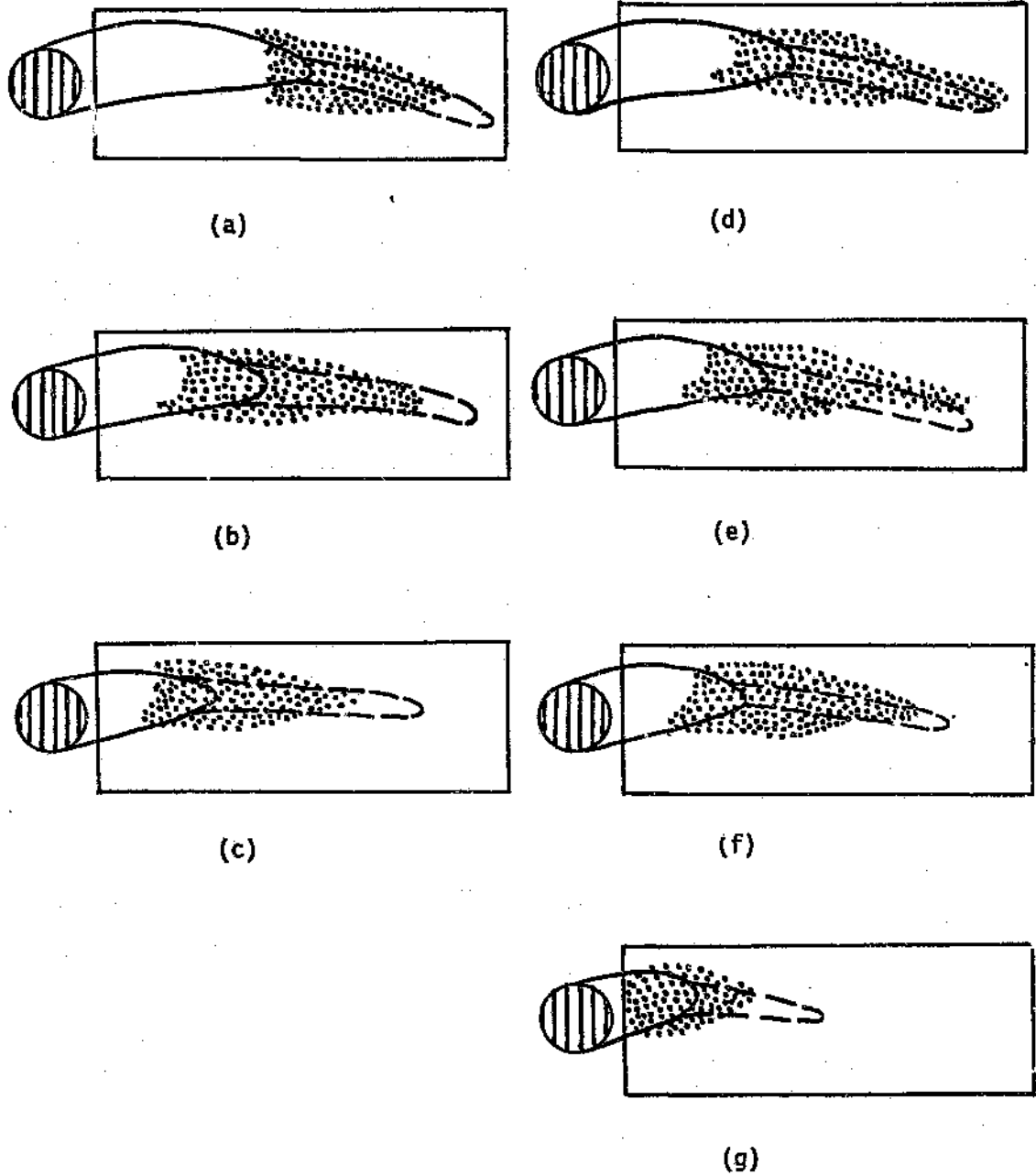


Figure 5.2: Cavitation cloud and associated erosion zone for the following sample velocities (m/s) and static pressures (MPa): (a) 48 and 0,10; (b) 48 and 0,12; (c) 48 and 0,135; (d) 51 and 0,12; (e) 51 and 0,135; (f) 51 and 0,15; (g) 51 and 0,25

moved upstream with increasing pressure and decreasing velocity, and vice versa. This is illustrated in Figure 5.3 where the position of the erosion hole with respect to the inducer hole is plotted as a function of velocity and pressure. There is also a smaller change in the hole-cloud relation with velocity and pressure (Figure 5.4).

The relation between the geometry of the cavitation cloud and erosion zone on the one hand, and velocity and pressure on the other can be explained in terms of the dynamically created pressure differential. Consider the hypothetical pressure profile for two different static pressures in Figure 5.5(a). Since P_{02} is smaller than P_{01} but constant velocity is assumed, the pressure profile for P_{02} is displaced to lower pressures. As a result, the region of underpressure (hatched) increases. Thus the cavitation cloud as well as the erosion zone move further downstream. (Note also that the number of cavitating bubbles will increase, while the pressure gradient for collapse, i.e. ΔP_2 will decrease. These two opposing factors lead to the existence of a peak damage rate as discussed in Section 5.1.)

In the case of two different velocities (Figure 5.5(b)), the region of underpressure expands for the higher velocity v_{02} . Thus cavitation bubbles leave this region further downstream and the erosion zone shifts downstream. The figure also illustrates that damage will increase because the number of cavitating bubbles increases (except under well-developed cavitation conditions where the underpressure region ceases to expand).

5.3.2 Erosion data

The volume loss data is detailed in Table 5.2. Average volume losses are plotted in Figure 5.6, showing that the volume loss was larger at the higher sample velocity of 51 m/s compared to a velocity of 48 m/s. When plotted against pressure, volume loss peaked at approximately 0,12 MPa for both velocities. Thus the general trends reported in the literature were confirmed.

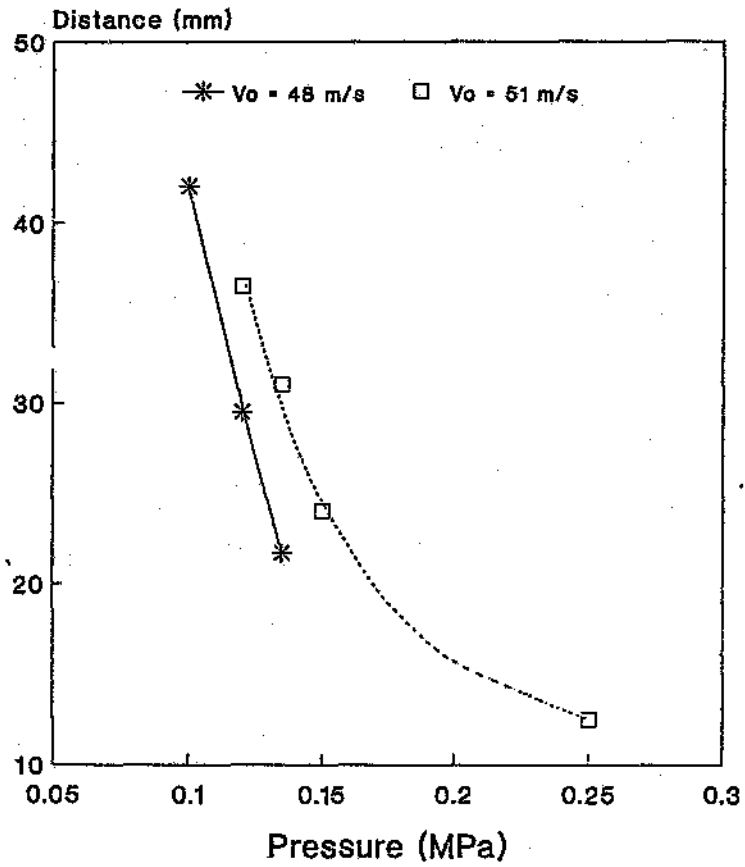


Figure 5.3: The distance between the downstream edge of the inducer hole and the centre of the primary erosion zone, plotted as a function of velocity and pressure

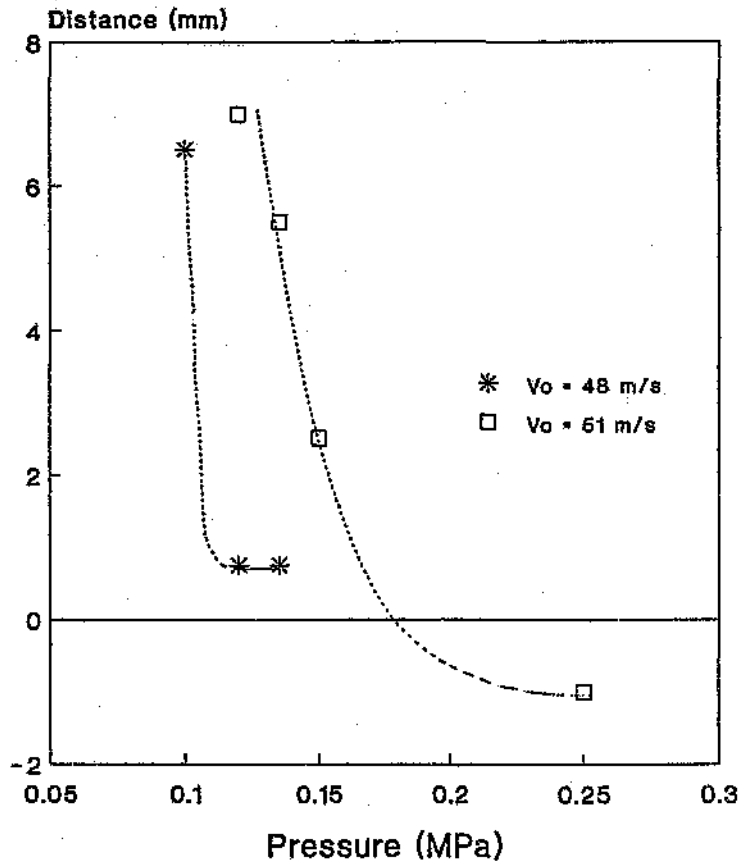
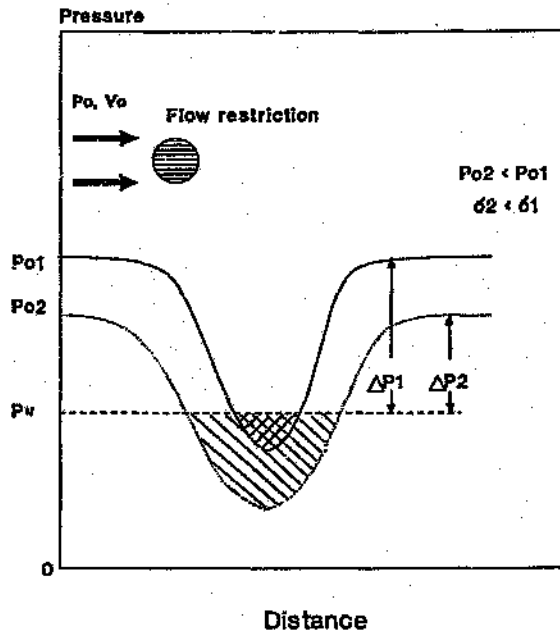
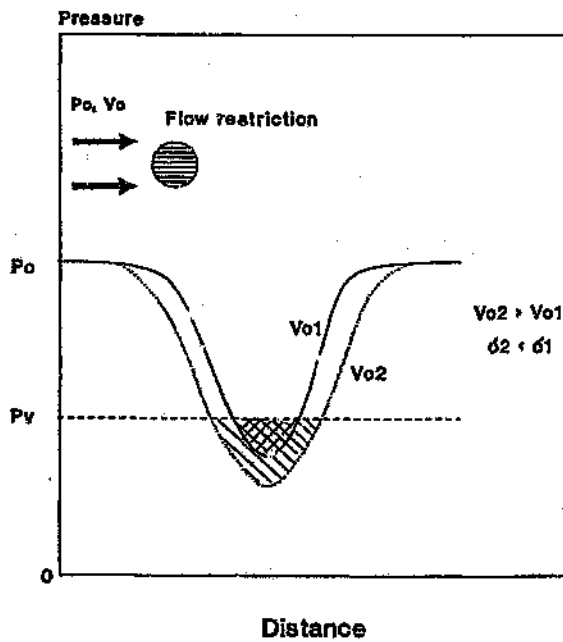


Figure 5.4: The distance between the downstream end of the fixed cavity and the centre of the primary hole, plotted as a function of velocity and pressure



(a)



(b)

Figure 5.5: Hypothetical curves of influence of (a) pressure and (b) velocity on cavitation pressure differential!

Table 5.2: Volume loss as a function of pressure and velocity

Test code	Velocity (m/s)			Static pressure (MPa)			1 h cumulative volume loss (mm ³)			Average volume loss (mm ³)
	nominal value	mean value	SD	nominal value	mean value	SD	A1	A2	A3	
SP6	48	48,5	0,08	0,10	0,10	0	44,7	34,1	63,1	47,3
SP7	48	48,5	0,10	0,12	0,12	0	60,7	66,7	53,7	60,3
SP5	51	50,9	0,07	0,10	0,10	0	70,1	66,5	93,0	76,5
SP1	51	50,8	0,05	0,12	0,12	0,001	106,7	78,2	112,9	99,3
SP4	51	50,8	0,04	0,135	0,137	0,001	86,3	86,3	102,0	91,5
SP2	51	50,8	0,05	0,15	0,15	0,001	88,3	73,2	97,3	86,3
SP3	51	50,9	0,06	0,25	0,25	0,009	37,9	36,1	16,0	30,0

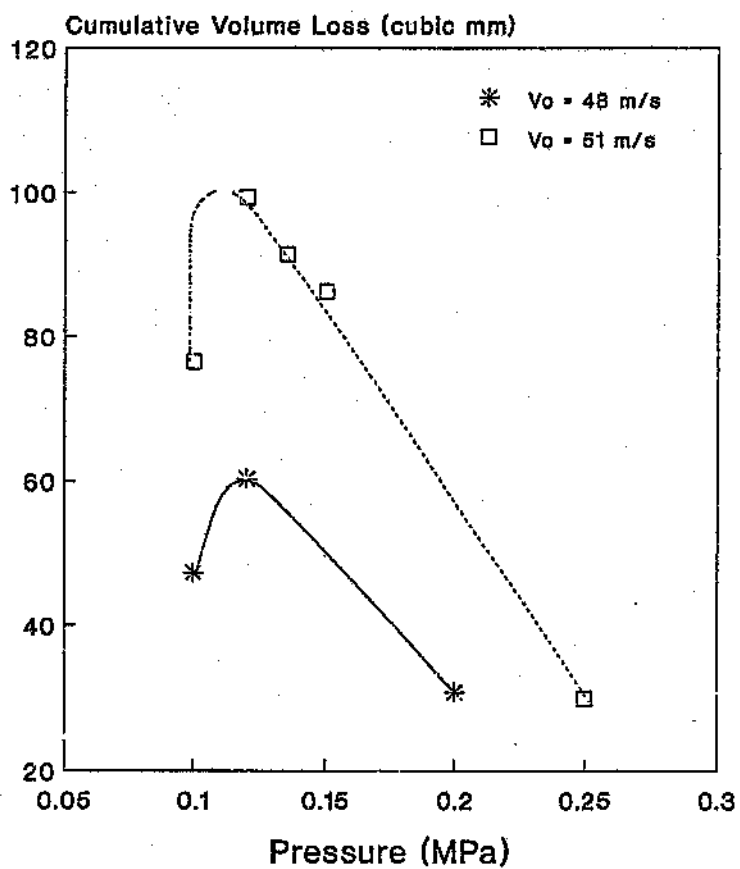


Figure 5.6: Curves for volume loss as a function of pressure at 48 and 51 m/s sample velocity

5.4 Summary

The influence of water pressure and velocity on flow-type cavitation erosion was confirmed, i.e. an increase in erosion rate with increasing velocity and peaking of erosion rate as a function of pressure.

Due to the importance of exercising control over the cavitation geometry, the effect of pressure and velocity on the position and shape of the cavitation erosion zone was systematically studied. The observed relationship was successfully explained in terms of the change in the cavitation-inducing pressure gradient with pressure and velocity.

References

- 1) R.T. Knapp: Recent Investigations of Cavitation and Cavitation Damage, Trans. ASME, Vol. 77, pp. 1045-1054, 1955.
- 2) J.Z. Lichtman, D.H. Callas, C.K. Chatten and E.P. Cochran: Cavitation Erosion of Structural Materials and Coatings, 17th Annual Conference, NACE, Buffalo, New York, pp. 119-127, 1961.
- 3) C.M. Preece: Cavitation Erosion, Treatise on Matls. Sci. Tech., Vol. 16, pp. 249-308, 1979.
- 4) A. Karimi and J.L. Martin: Cavitation Erosion of Metals, Metals Int. Met. Rev., Vol. 31, No. 1, pp. 1-26, 1986.

6. PRESSURE DIFFERENTIAL

6.1 Introduction

The pressure differential associated with bubble growth and collapse was illustrated in Figure 4.3. As discussed in Chapter 5, the shape of the differential curve i.e. minimum and maximum pressure values, as well as the negative and positive pressure gradients, determine the degree of cavitation and erosion. However, use of the cavitation parameter (Equation (2.4)) as an indication of severity of cavitation does not reflect the influence of the pressure gradients at all.

The purpose of the work described in this chapter was to study the relation between the pressure differential and the amount of damage. For example, is the collapse (positive) gradient the critical factor in damage increase, or the minimum pressure value, or the time spent in the underpressure region? This could provide a means of quantifying an acceptable pressure profile in terms of cavitation damage. As far as it could be established, this approach had not been practically applied before, although Hammitt [1] states that "it would be very desirable to know the effects of pressure and velocity gradients, boundary-layer parameters, etc., on the very complex chain of events apparently necessary to produce a damaging bubble collapse. If more detailed information of this type could be achieved, it might become possible to modify the design of fluid-handling machines in such a way that cavitation damage would be largely avoided or reduced."

It was shown in a venturi system [2] that the whole pressure differential could be measured under different hydrodynamic conditions (Figure 6.1). By in situ observation of the bubble cloud in the rotating disc-apparatus (e.g. Figure 5.1(a)), it was realized that the negative pressure gradient could however not be measured; cavitation always initiated within the inducer hole, indicating that the minimum pressure was already attained in the

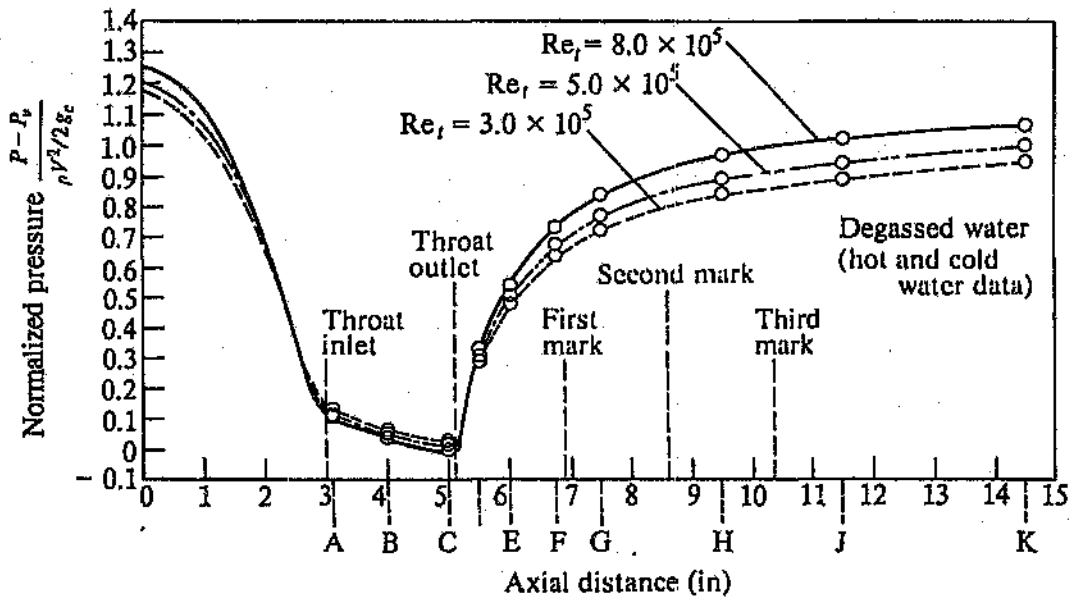


Figure 6.1: Normalised pressure as a function of axial position, measured at cavitation inception in a venturi (Re_t is the Reynolds number at the venturi throat.)

hole. On the other hand, the positive pressure gradient could be measured between the inducer hole and the upstream end of the erosion zone. This distance could be increased by for example, decreasing the pressure or increasing the velocity, but only until the downstream end of the erosion zone reached the edge of the sample. Thus a number of pressure and velocity combinations were selected based on these practical requirements. They were included in the erosion tests described in Chapter 5 (see Section 5.2).

6.2 Measurement of differential

Since the cavitation pressure profile is quasi-static under constant hydrodynamic conditions, the requirement was for a means of taking a significant number of static pressure measurements in the region between the inducer hole and the point of bubble collapse onset. Two measuring systems were devised as discussed below.

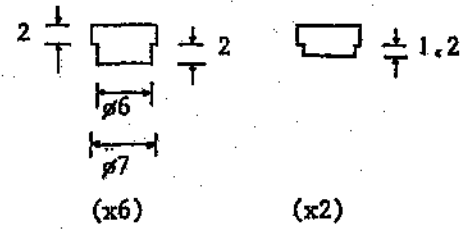
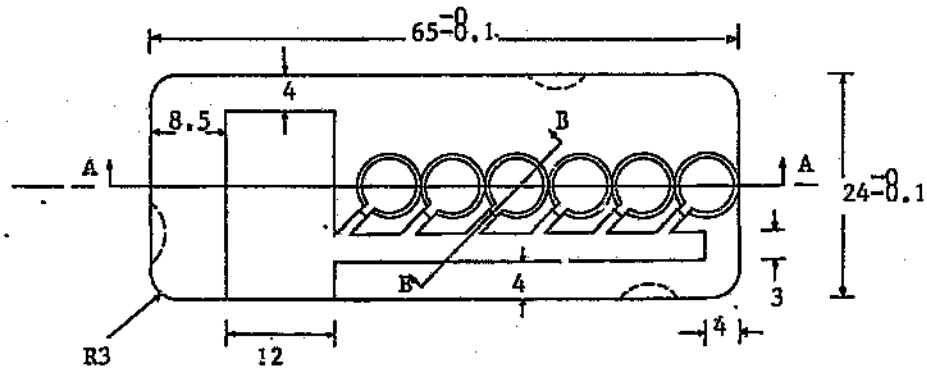
6.2.1 System using individual miniature pressure sensors

Strain-gauge based (full bridge) sensors, disc-shaped with diameter 6 mm, thickness 0,6 mm and a maximum pressure capacity of 0,5 MPa were used. When mounted in the aluminium disc shown in Figure 3.8, the sensor holder illustrated in Figure 6.2 was designed to expose the sensors to the water pressure at any of six possible positions downstream of the inducer hole. Figure 6.3 shows the mounted holder including one sensor (brown colour). The electric wires were connected to a voltmeter and power supply via the hollow disc drive shaft and slipping assembly as shown in Figure 3.10. Table 6.1 lists the pressure and velocity combinations used with the described measuring system.

Initially the pressure sensors were calibrated under static conditions against the 2 MPa pressure transducer mounted in the test chamber. Figure 6.4 shows the calibration curves for both probes.

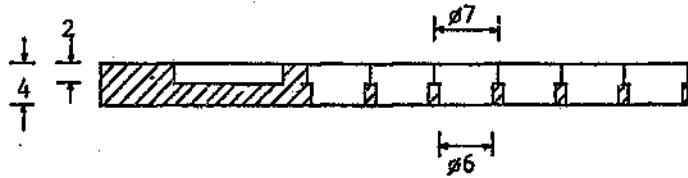
Due to cost considerations, the measuring procedure involved the use of one sensor at

Material: Aluminium 2S

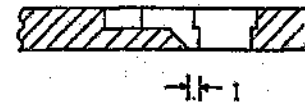


Note: Plugs must have a sliding fit with Holder, except short plug which must have a loose fit on the small section

All dimensions in mm.



Section AA



Section BB

Figure 6.2: Sensor holder for miniature pressure sensors

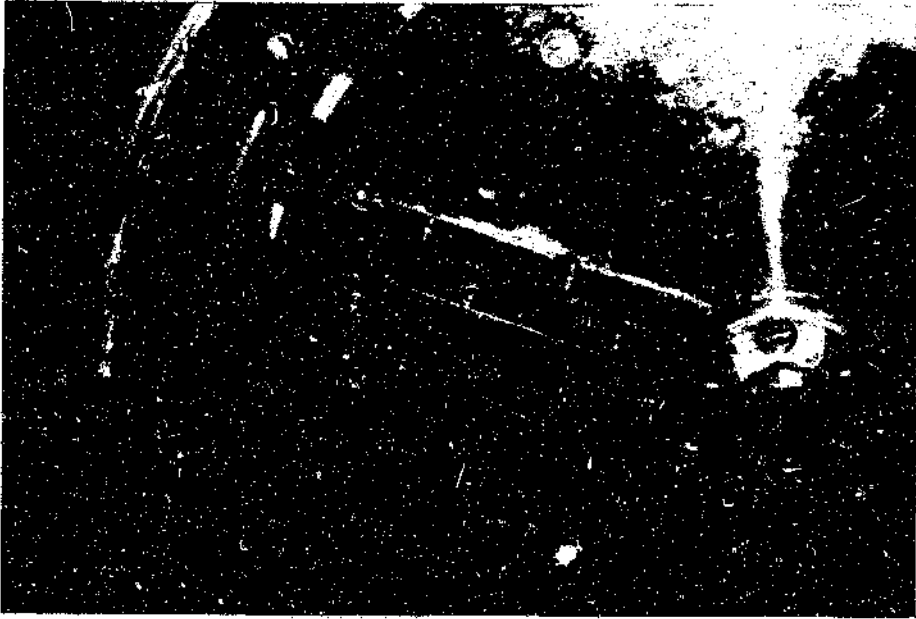
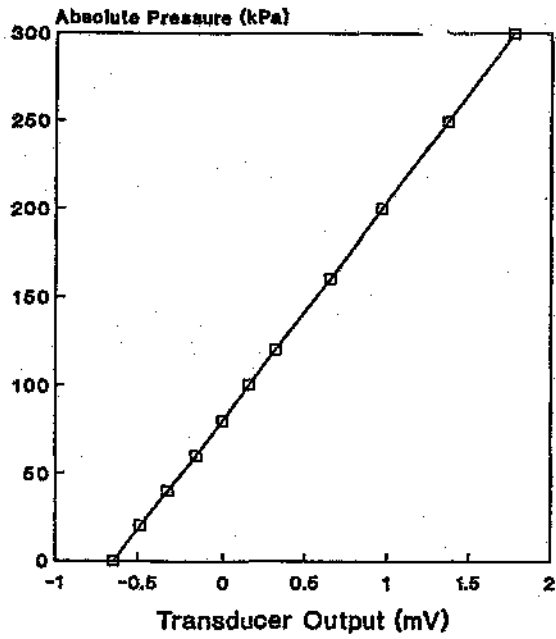


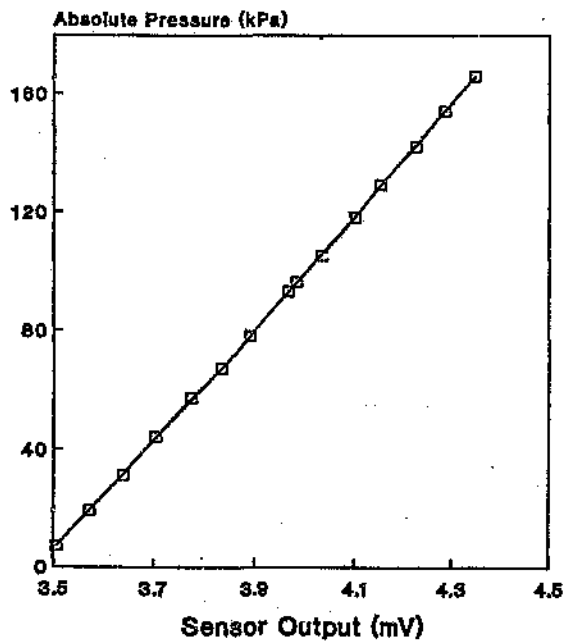
Figure 6.3: Holder for miniature pressure sensors mounted in aluminium disc. The sensor is second from the bottom, while the other recesses are filled by aluminium plugs

Table 6.1: Pressure and velocity parameters for the individual sensor-measuring system

Sample velocity (m/s)	Static pressure (MPa)	Number of pressure measurements possible	Comments
48	0,10	3	The minimum number of measurements required was 2
	0,12	2	
51	0,10	4	
	0,12	2	
	0,135	2	



(a)



(b)

Figure 6.4: Calibration curves for (a) 2 MPa pressure transducer and (b) miniature pressure sensor

a time. Having stabilized test conditions (Table 5.1) under static conditions, the disc was set in motion and pressure measurements taken at the velocity in question (determined by the pulley ratio) at the various pressures. The process was repeated for the other velocity, then the sensor position was changed and a new set of pressure measurements was taken. In this way the number of sensor position changes was minimized which saved a substantial amount of time and risk.

The number of successful measurements made with this system was low due to the high sensor failure rate (Table 6.2). However, the feasibility of measuring the pressure gradient was demonstrated as shown in Figure 6.5. It was concluded that the sensors were not robust enough for direct contact with the test fluid (and possibly pressure pulses during disc startup). A new measuring system thus had to be developed.

6.2.2 System using strain gauges

The system comprised the same measuring geometry as before. The aluminium sensor body shown in Figure 6.6 contained diameter 6 mm blind holes with 0,2 mm thick bottoms. The elastic deformation of the latter which had a unique relation with applied load was measured by means of foil-type strain gauges stuck onto the bottom walls. With this design the strain gauges were protected from the test fluid. The system was not used in practice due to time constraints and a lack of funds.

6.3 Summary

Due to the important relationship between the dynamically-induced pressure gradient versus the amount and location of flow-type cavitation damage, an effort was made to develop a technique for measuring the pressure profile in the rotating disc test rig. Promising results were obtained with the first prototype pressure sensor, which led to the development of a second prototype. Further work was suspended due to a lack of funds.

Table 6.2: Performance and failure history of miniature pressure sensors

Sensor no.	Pressure capacity (MPa)	Description of failure
1	0,5	During pressure calibration, a contact failure occurred in the strain gauge bridge circuitry. Slight (allowable) overpressure or pressure fluctuations were possible reasons for failure.
2	0,5	The sensor showed zeropoint drift. During the third pressure measurement, the glue holding the sensor in position on its mounting stub became unstuck and the sensor was lost. After this, a more water-resistant glue was used.
3	0,5	During the second pressure measurement with this sensor, a contact failure occurred.
4	1,0	When submerged in the test chamber under flowing conditions, a contact failure occurred.

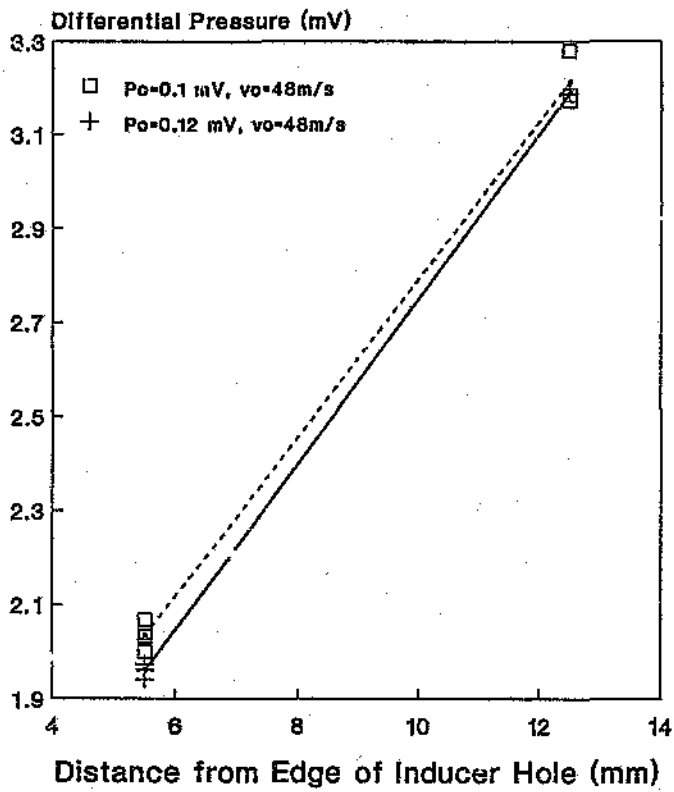


Figure 6.5: Pressure profile downstream of inducer hole

Material: Aluminium 2S

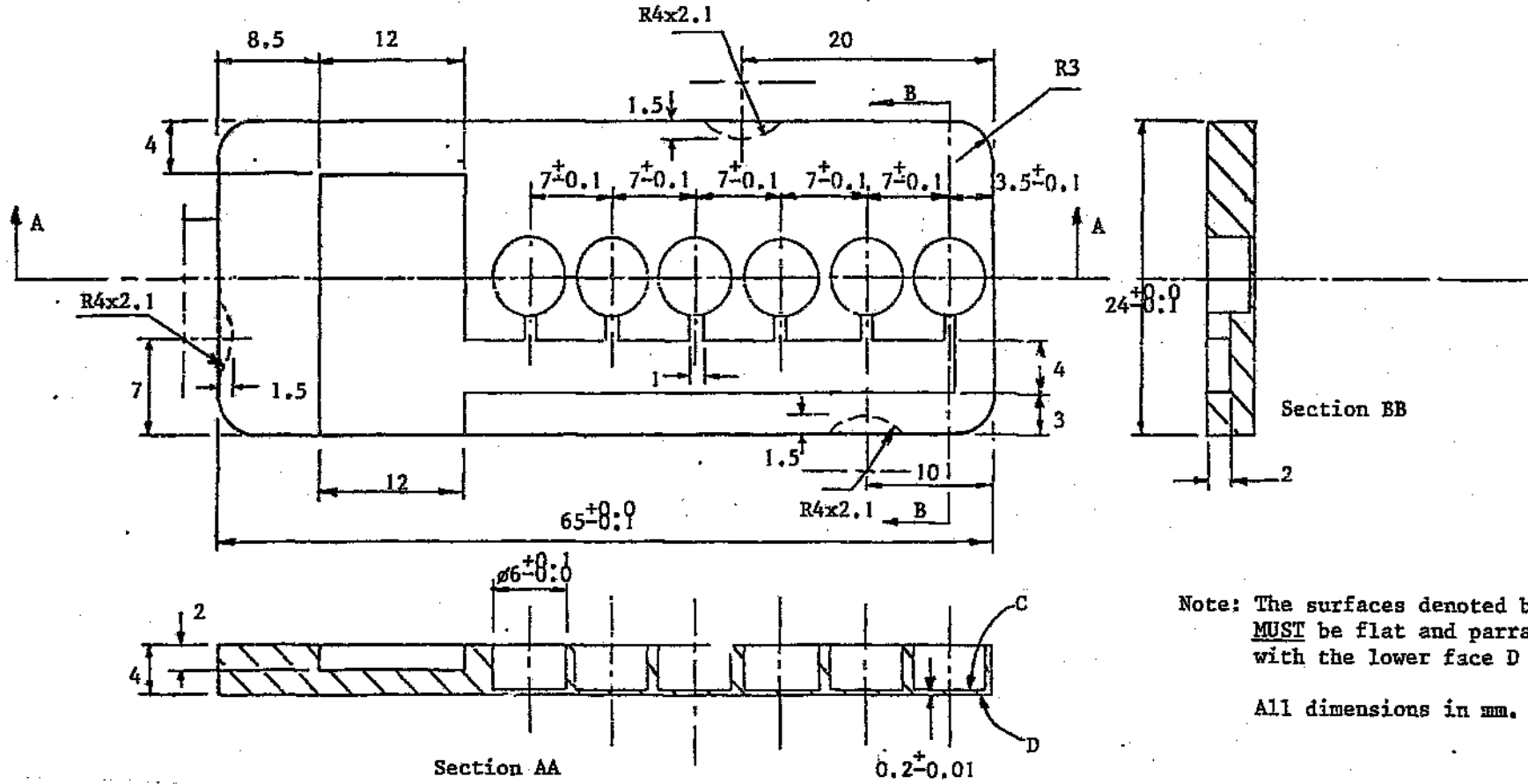


Figure 6.6: New pressure sensor design using strain gauges

References

- 1) F.G. Hammitt: *Cavitation and Multiphase Flow Phenomena*, McGraw-Hill, 1980.
- 2) F.G. Hammitt, O.S.M. Ahmed and J.B. Hwang: *Performance of Cavitating Venturi Depending on Geometry and Flow Parameters*, *Cavitation and Polyphase Flow Forum*, ASME, pp. 18-21, 1976.

CHAPTER 7

7. INFLUENCE OF SOLID IMPURITIES

7.1 Introduction

Typically the largest part of solids found in South African mine waters consists of silica in the form of quartzite. This quartzite has a high hardness and degree of angularity and is thus highly abrasive (Figure 7.1). Although the standard for solid content levels has been set at 5 ppm for mine waters [1], in practice these levels can be quite high (Table 7.1) with typical values of a few hundred parts per million.

In cavitating slurries (corresponding to very high solid concentrations) the combined effect of cavitation erosion and solid particle erosion can be substantial, as discussed in Section 2.3.9. However, even in nominally pure fluids the stabilization of cavitation nuclei is controlled by the presence of microscopic solid particles. In the intermediate concentration range, investigators focused their efforts on the inhibiting effect of soluble polymers. The exception was Wang and Hammitt [2], who reported that the presence of SiC and SiO₂ particles in the thousands of parts per million-range increased the erosion rate of aluminium and carbon steel. This was associated with three possible mechanisms: facilitation of nucleation (and thus cavitation), decrease in inception threshold, and the addition of an abrasion component by the impingement of solids-containing microjets onto the eroding surface. (The possibility also exists of increased corrosion of the eroded sample surface due to solid particle impingement facilitated by the solids. The synergism between wear and corrosion has been discussed in Section 2.3.8) Particle sizes were 6-8 and 30-40 microns, a mixture of which was apparently used.

In the course of the present study, two powders with similar particle size distribution but contrasting abrasivity were mixed with distilled water in various concentrations. The effect of the mixtures on cavitation erosion was investigated in the rotating disc test rig.

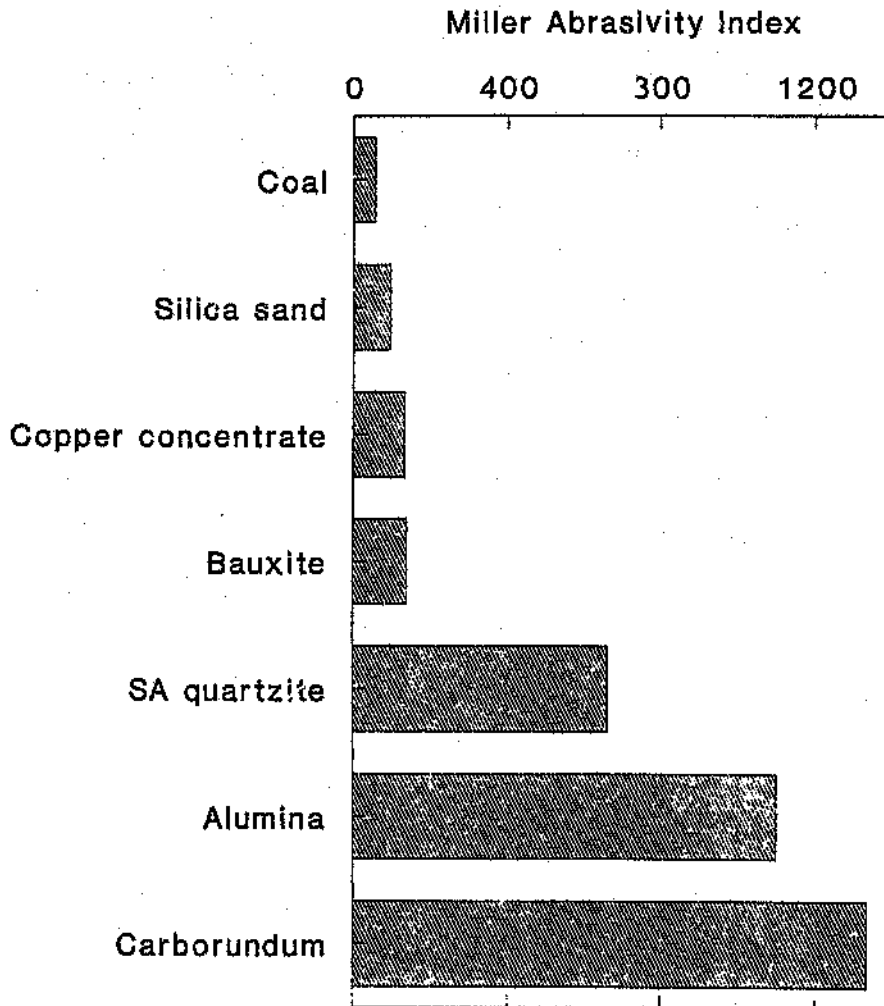


Figure 7.1: Relative abrasivity of quartzite found in South African mines

IONIC SPECIES (concentration in ppm)	NAME OF MINE	PH	Total Dissolved Solids		Total Suspended Solids		Total Hardness (as CaCO ₃)		Sulphate	Chloride	Sulphite	Sulphide	Nitrate	Free Saline Ammonia	Hypochlorite	Bicarbonate	Fluoride	Calcium	Magnesium	Sodium	Potassium	Ferrous Ion	Ferric Ion	Nickel	Copper	Langlier Index	Aluminum	Zinc	Nitrite	Conductivity (mS/m)	Total Alkalinity (as CaCO ₃)	pH of Saturation	Calcium Hardness (as CaCO ₃)	Magnesium Hardness (as CaCO ₃)
MINE A	6.5	1150	26	457	425	172	*	*	49	0.7	*	44	0.4	115	25	166	6	0.1	0.3	1.05	*	-1.49	*	*	*	na	na	na	na	na	na	na	na	na
MINE B (SHAFT 1)	6.0	3502	64	811	711	1037	*	*	246	27	170	5	0.8	245	50	930	7.3	0.7	11.7	1.36	*	-2.67	2.7	0.64	12.1	469	4	na	na	672	139	na	na	
MINE B (SHAFT 2)	6.5	3038	18	639	265	1203	*	*	144	12	157	31	1.1	182	44	790	5.5	0.2	2.9	0.21	*	-1.46	0.8	0.19	37	490	26	na	na	511	124	na	na	
MINE C (DAY 1)	6.1	3790	7	448	153	1865	*	*	65	0.8	*	94	1.2	182	5.8	1010	12	0.1	0.1	*	*	-2.0	*	*	1.0	614	24	8.10	402	46	na	na		
MINE C (DAY 2)	7.2	3520	22	414	150	1574	*	*	43	4.0	67	49	1.3	138	16	1290	7.6	0.3	2.9	0.22	*	-0.94	5.1	*	27.2	na	40	na	371	43	na	na		
GRAND WATER BOARD	7.4	364	32	184	102	38	*	0.3	*	0.8	*	201	0.3	48	12	37	4.5	0.1	0.2	*	*	-0.56	*	*	54.7	101	na	na	na	na	na	na	na	
MINE D	6.5	2184	19	518	829	39	1.1	0.8	327	91	142	10	1.5	158	30	290	15.2	0.23	1.8	1.98	*	-2.02	0.5	1.77	18.6	255	8	8.52	435	83	na	na		
MINE E	6.3	4975	42	1034	821	1812	*	0.9	228	36	*	39	1.0	368	28	1130	13.9	*	*	0.37	*	-1.37	*	*	6.5	700	32	7.67	961	73	na	na		
MINE F	5.8	10870	4	3689	2018	2766	*	0.9	1650	55	0.1	40	0.9	1250	138	1520	70	*	*	0.46	*	-1.52	*	0.12	58	1209	53	7.32	3322	367	na	na		
MINE G	6.3	8180	20	769	901	1230	*	*	191	0.8	*	14	1.0	268	18	900	31	0.1	0.1	0.31	*	-1.55	*	*	619	7	7	na	na	na	na	na	na	
MINE I (DAY 1)	4.7	3490	4	2173	2700	36	0.8	*	22	3.9	9	2.5	0.6	620	152	69	2.3	*	*	10.7	0.23	-3.24	23	8.5	9.9	na	2	8.64	na	na	na	na		
MINE I (DAY 2)	6.9	2824	4	1526	1588	36	1.0	*	9.3	3.1	2.2	42	0.7	600	6.9	70	2.4	*	1.5	*	*	-0.44	49	*	0.7	240	40	7.34	1908	18	na	na		
MINE K (DAY 1)	5.5	740	284	849	760	92	1.0	2.0	-194	10.6	*	4.9	0.7	276	39	111	21	0.16	0.12	1.80	*	-3.00	1.1	0.19	4.1	na	4	8.30	na	na	na	na	na	
MINE H (DAY 2)	7.6	1820	2675	738	677	103	1.2	*	188	17.4	100	78	0.5	250	20	104	19.7	0.13	2.0	0.33	*	0.18	1.4	0.1	9.8	175	64	7.42	664	74	na	na		
MINE J	6.5	6756	44	1785	2176	1564	*	*	1185	93	107	12	0.6	580	32	1480	87	0.8	1.6	1.83	*	-1.36	2.3	0.62	30.5	850	10	na	1554	221	na	na		

* = LESS THAN 0.1 PPM

na - NOT AVAILABLE

Table 7.1: Mine water composition (after COMRO, 1983)

7.2 Test procedure

The powders used to make up fluid mixtures were PVC polymer with a density of 1,32 g/cc and a 25-50 microns particle size, and SiO₂ (silica) with a density of 2,6 g/cc and a 140 mesh particle size (i.e. 6% > 105 microns). The silica powder was screened to obtain a narrower particle size distribution compatible with that of the PVC. Optical and electron microscopy (Figure 7.2) showed that the PVC particles were fairly spherical, while the silica was angular and irregularly shaped. Particle surfaces appeared to have the same order of roughness. The powders were thoroughly mixed with distilled water, although the PVC tended to agglomerate slightly. Real solids concentrations at the test chamber were determined before and after testing by filtering a 2,5 ℓ fluid sample.

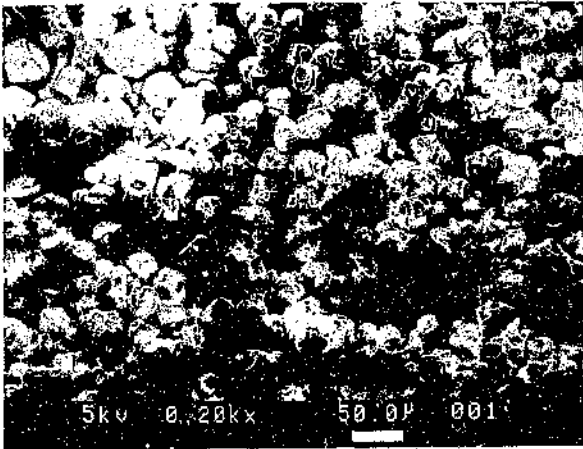
Test samples were made from 2S Al alloy and tested using the same sample treatment and test procedures described in Section 4.2 for the 1 hour temperature tests. Initially tests were carried out at 40 °C using relatively small solids concentrations. (Some of these tests were interruptive i.e. a number of mass measurements were taken over the 1 hour test period, in order to study the shape of the erosion curve.) The test parameters are listed in Table 7.2.

Since these results were inconclusive, additional tests were done at 50 °C, a temperature which resulted in higher volume loss and better reproducibility of results (see Chapter 4). At the same time, higher solids concentrations coupled with improved mixing procedures were used. Table 7.3 shows the test parameters.

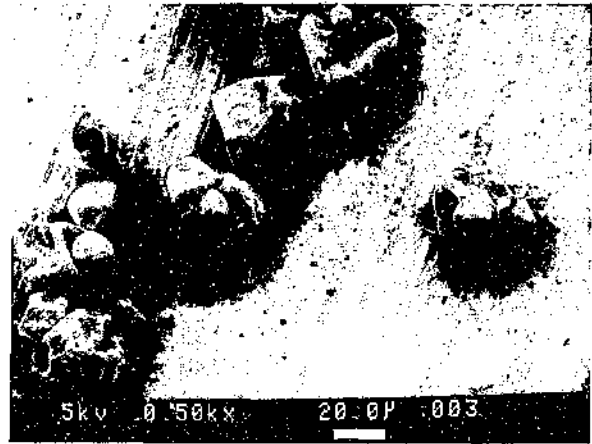
7.3 Erosion data

7.3.1 40 °C tests

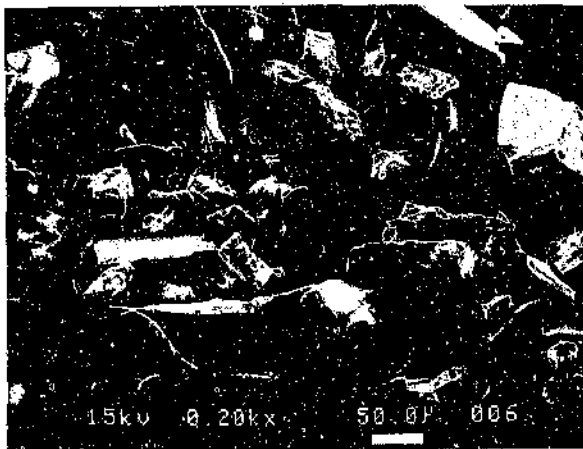
The test matrix and volume loss results for these tests are shown in Table 7.4. Volume loss data against real solids concentration (taken as the average of the before and after testing values) is plotted for a selection of tests in Figure 7.3. The experimental data range determined from the distilled water tests is shown by vertical bars. No distinctive



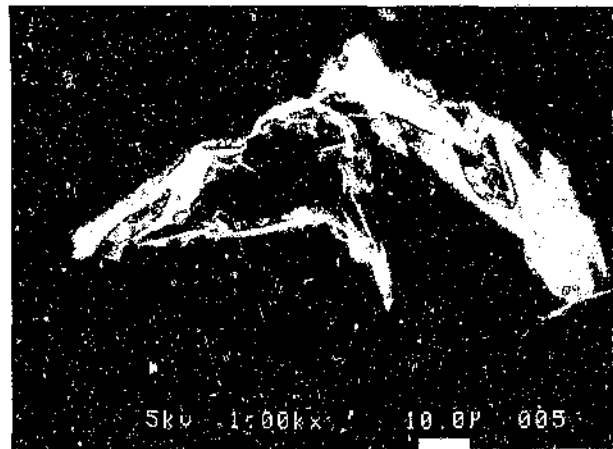
(a)



(b)



(c)



(d)

Figure 7.2: SEM micrographs of (a), (b) PVC and (c), (d) silica powder

Table 7.2: Test parameter values for solids erosion tests at 40 °C

Parameter	Mean value	SD	Comment
Temperature (°C)	40,2	0,5	Water was preheated
Pressure (MPa)	0,15	0,002	
DO content (mg/ℓ)	5,97	1,00	Not directly controlled
Flow rate (ℓ/min)	~30		
Disc velocity	3614	26	

Table 7.3: Test parameter values for solids erosion tests at 50 °C

Parameter	Mean value	SD	Comment
Temperature (°C)	49,7	1,5	Water was preheated
Pressure (MPa)	0,15	0,001	
DO content (mg/ℓ)	6,29*	0,54	Not directly controlled
Flow rate (ℓ/min)	~30		
Disc velocity	3625	13	

* Value for 1000 ppm silica was considerably higher at $9,18 \pm 2,0$ mg/ℓ

Table 7.4: Volume loss data for solids erosion test at 40 °C

Test fluid	Test code	Nominal solids conc. (ppm)	Real solids conc. (ppm)			Cumulative 1 h volume loss (mm ³)	Comment
			Begin	End	Mean		
Distilled water	IS1	0				75,22	Average value 76,7 ± 2,1
	IS2	0				76,30	
	IS7*	0				74,51	
	IS8*	0					
Distilled water with PVC	IS3	61				72,72	
	IS4	125				76,95	
	IS6*	125				79,95	
	IS9*	125	27,0	10,5	18,8	83,59	
Distilled water with silica	IS5*	250				80,00	
	IS10*	250	13,0	7,0	10,0	81,93	
	IS11*	500	49,5	15,8	30,9	77,42	

* Testing interruptive, i.e. more than one mass measurement taken

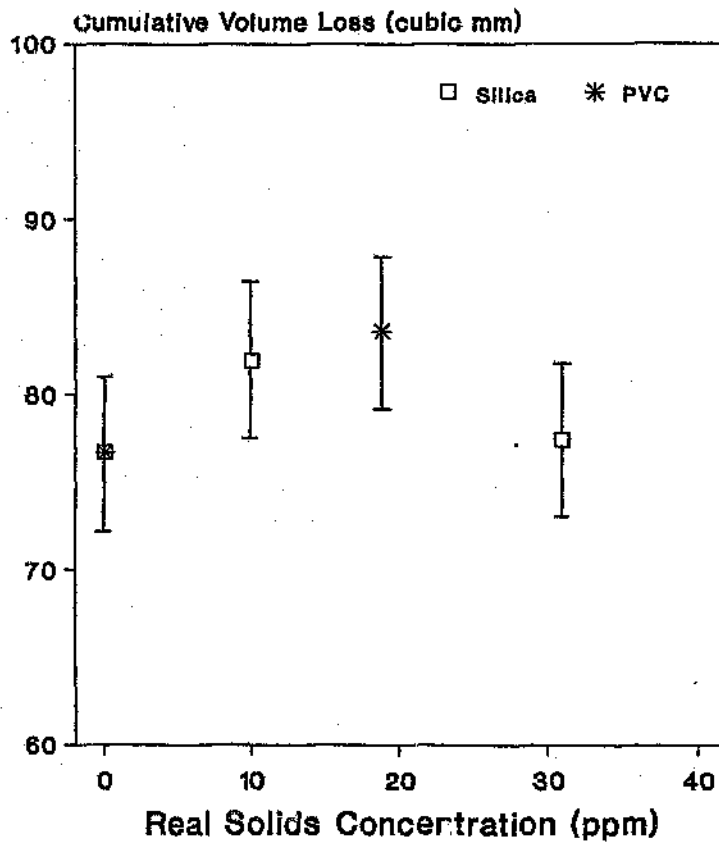


Figure 7.3: Volume loss as a function of real solids concentration for the 40 °C solids erosion tests

trend could be derived, the main reason being that any possible effect of the solids on volume loss was of the same order as the experimental precision because of the extremely small real solids concentrations (Table 7.4). The latter was due to the fact that a large percentage of the solids settled out in the system during testing, as shown by the decrease in real concentration during testing.

Having thus identified the need for higher real solids concentrations, an appropriate series of tests were carried out.

7.3.2 50 °C tests

Table 7.5 gives the test matrix and volume loss data for these tests. In tests involving the relatively heavy silica particles, the flow rate was increased to improve the mixing process and keep the silica in suspension. Volume loss is plotted against real solids concentration in Figure 7.4. Initially, the curves for PVC and silica run together and horizontal, but these separate at higher concentrations where PVC and silica show respectively a decrease and an increase in volume loss.

7.4 Discussion

Due to the unstable "pulsating" nature of the cavitation cloud in the rotating disc-test rig, the influence of solids on cavitation inception or desinence (suppression) could not be accurately verified. It may be assumed, however, that the surface irregularities on solid particles (Figure 7.2) will assist nucleation and decrease the cavitation inception threshold.

Erosion testing was carried out under well-developed cavitation conditions where the abovementioned factors had no influence. The increase in volume loss observed for silica was associated with solid particle impingement. Visual inspection of the samples showed increased roughness manifested as dulling of the polished surface. SEM investigation (Figure 7.5) confirmed that the sample surfaces were heavily scratched.

Table 7.5: Volume loss data for solids erosion tests at 50 °C

Test fluid	Test code	Nominal solids conc. (ppm)	Real solids conc. (ppm)			Cumulative 1 h volume loss (mm ³)	Comment
			Begin	End	Mean		
Distilled water	IS12	0	0,6	3,8	2,2	88,40	
Distilled water with PVC	IS13	125	56,4	19,7	38,1	87,37	
	IS14	500	150,6	19,6	85,1	39,22	
Distilled water with silica	IS15	500	33,3	70,2*	51,8	96,26	Higher flow rate
	IS16	1000	65,5	171,2*	118,4	103,69	Higher flow rate

* Higher concentration at end of test probably due to settled out silica from previous tests which have been brought in circulation due to the higher flow rate. Microscopic evaluation of end-of-test solids showed no significant amounts of other materials (e.g. PVC).

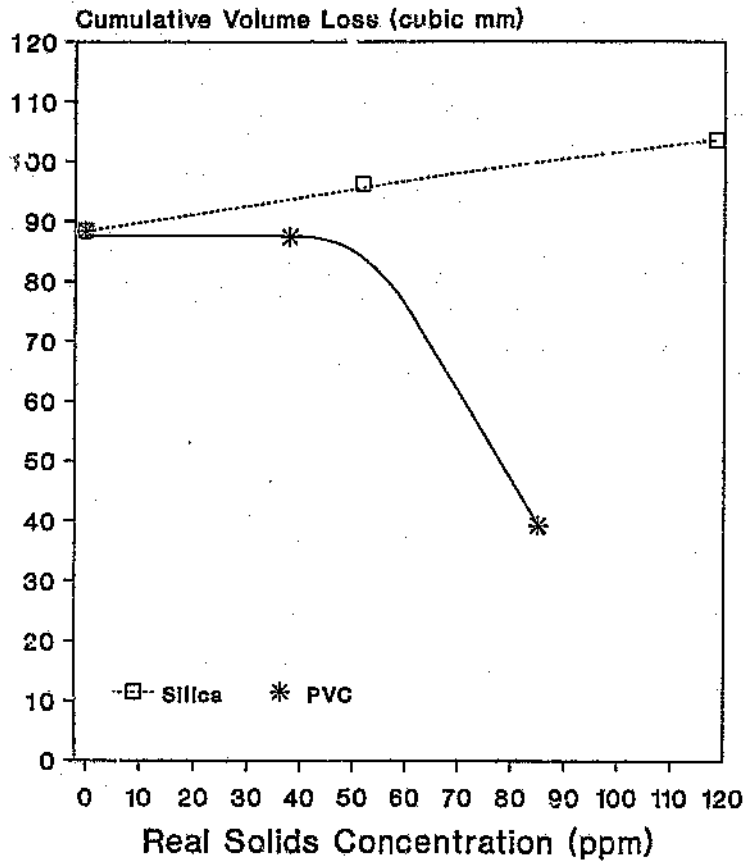
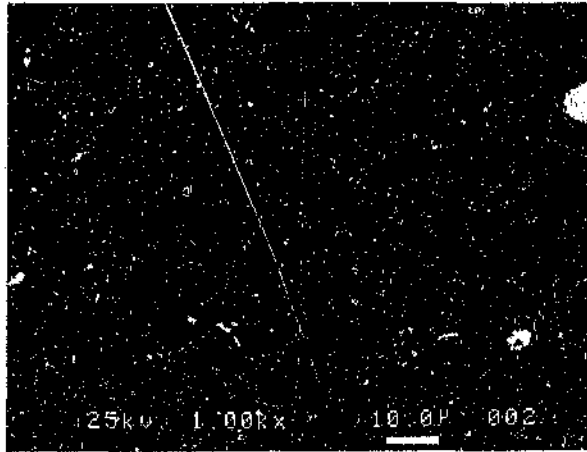
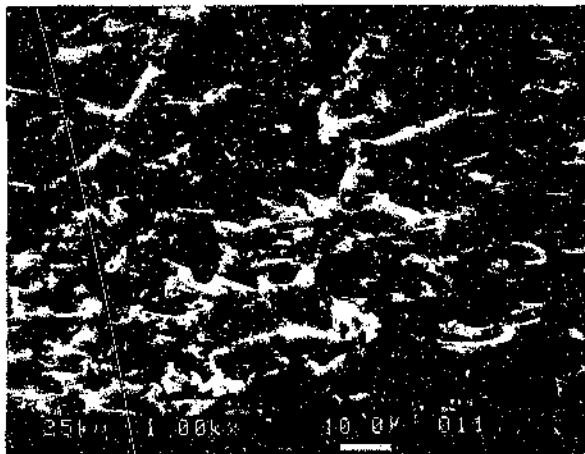


Figure 7.4: Volume loss as a function of real solids concentration for the 50 °C solids erosion tests



(a)



(b)

Figure 7.5: SEM micrographs of typical areas outside the erosion zone on samples tested (a) in distilled water and (b) in distilled water mixed with 500 ppm silica

The situation was more complex for PVC. Since PVC is soft and has a low density compared to silica, the absence of solid particle erosion was expected. The decrease in volume loss with increasing real solids concentration may be explained in a couple of ways: Firstly the presence of PVC particles in a microjet impinging onto the eroding surface may absorb some of the impact energy by elastic deformation. Secondly, due to the hydrophobic nature of PVC (compared to silica which is wettable), air pockets may be trapped on PVC particles giving rise to so-called gaseous cavitation (Section 2.2.1). This assumes a permanent air content within the bubbles and consequently cushioning of bubble collapse.

7.5 Summary

Very little information was previously available on the influence of solid particles, contained in cavitating liquids, on cavitation erosion. The effect of an abrasive (silica) and a non-abrasive (PVC) powder with similar particle sizes on cavitation erosion was studied in the rotating disc apparatus.

For solid concentrations above ~40 ppm, it was found that the damage rate increased with the addition of increasing amounts of silica, due to solid particle erosion. On the other hand, damage was reduced by the addition of progressively larger amounts of PVC. This may have been caused by energy-absorbing elastic deformation of the PVC particles, or by the accommodation of free gas, leading to bubble collapse cushioning.

References

- 1) COMRO WHP70, Internal Publication, 1989.
- 2) X. Wang and F.G. Hammit: Effects of Solid Particles in Water on Vibratory Cavitation Erosion, Cavitation and Multiphase Flow Forum, ASME, 1984.

CHAPTER 8**8. INFLUENCE OF WATER CHEMISTRY****8.1 Introduction**

In-service, as well as laboratory results, have shown the synergistic action between cavitation erosion and corrosion, due to roughening and mechanical degradation of the corroding surface on the one hand, and the removal of protective layers and improved oxygen supply caused by cavitation on the other (see also Section 2.3.8). Erosion results were almost exclusively achieved with vibratory-type test facilities.

South African mine waters can be highly corrosive due to low pH, high levels of chlorides and sulphates and high levels of dissolved solids (Table 7.1). In order to evaluate the influence of water chemistry under flow cavitation conditions, tests were carried out in the rotating disc device using a synthetic solution with typical mine water composition.

8.2 Procedure for erosion testing

As sample materials, 2S Al alloy and low carbon steel BS 1449 KHR1 were used. The steel was included because its corrosion behaviour is typical of a material not forming a protective surface layer (viz. aluminium or passivating alloys). It was received in hot rolled sheet form and machined to the appropriate dimensions, ground and then polished in the normal way. Typical physical properties of the steel are given in Table 8.1.

Two test solutions were used for erosion testing i.e. distilled water and a synthetic mine water [1]. The latter was a relatively aggressive electrolyte prepared by dissolving a number of salts in distilled water:

Table 8.1: Composition and mechanical properties of low carbon steel
BS 1449 KHR1

Chemical composition (%)				
C	Mn	P	S	Si
0,04	0,2	0,012	0,01	0,016

Yield stress	220 MPa
Tensile strength	374 MPa
% elongation (200 mm)	27
Hardness (test surface) (100 N load)	130 HV

CaCl ₂ ·2H ₂ O	3411 ppm
Mg(NO ₃) ₂ ·6H ₂ O	1170 ppm
NaNO ₃	940 ppm
Na ₂ SO ₄	2515 ppm
NaCl	475 ppm

The pH of this mine water was ~7.

Erosion tests were carried out using three aluminium samples on the front side of the disc (positions A1 to A3) and three low carbon steel samples at the back (positions B1 to B3). Samples were treated in the same way as described for the 1 hour temperature tests (Section 4.2), except that mass measurements were regularly taken. After 1 hour of testing the aluminium samples were removed and replaced with dummy samples, while the steel samples were tested for a total period of 7 hours. Before weighing, they were scrubbed with a nailbrush in water to remove loose corrosion product. Test parameters are given in Table 8.2.

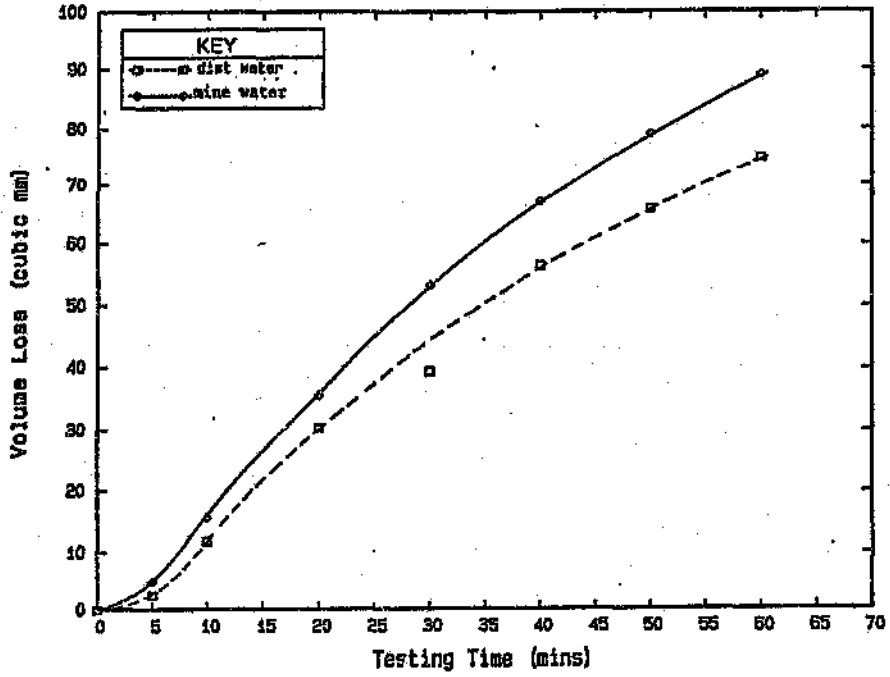
8.3 Results and discussion

The erosion curves for the aluminium and the steel tested in distilled water and the synthetic mine water are plotted in Figure 8.1. The aluminium curves have the classical S-shape (Figure 2.4) indicating that the maximum erosion rate had been reached, while the steel curves show that erosion rate had not yet peaked. The decrease in the steel erosion rate during the early period of the test in mine water may be attributed to temporary protection against erosion afforded by the formation of corrosion products. With the advent of large-scale surface fracturing this protection becomes ineffective.

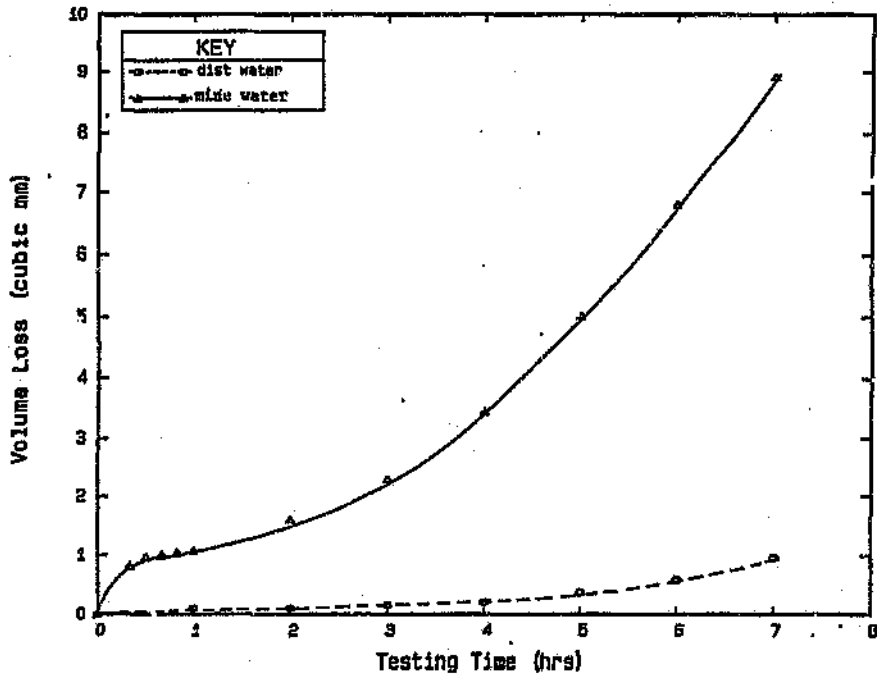
Both the aluminium and steel samples tested in mine water showed increased volume loss compared to the distilled water tests. The increase was in the order of 20% and 850% for aluminium and steel respectively. (Note that the size of the effect depends on the relation between erosion rate and corrosion rate. Thus if cavitation intensity is for example decreased on aluminium, the synergistic effect may account for a larger than

Table 8.2: Test parameter values for chemistry erosion tests

Parameter	Mean value	SD	Comment
Temperature (°C)	40,0	0,2	Water was preheated
Pressure (MPa)	0,15	0,002	
DO content (mg/l)	5,42	0,47	Not directly controlled
Flow rate (l/min)	~30		
Disc velocity (rpm)	3596	17	



(a)



(b)

Figure 8.1: Volume loss as a function of test time for chemistry erosion tests with (a) 2S Al alloy and (b) low carbon steel BS 1449 samples

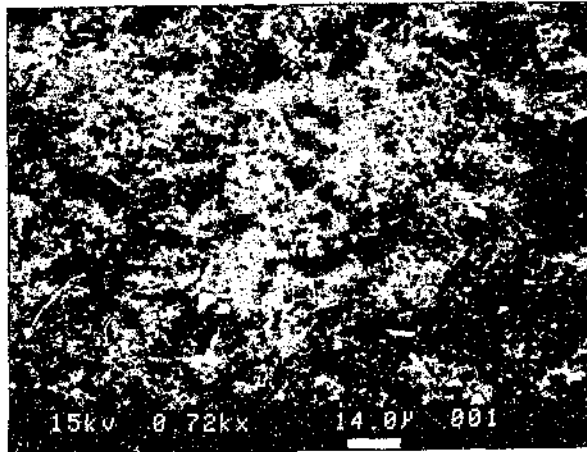
20% increase.)

In order to elucidate the damage process as a result of cavitation and corrosion, the eroded aluminium and steel samples were investigated visually and microscopically. The aluminium samples tested in the synthetic mine water showed fine pitting (Figure 8.2(a)) which appeared uniformly across the whole exposed surface. A couple of macroscopic pits also appeared as shown in Figure 8.2(b). Corrosion occurred across the whole exposed surface in the case of steel samples tested in the mine water, but the corrosion products were partially removed in and around the erosion zone (Figure 8.3(a)). The rear and sides of the steel samples were also covered with a relatively thick corrosion product layer (Figure 8.3(b)). The test surface contained large-scale as well as fine pitting (Figure 8.4). Thus the pits on both aluminium and steel could have acted as initiation sites for cavitation attack, while the removal of the corroded layer by cavitation took place on steel.

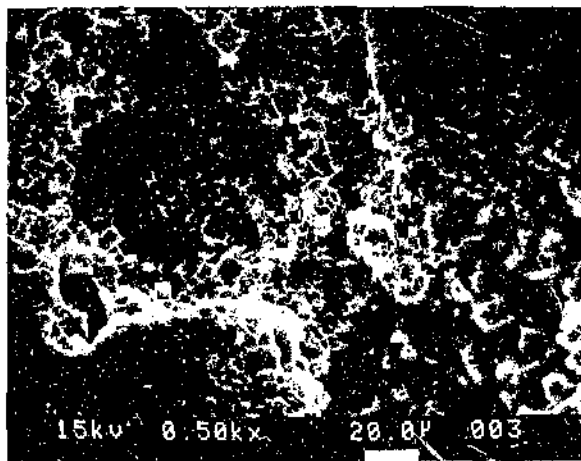
These results which describe for aluminium and steel the increase in erosion rate as a result of increased liquid corrosivity, must be considered in conjunction with the increase in corrosion rate of aluminium under cavitating conditions discussed in Section 4.4.2. Together they serve to elucidate the simultaneous action of erosion and corrosion in a flow cavitation system.

8.4 Summary

A typical South African mine water contains high concentrations of dissolved salts. Tests carried out on aluminium and low carbon steel in the rotating disc device showed that cavitation damage in such a mine water can be significantly increased, due to the increase in corrosion rate. Microscopic studies provided evidence for the synergistic action between cavitation erosion and corrosion: local corrosion (pitting) of the exposed surfaces created initiation sites for cavitation erosion, while general corrosion resulted in the formation of an easily erodible surface layer. At the same time, mechanical deformation of the surface by the cavitation attack caused increase of the surface area and stimulated pitting and corrosion.

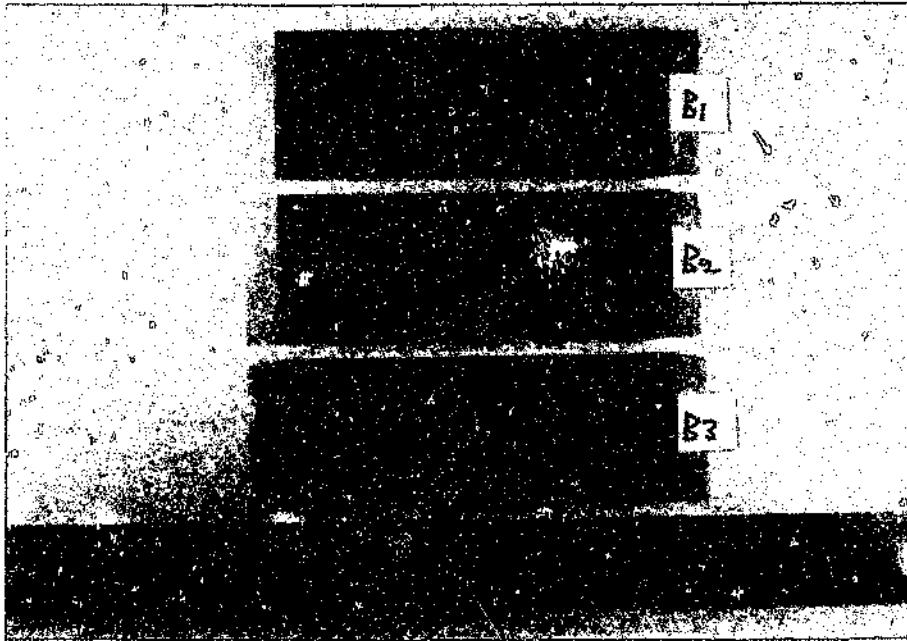


(a)

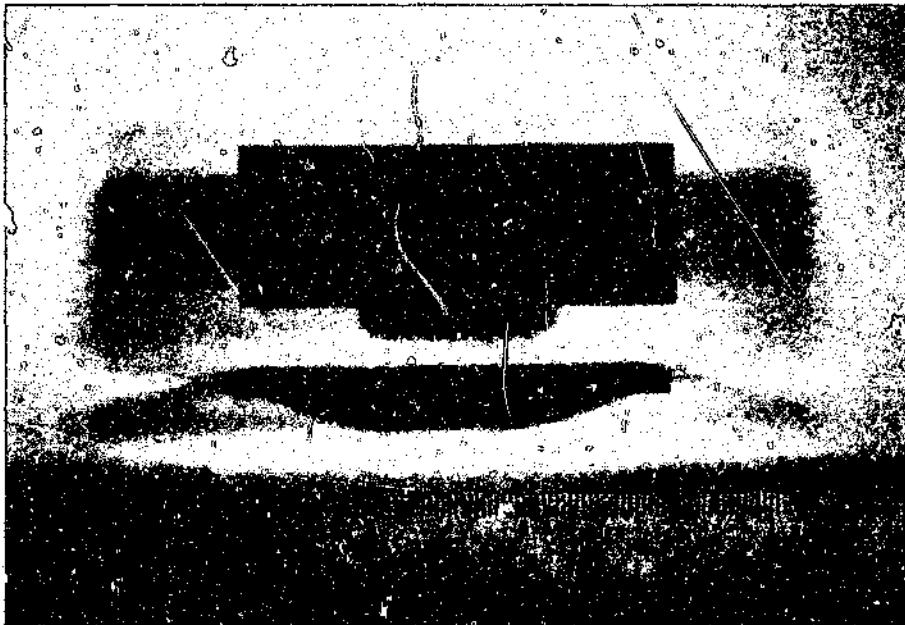


(b)

Figure 8.2: SEM micrographs of 2S Al alloy samples eroded in the synthetic mine water showing (a) fine pitting and (b) macropits



(a)



(b)

Figure 8.3: (a) Test surface and (b) rear and sides of low carbon steel BS 1449 samples tested in the synthetic mine water showing corrosion pattern

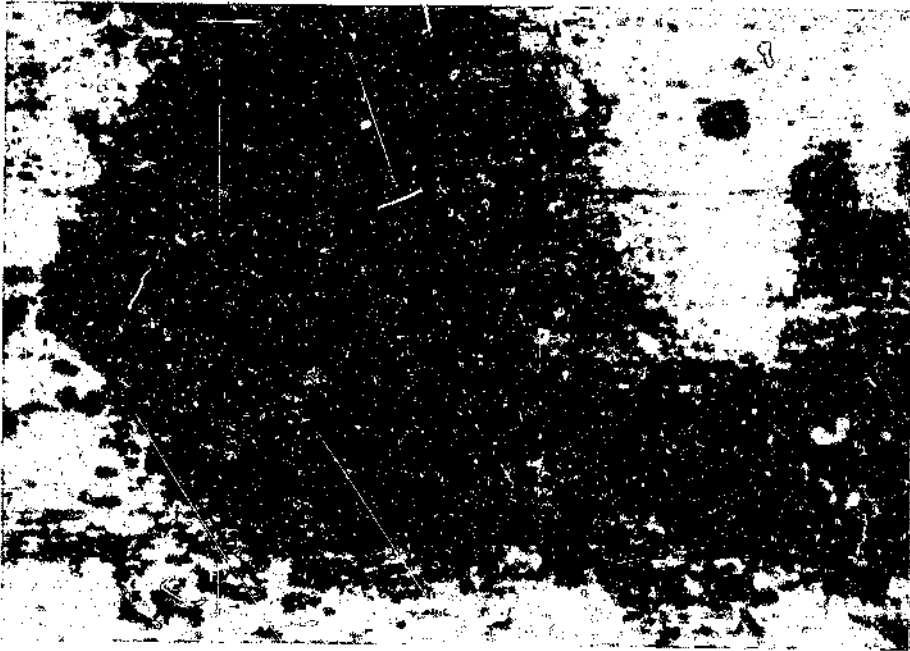


Figure 8.4: Optical micrograph of staining (orange colour) as well as fine and large-scale pitting on low carbon steel BS 1449 sample tested in the synthetic mine water

References

- 1) R. Paton and D. Howarth: Corrosion Properties of New Development Steels for the Gold Mining Industry, Proc. 5th Int. Conf. Appl. Corr. Tech., SACI, Johannesburg, South Africa, Aug. 1990.

CHAPTER 9**9. INFLUENCE OF EXTERNALLY APPLIED POTENTIALS****9.1 INTRODUCTION**

Literature results regarding the effect of cathodic and anodic potentials applied to cavitating bodies appear to be inconclusive, and even contradictory (Section 2.3.8). However, it is suggested that careful analysis of factors influencing cavitation damage will remove most of the apparent anomalies.

Most past workers agree that cavitation damage can be reduced by the application of a cathodic potential [1-6]. Some consider gas (mainly hydrogen) development to play an essential part in the protection process [2-4], since decrease in damage is only observed when gas is visibly developed. On the other hand, reduction in corrosion rate is another important protective mechanism [1,3].

The situation for anodic potentials is more complicated since the balance between a number of opposing factors determine whether cavitation damage is increased or reduced. It is thus not surprising that contradictory results were obtained, including damage reduction [2,4,7,8] and increase in damage [9-14] with the application of anodic currents. The factors involved in the application of anodic potentials are:

- . Gas (mainly oxygen) development in the case of passive metals and alloy which will cushion bubble collapse and reduce damage
- . A higher rate of material dissolution, i.e. volume loss
- . The mode of material dissolution which may serve to enhance or retard cavitation attack. For example, stressed material may be removed, resulting in a smoother surface less prone to cavitation attack [7,8]. Also, passivating materials like titanium may suffer localised corrosion attack leading to pitting and increased cavitation erosion [14,15]. Thirdly, the roughening of the exposed surface caused by cavitation erosion may stimulate localised corrosive attack which will again

facilitate increased damage through cavitation [16].

In this chapter, the role of cathodic and anodic potentials in cavitation erosion was investigated. It was shown that the net result of the factors discussed above can yield widely different damage rates depending on material properties and gas development. Two alloys, i.e. B51S Al alloy and type 304 stainless steel, were used. Testing was done in an artificial mine water (see Section 8.1) using a vibratory-type cavitation test rig.

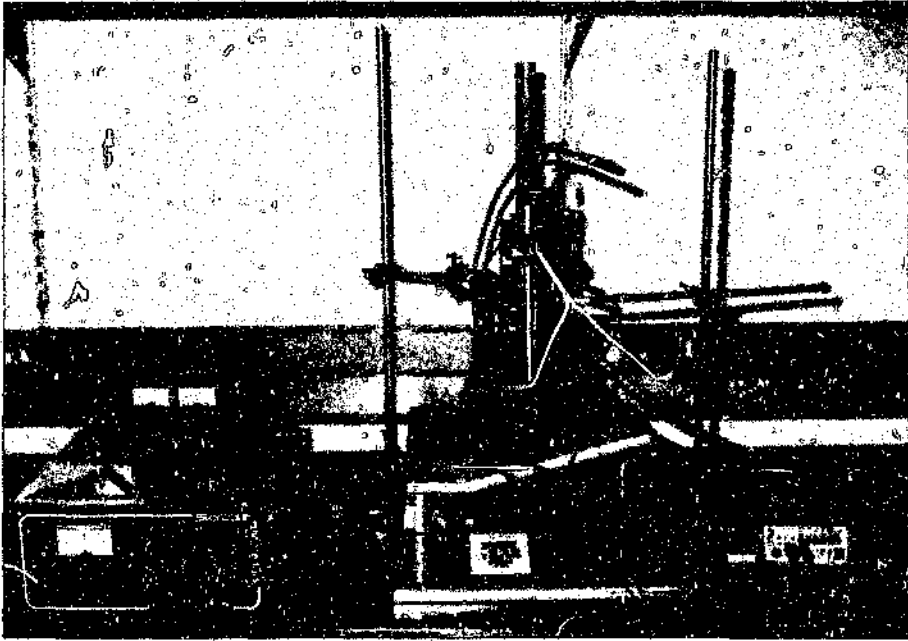
9.2 Vibratory-type test rig

An attempt was initially made to execute the tests in the rotating disc device using an electrochemical cell similar to the one described in Section 4.4.1. However, although this technique was thoroughly investigated, it proved unsuccessful because of the interference caused by the different metallic materials in close proximity to, and electrically connected to the cell by means of the salt solution.

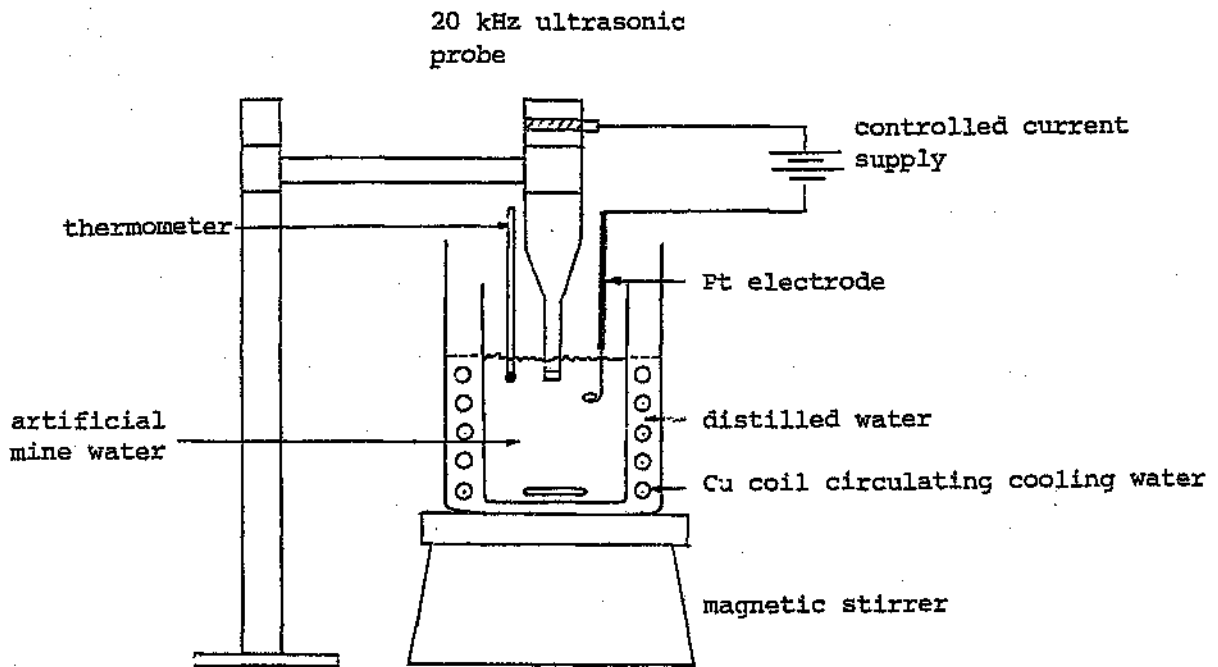
Since a vibratory probe is ideal for this type of test work, a vibratory-type test rig was subsequently constructed as described below.

The test rig is shown in Figure 9.1. A 20 kHz, 250 W ultrasonic probe was used to create vibration levels sufficient to generate cavitation in the test liquid. Vibrations were generated by a piezo-electric transducer and increased in amplitude by a tapered horn. The test sample, or a standard tip made of a titanium alloy, was screwed into the front end of the horn (diameter 12,7 mm). The probe was vertically mounted with the sample immersed in the test liquid contained in a 800 ml glass beaker. The temperature of the liquid was controlled by circulating chilled water (18 °C) through a copper tube coiled around the beaker. The coil was immersed in distilled water to improve heat exchange between the coil and the beaker. A magnetic stirrer rotated the test liquid to ensure temperature homogeneity in the liquid.

For the application of external potentials, an electric lead was connected to the body of the probe (which was insulated from the stand), and another was fixed to a platinum



(a)



(b)

Figure 9.1: (a) The vibratory-type cavitation test rig after completion, and (b) schematic layout of rig

electrode which was immersed in the test fluid. A stabilised power supply was used to generate a potential between the sample (working electrode) and the platinum electrode (auxiliary electrode). The current through the electrodes was determined by measuring the potential over a stable, calibrated resistance which was connected in series with the electrodes.

9.3 Preliminary testing

The influence of cooling water flow rate, sample immersion depth, vibration amplitude (measured optically in air), stirring speed and the position of the platinum electrode was determined during preliminary tests using a standard tip. This information was used to select appropriate test conditions. As far as possible, these were chosen to conform to the ASTM Standard Vibratory Test [17].

A B51S Al alloy sample was used to select appropriate anodic and cathodic currents. (Current measurement was preferred to potential measurement, as the current is directly proportional to the amount of electrolytic gas developed.) Electrolytic gas was formed at all currents selected for cavitation erosion testing. When a cathodic current was applied, hydrogen gas was developed at the sample [18]:



The application of an anodic current caused the formation of oxygen at the sample [18]:



The above equations show that the anodic current has to be twice the cathodic current to develop the same amount of gas.

The effect of cavitation on cathodic currents applied to B51S Al alloy was also studied.

As shown in Figure 9.2, the current during cavitation was higher than without cavitation. This result is in agreement with previous studies [2,18] and is ascribed to the balance between the destruction of the passive film on the one hand and the rate of repassivation on the other.

9.4 Test procedure

Initially, the probe was warmed up for 1,5 hours using a standard tip in the test liquid. During testing, cavitation erosion was quantified by regular mass measurements on the sample, carried out as follows:

The probe and power supply (where applicable) were switched off. The sample was removed from the probe, washed in water and dried with compressed air, and subsequently washed in acetone and dried. Thereafter it was weighed to 0,1 milligram and put back in the probe. The probe and power supply were then switched on again.

The mass losses were converted to volume losses and plotted against time eroded, producing typical erosion versus time curves (Section 2.3.3). Cavitation erosion was expressed as the gradient of the steady-state part of the curves, as this approach gave excellent reproducibility of results.

Two materials were tested, i.e. B51S Al alloy and AISI type 304 stainless steel. Most tests were duplicated; reproducibility was excellent.

9.5 Results and discussion

B51S Al alloy

Material data for B51S Al alloy is listed in Table 9.1. Samples for testing were machined as per Figure 9.3, followed by grinding and polishing of the faces to $R_a \sim 0,1 \mu\text{m}$ before testing. The test parameters were:

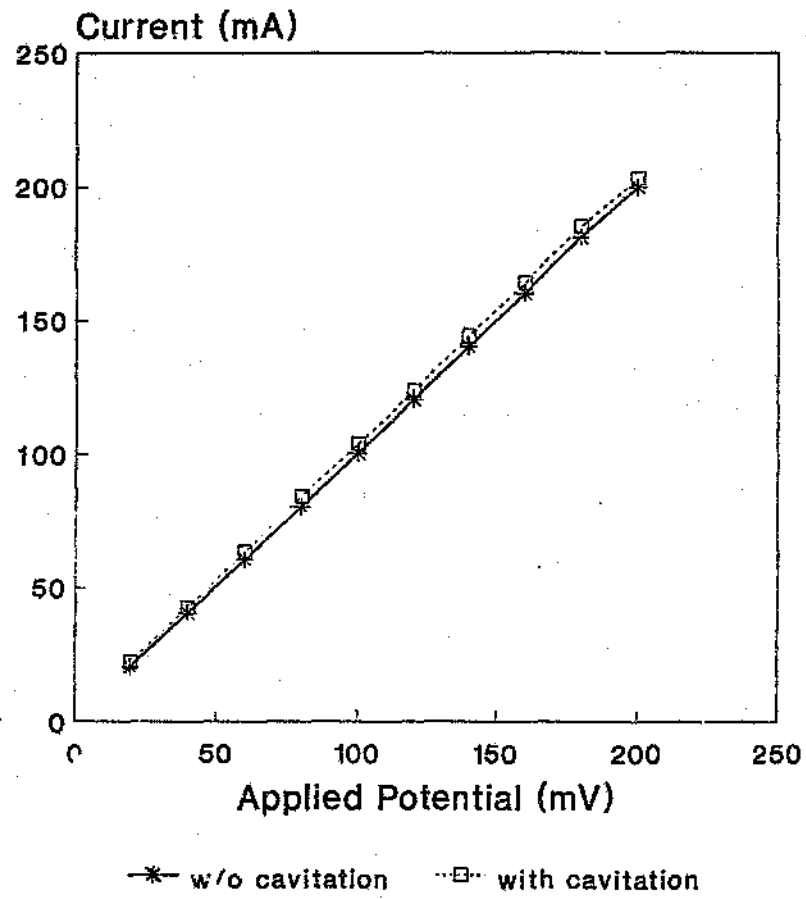
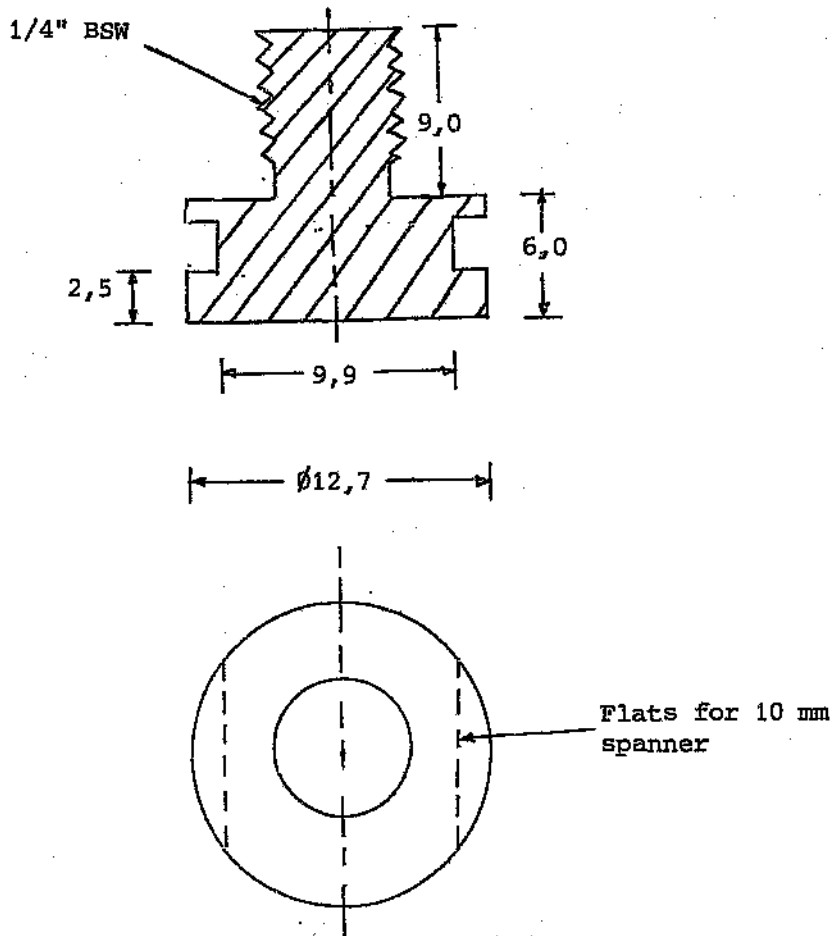


Figure 9.2: The effect of cavitation on a cathodic current applied to a B51S Al alloy sample

Table 9.1: Material data for B51S Al alloy

Aluminium Association	Obsolete System	British Standard	Germany	France	Italy
6082	B51S	H30	AlMgSi1	A-SGM0,7	P-AS1G UNI3571

Chemical Composition Limits (%)	Cu	Mg	Si	Fe	Mn	Zn	Ti	Cr
	0,1	0,6 1,2	0,7 1,3	0,5	0,4 1,0	0,2	0,1	0,25
Density (g/cc)	2,70							
Modulus of Elasticity (GPa)	70							
Melting Range (°C)	555-650							
Thermal Conductivity at 100 °C (W/m°C)	180-189							
0,2% Proof Stress (MPa)	270							
Ultimate Tensile Strength (MPa)	310							
% Elongation in 50 mm	7							



All dimensions in mm
Material: B51 Al alloy
Sample mass: 2,75 g

Figure 9.3: B51S Al alloy sample design

Liquid volume	:	800 ml
Tip immersion depth	:	10 mm
Vibration amplitude	:	58 μ m (peak-to-peak)
Temperature	:	17,5 \pm 1,3 $^{\circ}$ C

The volume losses obtained with the application of anodic currents were reduced by the fractions due to corrosion only, to obtain the purely "mechanical" [7,8] contributions. (This statement is not entirely correct, as compensation could not be made for the synergistic effect between cavitation erosion and corrosion.) The corrosion-induced volume losses were determined using a similar test configuration as for the cavitation erosion tests, but with the probe switched off. The results are shown in Table 9.2 and Figures 9.4 and 9.5.

Figure 9.5 shows that the development of cathodic gas served to reduce cavitation erosion, and that the damage reduction increased with the cathodic current (or amount of gas formed). Consequently, it would appear that gas development, together with reduced corrosion, played a major role in the protection process.

When anodic currents were applied, there was a small reduction in erosion rate at low current levels, compared to zero current. This implied that gas development caused a protective effect large enough to overcome material dissolution at these current levels. The erosion rate rose sharply at higher currents due to the increased rate of corrosion (Figure 9.6), coupled with the synergistic action between corrosion and cavitation erosion.

Further evidence for gas protection was found by studying the worn sample faces (Figure 9.7). The damaged surfaces of the samples where electrolytic gas had been developed, had similar geometries and were significantly smoother than the surfaces of samples where no currents had been applied. This observation supported the arguments given in Section 2.3.7 for cushioning of cavitation bubble collapse, and thus damage reduction, by increase of the gas content of the liquid.

The abovementioned results showed that, in the case of the B51S Al alloy, it was not

Table 9.2: Cavitation erosion data for B51S Al alloy with external currents applied

Current (mA)	Test no.	Volume loss rate (mm ³ /min)	Average VLR
0	3	0,1683	0,1686
	6	0,1689	
Cathodic 100	4	0,1151	0,1186
	7	0,1221	
Cathodic 50	15	0,1324	0,1398
	16	0,1472	
Cathodic 21	10	0,1507	0,1507
Anodic 200	5	0,2811	0,2811
Anodic 100	13	0,1600	0,1578
	14	0,1556	
Anodic 50	12	0,1513	0,1513
Anodic 42	8	0,1672	0,1663
	9	0,1653	

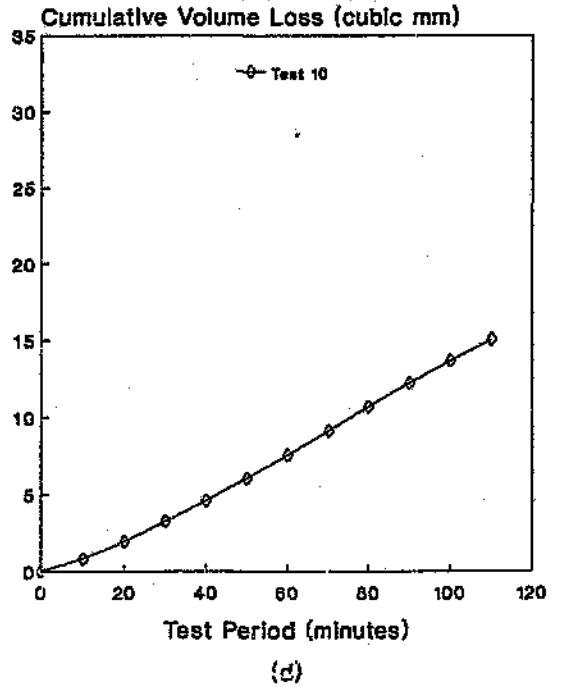
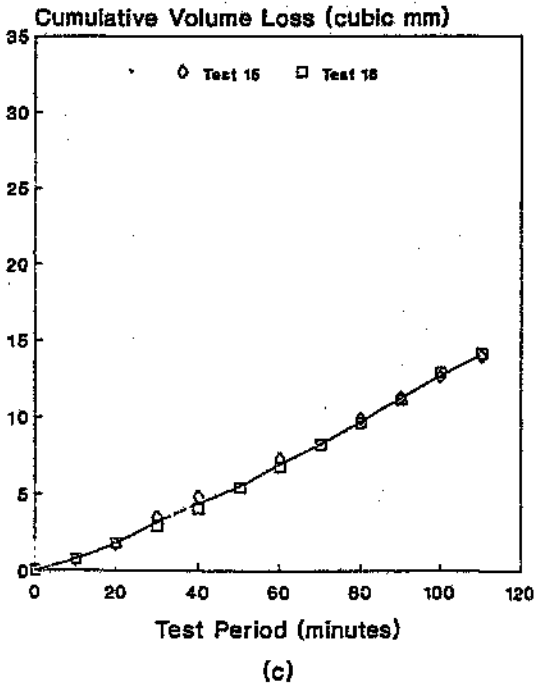
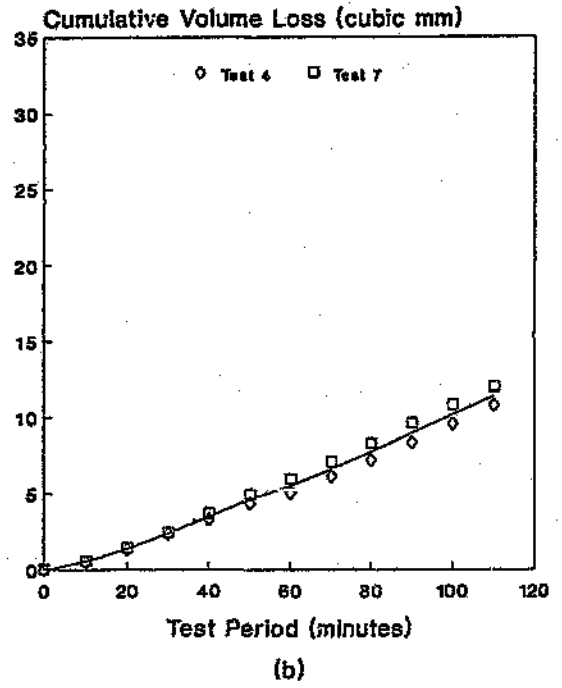
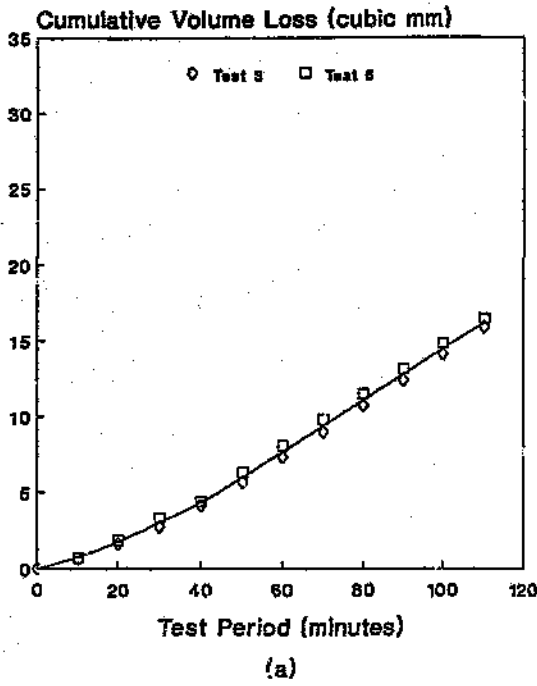


Figure 9.4: Volume loss versus test period curves for B51S Al alloy with the following applied currents: (a) 0, (b) cathodic 100 mA, (c) cathodic 50 mA, (d) cathodic 21 mA

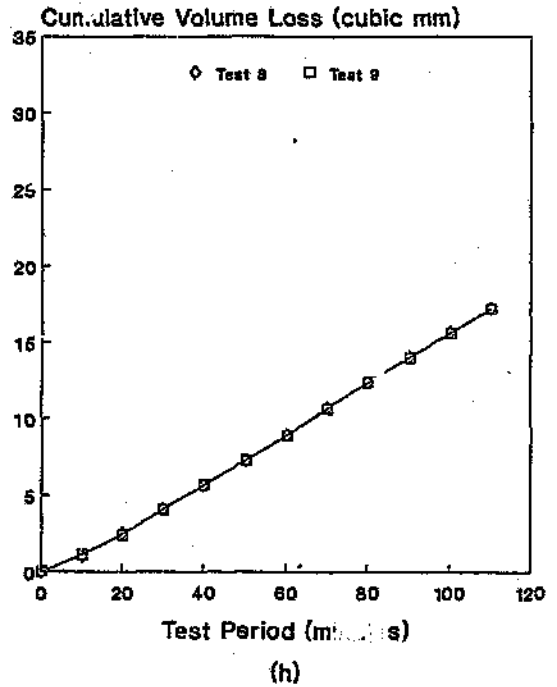
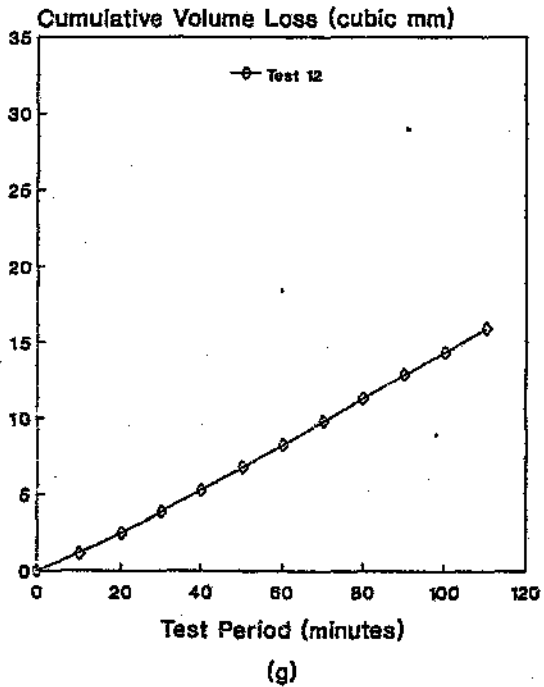
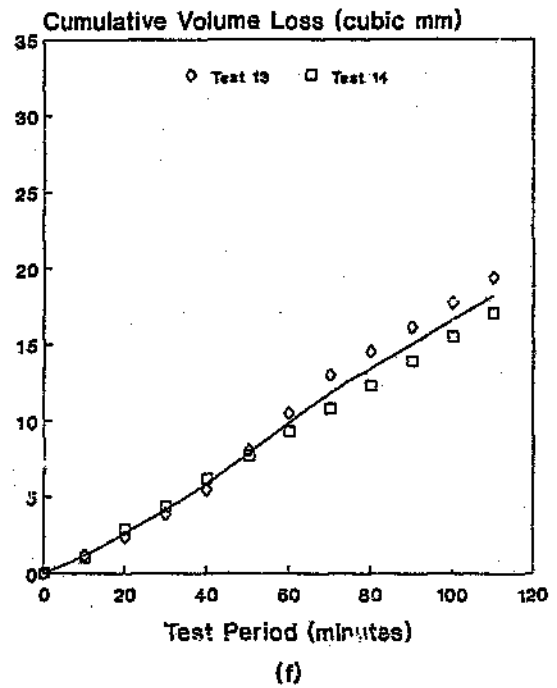
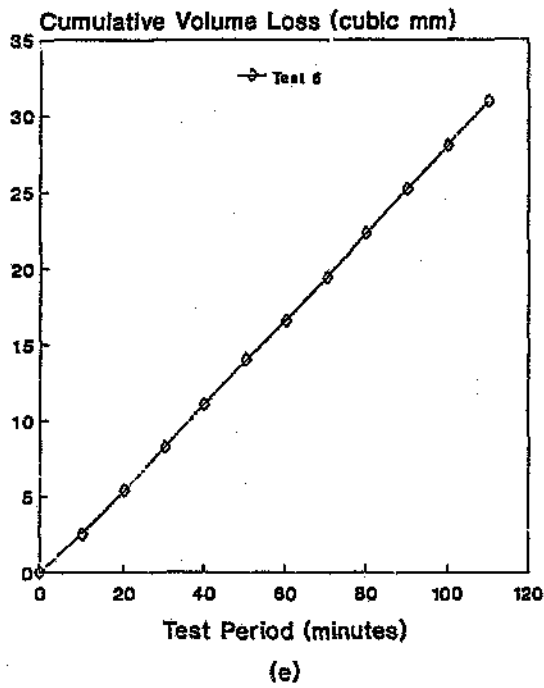


Figure 9.4 (cont): Volume loss versus test period curves for B51S Al alloy with the following applied currents: (e) anodic 200 mA, (f) anodic 100 mA, (g) anodic 50 mA, (h) anodic 42 mA

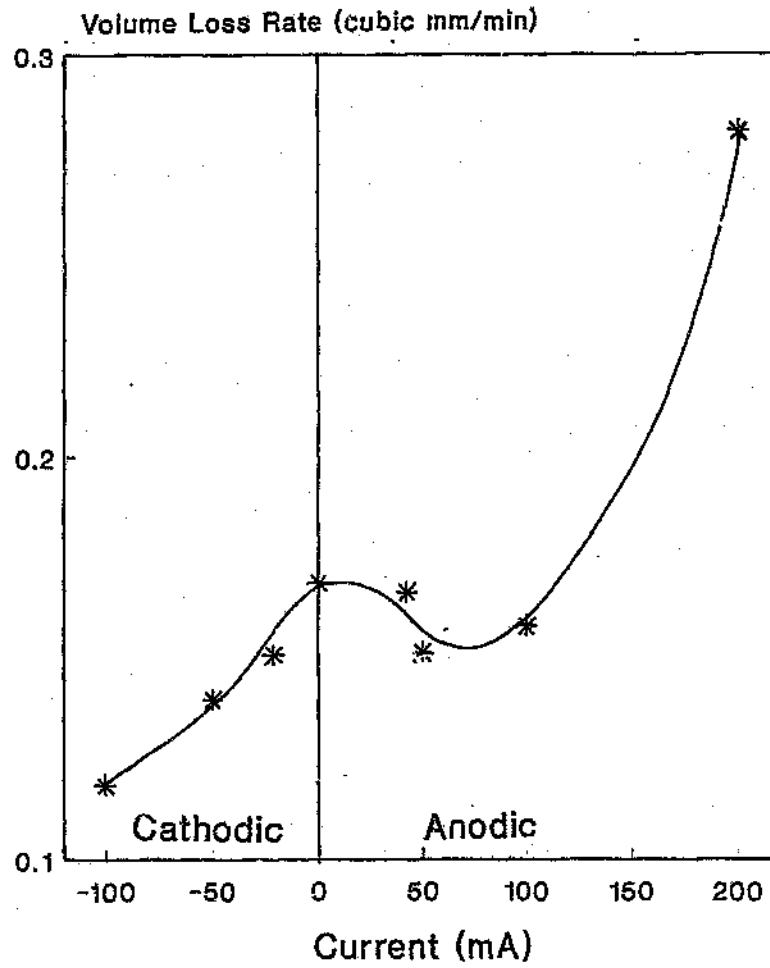


Figure 9.5: The effect of anodic and cathodic currents on the cavitation erosion of B51S Al alloy

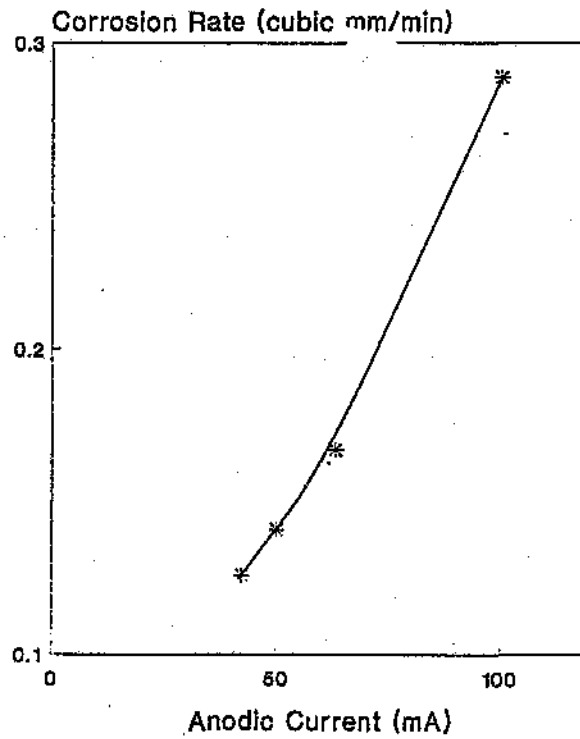


Figure 9.6: Relation between anodic current and corrosion rate for a B51S Al alloy sample

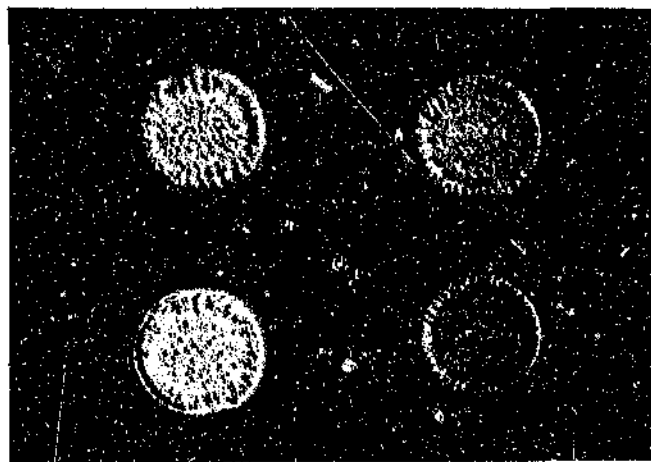


Figure 9.7: Samples eroded with no external current (left: top and bottom), a 100 mA cathodic current (right top), and a 50 mA anodic current (right bottom) applied

possible to unambiguously prove that gas development - and not reduction of the corrosion rate - was the main cause of reduced overall damage. The influence of gas development had to be verified by repeating the tests on a nobler material than aluminium, since for such a material the effect of gas development would be more pronounced because of the smaller role played by corrosion. Type 304 stainless steel was selected for this purpose.

AISI type 304 stainless steel

This is an austenitic stainless steel with composition and material properties as shown in Table 9.3.

Samples were machined as per Figure 9.8. (The reduced sample length was necessitated by the requirement for a total sample mass of $\sim 2,75$ g.) Thereafter, the faces were ground and polished to $R_a \sim 0,1 \mu\text{m}$. The following test parameters were used:

Liquid volume	:	800 ml
Tip immersion depth	:	10 mm
Vibration amplitude	:	65 μm (peak-to-peak)
Temperature	:	22,2 \pm 1,3 °C

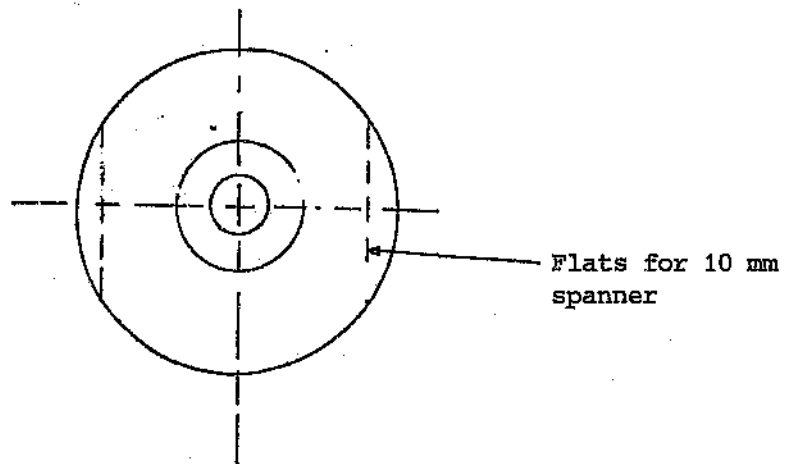
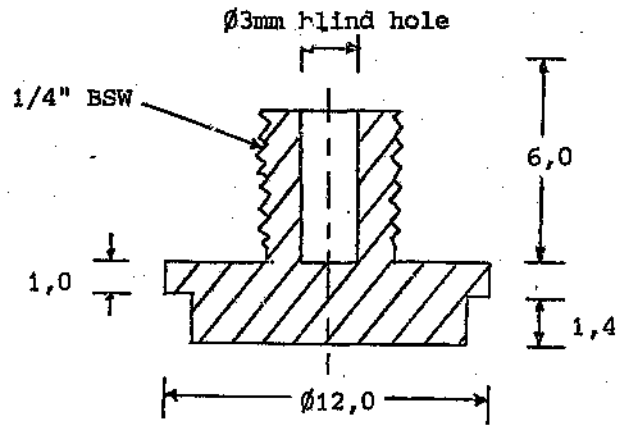
The mechanical volume losses were again calculated for the application of anodic currents. In this case, the corrosion components at each current level (Figure 9.9) were measured under low intensity (non-damaging) vibration conditions, as the samples did not repassivate fast enough under stationary conditions. Results are shown in Table 9.4 and Figures 9.10 and 9.11.

As shown in Figure 9.11, no significant change in cavitation erosion rate was experienced at different cathodic currents. A possible reason is that, even at the smallest cathodic current applied, the protection was optimal.

The application of anodic currents resulted in a decrease of erosion damage with increasing current, despite the higher material dissolution rates (Figure 9.9) This result

Table 9.3: Material data for AISI type 304 stainless steel

Chemical Composition Limits (%)	C	Mn	Si	Cr	Ni	P	S
		0,08	2,00	1,00	18,0 20,0	8,0 10,5	0,045
Density (g/cc)	8,0						
Modulus of Elasticity (GPa)	193						
Melting Range (°C)	1400-1450						
Thermal Conductivity at 100 °C (W/m°C)	15,7						
0,2% Proof Stress (MPa)	310						
Ultimate Tensile Strength (MPa)	600						
Elongation (% in $L_0 = 5,65\sqrt{S_0}$)	60						



All dimensions in mm
Material: Type 304 stainless steel
Mass: 2,80 g

Figure 9.8: Type 304 stainless steel sample design

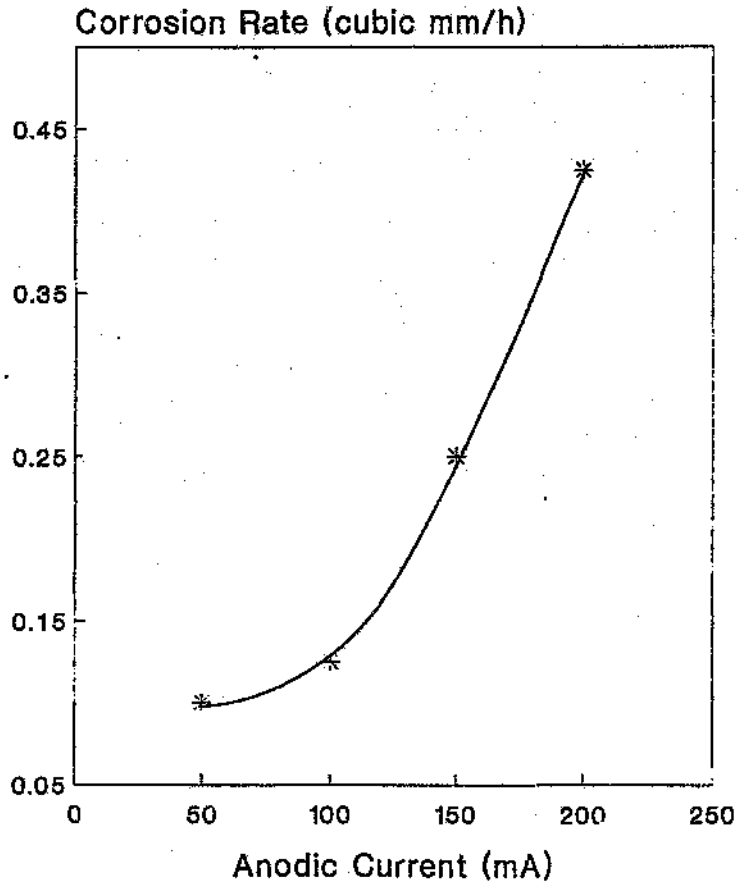


Figure 9.9: Relation between anodic current and corrosion rate for a type 304 stainless steel sample

Table 9.4: Cavitation erosion data for type 304 stainless steel with external currents applied

Current (mA)	Test no.	Volume loss rate (mm ³ /h)	Average VLR
0	1	0,8125	0,8181
	2	0,8237	
Cathodic 100	8	0,3000	0,3813
	11	0,4625	
Catf - 75	9	0,3625	0,3625
Cathodic 50	10	0,3743	0,3689
	12	0,3634	
Anodic 200	3	0,5575	0,5575
Anodic 150	4	0,7300	0,7363
	5	0,7425	
Anodic 100	6	0,8725	0,8575
	7	0,8425	

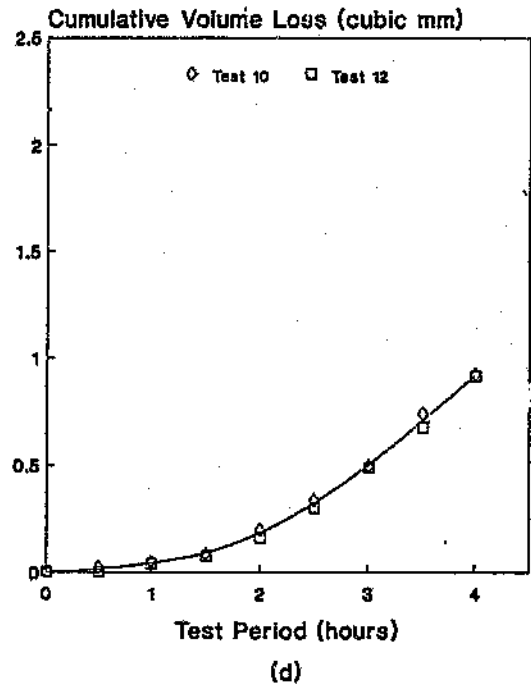
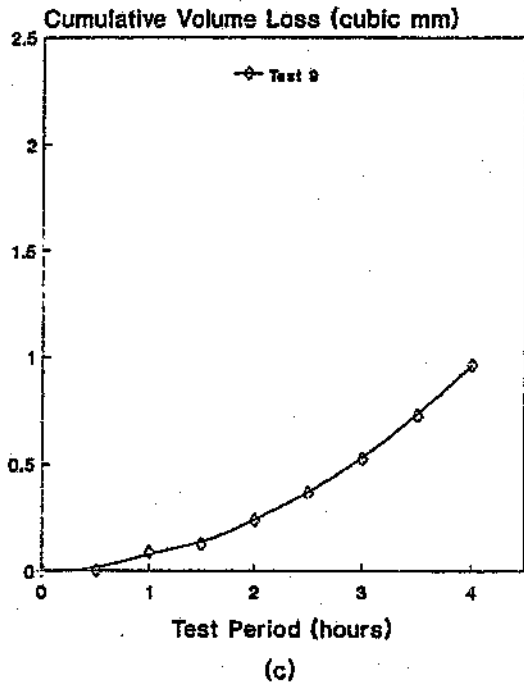
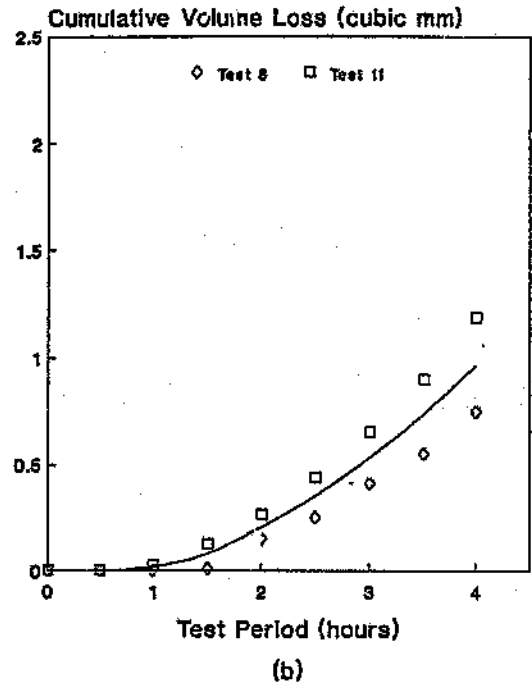
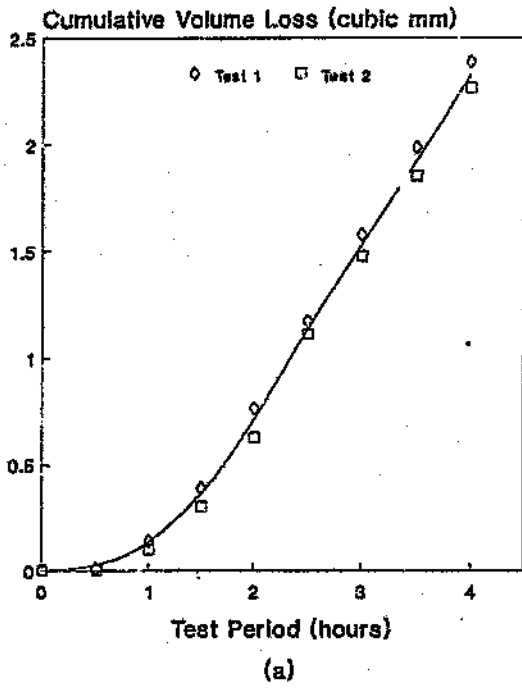


Figure 9.10: Volume loss versus test period curves for type 304 stainless steel with the following applied currents: (a) 0, (b) cathodic 100 mA, (c) cathodic 75 mA, (d) cathodic 50 mA

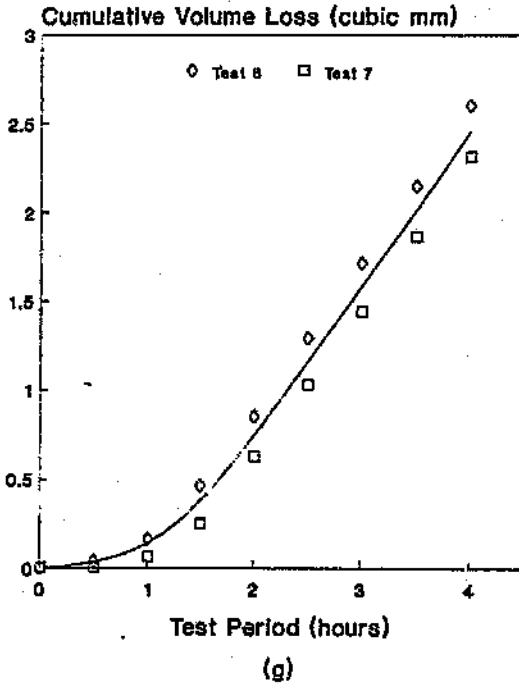
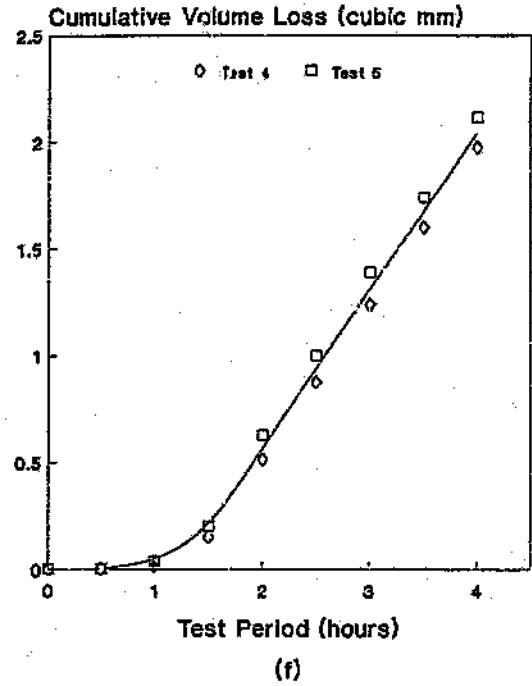
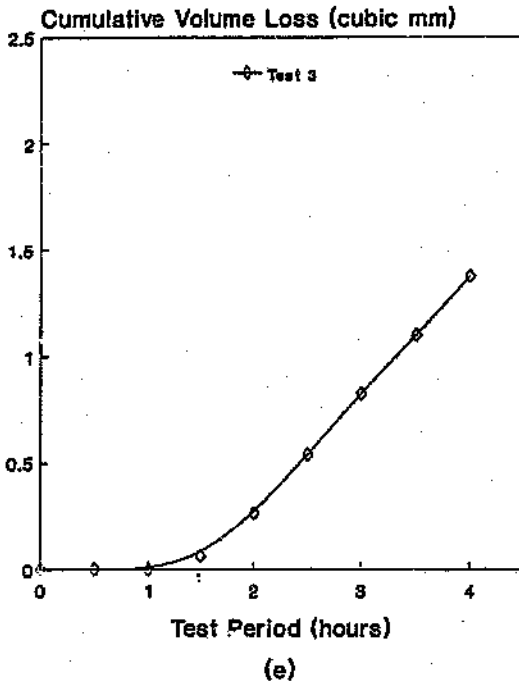


Figure 9.10 (cont): Volume loss versus test period curves for type 304 stainless steel with the following applied currents: (e) anodic 200 mA, (f) anodic 150 mA, (g) anodic 100 mA

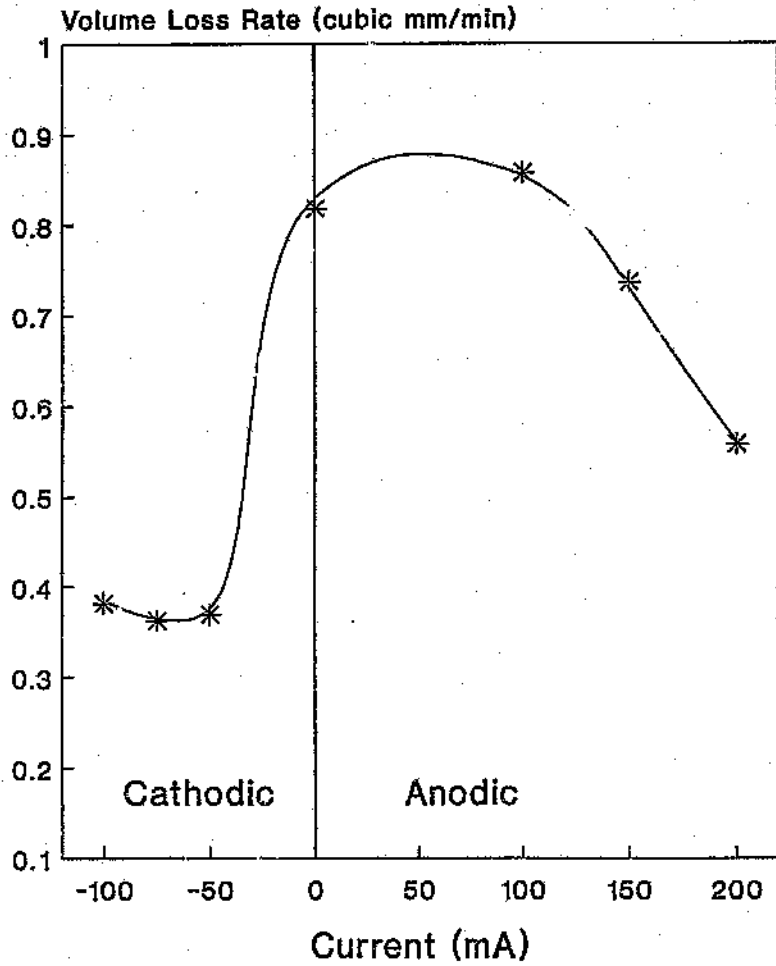


Figure 9.11: The effect of anodic and cathodic currents on the cavitation erosion of type 304 stainless steel

confirmed that electrolytic gas protects a cavitating body.

9.6 Summary

A vibratory-type cavitation test rig was developed to study the effect of external potentials applied to a cavitating body. It was found that the development of electrolytic gas results in a reduction of the mechanical attack on a cavitating body due to bubble collapse cushioning. The net effect on damage depends on the balance between the changes in intensity of mechanical attack, corrosion rate and surface roughness. Thus a cathodic potential always results in a decrease of the overall volume loss rate, whereas the volume loss rate may be increased or reduced in the case of an anodic potential.

References

1. G. Petracchi: Investigation of Cavitation Erosion (in Italian), *Metall. Ital.*, Vol. 41, pp. 1-6, 1944; English summary in *Engr's Digest*, Vol. 10, pp. 314-316, 1949.
2. M.S. Plesset: On Cathodic Protection in Cavitation Damage, *Trans. ASME, J. Basic Engr.*, pp. 808-820, 1960.
3. H.S. Preiser and B.H. Tytell: The Electrochemical Approach to Cavitation Damage and its Prevention, *Corrosion*, Vol. 17, pp. 107-121, 1961.
4. C.M. Preece: Cavitation Erosion, pp. 249-308 in *Treatise on Materials Science and Technology*, Vol. 16, edited by C.M. Preece, Academic Press, 1979.
5. W.C. Leith and A.L. Thompson: Some Corrosion Effects in Accelerated Cavitation Damage, *Trans. ASME, J. Basic Engr.*, pp. 795-807, 1960.
6. P.V. Rao, K. Seetharamiah and T.L. Rama Char: Prevention of Cavitation damage of Aluminium by Corrosion Inhibitors and Cathodic Protection, *J. Electrochem. Soc. India*, Vol. 23, No. 1, pp. 7-23, 1974.
7. C.M. Preece and B. Vyas, p. 811 in *Proc. 4th Int. Conf. Rain Eros.*, edited by A.A. Fyall and R.B. King, Royal Aircraft Establishment, Farnborough, UK, 1974.
8. A.F. Derendowski, M.K. Bologna and K.K. Shal'nev (in Russian), *Dokl. Akad. Nauk. USSR*, Vol. 183, pp. 1292-1294, 1968.
9. F.W. Von Hirth and H. Speckhardt, *Werkst. Korros.*, Vol. 23, p. 1112, 1972.
10. W.H. Wheeler: Mechanism of Cavitation Erosion, *Fluid Note 18*, Dept. Sci. Ind. Res., Glasgow, UK, 1954.
11. V. Ashworth, L. Cifuentes and R.P.M. Proctor, p. 66-1 in *Proc. 5th Int. Conf. on Erosion by Solid and Liquid Impact*, Farnborough, UK, 1979.
12. R. Simoneau, J.L. Filhey and R. Roberge, pp. 71-82 in *Cavitation Erosion in Fluid Systems*, edited by W.L. Swift and R.E.A. Arndt, McGraw-Hill, New York, 1981.
13. P. Eisenberg, H.S. Preiser and A. Thiruvengadam: On the Mechanisms of Cavitation Damage and Methods of Protection, *Trans. Soc. Naval Archit. Mar. Eng.*, Vol. 73, p. 241, 1965.
14. F.C. von Altof, H. Buhl and H. Voight, *Werkst. Korros.* Vol. 24, No. 1020,

- pp. 606-673, 1973.
15. G. Engleberg and J. Yahalom, *Corros. Sci.*, Vol. 12, p. 469, 1972.
 16. R. Beeching, *Trans. Inst. Eng. Shipbuild. Scotl.*, Vol. 85, p. 210, 1942.
 17. ASTM G32-85: Standard Method of Vibratory Cavitation Erosion Test, 1985.
 18. B. Vyas: Erosion-corrosion, pp. 357-394 in *Treatise on Materials Science and Technology*, Vol. 16, edited by C.M. Preece, Academic Press, 1979.

CHAPTER 10**10. INFLUENCE OF THE AIR CONTENT OF THE FLUID****10.1 Introduction**

As mentioned in Section 2.3.7, the fact that the onset of cavitation occurs at about vapour pressure of a cavitating fluid may be ascribed to the existence of miniature gas bubbles (nuclei) in the fluid. The amount of cavitation at a given underpressure and thus the nucleation threshold depend strongly on the number and size spectrum of the nuclei. Since this spectrum is difficult to determine and requires sophisticated equipment, the total gas content has been measured in most studies. This is made up of dissolved gas (usually more than 99% of the gas) and a very small entrained portion in the form of microbubbles. As a general principle, the number of nuclei increases with the total or dissolved gas content. Dissolved gas may enhance bubble growth via diffusion processes, with a high resulting cushioning effect in the collapse phase and decrease of erosion damage. On the other hand, the presence of oxidizing gases will influence corrosion reaction rates as discussed in Section 2.3.7.

The influence of gas content on nucleation thresholds has been thoroughly investigated. Generally, inception sigma (Section 2.3.2) was found to increase with increasing gas content, i.e. cavitation happened quicker. Results regarding the effect of gas content on cavitation erosion are relatively scarce, but studies have been reported using flow-type as well as vibratory-type testing equipment. The minimum quantity of gas required to initiate cavitation is always present in practical fluids. Further increase in gas content will enlarge the number of nuclei. This will result in an enhanced damage rate until the optimum number of nuclei is reached. On the other hand, large quantities of gas (as in the case of saturated and supersaturated solutions) will promote gaseous cavitation and a resulting decrease of damage. The net effect is that a peak erosion rate exists as a function of gas content.

The air content in hydropower mining systems may be assumed to vary over a wide range. The influence of air content on cavitation erosion in a flow cavitation system has been investigated by means of the rotating disc test facility. Different techniques for controlling air content have been considered, with respect to their applicability in practical hydropower systems.

10.2 Erosion test procedure

Three 2S Al alloy samples were eroded for 1 hour in distilled water during each test. Details of sample treatment and the flow system are as for the 1 hour temperature tests (Section 4.2). Test parameters are listed in Table 10.1.

Part of the study involved variation of the total air content of the water between low and saturated values. The dissolved oxygen (DO) content of the water was measured at the position shown in Figure 3.10 and related to dissolved air content as follows:

$$x \text{ mg/l O}_2 = x/1,43 \text{ ml/l O}_2 = (x/1,43)(100/20,9) \text{ ml/l air}$$

$$(\rho_{\text{O}_2} = 1,43 \text{ g/l at } 0^\circ\text{C})$$

Under atmospheric conditions (25 °C ; 0,1 MPa):

$$\text{Oxygen solubility in water} = 8,38 \text{ mg/l} = 5,86 \text{ ml/l}$$

$$\text{Thus the saturated air content} = 28,04 \text{ ml/l}$$

Increase of air content was achieved by blowing compressed air through a diffusing nozzle into the reservoir at various rates. To diminish the air content in the water, it was boiled before entering it into the flow system. (An attempt to decrease the air content by drawing a vacuum over the water while circulating it through the flow system was not successful.)

Supersaturated conditions, corresponding to increase of the entrained air portion, were achieved by blowing compressed air directly into the test chamber. For these tests, the degree of supersaturation was assumed to be proportional to the rate at which air was released.

Table 10.1: Test parameter values for air content erosion tests

Parameter	Mean value	SD	Comment
Temperature (°C)	40,1	0,6	Water was preheated
Pressure (MPa)	0,15	0,002	
Flow rate (l/min)	~30		
Disc velocity (rpm)	3620	18	

10.3 Results and discussion

Figure 10.1 shows the variation of dissolved oxygen (DO) content with test time for the various undersaturated tests. In all cases, a stable dissolved oxygen value was soon assumed. These values are listed in Table 10.2 together with the volume losses obtained. Over the dissolved oxygen range tested, the trend was for decreasing damage with increasing oxygen level, as shown in Figure 10.2. This decrease may be ascribed to the increased diffusion rate of air into cavitation bubbles during the growth cycle, leading to collapse cushioning. It may also be assumed that at very low dissolved oxygen levels a decrease in the damage rate will occur due to the diminishing of nuclei numbers and the resulting increase in water tensile strength [1,2]. However, such conditions are not achievable in practical hydraulic systems.

Gaseous cavitation developed with increasing feed rates in tests in which air was blown into the test chamber, thus creating oversaturated conditions. In situ observation showed the presence of large (1-2 mm) air-filled "nuclei" in water entering the test chamber. This resulted in collapse cushioning and perhaps attenuation of shock waves from collapsing bubbles [3] and thus reduction in volume loss. Almost complete termination of damage (Figure 10.3) was achieved at relatively low air flow rates.

10.4 Summary

The influence of increased air content of the cavitating liquid (distilled water) was studied in the rotating disc test rig. A rise in the total air content (including dissolved and entrained air) of the water in the undersaturated range resulted in bubble collapse cushioning and reduction of cavitation damage. When the water was oversaturated with air, large air bubbles formed and cavitation damage was drastically reduced, probably due to both bubble collapse cushioning and shock wave attenuation.

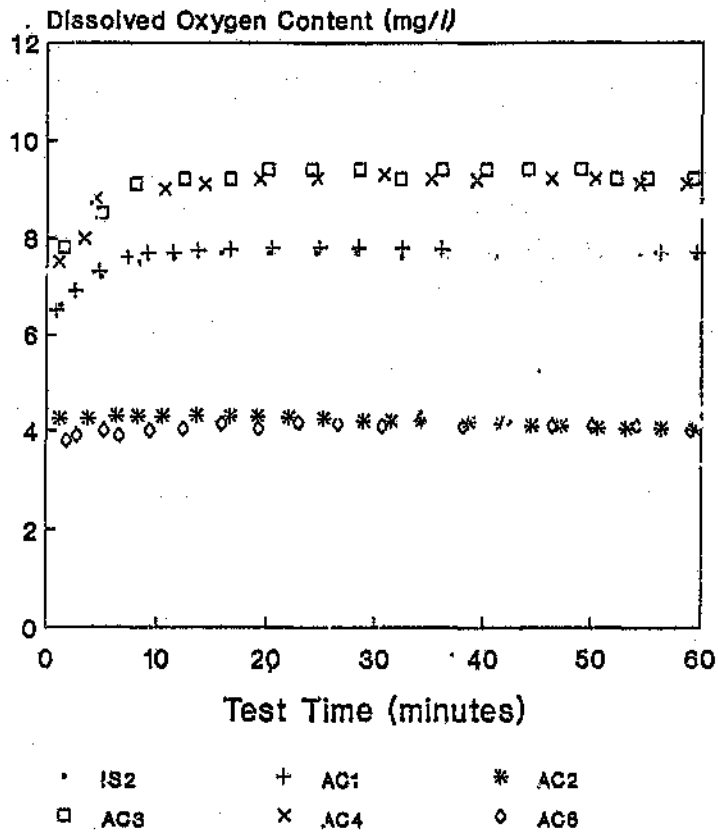


Figure 10.1: Dissolved oxygen (DO) levels for the undersaturated air content tests

Table 10.2: Stable dissolved oxygen (DO) values and volume losses for tests with various air content conditions

Test code	Air content condition	Stable DO cont. value (mg/l)	1 h cumulative volume loss (mm ³)
IS1	Ambient conditions, open flow systems	-	75,22
IS2	Ambient conditions, open flow systems	7,60	76,30
AC1	Compressed air bubbled through reservoir at ~2400 l/min, open flow system	7,70	84,04
AC3	Compressed air bubbled through reservoir at ~2400 l/min, open flow system	9,20	71,96
AC4	Compressed air bubbled through reservoir at ~2400 l/min, closed flow system	9,15	81,49
AC2	Water boiled, closed flow system	4,04	87,93
AC6	Water boiled, closed flow system	4,10	88,86

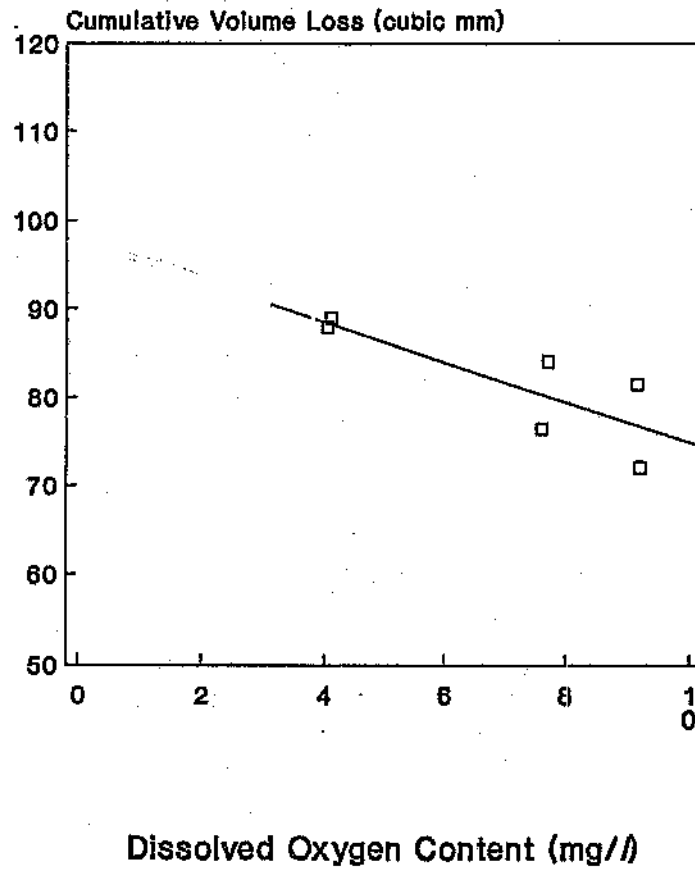


Figure 10.2: 1 hour cumulative volume loss as a function of dissolved air content for the tests under non-saturated conditions

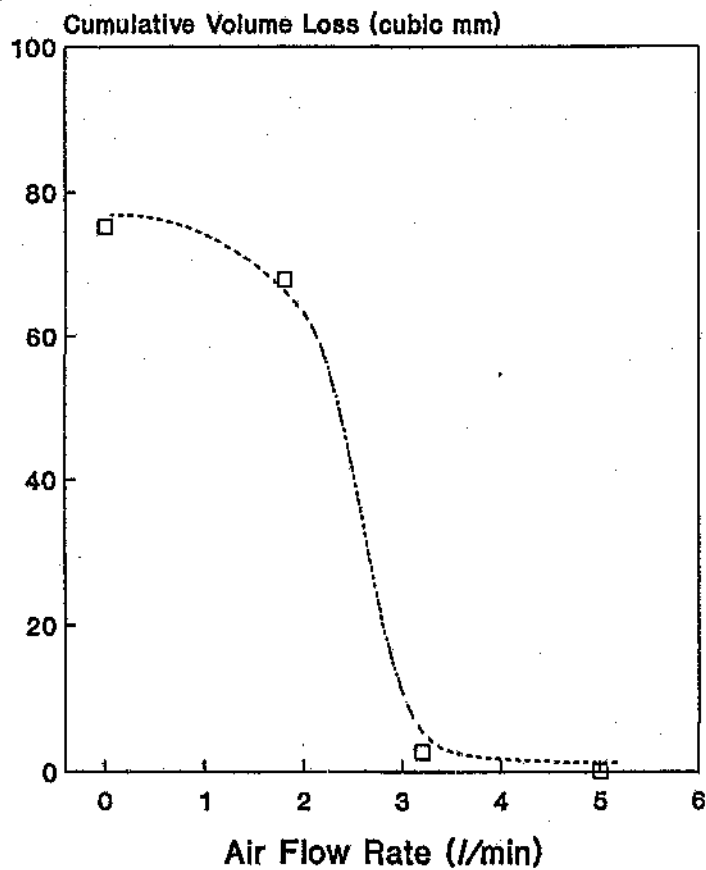


Figure 10.3: 1 hour cumulative volume loss as a function of air flow rate for the supersaturated air content tests

References

- 1) E.N. Harvey, W.D. McElroy and A.H. Whiteley: On Cavity Formation in Water, *J. Appl. Phys.*, Vol. 18, No. 2, pp. 162-172, 1947.
- 2) R.T. Knapp: Cavitation and Nuclei, *Trans. ASME*, Vol. 80, pp. 1315-1324, 1958.
- 3) F.G. Hammitt: *Cavitation and Multiphase Flow Phenomena*, McGraw-Hill, 1980.

CHAPTER 11**11. CONCLUSIONS****11.1 General**

A study of the existing literature on cavitation and cavitation erosion showed that it is a highly complex phenomenon governed by a multitude of interrelated factors. The major problem remains accurate prediction of damage from easily measurable parameters - deviations from expected results occur due to the effects of fluid, flow and material properties.

With the purpose to investigate the influence of fluid and flow parameters on particularly flow cavitation and erosion, a rotating disc-type cavitation test rig was developed. Parameters like water temperature, pressure, chemistry, solids content and air content, could be varied over a wide range of values. The rig facilitated in situ observation of cavitation dynamics as well as quantification of cavitation damage. A second, vibratory-type test rig was also developed because it was more suitable for the study of external potential effects on cavitation erosion. The contribution made by these studies to the local and international expertise base on the phenomenon of cavitation is illustrated by the discussion of key results below.

Although the erosion rate of copper samples peaked at approximately 50 °C, i.e. exhibited the normal temperature dependence, this was not the case for aluminium. The damage rate did not decrease at higher temperatures up to 80 °C. A similar result had been obtained before in a vibratory test rig, but the underlying reasons were not established. A detailed study was carried out to establish the contribution of material effects, i.e. softening and increased corrosion. No significant local heating of the eroding surface was detected. It was found that increased corrosion was the main contributing factor to the high damage rate.

In accordance with literature results, a peak damage rate was found to exist as a function of water static pressure. This occurred at -0.135 MPa under the test conditions used. A substantial drop-off in damage took place at higher pressures, associated with shrinking of the bubble cloud and damage zone as well as a decrease in the number of cavitating bubbles. At lower pressures, the damage also decreased, probably due to the smaller pressure gradient over which bubble collapse took place. Over the velocity range used (48 to 51 m/s average sample velocity), there was an increase in volume loss and in the extent of the damage zone with velocity. Measurement of the pressure differential controlling cavitation and erosion was only partly successful, as the pressure probe required further development.

Existing results on the influence of solid impurities was found to be severely limited and limited to polymeric solutions. The influence of the physical properties of the solid (hardness, angularity, wettability) was investigated using silica and PVC powders in various concentrations. At very low concentrations, damage rates were not significantly affected. Above ~ 40 ppm, however, an increased silica concentration resulted in damage increase which was ascribed to solid particle erosion caused by the highly abrasive silica particles. On the other hand, damage diminished with increasing PVC concentration. Various mechanisms, including impact absorption and the accommodation of air pockets on PVC particles, may be responsible for this result. It may thus be concluded that the nature of the solid impurity determines whether it will cause suppression or stimulation of erosion damage, while the concentration of solids determines the size of the damage variation.

The synergistic effect between cavitation erosion and corrosion was studied both via tests at elevated temperature (on aluminium and copper samples) and by increasing the concentration of corrosive chemicals in the test fluid (using aluminium and low carbon steel samples). Quantitative determination of the size of the effect illustrated that given the right conditions, damage may be exponentially increased.

A study employing a vibratory-type test rig showed unambiguously that electrolytically generated gas, developed as a result of the application of cathodic and anodic potentials

to cavitating bodies, plays a protective role against cavitation erosion. Previous contradictory results could have been caused by the influence of corrosion. Tests with aluminium and stainless steel samples revealed that the overall volume loss rate can either increase or decrease, depending on the corrosion resistance of the material.

Various simple techniques for controlling the air content, and the resulting effect on damage was investigated both in the undersaturated and supersaturated regimes. Heating, and flushing with compressed air, resulted in a significant variation (50-110% of atmospheric saturation level) in dissolved air content of the water around the ambient value. In this range, increasing air content resulted in a relatively mild decrease in damage, which may be ascribed to higher air diffusion rates into bubbles and thus collapse cushioning.

Damage was drastically reduced and even terminated in cases where air bubbles were released directly into the cavitation region to create supersaturated conditions, due to the development of gaseous cavitation and bubble collapse cushioning.

11.2 Hydropower mining systems

The cavitation test rig simulates flow-type cavitation over a range of conditions compatible with hydropower systems like the rockdrill. Investigations have been carried out of cavitation dynamics and damage development, as well as the influence of various fluid and flow parameters playing a major role in water-powered mining devices. Some principles have been derived to apply in the design and operation of such devices, which will be discussed briefly. The test rig may with moderate upgrading also be used for the testing and development of erosion-resistant materials for application in water-powered equipment.

One approach followed by designers of hydraulic equipment is to choose the flow geometry and operating conditions in such a way that cavitation takes place in a region where damage is less critical or where no damage will occur. This requires a proper understanding of cavitation dynamics and the behaviour of the cavitation region. The

present study confirmed that the location and geometry of the cavitation region is dependent on water velocity and pressure, and showed that water temperature has also a significant effect within the range compatible to possible mining conditions.

On the other hand, cavitation damage may be reduced by diversion from peak erosion rates associated with velocity, pressure or temperature. Although dynamic pressure and velocity changes occur in the operating cycle of rockdrills, damage has in practice almost been eliminated by the application of an appropriate backpressure. With regards to temperature effects, hydraulic water is chilled to about 5 °C because it doubles as a coolant. At such temperatures, cavitation damage is relatively low. Care has to be taken, however, in situations where significant local heating of the water may occur due to cavitation and/or cavitation erosion.

Elevated temperatures will also have an effect on corrosion, which acts synergistically with cavitation erosion to produce increased damage rates. Typical mine waters have high corrosivity and will cause substantially intensified damage of corrodible materials, unless they are treated to become less aggressive.

The solids contained in South African mine waters comprise a large percentage of abrasive quartzite. It has been found in this study that relatively low concentrations of silica may increase cavitation erosion, probably by the inclusion of silica particles in impinging jets. This emphasizes the necessity for the purification (filtering) of hydraulic waters. On the other hand, the amount of damage could be drastically reduced by the addition of a relatively soft, deformable substance like PVC. However, this type of solution may not conform to mining policy, except if the amount of material used could be tightly controlled, e.g. by recycling.

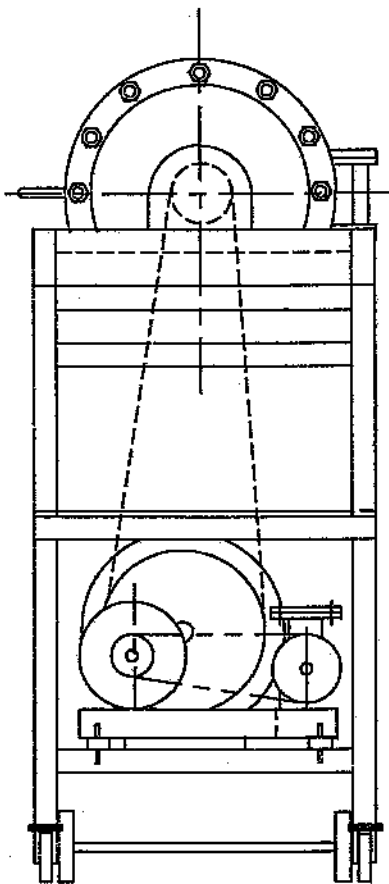
Where practically possible, metallic components suffering from cavitation damage in hydropower systems can be successfully protected by the application of cathodic potentials. Potentials have to be large enough to facilitate gas formation.

In practice, hydraulic waters will be aerated due to their initial exposure to the

atmosphere. Deaeration of the water will reduce cavitation damage, if a deaeration unit may be operated cost-effectively. It appears impractical to oversaturate the water with air in the vicinity of a rockdrill or similar device, because of the additional infrastructure required and high water pressure.

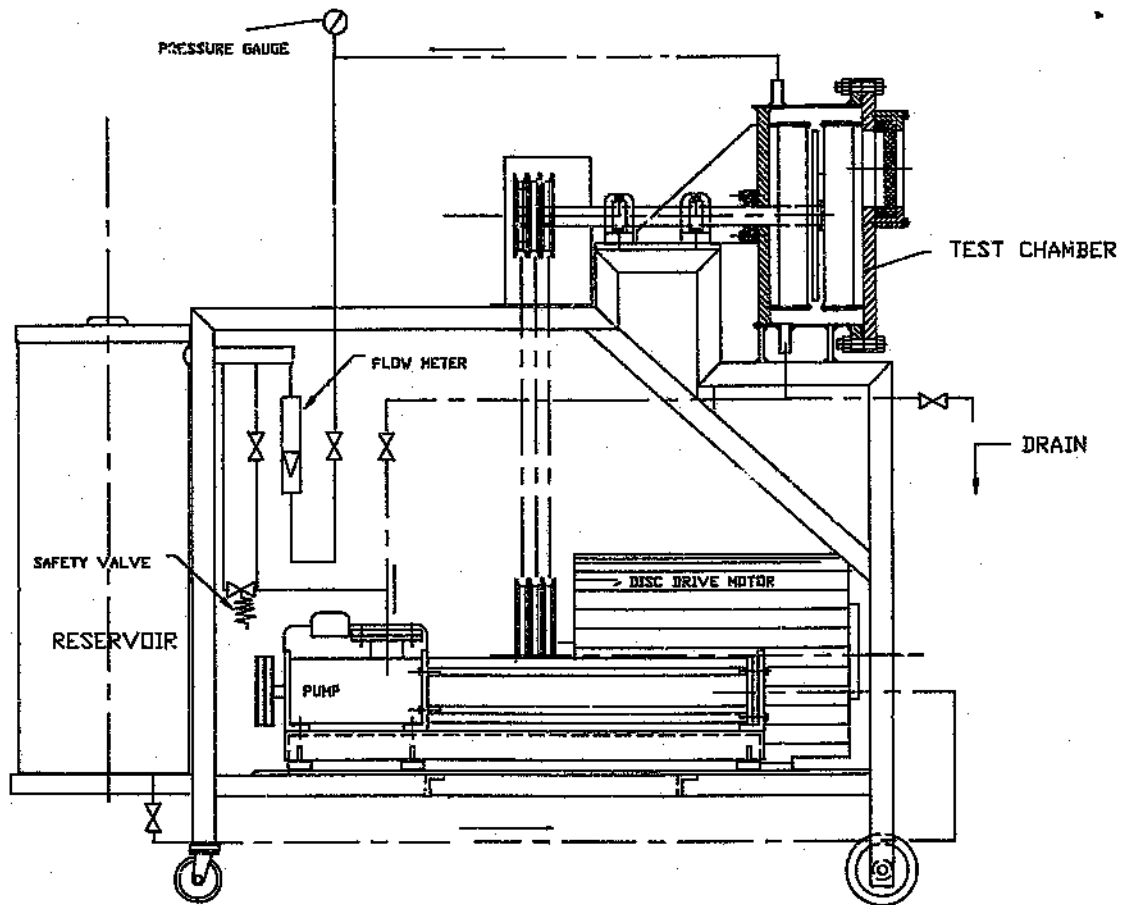
APPENDIX

Design drawings for rotating disc test apparatus



END VIEW

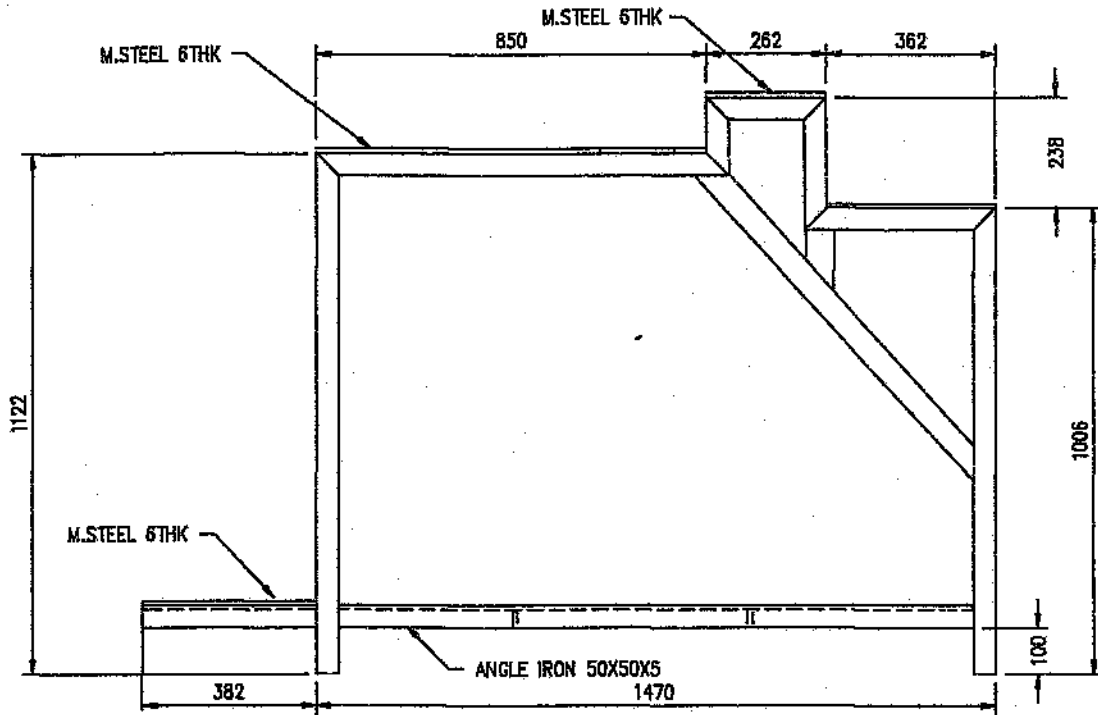
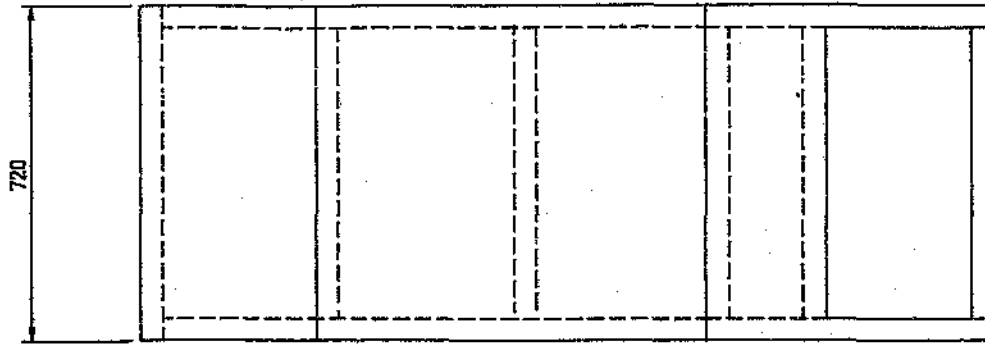
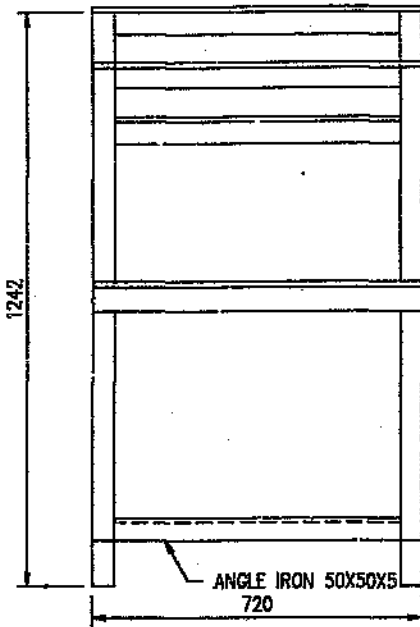
(RESERVOIR REMOVED)



3	09/2/8	JM	
ISSUE	DATE	DRAWN	REMARKS
UITGAVE	DATUM	GETEKEN	AANMERKING
M.A.T.		SCALE	
DESTEK		SKAAL	
DESIGN CC		DRAWN MK	
CHECKED MK		DATE 09/20/88/23	

CAVITATION TEST RIG

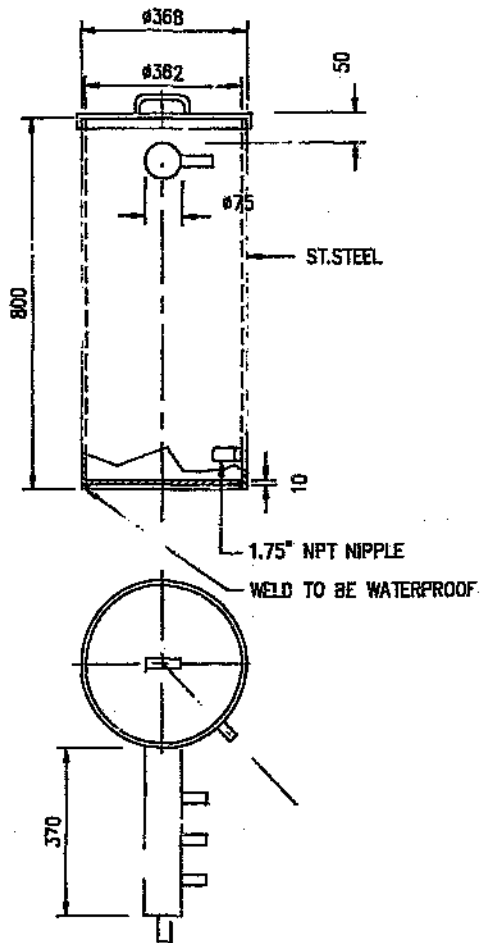
2654-1



	21/7/85		
ISSUE	DATE	DRAWN	REMARKS
UITGAWE	DATUM	GETEKEN	AANMERKING
MAT.	50 SQ TUBING	SCALE	1:10
		SKAAL	
ISS	PHOTOLA	YTD	SABS 0111
CSIR		VNR	

FRAME

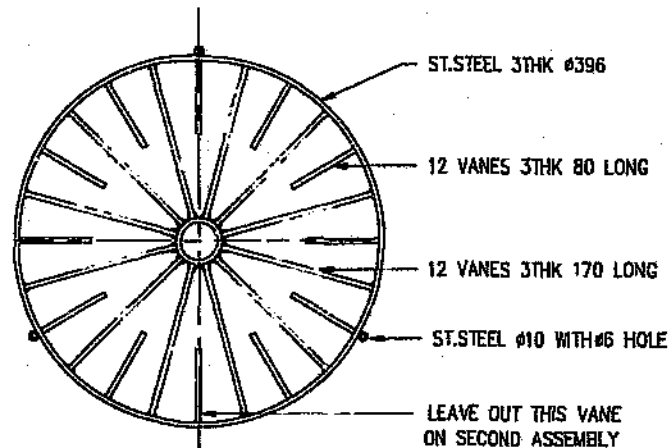
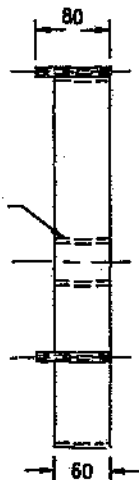
2654-2



RESERVOIR (SCALE 1:10)

TOP VIEW

ST. STEEL BUSH
OD 50, ID 42



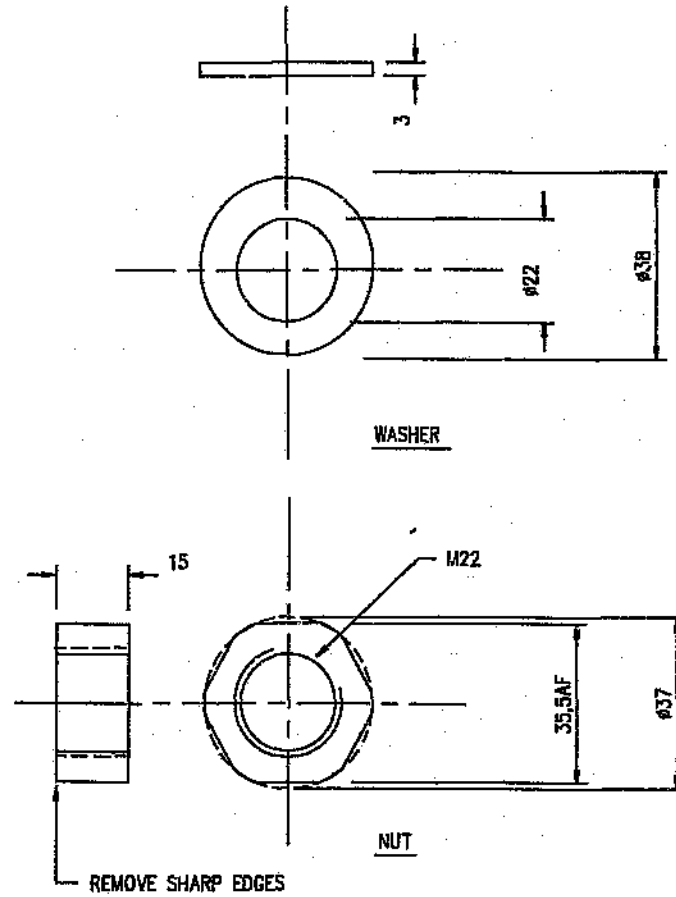
STATOR ASSEMBLY (SCALE 1:5)


2 X OFF

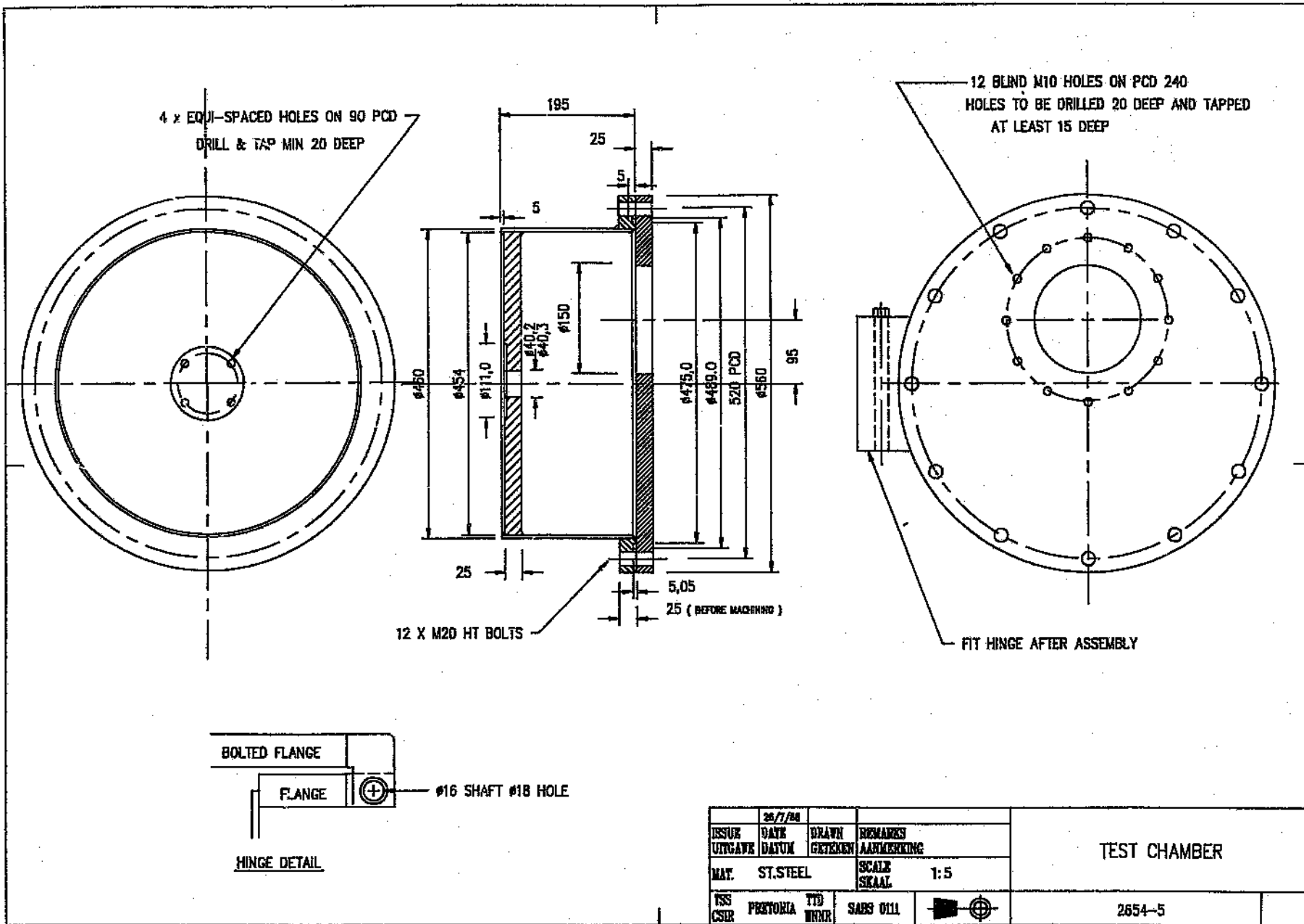
ISSUE	20/11/88	DATE	20/11/88	DATE	20/11/88	REMARKS
UITGAWE	DATUM	TREK	TEKENEK	TEKENEK	TEKENEK	AANMERKING
MAT.	ST. STEEL	SCALE	SKAAL			
TSE	PRETORIA	TID	WIMR	SABS 0111		

RESERVOIR AND
STATOR ASSEMBLY

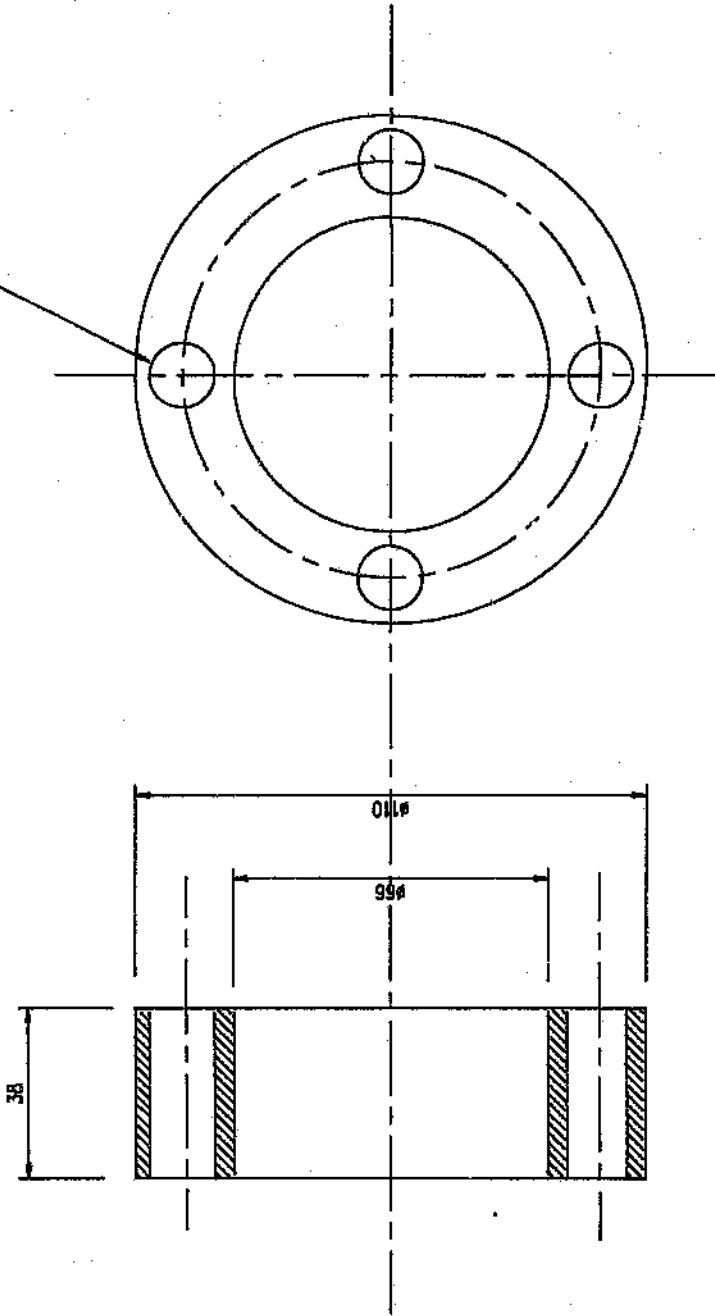
2654-3



ISSUE	22/7/20			
DATE				
UITGANG	DATUM	TREK	REMARKS	
			AANMERKING	
MAT.	AS SHOWN		SCALE	1:1
			SKAAL	
TSS	PRETORIA	TTO	SABS 0111	
CSR		WNR		
				SHAFT WASHER & NUT
				2654-4

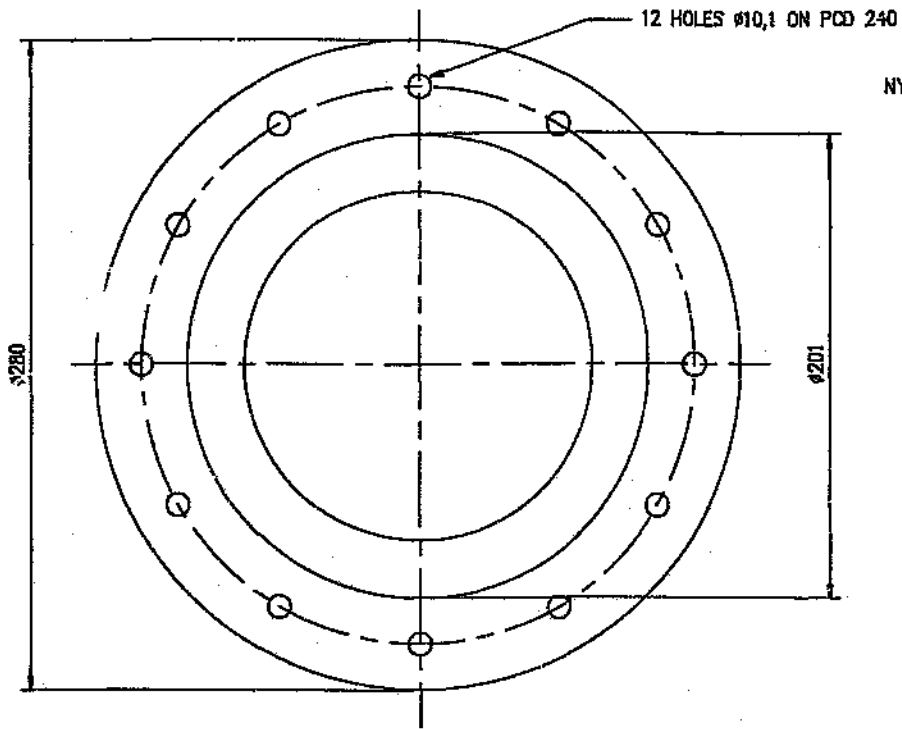


4X Ø 14 HOLES EQUI-SPACED ON 90 PCD

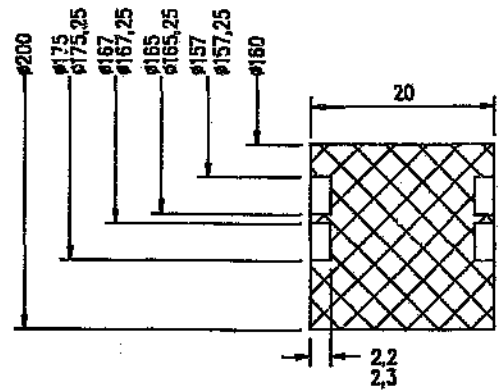
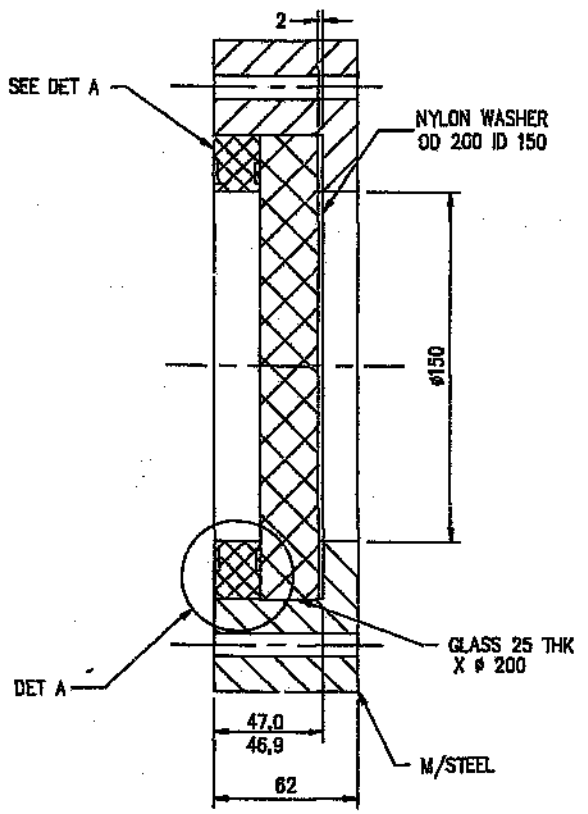


ISSUE DATE		DRAWN BY		REMARKS	
01/11/86		G. J. VAN DER MERWE		AMENDMENT	
MATERIAL		SCALE		1:1	
M/STEEL		SEAL		SEAL	
TSS CODE		TSS PART		SANS OIL	
PRETORIA		100		2654-6	

SEAL HOUSING



NYLON WASHER SEE DET A

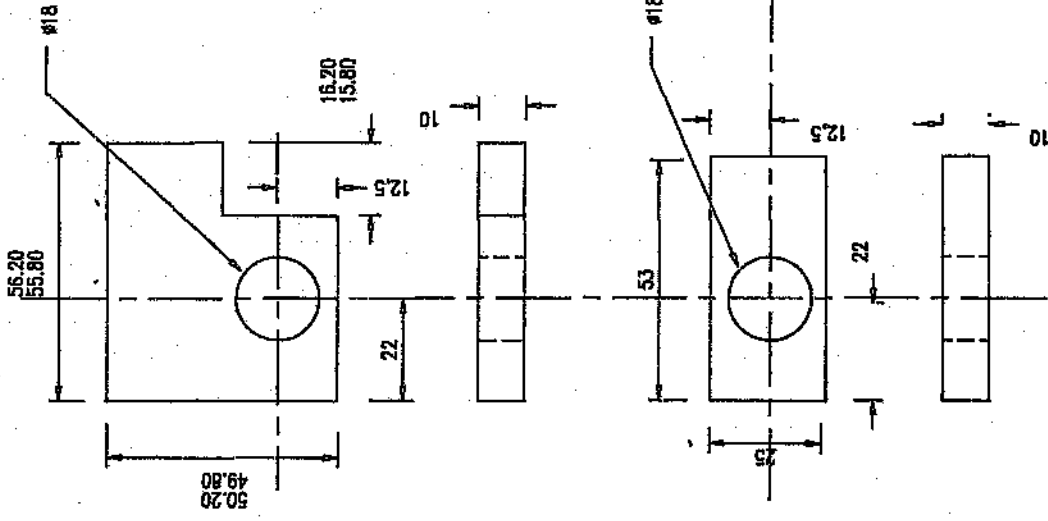
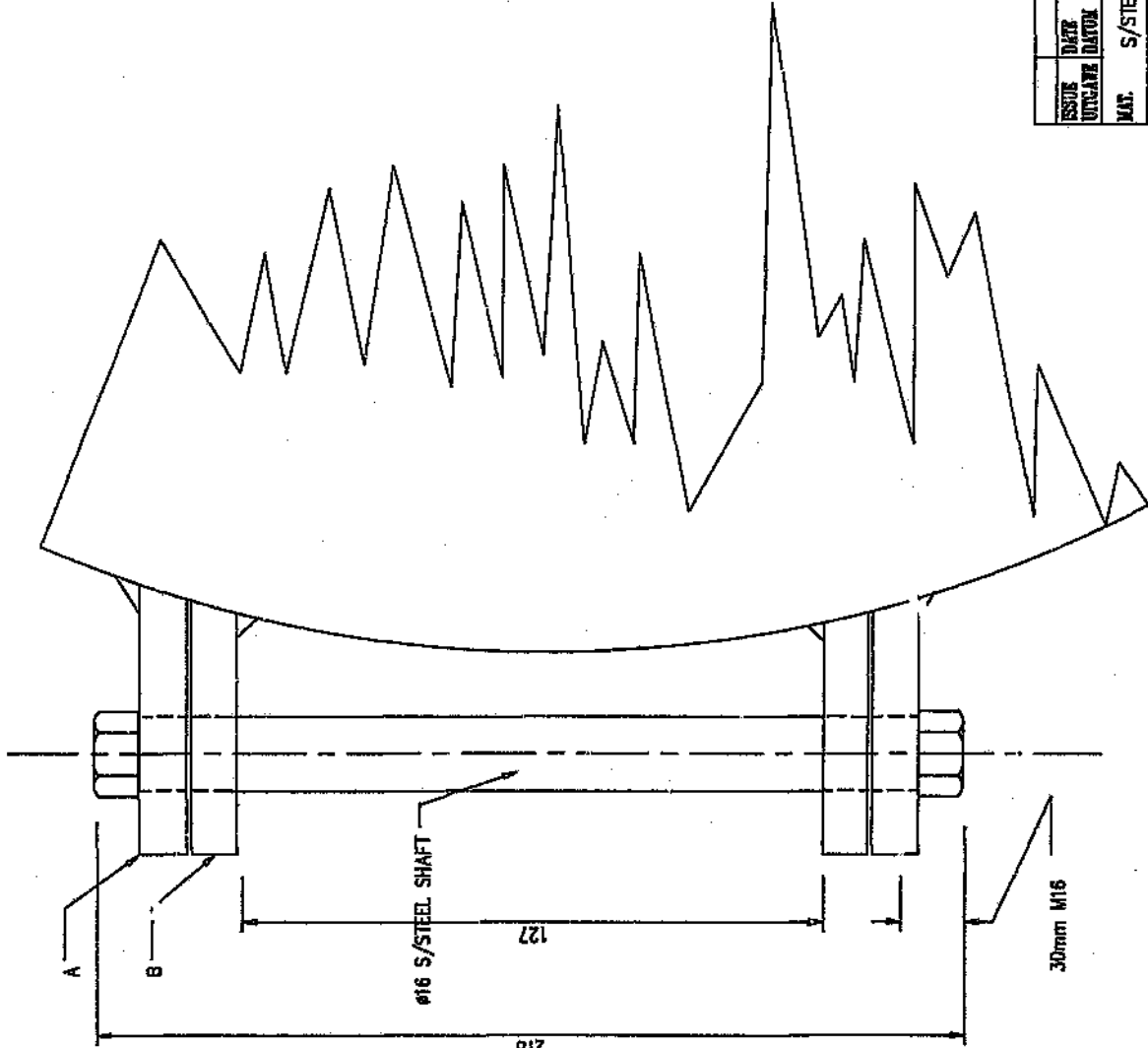


2 X OFF O-RING GACO RM1595-30
 2 X OFF O-RING GACO RM1695-30

ISSUE	29/7/03	DATE	DRAWN	REMARKS
OUTGAVE	DATUM	GETEKEN	AANKOMING	
MAT.	AS SHOWN	SCALE	1:2	
TSS	PRETORIA	TTD	SABS 0111	
CSIR	WVNR			

WINDOW HOUSING

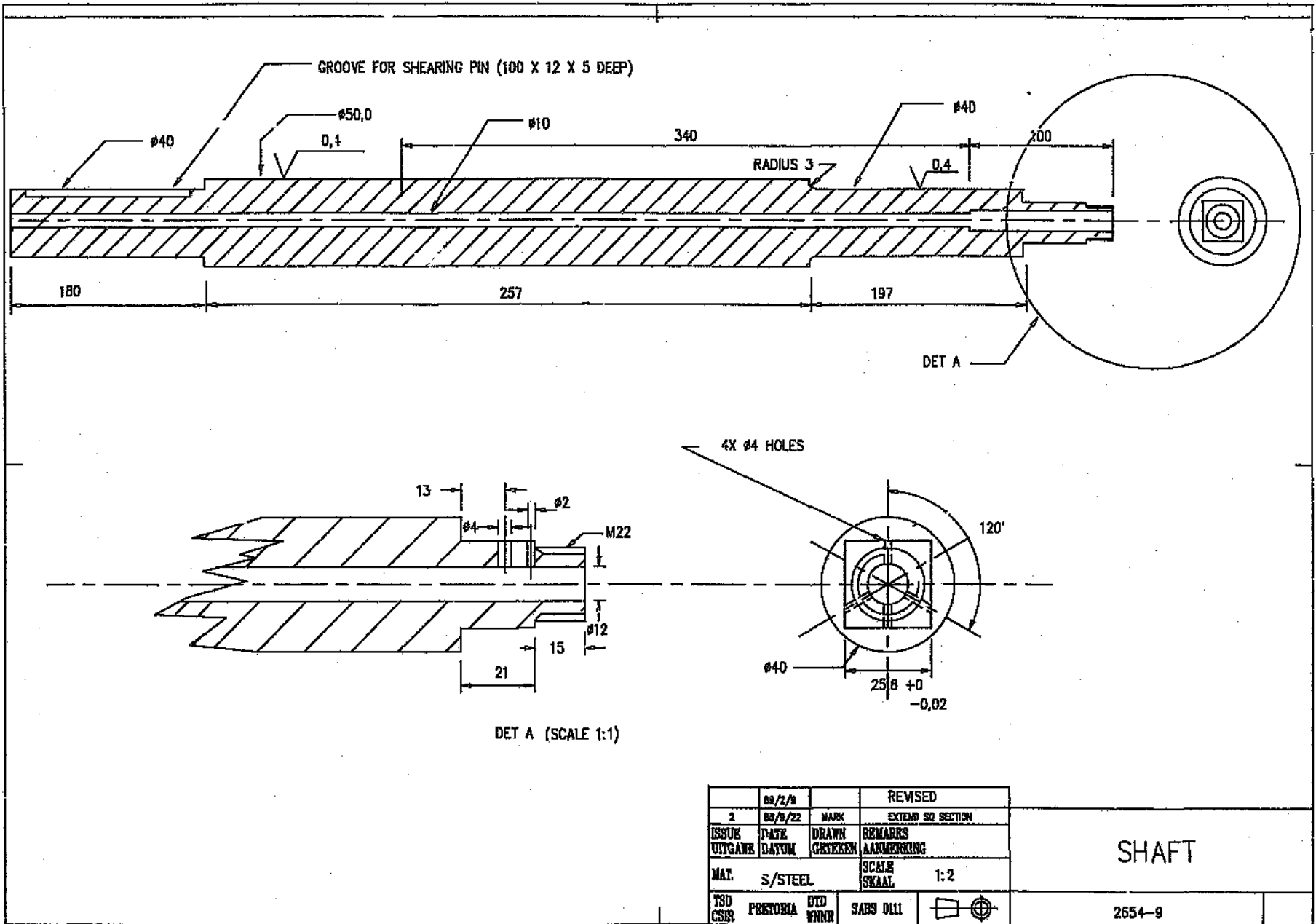
2654-7

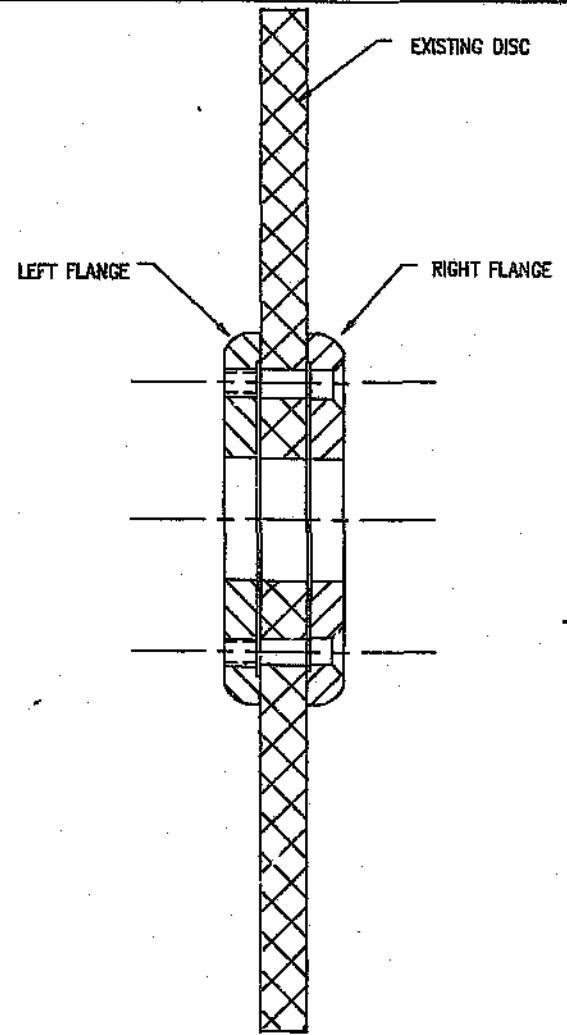
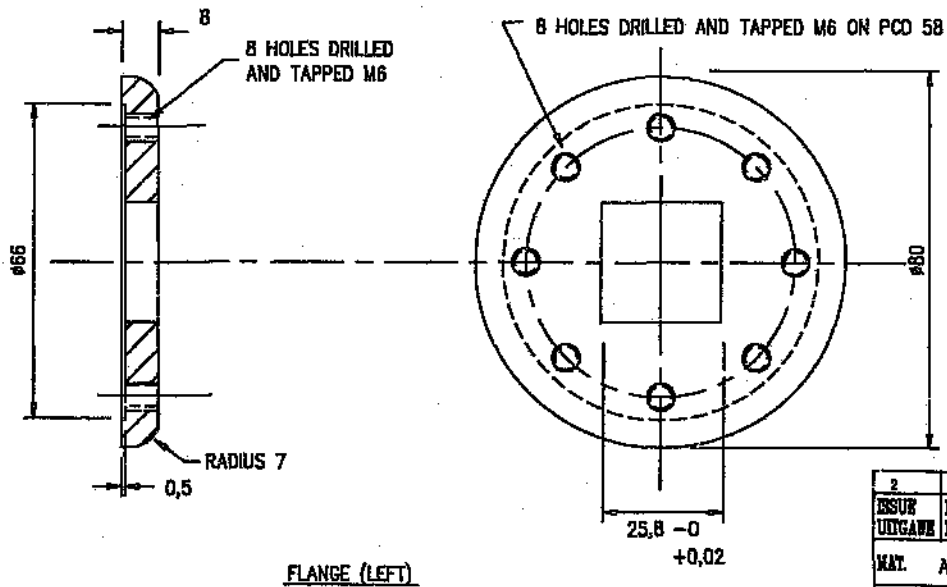
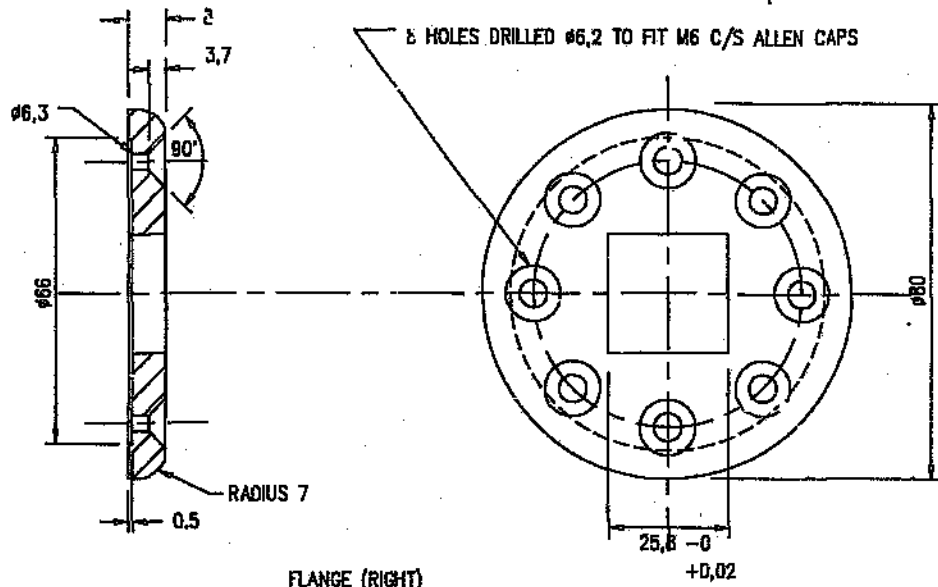


ISSUE	DATE	DRAWN	REMARKS
0001	01/01/01	GETTICK	AMENDMENT
MAT.	S/STEEL	SCALE	1:1
150	PROTECTOR	UNIT	SABS OIL
CSR	WINN		

HINGE

2654-8





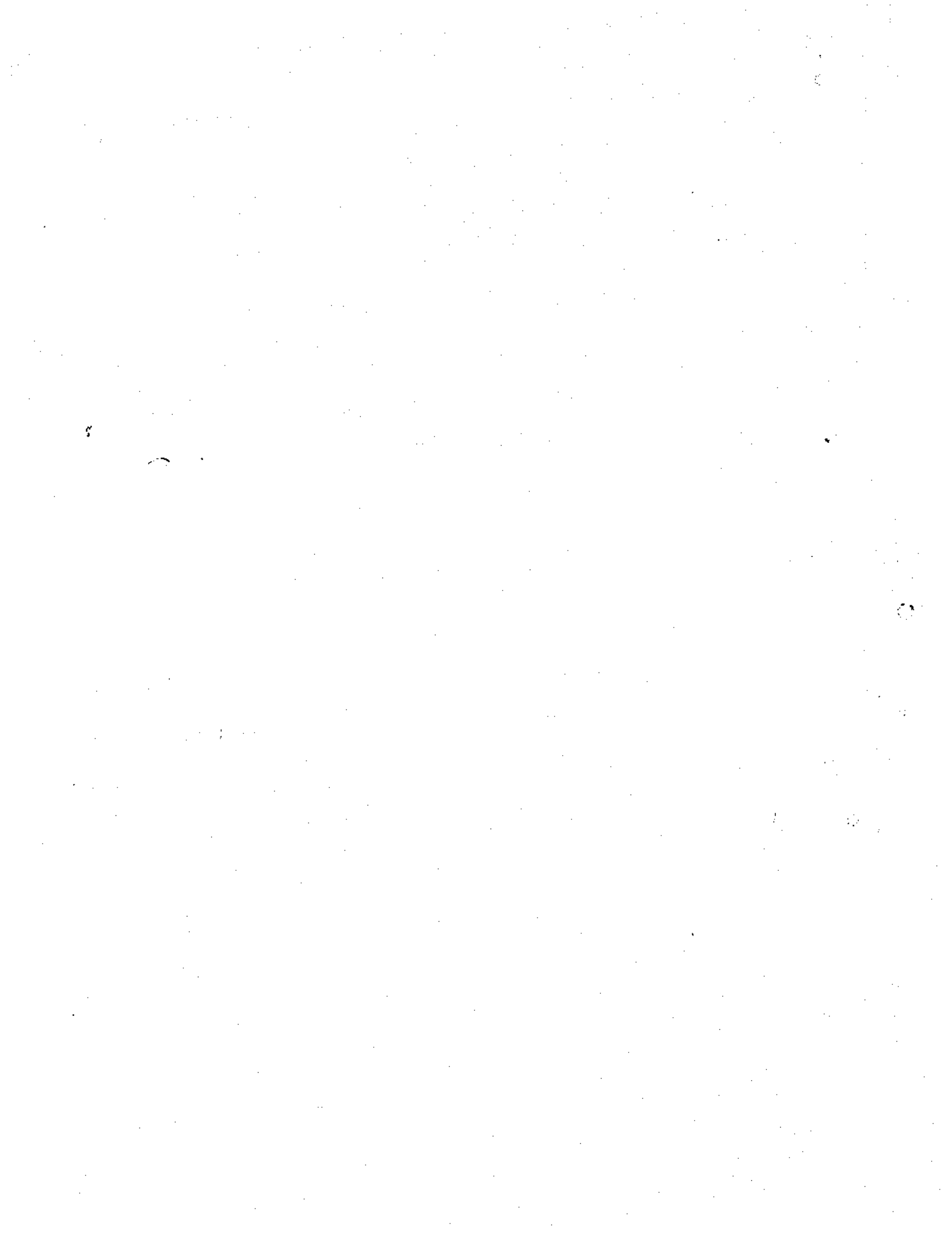
ASSEMBLY DRAWING

2	30/2/9		
ESUR	DATE	DRAWN	REMARKS
UDGANE	DATUM	GETEKEN	AANMERKING
MAT.	AS SHOWN	SCALE	1:1
ESD	PRETORIA	DTD	
CSIR	WVRR	SABS 0111	

CLAMPING FLANGES

2654-0





Author: Auret Johannes Gerhardus.

Name of thesis: Cavitation erosion- the effect of fluid and flow parameters.

PUBLISHER:

University of the Witwatersrand, Johannesburg

©2015

LEGALNOTICES:

Copyright Notice: All materials on the University of the Witwatersrand, Johannesburg Library website are protected by South African copyright law and may not be distributed, transmitted, displayed or otherwise published in any format, without the prior written permission of the copyright owner.

Disclaimer and Terms of Use: Provided that you maintain all copyright and other notices contained therein, you may download material (one machine readable copy and one print copy per page) for your personal and/or educational non-commercial use only.

The University of the Witwatersrand, Johannesburg, is not responsible for any errors or omissions and excludes any and all liability for any errors in or omissions from the information on the Library website.